

## N O T I C E

THIS DOCUMENT HAS BEEN REPRODUCED FROM  
MICROFICHE. ALTHOUGH IT IS RECOGNIZED THAT  
CERTAIN PORTIONS ARE ILLEGIBLE, IT IS BEING RELEASED  
IN THE INTEREST OF MAKING AVAILABLE AS MUCH  
INFORMATION AS POSSIBLE



Technical Memorandum 83907

STAR  
(1436)

# RESEARCH REVIEW-1980/81

(NASA-TM-83907) MODELING AND SIMULATION  
FACILITY: RESEARCH REVIEW, 1980 - 1981  
(NASA) 213 p HC A10/MF A01

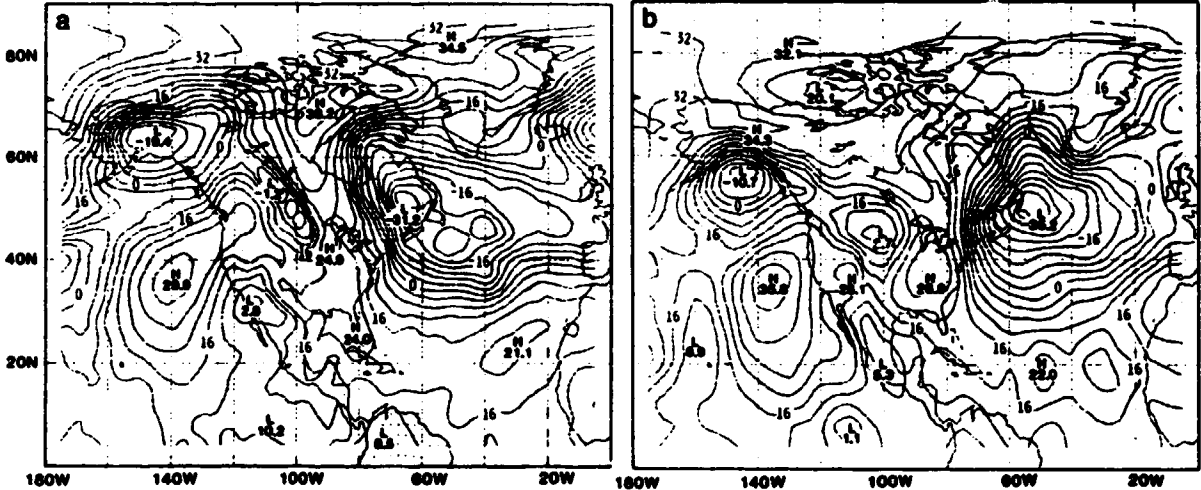
CSCCL 08F

N82-25551  
THRU  
N82-25587  
Unclas

G3/42 21233

**GLAS EIGHT-DAY FORECAST  
FROM JAN. 29, 1979**

**SEA LEVEL PRESSURE VERIFICATION  
FOR FEB. 6, 1979**



**MODELING AND SIMULATION FACILITY  
LABORATORY FOR ATMOSPHERIC SCIENCES  
DECEMBER 1981**

National Aeronautics and  
Space Administration

**Goddard Space Flight Center  
Greenbelt, Maryland 20771**



RESEARCH REVIEW - 1980/81

MODELING AND SIMULATION FACILITY  
LABORATORY FOR ATMOSPHERIC SCIENCES

DECEMBER 1981

NASA GODDARD SPACE FLIGHT CENTER  
GREENBELT, MARYLAND

## TABLE OF CONTENTS

I.	INTRODUCTION . . . . .	3
II.	GLOBAL WEATHER/OBSERVING SYSTEMS	
	A. Analysis and Forecast Studies	
	The Effect of Varying Amounts of Satellite Data, Orography and Diabatic Processes on the Numerical Prediction of an Intense Cyclone . . . R. ATLAS . . . . .	7
	The Relative Contributions of Increased Resolution in the Data Assimilation and in the Forecast Model to Satellite Data Impact . . R. ATLAS, M. GHIL, and M. HALEM . . . . .	11
	The Effects of Tropical Wind Data on the Prediction of Ultralong Waves . . W. E. BAKER . . . . .	14
	The State of the Atmosphere as Inferred from the FGGE Satellite Observing System During SOP-1 . . M. HALEM, E. KALNAY, W. E. BAKER, and R. ATLAS . . . . .	20
	Numerical Prediction of the Large Scale Tropical Flow . . E. KALNAY, W. E. BAKER, and J. SHUKLA . . . . .	37
	B. Satellite Temperature and Wind Retrievals	
	Interactive Processing of SEASAT Scatterometer Data . . R. ATLAS, G. COLE, A. PURSCH, and C. LONG . . . . .	49
	Preliminary Evaluation of the FGGE Special Effort for Data Enhancement . . R. ATLAS, A. PURSCH, C. LONG, G. COLE, and R. ROSENBERG . . . . .	52
	Comparison of Observed and Computed Brightness Temperatures for the HIRS2 and MSU Sounders on TIROS-N . . J. SUSSKIND, J. ROSENFELD, and D. REUTER . . . . .	61
	C. Analysis and Model Development	
	Solution of Linear System of Equations When the Matrix Is Circulant . . R. C. BALGOVIND . . . . .	71
	An Analysis of Intermittent Updating for the Shallow Water Equations . . K. P. BIJBE . . . . .	74

TABLE OF CONTENTS (Continued)

Assimilation of Asynoptic Data and the Initialization Problem . . . . . 78  
 K. P. BUBE and M. GHIL . . . . .

Applications of Estimation Theory to Numerical Weather Prediction . . . . . 79  
 S. COHN, M. GHIL, and E. ISAACSON . . . . .

A Stochastic-Dynamic Model for Global Atmospheric Mass-Field Statistics . . . . . 81  
 M. GHIL, R. BALGOVIND, and E. KALNAY . . . . .

A Variable Vertical Resolution Weather Model with an Explicitly Resolved . . . . . 82  
 Planetary Boundary Layer . . H. M. HELFAND . . . . .

A Four Dimensional Variational Analysis Experiment . . R. HOFFMAN . . . . . 84

SASS Wind Ambiguity Removal by Direct Minimization . . R. HOFFMAN . . . . . 87

A Simple Atmospheric Model on the Sphere with 100% Parallelism . . . . . 89  
 E. KALNAY and L. L. TAKACS . . . . .

On the Effect of High Latitude Filtering in Global Grid Point Models . . . . . 96  
 L. L. TAKACS, R. BALGOVIND, M. IREDELL, AND E. KALNAY . . . . .

Shallow Water Experiments Using an Improved Kreiss-Oliger . . L. L. TAKACS  
 and R. C. BALGOVIND . . . . . 105

D. Atmospheric Dynamics and Diagnostic Studies

A Model to Determine Open or Closed Cellular Convection . . H. M. HELFAND,  
 and E. KALNAY . . . . . 117

Large Amplitude Stationary Rossby Waves in the Southern Hemisphere . . . . . 119  
 E. KALNAY and M. HALEM . . . . .

Multiple Equilibria and Vacillation on the Sphere, with Application to  
 Blocking . . B. LEGRAS and M. GHIL . . . . . 131

The Role of Zonally Asymmetric Heating in the Vertical and Temporal  
 Structure of the Global Scale Flow Fields During FGGE SOP-1 . . . . . 132  
 J. PAEGLE, E. KALNAY, and W. E. BAKER . . . . .

Integrated and Spectral Energy Flows of the GLAS GCM . . J. TENENBAUM . . . . . 142

A Numerical Model Study of Long-Term Planetary Waves . . R. L. WOBUS . . . . . 145

## TABLE OF CONTENTS (Continued)

### III. CLIMATE/OCEAN-AIR INTERACTIONS

#### A. Data Analysis

Climate Model Postprocessing . . . J. ABELES, E. PITTARELLI, and D. A. RANDALL . . . . .	149
Seasonal Cycle of Heights, Temperatures, and Sea Level Pressure Over the Northern Hemisphere . . . B. DOTY AND K. C. MO . . . . .	153
Analysis of the Surface Heat Balance Over the World Ocean . . S. K. ESBENSEN . . . . .	158
Spatial and Temporal Scales of Time-Averaged 700 mb Height Anomalies . . D. GUTZLER . . . . .	163
Mid-Latitude Wind Forced Ocean Circulation Studies . . D. E. HARRISON . .	170
Sea Surface Data Studies . . D. E. HARRISON . . . . .	176
Global Fields of Soil Moisture and Land-Surface Evapotranspiration . . Y. MINTZ and Y. SERAFINI . . . . .	178
Seasonal Variation of Blocking . . J. SHUKLA and K. C. MO . . . . .	181

#### B. Climate Modeling

The Seasonal Cycle Climate Model . . L. MARX and D. RANDALL . . . . .	185
Quasi-Lagrangian Models of Nascent Thermals . . S. RAMBALDI and D. A. RANDALL . . . . .	188
Second-Order Closure Studies of Entrainment into a Stratocumulus Layer with Distributed Radiative Cooling . . D. A. RANDALL and C.-H. MOENG . . .	193
Some Aspects of Southwest Monsoon as Seen in a GLAS GCM Simulation . . V. SATYAN . . . . .	195

## TABLE OF CONTENTS (Continued)

### C. Sensitivity Experiments

An Analysis of the Cloud Fields Simulated by the GLAS Climate Model . . . C.-H. MOENG and D. A. RANDALL . . . . .	205
Climatology of Blocking in the GLAS Climate Model . . J. SHUKLA, K. C. MO, and M. EATON . . . . .	207
Structure and Dynamics of Monsoon Depressions: The MONEX Depression (1979) J. SHUKLA . . . . .	217
Numerical Prediction of the Monsoon Depression of 5-7 July 1979 . . J. SHUKLA, R. ATLAS, and W. E. BAKER . . . . .	223
Global and Local Fluctuations of Winter and Summer Simulations with the GLAS Climate Model . . D. M. STRAUS and J. SHUKLA . . . . .	231
Influence of Surface-Albedo in Subtropical Regions on July Circulations . . Y. SUD and M. FENNESSY . . . . .	237

### IV. SUMMER LECTURE SERIES

Does El Nino Affect Our Winter Climate? . . J. M. WALLACE . . . . .	243
An Attempt to Separate Changes Due to Statistical Sampling from Real Climate Change . . R. A. MADDEN . . . . .	244
Simulation of the January 1977 Blocking Event . . K. MIYAKODA . . . . .	245
On the Global Distribution of the Heat Sources and Sinks of the Atmosphere and the Thermally Forced Planetary Scale Response . . D. R. JOHNSON .	246
Comparisons of Visible and Infrared Distributions of Global Cloud Covers M. T. CHAHINE . . . . .	247
Dynamics of Sudden Stratospheric Warmings . . J. R. Holton . . . . .	251
The Behavior of Eddy Heat Fluxes on Short Time Scales . . P. H. Stone . . .	252
Normal Mode Initialization at ECMWF . . C. Temperton . . . . .	253
Large-Scale Boundary Layer Winds . . J. A. Young . . . . .	254
The Role of the Ocean in the Transient Climatic Response to Increasing Atmospheric CO <sub>2</sub> . . K. Bryan . . . . .	256
Transition to Turbulence in Shear Flows . . S. A. Orszag . . . . .	258

TABLE OF CONTENTS (Continued)

V. RECENT PUBLICATIONS . . . . . 261

VI. GMSF STAFF . . . . . 269

# I. INTRODUCTION

## I. INTRODUCTION

The Goddard Modeling and Simulation Facility (GMSF) of the Laboratory for Atmospheric Sciences (GLAS) is engaged in general circulation modeling studies related to global atmospheric and oceanographic research. The research activities are organized into two disciplines: Global Weather/Observing Systems and Climate/Ocean-Air Interactions.

The Global Weather activities are grouped in four areas: 1) Analysis and Forecast Studies, 2) Satellite Temperature and Wind Retrievals, 3) Analysis and Model Development, 4) Atmospheric Dynamics and Diagnostic Studies. During the period of this review, Global Weather Research was directed primarily toward the development of techniques for the utilization and analysis of the First GARP Global Experiment (FGGE) data sets. This involved acquisition and data file management efforts, development of improved techniques for the analysis of FGGE data, observing performance assessments, extended-range forecasts, and diagnostic studies. Observing system studies were concerned with the development of a GLAS TIROS-N sounding retrieval system and preparation for the joint NOAA/NASA Advanced Moisture and Temperature Sounder simulation study. Brief descriptions of several theoretical studies in the areas of analysis, forecast, and atmospheric dynamics are also included.

Climate research activities are focused in three areas: 1) Data Analysis, 2) Climate Modeling, and 3) Sensitivity Experiments. Ocean/air interaction studies are concentrated on the development of models for the prediction of upper ocean currents, temperatures, sea state, mixed-layer depths, and upwelling zones, and on studies of the interactions of the atmospheric and oceanic circulation systems on time scales of a month or more.

This research review contains a synopsis of extended abstracts in the Global Weather/Observing System studies, and Climate/Ocean-Air Interaction studies conducted at the Modeling and Simulation Facility for 1980-81 (Sections 2 and 3). Abstracts of the Summer Lecture Series, jointly sponsored by GMSF and the University of Maryland, are present in Section IV. Section V lists the recent publications by the GMSF and visiting scientists.

PRECEDING PAGE BLANK NOT FILMED

PRECEDING PAGE BLANK NOT FILMED

II. GLOBAL WEATHER/OBSERVING SYSTEMS

A. ANALYSIS AND FORECAST STUDIES

PRECEDING PAGE BLANK NOT FILMED

## THE EFFECT OF VARYING AMOUNTS OF SATELLITE DATA, OROGRAPHY AND DIABATIC PROCESSES ON THE NUMERICAL PREDICTION OF AN INTENSE CYCLONE

R. Atlas

Studies of the growth of forecast error for numerical models have resulted in quantitative estimates of the amount of error contributed by each of the major features of the dynamical prediction system (Robert, 1976). In recent years, a number of experiments have been conducted to assess the usefulness of satellite temperature sounding data in weather prediction (Ohring, 1979). Objective measures of forecast accuracy have served as the primary tool for evaluating the predictive impact of the satellite sounding data. In addition, a limited number of subjective evaluations and case studies have been performed. Recently, a detailed subjective evaluation of the effect of horizontal resolution on satellite sounding data impact for the January-March 1976 Data Systems Test (DST-6) period was performed (Atlas et al., 1979). Assimilation cycles were carried out from 29 January to 21 February 1976 with coarse ( $4^\circ$  latitude by  $5^\circ$  longitude) and fine ( $2.5^\circ$  latitude by  $3^\circ$  longitude) resolution versions of the GLAS second-order general circulation model. For each model resolution, an assimilation cycle (referred to as SAT) was run using both conventional and special DST data, which included temperature soundings from the NOAA-4 and Nimbus-6 satellites. A second cycle (referred to as NOSAT) was run using the same data but excluding the satellite-derived temperature soundings. Eleven 72 h forecasts utilizing the same resolution in the forecast model as in the data assimilation were performed at 48 h intervals for each assimilation. This evaluation revealed a larger beneficial influence of the satellite sounding data with the fine model than had previously been found with the coarse model (Ghil et al., 1979). In this paper, descriptive results from a study of cyclone evolution in the DST-6 forecast case from 0000 GMT 19 February 1976 will be presented. This study was aimed at assessing the effects of satellite data, orography and diabatic processes on the numerical prediction of cyclone development and displacement.

## 2. SYNOPTIC SITUATION

At 0000 GMT 19 February 1976, a moderately intense low-pressure system, associated with an upper-level short-wave trough, was located off the northwest coast of the United States. As the system moved inland, a new low developed along an existing stationary front, and became the dominant feature by 1200 GMT on February 19. During the next 24 h, the low moved southeastward and intensified, after which time it recurved and then accelerated toward the northeast. This cyclone was accompanied by heavy snow, blizzard conditions, and severe thunderstorms and tornadoes.

## 3. THE EVOLUTION OF SATELLITE SOUNDING DATA IMPACT

Fig. 1 shows the sea-level pressure analysis at 0000 GMT 22 February and the observed cyclone track. Figs. 2 and 3 depict the 72 h NOSAT and SAT sea level pressure forecasts and predicted cyclone tracks that were obtained using fine ( $2.5^\circ$  lat. by  $3^\circ$  long.) resolution in the assimilation and in the forecast model. Comparisons of these charts reveal that a very significant improvement

in the predicted displacement of the surface low resulted from the inclusion of satellite data. The fine model forecast from NOSAT initial conditions predicted the low to move southward during the last half of the forecast, while the fine model SAT prediction correctly indicated recurvature of the low to the northeast. As a result, there was a more than 1000 km reduction in the vector error of the low pressure center's predicted position.

A study was conducted to determine (1) why the surface lows in the two forecasts suddenly diverge and more differently during the latter half of the forecast, and (2) if differences in the forcing for the cyclone, at the time the two forecasts diverge, can be traced to initial state differences between the SAT and NOSAT systems. To answer these questions, maps and cross-sections of a number of primary variables and derived quantities related to the dynamics of the cyclone were examined. The synoptic results of this study (presented by Atlas et al., 1979) showed how the prognostic impact evolved from an enhancement of the thermal and vorticity fields in the SAT initial state. As shown by Atlas et al., amplification of the initial state differences resulted in differing phase relationships between the upper-level vorticity maximum and the surface low and differing thickness advection patterns by 0000 GMT 21 February, which produce the diverging paths of the surface low throughout the remainder of the forecasts.

The initial state differences for this forecast were the result of a time-continuous assimilation of satellite temperature sounding data which began on 29 January 1976. To further understand the role of the sounding data, additional fine model forecasts were generated in which varying amounts of satellite data were excluded from the assimilation. Exclusion of satellite soundings after 1800 GMT 18 February produced no noticeable change in the initial state at 0000 GMT 19 February or the 72 h forecast from this time. However, major initial state and prognostic differences were observed when satellite data was excluded during the 12 h or 24 h of the assimilation preceding 0000 GMT 19 February. Figs. 4 and 5 show the 72 h sea-level pressure forecasts from 0000 GMT 19 February produced by the fine model when satellite data is excluded from the assimilation after 0000 GMT and 1200 GMT 18 February respectively. Comparison of these figures with (Figs. 2 and 3) shows the progressive improvement of the prediction which results from the assimilation of additional satellite data. Examination of the initial states for these forecasts (charts not shown) revealed a gradual enhancement of the thermal vorticity field with the assimilation of additional satellite data.

#### 4. EFFECT OF PHYSICAL PROCESSES

A fine model forecast from SAT initial conditions was performed in which all moist and radiative processes were excluded from the model. Comparison of this prediction with the corresponding forecast which utilized full model physics, showed the effect of diabatic processes to be very small during the first 48 h of the prediction. Following the recurvature of the low, diabatic processes became more important, as warm moist air was advected northward in advance of the cyclone and severe convective activity developed. From 48-60 h, the rate of intensification of the cyclone in the full physics forecast was twice as large as that for the forecast which did not include diabatic processes. During the last 12 h of the forecast this effect did not amplify. Fig. 6 shows the 72 h sea-level pressure prognosis for the forecast which excluded diabatic

processes. Comparison of this figure with Fig. 3 shows the small diabatic effect on the intensity of the cyclone. We can conclude that moist and radiative processes in the model did not significantly affect the prediction in this case.

## 5. EFFECT OF OROGRAPHY

A fine model forecast from SAT initial conditions was performed with the height of all land above sea level set equal to one meter. Although this introduces an artificial representation of the atmosphere below high terrain, it still provides an indication of what the evolution of the cyclone would be if orographic effects were not present. During the first 12 h of the forecast, as the cyclone approaches the Rocky Mountains, there are no noticeable differences between the prediction with and without orography. After this time, as the cyclone crosses the mountains, major differences develop between the predictions, and the role of orography in modifying the evolution of the cyclone becomes evident. In particular, the maximum generation of low level cyclonic vorticity is shifted southward, to the lee of the largest slope of the terrain, in the run with orography. Fig. 7 shows the 72 h sea level pressure prognosis and cyclone track for the fine model forecast without mountains. In addition to the more northerly track, the cyclone in this forecast is larger in scale than the cyclone in Fig. 3.

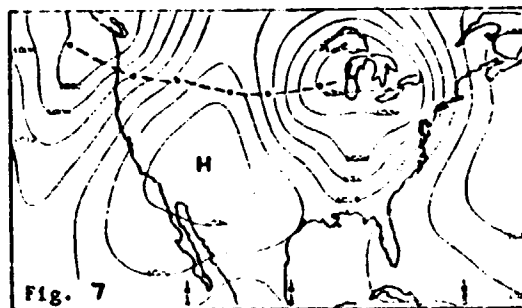
## ACKNOWLEDGEMENTS

Discussions with Drs. W. E. Baker, M. Ghil, M. Halem, D. R. Johnson, E. Kalnay, N. Phillips and L. Uccellini contributed greatly to this work.

## REFERENCES

- Atlas, R., M. Halem, and M. Ghil, 1979: Subjective evaluation of the combined influence of satellite temperature sounding data and increased model resolution on numerical weather forecasting. Preprints, Fourth Conference on Numerical Weather Prediction, Silver Spring, Maryland, Amer. Meteor. Soc., 319-328.
- Ghil, M., M. Halem, and R. Atlas, 1979: Time-continuous assimilation of remote-sounding data and its effect on weather forecasting. Mon. Wea. Rev., 107, 140-171.
- Ohring, G., 1979: Impact of satellite temperature sounding data on weather forecasts. Bull. Amer. Meteor. Soc., 60, 1142-1157.
- Robert, A., 1976: Sensitivity experiments for the development of NWP models. Proceedings of the (Eleventh) Stanstead Seminar, Publication in Meteorology No. 114, McGill University, Montreal, Canada, 68-81.

ORIGINAL PAGE IS  
OF POOR QUALITY



Figures 1-7. Sea-level pressure analysis and 72h forecasts for 0000 GMT 22 February 1976. Cyclone positions at 12h intervals denoted by dots. See text for additional details.

THE RELATIVE CONTRIBUTIONS OF INCREASED RESOLUTION IN THE DATA ASSIMILATION  
AND IN THE FORECAST MODEL TO SATELLITE DATA IMPACT

R. Atlas, M. Ghil, and M. Halem

The results presented by Atlas et al. (1979) indicate that the GLAS model forecast accuracy during the January-March 1976 Data Systems Test (DST-6) was significantly improved by the assimilation of satellite sounding data as well as by increased horizontal resolution, and that the practical utility of the sounding data was actually enhanced by the increased resolution. The question remains as to whether increased resolution had a larger effect on the forecasting skill of the numerical prediction model, or on the assimilation cycle. Assimilation cycles were carried out with data from 0000 GMT 29 January to 0300 GMT 21 February 1976 with two versions of the GLAS second-order GCM: a coarse version with 4° latitude by 5° longitude resolution, called the C-model, and a fine version with 2.5° latitude by 3° longitude resolution called the F-model. For the two DST-6 cases where the combined influence of satellite data and model resolution are at a maximum at sea level, i.e., the forecasts from 11 February and 19 February 1976, the relative contributions of increased resolution in the data assimilation and in the forecast models have been evaluated. F-model forecasts were generated from the C-model SAT assimilation interpolated to the F-grid, and C-model forecasts were generated from the F-model SAT assimilation interpolated to the C-grid. We shall denote the former by CFS and the latter by FCS. These forecasts were then compared with the corresponding forecasts which had utilized the same grid resolution in the data assimilation and forecast models, CS and FS.

Fig. 1 presents the  $S_1$  scores for the sea level pressure forecasts from 19 February 1976 as verified over North America at 12 h intervals; Fig. 2 shows the  $S_1$  scores for the 11 February case. The combined effect of increased resolution in the data assimilation and in the forecast model is represented by the difference in  $S_1$  between the F-model forecasts from the F-assimilation (FS) and the C-model forecasts from the C-assimilation (CS). The impact of increased resolution in the data assimilation alone is obtained by subtracting the  $S_1$  scores for the C-model forecasts from the F-assimilation (FCS) from the corresponding  $S_1$  scores for the C-model forecasts from the C-assimilation (CS). The impact of increased resolution in the forecast model, but not in the assimilation, is obtained in a similar manner by subtracting the  $S_1$  scores for the F-model forecasts from the C-assimilation (CFS) from the  $S_1$  scores for the C-model forecast from the C-assimilation (CS).

Comparison of the forecasts from 19 February (Fig. 1) indicates that both increased resolution in the assimilation and increased resolution in the forecast model contributed to the improvement of forecast accuracy at most verification times; the effects, however, are not strictly additive. The improvement of forecast accuracy resulting from increased resolution in both the assimilation and forecast model is larger than the sum of the impacts of increased resolution in the assimilation and increased resolution in the forecast model at all verification time periods. During the first 24 h, increased assimilation results in a small improvement in accuracy, while increased forecast model resolution results in a slight degradation of forecast skill. At 36 h, both effects are beneficial and of comparable magnitude. From 48 h to 60 h,

the beneficial effect of forecast model resolution is much larger than the effect of assimilation resolution. At 72 h, they are once again of similar magnitude.

The  $S_1$  verification for the forecasts from 11 February (Fig. 2) shows what difference results. In this case, the effect of increased assimilation resolution (CS-FCS) and that of increased forecast model resolution (CS-CFS) taken separately are both slightly negative and of nearly identical magnitude at 12 h. In contrast, the forecast which utilized increased resolution in both the assimilation cycle and in the forecast model shows a modest improvement at this time. At 24 h, there is a negligible impact of increased resolution in the assimilation, but a modest beneficial impact of increased forecast model resolution. The latter impact by itself is slightly larger than the combined effect of increased resolution in both the assimilation and the forecast model. From 36 h to 60 h, the beneficial influence of increased forecast model resolution is much larger than the improvement resulting from increased resolution in the assimilation and nearly as large as the combined effect of increased resolution in both the assimilation and forecast model. At 72 h, there is a negligible influence of increased assimilation resolution, while the improvement of increased forecast model is significant and larger than the combined impact.

Our discussion of objective impact measures indicates that both increased resolution in the assimilation and increased resolution in the forecast model can act to improve forecast accuracy. In the 19 February case, each effect was important although the influence of forecast model resolution dominated at most time periods. In the 11 February case, the effect of forecast model resolution clearly was responsible for the large increase in accuracy between the C- and F-model results.

A subjective evaluation of the forecasts for these cases was conducted in order to determine if similar results would be found for the improvement of practical forecast utility. Comparison of the sea level pressure prognostic charts for each of the forecasts from 19 February showed the forecast which utilized increased resolution in both the assimilation and forecast model to be superior to all other forecasts at each time period, in agreement with the  $S_1$  verification. However, the C-model forecast from the F-assimilation (FCS) was substantially less useful than the F-model forecast from the C-assimilation (CFS) at all time periods after 12 h. In particular, the track and intensity of the cyclone over the United States was better predicted by CFS. The subjective evaluation of the forecasts from 11 February was in close agreement with the  $S_1$  verification. Comparison of these forecasts confirmed a greater beneficial influence of increased resolution in the forecast model.

## REFERENCES

- Atlas, R., M. Halem, and M. Ghil, 1979: Subjective evaluation of the combined influence of satellite temperature sounding data and increased model resolution on numerical weather forecasting. Preprints, Fourth Conference on Numerical Weather Prediction, Silver Spring, Maryland, Amer. Meteor. Soc., 319-328.

ORIGINAL PAGE IS  
OF POOR QUALITY

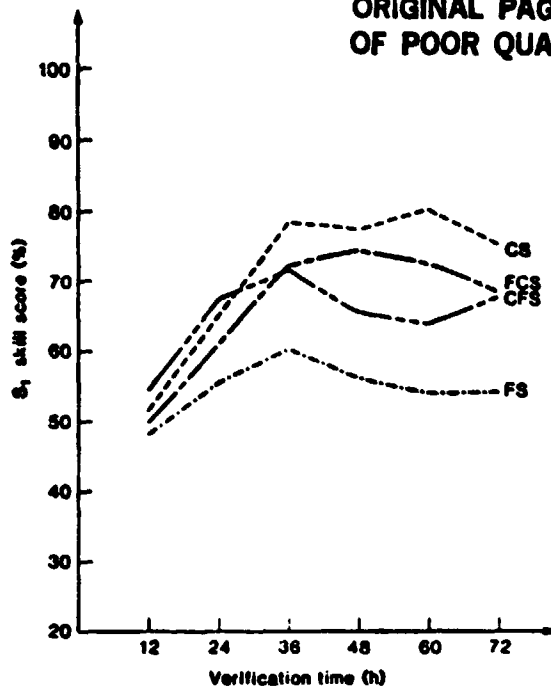


Fig. 1  $S_1$  score verification for the sea-level pressure forecasts for North America from 0000 GMT 19 February 1976. Results are presented for the coarse-model forecasts from coarse SAT initial conditions (CS) and fine SAT initial conditions (FCS), and for the fine model forecasts from fine SAT initial conditions (FS) and coarse SAT initial conditions (CFS).

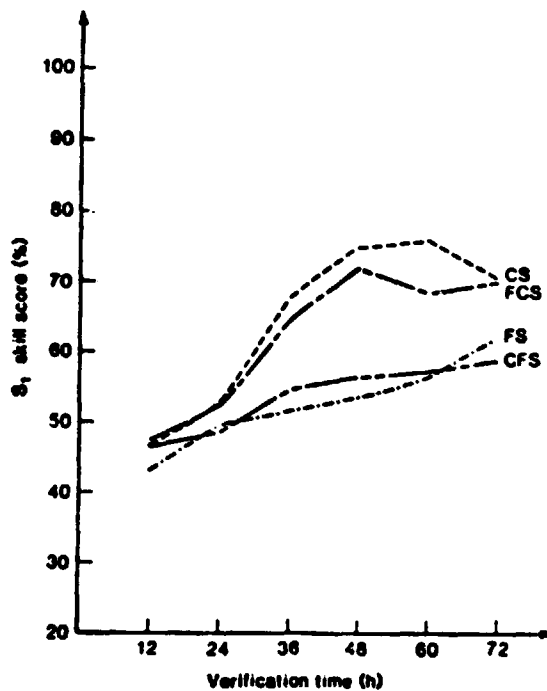


Fig. 2 Same as Fig. 1 for the forecasts from 0000 GMT 11 February 1976.

## THE EFFECTS OF TROPICAL WIND DATA ON THE PREDICTION OF ULTRALONG WAVES

W. E. Baker

Summary: This paper is a preliminary study of the influence of tropical wind data on the prediction of planetary waves in which two assimilation experiments are performed, one with and one without FGGE tropical winds. The planetary wave error is then analyzed in 72 h forecasts from the initial conditions provided by the two assimilations.

## 1. INTRODUCTION

Inaccurate specification of the initial conditions for numerical models is recognized as an important source of forecast error. Of particular concern is the contribution of the planetary wave error variance to the total error variance, estimated to be as much as 50% in the first two planetary waves by Baumhefner and Bettge (1981). The augmented observational database provided by FGGE offers a unique opportunity to further examine the role of initial data in numerical weather prediction, especially the effects of the data on planetary wave forecasts.

Recent model studies (Paegle, 1978) indicate that tropical disturbances may influence the subtropical jet streams, while analyses of a DST-6 assimilation experiment (Paegle *et al.*, 1979) suggest that low-latitude convective activity may propagate energy outside the tropics on short time scales. Kung and Burqdorf (1978) also found the A-B scale disturbances over the GATE region to be a source of eddy potential energy outside the region. In a simulation study (Gordon *et al.*, 1972), the insertion of tropical wind data resulted in a reduction of the wind error in the extratropics. Recently, Somerville (1980) has suggested that tropical data may affect the forecast of ultralong waves.

In the present study we examine the effects of tropical wind data from FGGE on the numerical prediction of ultralong waves by performing the real-data counterpart to the simulation study of Kasahara and Williamson (1972), which indicated a preferred global data coverage of winds in the tropics and temperatures outside the tropics, in agreement with geostrophic adjustment theory (Blumen, 1972). Using the Goddard Laboratory for Atmospheric Sciences (GLAS) 4th order general circulation model (Kalnay-Rivas and Hoitsma, 1979), two assimilation experiments are conducted. Experiment 1 utilizes wind data in the tropics (20°S to 20°N) and temperature data outside the tropics. Experiment 2 is the same as Experiment 1 except that no wind data are assimilated. Both experiments begin from the initial conditions of 0000 GMT 9 January 1979 provided by the 6 h first guess of the GLAS FGGE assimilation cycle. The data are then assimilated for a period of several days followed by a series of 72 h forecasts generated from initial conditions provided by each experiment. In the following sections, we describe the assimilation/forecast model, the FGGE data utilized in these experiments, the objective analysis and assimilation procedure, and the differences in the ultra-long wave predictions.

## 2. OBJECTIVE ANALYSIS AND ASSIMILATION OF THE FGGE DATA

In this section the objective analysis and assimilation procedure utilized with the FGGE data is described.

### 2.1 The Assimilation/Forecast Model

The model utilized in this study is the global 4th order GLAS general circulation model described in detail in Kalnay-Rivas *et al.* (1977) and Kalnay-Rivas and Hoitsma (1979). The model is based on an energy conserving scheme with horizontal differences computed with 4th order accuracy. A 16th order Shapiro (1970) filter is applied every 2 h to the sea level pressure, wind, and potential temperature fields. There are 9 vertical layers equal in sigma with a uniform horizontal grid (4° in latitude by 5° in longitude). A non-staggered horizontal grid, the Arakawa (1972) A grid, is used in the current model. The Arakawa B grid was employed in the earlier 2nd order version of the model (Somerville *et al.*, 1974). With the exception of the computation of the longwave radiation (Wu, 1980), the parameterization of the physical processes in the 4th order model is substantially the same as in the 2nd order model.

### 2.2 The Data

For this study we utilize the data collected during the first FGGE Special Observing Period (SOP-1) from 9-17 January 1979. This period was selected because of the presence of strong high-level divergence in the tropical Pacific during this time (Paegle, 1981). Table 1 summarizes the data assimilated in the two experiments.

Table 1. Tropical (20°S to 20°N) and extratropical FGGE data assimilated from 9-17 January 1979. Experiment 1 is denoted by a "1" and Experiment 2 by a "2".

Observing system (tropics)	Data analyzed in each exp.				Time data available (GMT)			
	p	T	u,v	RH	00	06	12	18
Rawinsondes			1	1,2	X	X	X	X
Pilot balloons			1		X	X	X	X
NAVAIDS			1	1,2	X	X	X	X
Dropwindsondes			1	1,2	X	X	X	X
Aircraft			1		X	X	X	X
ASDAR			1		X	X	X	X
NESS CTW			1		X		X	X
European CTW			1		X		X	X
Japanese CTW			1		X		X	
Wisconsin CTW (E/W)			1				X	X
Wisconsin CTW (I.O.)			1		X		X	
Const. lvl. balloons			1		X	X	X	X
Surface (land)	1,2	1,2			X	X	X	X
Ships	1,2				X	X	X	X
(extratropics)	p	T	u,v	RH	00	06	12	18
Rawinsondes		1,2		1,2	X	X	X	X
TIROS-N		1,2			X	X	X	X
VTPR		1,2			X	X	X	X
Aircraft		1,2			X	X	X	X
Ships	1,2				X	X	X	X
Drifting buoys	1,2				X	X	X	X

As may be seen in Table 1, the tropical wind database is dominated by the cloud-track winds (denoted by CTW) from five geosynchronous satellites (GOES East, West, and Indian Ocean, METEOSAT, and the Japanese satellite). The cloud-track winds are, therefore, likely to be the data primarily responsible for the differences in the numerical predictions discussed in Section 3.

### 2.3 The Objective Analysis Procedure

In the GLAS objective analysis scheme (Baker et al., 1981), eastward and northward wind components, geopotential height and relative humidity are analyzed on mandatory pressure surfaces. The 6 h model forecast provides a first guess for these fields at 300 mb and sea level, where sea level pressure and sea level temperature are also analyzed. The first guess for the other levels is obtained from the model first guess, modified by a vertical interpolation between the two closest completed analyses. Vertical consistency is maintained through static stability constraints. The analysis at each level is performed with a successive correction method (Cressman, 1959) modified to account for differences in the data density and the statistical estimates of the error structure of the observations. The average distance between data points is found in a circle with a radius of 800 km centered at each grid point. Three scans are performed with a radius of influence  $R_i = c_i d$ , where the coefficients  $c_i$  (1.6, 1.4, 1.2) were chosen to minimize the analysis error (Stephens and Stitt, 1970). However, the radius of influence is not allowed to become smaller than 300 km. During this process, all data are checked for horizontal consistency. The completed analyses are smoothed and then interpolated to the model sigma levels.

The assimilation procedure provides for the intermittent analysis of batches of data grouped in a  $\pm 3$  h window about each synoptic time. In these experiments, the wind and height fields are analyzed independently with no explicit coupling or balancing. However, a geostrophic correction is applied to the first guess wind field every 6 h in the extratropics using a technique similar to that proposed by Kistler and McPherson (1975). The correction is computed from the change to the mass field (surface pressure) only.

## 3. RESULTS

Only a limited number of forecasts have been completed, and only the results for the 72 h 500 mb forecast from 0000 GMT 15 January 1979 are presented here. In Fig. 1, the 72 h planetary wave (zonal wavenumbers 1-3) error (analysis-forecast difference), as verified against the NMC global O/I analysis on 0000 GMT 18 January 1979, is shown for the western half of the northern hemisphere. Fig. 1a illustrates the planetary wave forecast error from the initial conditions provided by Experiment 2 (no wind data assimilated), and Fig. 1b illustrates that for Experiment 1 (tropical wind data assimilated). The reduction in the error in Fig. 1b is striking, particularly between 40°N to 50°N, along the west coast of North America. There is also an eastward shift in the maximum positive error. The wavenumber 2 dominance of the error field at 40°N is noteworthy. A smaller reduction in the error over the Atlantic may also be seen. The ultralong wave error is also reduced over Eurasia (not shown) with the assimilation of tropical winds by an amount comparable to that seen over the Atlantic.

The strong divergence in the tropical Pacific during the time period of this study (Paegle, 1981) may be responsible in part for the differences in the ultralong wave predictions. This possibility is being explored. Additional cases are being analyzed and will be reported at the Symposium.

ORIGINAL PAGE IS  
OF POOR QUALITY

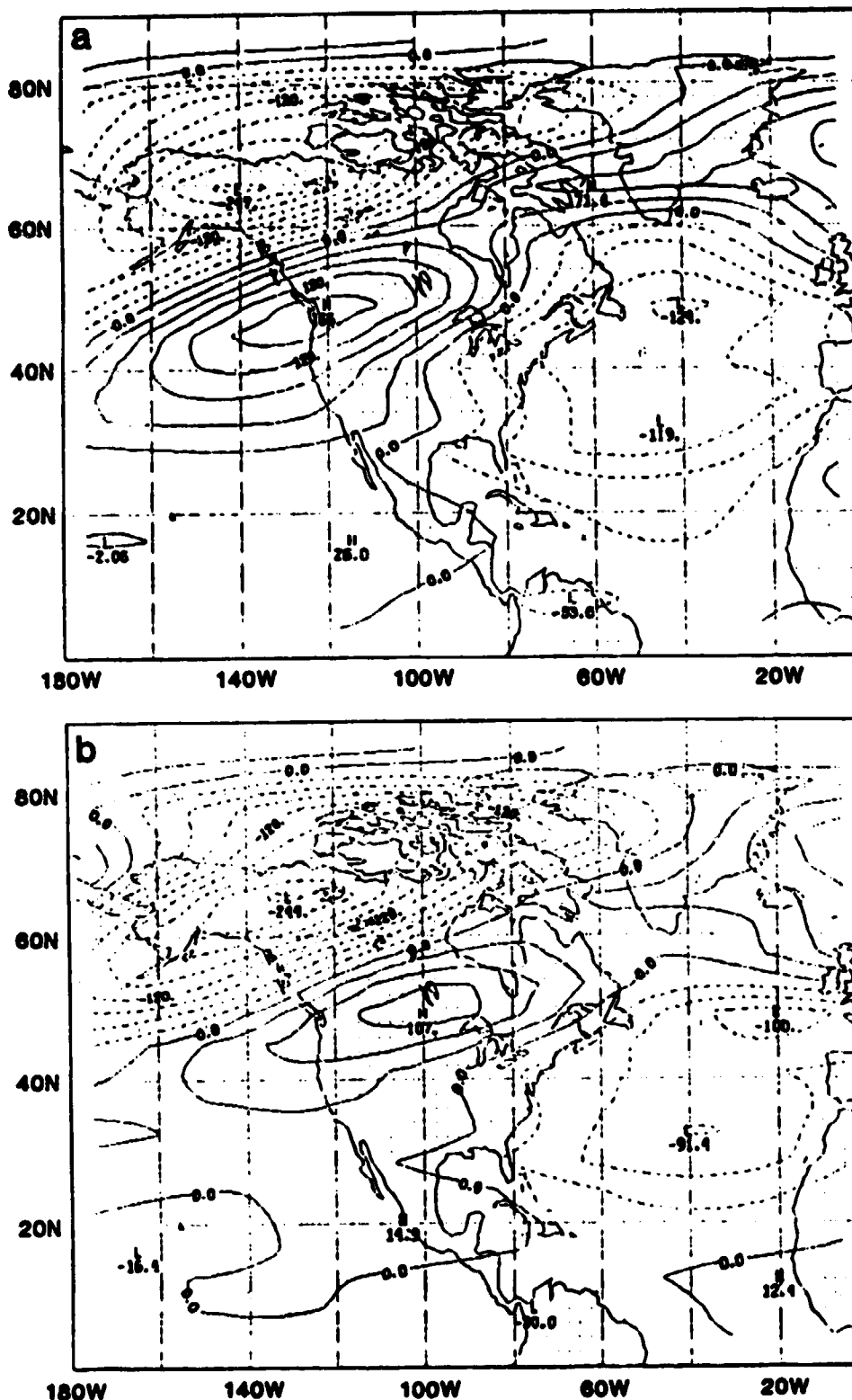


Fig. 1. The 500 mb planetary wave error for the 72 h forecast from 0000 GMT 15 January 1979. The verification is the NMC global O/I analysis for 0000 GMT 18 January 1979. The forecast error for Experiment 2 (no wind data) is shown in 1a and that for Experiment 1 (tropical wind data) in 1b. The contour interval is 30 m.

## ACKNOWLEDGEMENTS

The author gratefully acknowledges the encouragement and support of Dr. M. Halem. Dr. E. Kalnay provided the numerical model used in this study. Discussions with Messrs. D. Baumhelfner and T. Bettge, Drs. R. Atlas and E. Kalnay, and Profs. J. Paegle and J. N. Paegle were very helpful. Excellent technical assistance with the objective analysis and the numerical experiments was provided by Messrs. D. Edelmann, J. Molini, and M. Iredell, and by Ms. M. Almeida. Ms. Y. Brin ably assisted with the spectral analysis of the forecast error, and Ms. L. Thompson typed the manuscript.

## REFERENCES

- Arakawa, A., 1972: Design of the UCLA atmospheric general circulation model. Tech. Rep. 7, Dept. of Meteorology, University of California at Los Angeles.
- Baker, W. E., D. Edelmann, M. Iredell, D. Han, S. Jakkempudi, 1981: Objective analysis of observational data from the FGGE observing systems. NASA Tech. Memo. 82062, Goddard Space Flight Center, Greenbelt, Maryland 20771, 132 pp.
- Baumhelfner, D. P. and T. W. Bettge, 1981: Characteristics of atmospheric planetary circulation and associated model forecast skill during FGGE case studies selected by WGNE. Proceedings International Conference on Early Results of FGGE and Large-Scale Aspects of Its Monsoon Experiments, Tallahassee, Florida, January 1981.
- Blumen, W., 1972: Geostrophic adjustment. Rev. Geophys. Space Phys., 10, 485-528.
- Cressman, G. P., 1959: An operational objective analysis system. Mon. Wea. Rev., 87, 367-374.
- Gordon, C. T., L. Umscheid, and K. Miyakoda, 1972: Simulation experiments for determining wind data requirements in the tropics. J. Atmos. Sci., 29, 1064-1075.
- Kalnay-Rivas, E., A. Bayliss, and J. Storch, 1977: The 4th order GISS model of the global atmosphere. Beitr. Phys. Atmos., 50, 229-311.
- Kalnay-Rivas, E., and D. Hoitsma, 1979: The effect of accuracy, conservation and filtering on numerical weather forecasting. Preprints, Fourth Conference on Numerical Weather Prediction, Silver Spring, Maryland, Amer. Meteor. Soc., 302-312.
- Kasahara, A., and D. Williamson, 1972: Evaluation of tropical wind and reference pressure measurements: Numerical experiments for observing systems. Tellus, 24, 100-115.
- Kistler, R. E., and R. D. McPherson, 1975: On the use of a local wind correction technique in four-dimensional data assimilation. Mon. Wea. Rev., 103, 445-449.

- Kung, E. C., and H. A. Burgdorf, 1978: Maintenance of kinetic energy in large-scale tropical disturbances over the eastern Atlantic. Quart. J. Roy. Meteor. Soc., 104, 393-412.
- Paegle, J., 1978: The transient mass-flow adjustment of heated atmospheric circulations. J. Atmos. Sci., 9, 1678-1688.
- Paegle, J., J. N. Paegle, F. P. Lewis, and A. J. McGlasson, 1979: Description and interpretation of planetary flow structure of the winter 1976 DST data. Mon. Wea. Rev., 107, 1506-1514.
- Paegle, J. N., 1981: Short-term influence radius of monsoonal overturnings. Proceedings International Conference on Early Results of FGGE and Large-Scale Aspects of Its Monsoon Experiments, Tallahassee, Florida, 12-17 January 1981.
- Shapiro, R., 1970: Smoothing, filtering, and boundary effects. Rev. Geophys. Space Phys., 8, 359-387.
- Somerville, R. C. J., P. H. Stone, M. Halem, J. E. Hansen, J. S. Hogan, L. M. Druryan, G. Russell, A. A. Lacis, W. J. Quirk and J. Tenenbaum, 1974: The GISS model of the global atmosphere. J. Atmos. Sci., 31, 84-117.
- Somerville, R. C. J., 1980: Tropical influences on the predictability of ultra-long waves. J. Atmos. Sci., 37, 1141-1156.
- Stephens, J. J., and J. M. Stitt, 1970: Optimum influence radii for interpolation with the method of successive corrections. Mon. Wea. Rev., 98, 680-687.
- Wu, M.-L. C., 1980: The exchange of infrared radiative energy in the troposphere. J. Geophys. Res., 85, 4084-4090.

THE STATE OF THE ATMOSPHERE AS INFERRED FROM THE FGGE  
SATELLITE OBSERVING SYSTEMS DURING SOP-1<sup>1</sup>

M. Halem, E. Kalnay, W. E. Baker, and R. Atlas

1. INTRODUCTION

At the Goddard Laboratory for Atmospheric Sciences (GLAS), we performed a series of data assimilation experiments to test the influence of different elements of the satellite observing systems that were collected during the Special Observing Period (SOP-1). In this paper we present results from some of the experiments. These findings show that the FGGE satellite systems are able to infer the three-dimensional motion field and improve the representation of the large-scale state of the atmosphere. We also present some preliminary results of the forecast impact of the FGGE data sets.

The GLAS analysis/forecast system for producing a global gridded analysis consists of an objective analysis scheme making use of the continuity provided by a model first guess integrated from a previous analysis. The first guess is then corrected by data collected in a + 3 hour window about each analysis time. The results are obtained with the GLAS analysis cycle (Baker et al., 1981).

The assimilation/forecast model is the 4th order global atmospheric model described in Kalnay-Rivas et al. (1977) and Kalnay-Rivas and Hoitsma (1979). It is based on an energy conserving scheme with all horizontal differences computed with 4th order accuracy combined with the periodic use of a 16th order Shapiro filter.

2. COVERAGE AND ACCURACY OF THE FGGE SATELLITE DATA

There are approximately 6000 temperature soundings per day produced operationally from the TIROS-N HIRS/MSU sounders, 1000 temperature soundings from the NOAA-4 VTPR sounders, and roughly 6000 cloud-tracked winds per day from the five FGGE geostationary satellites. The influence of this large volume of satellite data on a global analysis system is one of the main concerns of this study. In this paper we briefly describe only the statistical properties and coverage of the temperature sounding data leaving the other data sets such as geostationary cloud-track wind motions, drifting buoys, etc., for a later detailed paper.

2.1 TIROS-N Sounding Data

Fig. 1a shows the geographical frequency distribution of TIROS-N temperature soundings observations per grid area per day for the period January 5 through January 21, 1979. If at least one sounding occurs in an area within + 3 hours

---

<sup>1</sup> Published in Condensed Papers and Meeting Report: International Conference on Early Results of FGGE and Large-Scale Aspects of its Monsoon Experiments, Jan. 12-17, 1981, Tallahassee, Florida. Published by the World Meteorological Organization, Geneva, Switzerland.

of an analysis time, then that area is considered to have been observed. Thus, the maximum possible frequency of observations per day for any area is four. The frequency distribution shown in Fig. 1a indicates that the tropics are being observed on the average of once every other day by TIROS-N while the extratropics are generally observed more than once per day but less than twice per day. It is also seen that operational TIROS-N soundings are not produced over mountainous regions, such as the Rockies and Himalayas, although they are generated over other land areas. Fig. 1b shows the combined frequency per day per grid area for the two satellite systems during FGGE, namely NOAA-4 and TIROS-N. Over oceans, the frequency is usually two to three observations per day. Although this frequency of observations still does not match the 6 h frequency at which analyses are produced operationally at NMC, i.e. four times daily, the synoptic coverage is comparable to the nearly twice daily coverage of the United States rawinsonde network.

The accuracy of the satellite observing systems is a more difficult problem to assess because of the lack of "ground truth" for verification over data-sparse regions. Two methods that have been used to estimate temperature sounding errors appear to present differing accuracy estimates. The methods are: 1) rms differences of layer mean temperatures obtained from collocating rawinsonde observations and satellite temperature profiles in space and time, (e.g. Phillips, et al., 1979), and 2) rms differences of layer mean satellite temperature soundings and the NMC analysis (e.g. Schlatter, 1981). Phillips' statistics show the rms differences at mandatory pressure levels for the TIROS-N type A soundings at selected ocean stations to be  $\sim 2.2^{\circ}\text{C}$  in the extratropical troposphere and  $\sim 1.3^{\circ}\text{C}$  in the tropics during SOP-1. The errors above 300 mb are larger, up to  $3.0^{\circ}\text{C}$  at 200 mb. Schlatter's statistics indicate a surface to 50 mb rms difference in thickness temperature to be  $\sim 0.8^{\circ}\text{C}$  over the United States. He ascribes this higher accuracy to the fact that small biases of opposite sign in the lower and upper tropospheric sounding temperatures cancel when integrated over large thicknesses.

The GLAS analysis system attempts to take advantage of the accuracy in the sounding thicknesses by performing a geopotential height analysis. Thus, we show in Fig. 2a and Fig. 2b the vertical rms differences between the final height analysis and the rawinsonde profiles, TIROS-N clear-column (type A) soundings, and the microwave soundings for land and ocean, respectively. The TIROS-N type A soundings over land are seen to be in slightly less agreement with the analysis than the rawinsondes up to 300 mb and in better agreement with the analysis above 300 mb. The rms differences in "microwave only" (type C) soundings over land consistently increase from 850 mb to 300 mb and then decrease above 300 mb. The surprising agreement for the type A soundings is not only consistent with Schlatter's findings but also shows the geopotential height to be accurate at the lower levels as well. Another factor contributing to these statistics may be that the rawinsonde captures more of the sub-grid scale variance and this variance cannot be represented on a coarse  $4^{\circ} \times 5^{\circ}$  analysis. Additionally, the rawinsondes utilized in this study were not corrected for the effects of solar radiation. Over the oceans, the rms differences in Fig. 2b show that both infrared and microwave TIROS-N retrievals fit the analyzed height better than the rawinsondes. This may be explained by the fact that the satellite soundings are the dominating data influencing the analyses over the oceans. Nevertheless, the larger differences in the microwave soundings over land and oceans, which constitute 50% of the retrievals, must be spuriously affecting the analysis.

### 3. EXPERIMENTAL ANALYSIS/FORECAST SYSTEM

Several experiments to assess the influence of the FGGE observing systems on the global analysis were performed for the period January 5 to March 5, 1979. Each experiment is characterized by a 6 h analysis/forecast cycle using a specified subset of the FGGE II-b data at each synoptic time. We confine ourselves in this section mainly to the study of the effect of satellite observations on the analysis. Table 1 describes the acronyms used to denote the different experiments and the combinations of FGGE data that were utilized in the assimilation cycles. The initial state for all of the assimilations was the January 5, 1979 final analysis provided by the National Meteorological Center (NMC).

#### 3.1 Rms Differences Between First Guess and Analysis

A measure of the influence of the observational data on an analysis cycle can be obtained by calculating the rms correction made between the forecast first guess and the completed analysis. In Figs. 3-5, we present the rms difference fields between the 300 mb 6 h forecast (i.e. first guess field) and the final analysis for the NOSAT, FGGE, and NORA0B experiments, respectively, for the period January 5 to January 21, 1979. The shaded areas in these figures indicate regions where the average difference during the 16 d period is less than 20 m; diagonal hatching indicates large errors greater than 60 m; blank areas correspond to intermediate values between 20 and 60 m.

Fig. 3a shows that the 6 h rms forecast error over the vast oceanic regions in both hemispheres is less than 20 m, while the differences over regions with dense rawinsonde observations are greater than 60 m. The observed structure in the 6 h forecast error can be explained by the fact that the 6 h forecast itself defines the atmosphere in data-sparse regions leading to lower "errors." Those small corrections are just an indication of the serious data gaps of the conventional network. We note that large 6 h errors are present in the Southern Hemisphere and in the tropics. By comparing with Fig. 4a which shows the distribution of rawinsondes, it is clear that the large corrections occur in data-sparse regions at isolated ocean and island stations and can be more than 120 m.

The rms differences are smaller over Europe than over North America, probably due to more frequent rawinsonde observations. It is interesting to note the maximum 6 h forecast error of 60 to 80 m which occurs along the full length of the western boundary of the North American continent, as well as in other regions downstream of data-sparse regions. Along the northwest coast of Europe this sharp error gradient does not appear because of the presence of rawinsonde ship stations in the Atlantic.

Fig. 3b depicts the FGGE 6 h forecast rms error in the 300 mb height field. Comparison with Fig. 3a reveals that large errors have been significantly reduced, especially along coastal boundaries and at the isolated oceanic stations. For example, the large errors along the west coast of North America have been reduced to about 40 m. On the other hand, we now observe increases in areas of large spatial extent such as over the northern Pacific ranging from 40 m to 60 m. This indicates that satellites and other FGGE observing systems have eliminated some of the data gaps in the NOSAT system and are introducing substantial modifications to the 6 h forecast fields used in the analysis. Moreover, the closer agreement of the rawinsonde heights to the 6 h forecast in the FGGE experiment suggests that the satellite data over the ocean have produced a more accurate initial state.

The rms difference between the final FGGE and NOSAT analyses is shown in Fig. 4b. In the data-sparse regions, the differences range from 80 m over the Pacific to more than 200 m in the Southern Hemisphere. The differences in the tropics and oceanic regions of the Southern Hemisphere are as large as those between randomly chosen synoptic situations. Only over the North American and Eurasian continents are the differences between the final analyses smaller than 20 m.

The sharp contrast in the difference fields between the land and sea in the two analyses raises a very important question. Is it possible that the inability of present models to accurately forecast the planetary scale waves may be partly due to the land-sea contrast in data coverage? It might be that large errors over the oceans give rise to spurious planetary scale wave components in the initial conditions which incorrectly travel during the forecast, adversely affecting the forecast skill.

To test the hypothesis that the satellite data alone can produce analyses which are consistent with the real atmosphere, we performed an additional experiment without rawinsonde data (NORAOB). Figs. 5a and 5b illustrate the 300 mb rms height differences between the 6 h forecast and NORAOB analysis and the difference between the FGGE and NORAOB analyses, respectively. The low rms error in Fig. 5b over the oceans is due to the predominance of the same satellite data in both experiments. This is analogous to the small differences we noted in Fig. 4b over land, where both experiments are dominated by rawinsondes. The largest differences occur downstream of the major mountain chains. For example, the rms differences are smaller over the western half of the United States and Canada than over the eastern regions of North America. This results from the fact that neither temperature sounding data nor cloud-tracked wind data were available operationally over the Rocky Mountains as indicated in the data coverage maps of Fig. 1. Around isolated island stations, there is good agreement, even without rawinsonde data.

#### 4. SYNOPTIC SCALE COMPARISONS

In this section we compare the NORAOB inferred height and wind fields with the FGGE analysis over data dense regions. The purpose of such a comparison is to assess the quality of the analysis over the oceans where little or no data is available for verification.

Figs. 6a and 6b present typical comparisons of the vertical structure of inferred wind profiles at two low-latitude isolated ocean stations with coincident rawinsondes. The panels on the left of the figures depict the wind direction as a function of pressure, and the panels on the right illustrate the wind speed. Also shown are the aircraft and cloud-tracked wind data available within 400 km of the station at + 3 h of analysis time. In both cases the NORAOB analysis defines the vertical wind speeds accurately at low and upper levels but underestimates the wind speed at 500 mb by about 10 to 20%. This is generally the case with many other profile comparisons we have examined. We also see in Fig. 6b that the NORAOB analysis can infer strong wind shear, change abruptly within a 100 mb interval from easterly to westerly, or exhibit multiple directional changes with height in a light wind situation as seen in Fig. 6a.

Figs. 7a and 7b show the 300 mb analysis of the geopotential height field for the FGGE and NORA OB experiments. The position of the trough in the NORA OB experiment is in excellent agreement with the FGGE analysis, although its intensity is slightly weaker. Part of the weakness in the trough is due to the lack of satellite data over the Rockies (see Figs. 1a and 1b). The difference between the FGGE and NORA OB analyses is small over the central United States, with the NORA OB analysis underestimating the ridge in the northeast. Figs. 8a and 8b show the corresponding 300 mb wind vector and isotach maps. The position of the isotach minimum and maximum is nearly identical as is the flow direction. The intensity of the system is, however, systematically underestimated over most of the United States by about 10% except in the intense jet streak located over the Gulf of Mexico, where it is nearly 40% weaker. This difference is traced to a weaker ageostrophic wind component in the NORA OB analysis. The absolute vorticity, vorticity advection, and thermal advection fields have a similar structure and position but weaker intensity. Whether this deficiency can be corrected over the western part of the United States through the use of cloud-tracked wind data or the extraction of temperature sounding data over high terrain is still a conjecture at this time. Nevertheless, the ability to capture much of the day-to-day detailed changes in the temperature and wind fields is highly encouraging.

## 5. FORECAST IMPACT RESULTS

Clearly the most important application of an objective analysis and, at the same time, the most sensitive test of its accuracy is the impact it has on forecasting skill. We have performed a series of short-term forecast impact tests with our coarse resolution model and a few selected extended range forecasts with a higher (2.5° latitude by 3° longitude) resolution model. The statistical sample of fourteen forecasts is small, but examining a number of geographically distinct regions increases the independent sample size, making the results statistically significant. Each forecast was of five days duration from initial conditions taken every fourth day from January 9 through March 2 from the analysis cycles described earlier. Figs. 9a and 9b present the S1 skill score for the three day forecasts evaluated relative to the NMC operational analysis over North America, Europe, and Australia. A consistently significant positive impact of the FGGE data occurs over Australia in the sea level pressure and 500 mb S1 skill scores. A smaller and consistent impact occurs over Europe. There is a small positive impact over North America at 500 mb, but a less consistent impact in the sea level pressure field. Also shown in these figures are the S1 scores for the forecasts from the NORA OB experiment. Over Australia, the accuracy of the three day forecasts is comparable to that of the FGGE system at 500 mb but slightly less accurate at sea level. Over Europe and North America for the limited number of cases, the NORA OB forecasts are, in general, poorer by about 24 h in forecast skill.

## 6. CONCLUSIONS

The major findings of this study are:

- (1) The rms geopotential height difference over land between the clear-column infrared TIROS-N retrievals and the completed analysis is only slightly larger than the rms difference between the rawinsonde height and the analysis

up to 300 mb. Above 300 mb, the completed analysis is substantially more consistent with the geopotential height of the infrared retrievals than with the rawinsondes. Microwave sounding differences over land and oceans are substantially poorer than infrared retrievals.

(2) The 6 h forecast error over land downstream of data-sparse regions is significantly reduced in the FGGE analysis as compared with the NOSAT analysis.

(3) The large-scale synoptic structure of the global geopotential height field produced by the NORAOB and FGGE systems is remarkably similar. The only exceptions occur in regions over and downstream of major mountain chains where soundings are not available. Similarly, the instantaneous wind vector field inferred from the NORAOB experiments over land is in good agreement with the FGGE analysis but has weaker intensity.

(4) The skill of the forecasts from initial conditions obtained with the NORAOB experiment are somewhat degraded when compared with forecasts from the full FGGE system.

(5) The forecast impact from the FGGE system over Australia is consistently significant and positive. The impact over North America and Europe is also consistent but slightly weaker at 500 mb and less consistent in sea level pressure over North America.

A serious limitation of the NORAOB system is the lack of observational soundings over mountains and cloud-tracked wind vectors over land.

## REFERENCES

- Baker, W. E., D. Edlmann, M. Iredell, D. Han, and S. Jakkempudi, 1981: Objective analysis of observational data from the FGGE observing systems. NASA Tech. Memo. 82062. Goddard Space Flight Center, Greenbelt, Maryland, 20771.
- Kalnay-Rivas, E., A. Bayliss, and J. Storch, 1977: The 4th order GISS model of the global atmosphere. Beitr. Phys. Atmos., 50, 299-311.
- Kalnay-Rivas, E., and D. Hoitsma, 1979: The effect of accuracy, conservation and filtering on numerical weather forecasting. Preprints Fourth Conf. on Numerical Weather Prediction, Silver Spring, Maryland, Amer. Meteor. Soc., 302-312.
- Phillips, N., L. McMillin, A. Gruber, and D. Wark, 1979: An evaluation of early operational temperature soundings from TIROS-N. Bull. Amer. Meteor. Soc., 60, 1188-1197.
- Schlatter, T. W., 1981: An assessment of operational TIROS-N temperature retrievals over the United States. Mon. Wea. Rev., 109, 110-119.

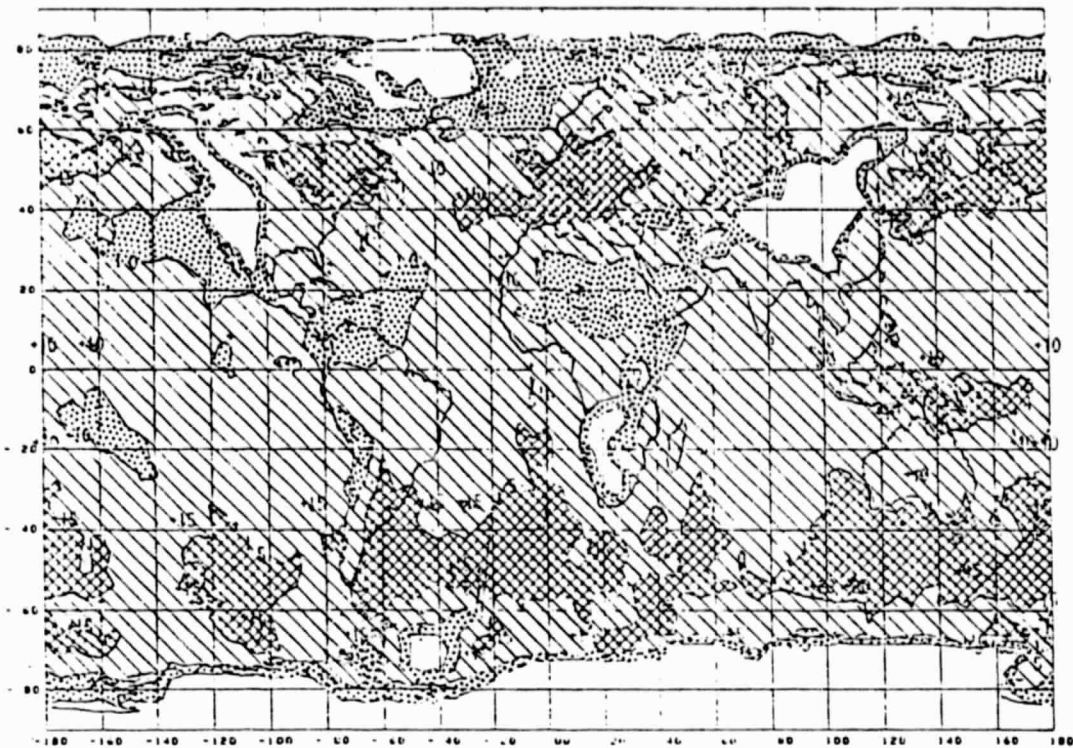
DATA UTILIZED FROM THE FGGE OBSERVING SYSTEM

EXPERIMENT	FGGE	NOSAT	NORA0B	NOGEO5	NO TIROS	NO BUOYS
Rawinsondes - 2A	X	X		X	X	X
NAVAIDS	X		X	X	X	X
Dropwindsondes	X		X	X	X	X
Aircraft - 2A	X	X	X	X	X	X
ASDAR	X		X		X	X
TIROS-N	X		X	X		X
VTPR	X		X	X		X
NESS CTW	X		X		X	X
European CTW	X		X		X	X
Japanese CTW	X		X		X	X
Wisconsin CTW (East/West)	X		X		X	X
Wisconsin CTW (Indian Ocean)	X		X		X	X
TWERLE (const. lev. balloon)	X		X		X	X
Surface stations (land) - 2A	X	X	X	X	X	X
Ships - 2A	X	X	X	X	X	X
Drifting buoys	X		X	X	X	

TABLE 1

DATA	LEVEL 2A SURFACE SHIPS	LEVEL 2A RAWINDS & PIBALA	LEVEL 2A & 2B SAT TERM	LEVEL 2A & 2B T W/MISC	LEVEL 2B BUOYS	LEVEL 2B ASDAR WINDS PROP WINDS NAVAIDS	LEVEL 2 SSTS SHOW AUTPN
FGGE	X	X	X	X	X	X	X
NO SAT	X	X	-	-	-	-	-
NO GEOS	X	X	X	-	X	X	X
NO POLAR	X	X	-	X	-	X	-
NO RA0B	X	-	X	X	X	X	X
OPER 2A	X	X	X	X/(-)	-	-	X
NO UP AIR	X	-	-	-	X	-	-
NO BUOYS	X	X	X	X	-	X	X

Fig. 1a. TIROS-N TEMPERATURE SOUNDINGS (FREQ./DAY)



ORIGINAL PAGE IS  
OF POOR QUALITY

Fig. 1b. COMBINED TIROS-N AND NOAA-4 TEMPERATURE SOUNDINGS (FREQ./DAY)

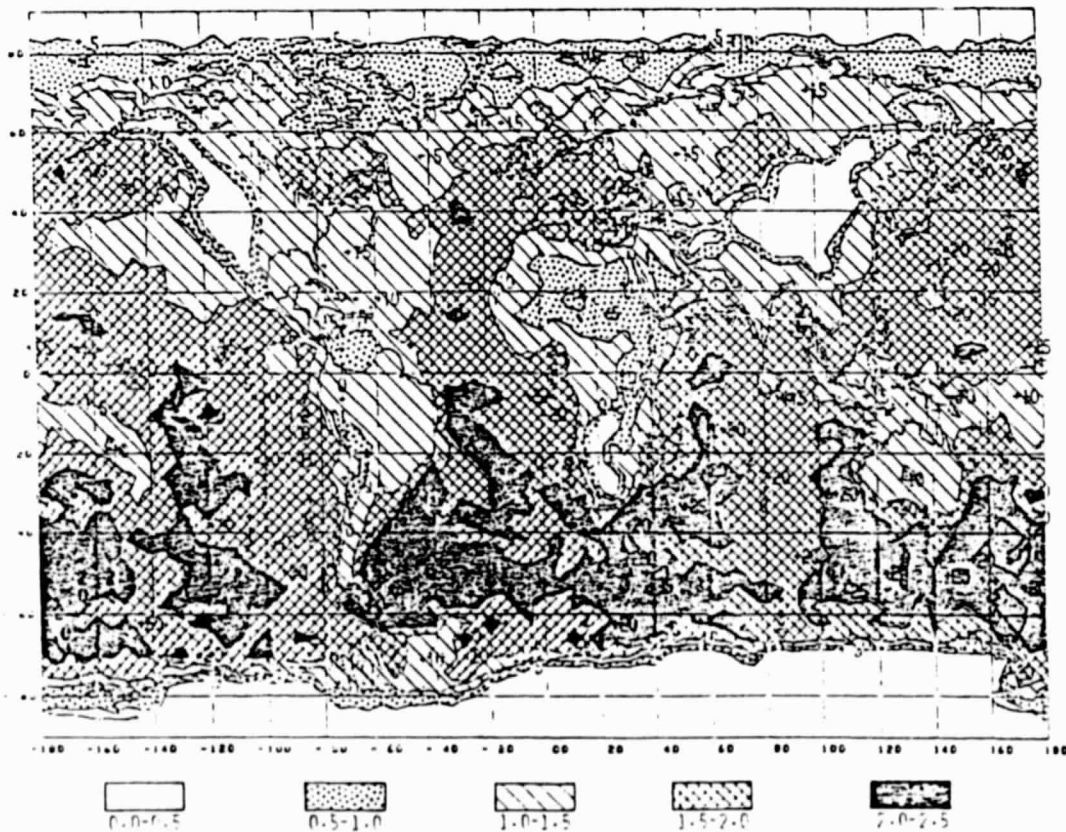


Fig. 2. VERTICAL PROFILE OF GEOPOTENTIAL HEIGHT RMS FIT

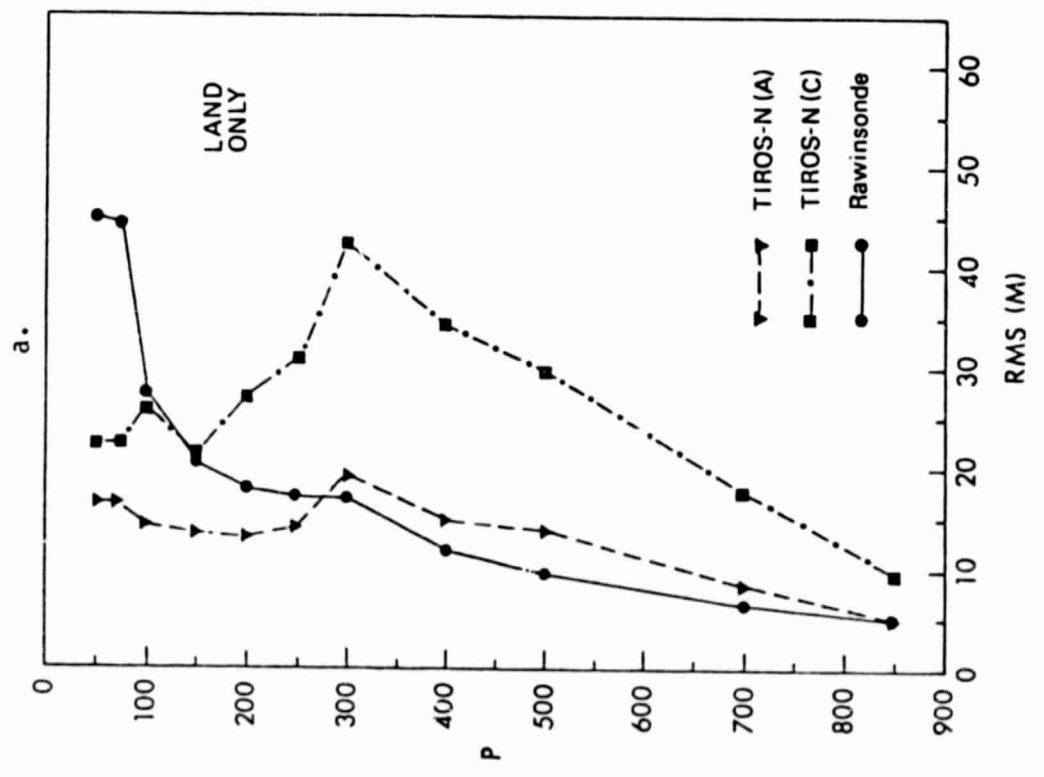
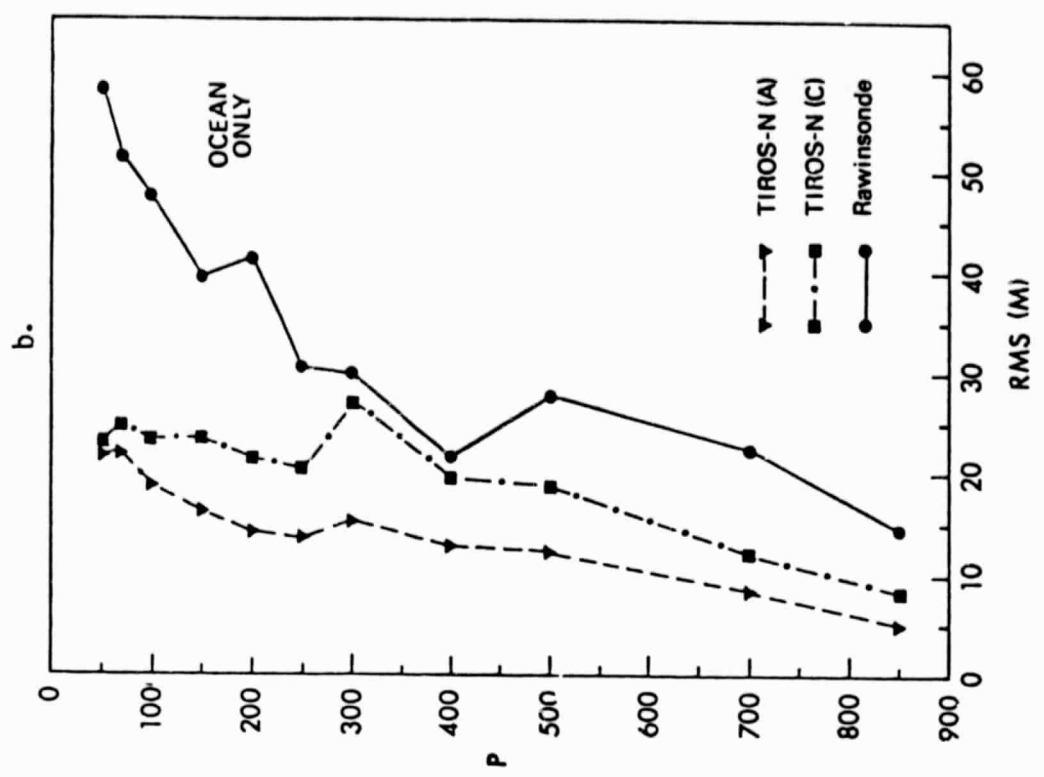


Fig. 3a. RMS DIFFERENCE BETWEEN 6 hr FORECAST AND NOSAT ANALYSIS

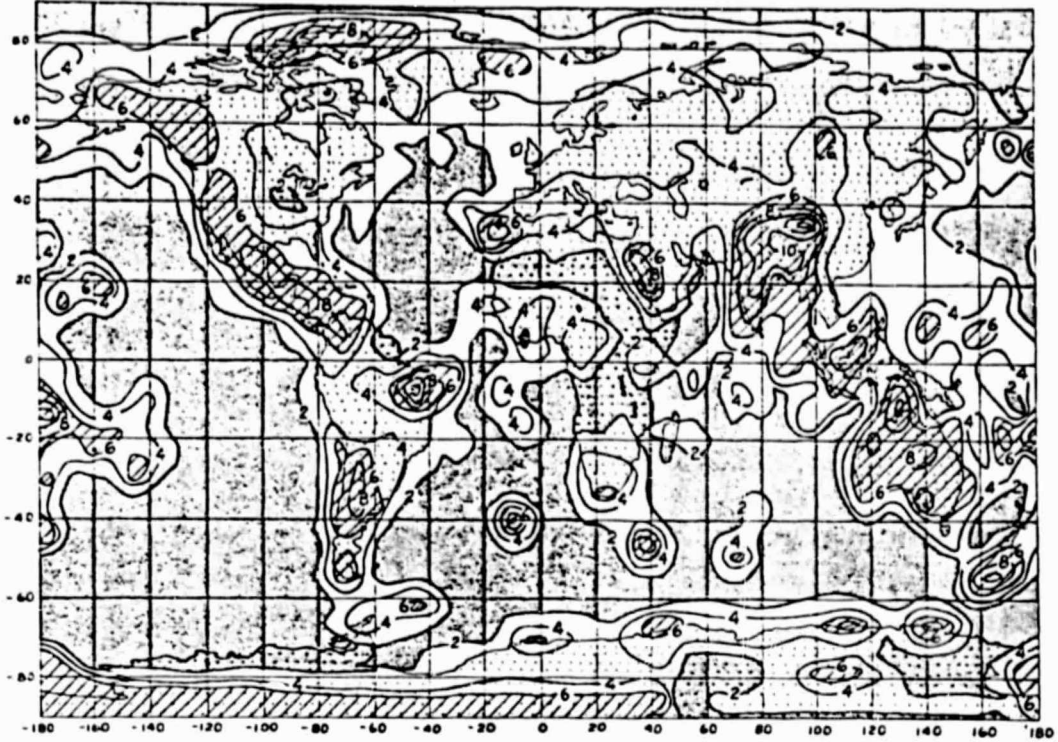


Fig. 3b. RMS DIFFERENCE BETWEEN 6 hr FORECAST AND FGGE ANALYSIS

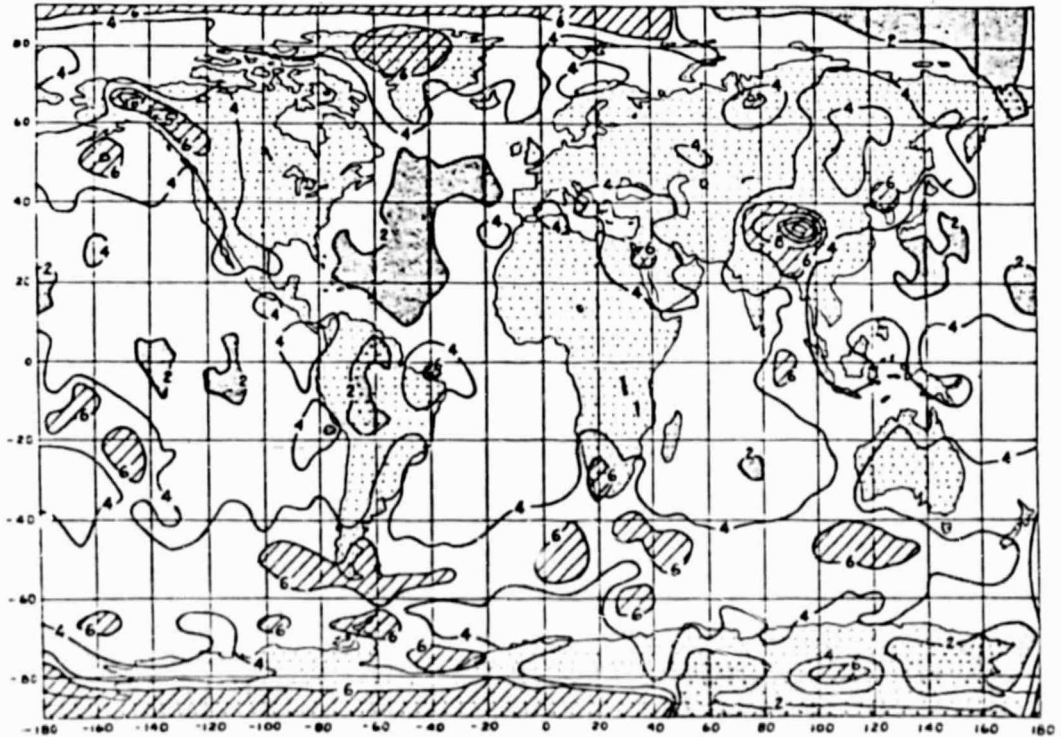


Fig. 4a. RADIOSONDE NETWORK 00Z 9 JANUARY 1979

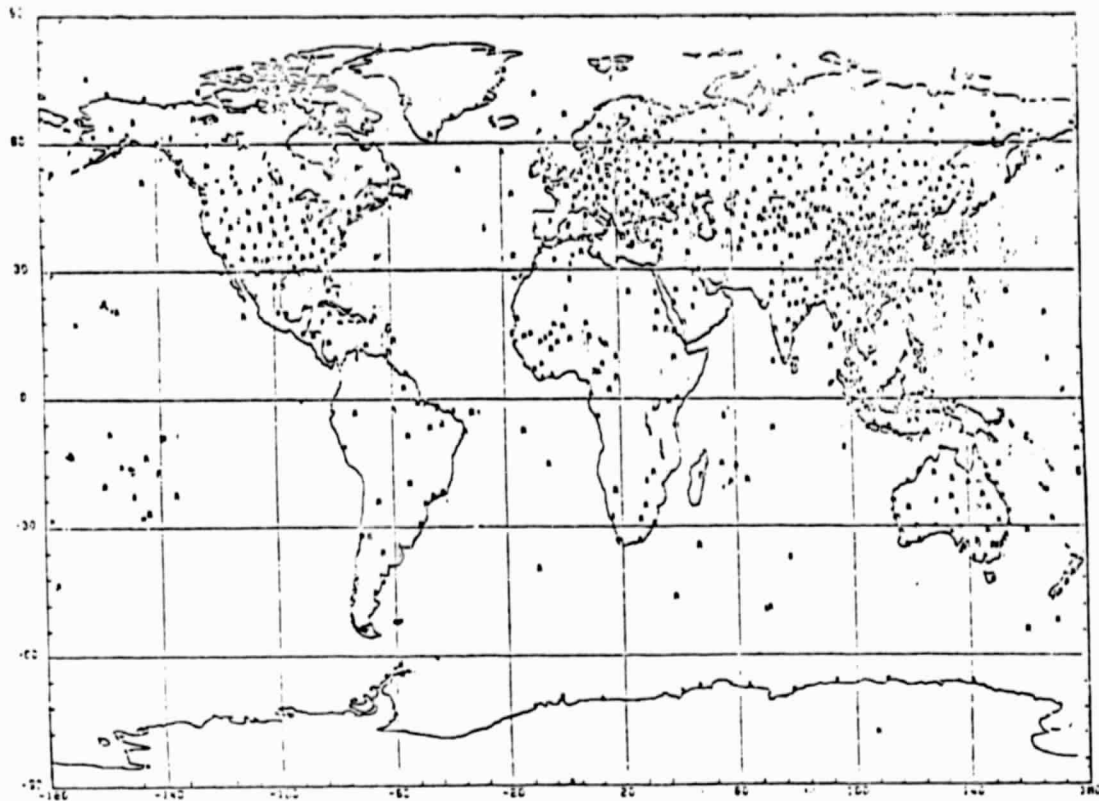


Fig. 4b. RMS DIFFERENCE BETWEEN NOSAT AND FGGE ANALYSES

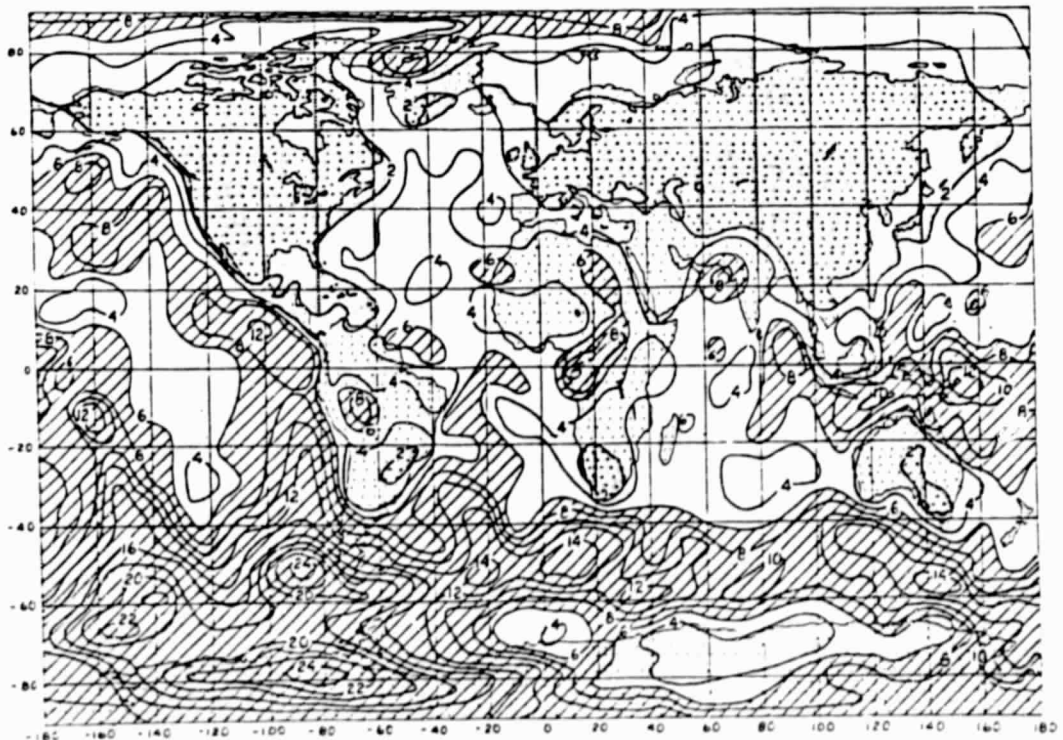


Fig. 5a. RMS DIFFERENCE BETWEEN THE 6 hr FORECAST AND NORAOB ANALYSIS

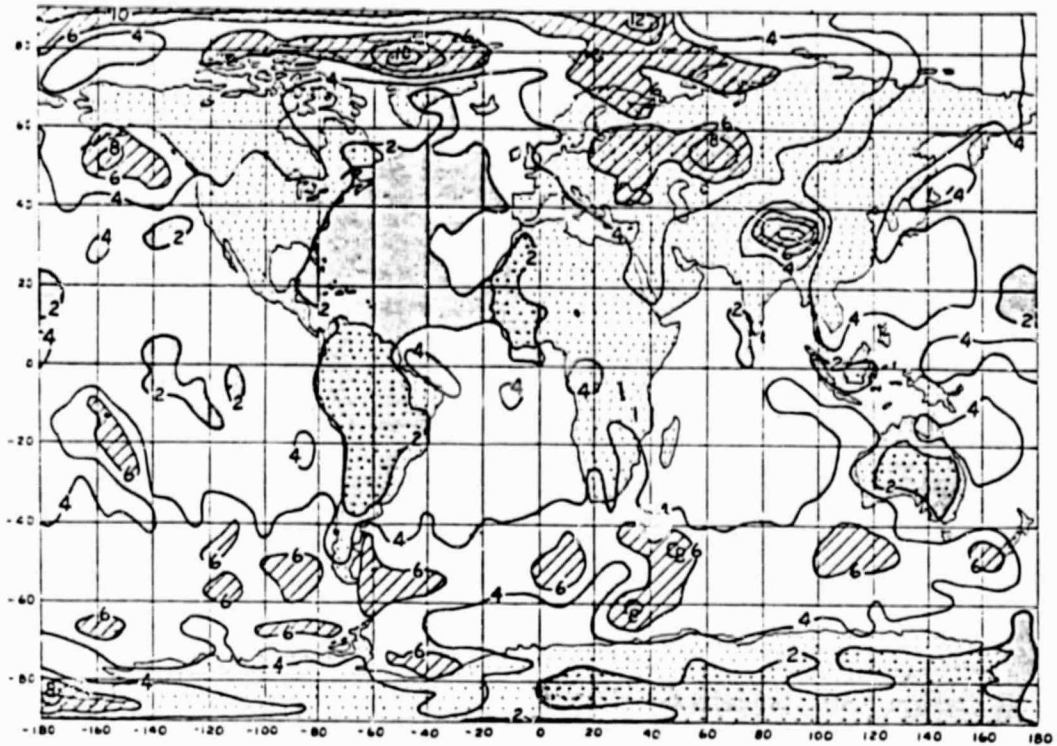


Fig. 5b. RMS DIFFERENCE BETWEEN NORAOB AND FGGE ANALYSES

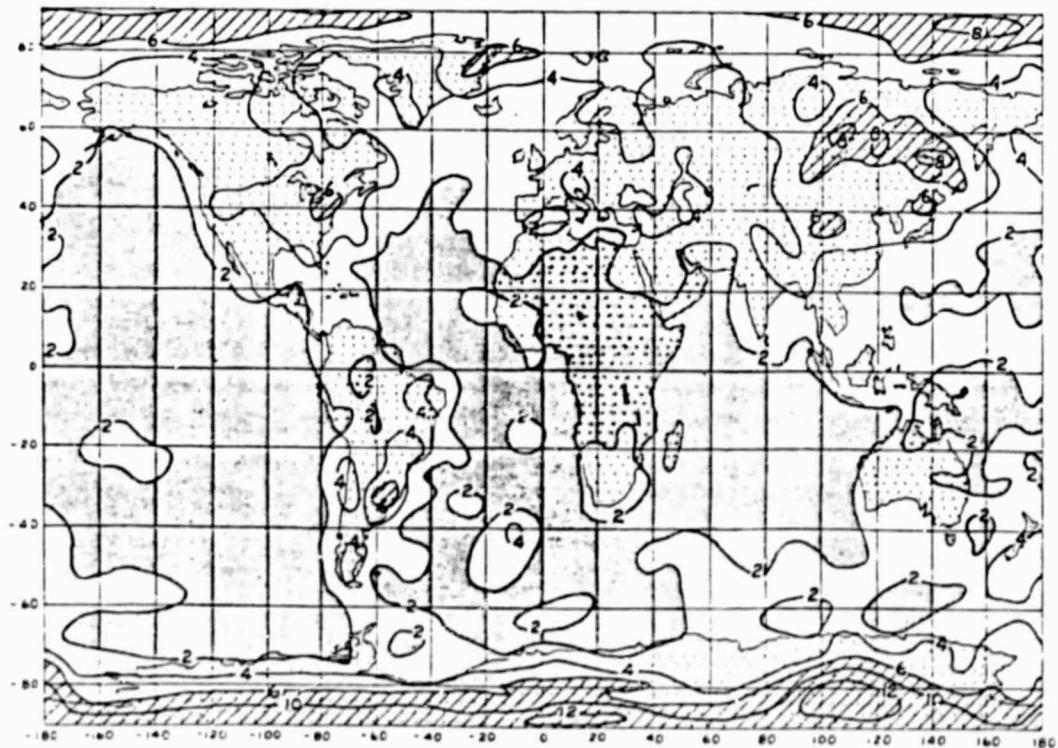


Fig. 5. WIND PROFILES FROM NORAOB ANALYSIS COMPARED WITH RAWINSONDES

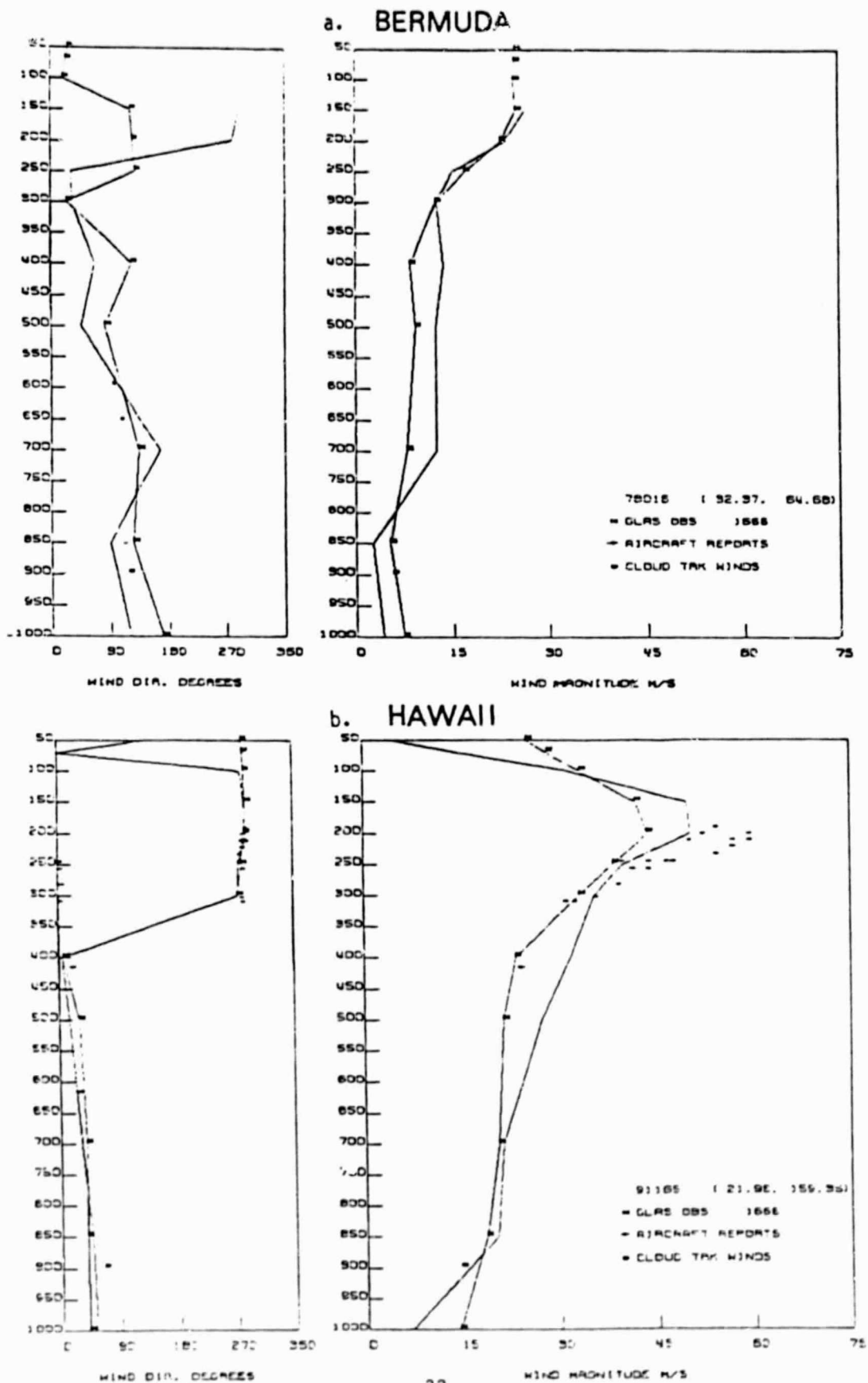


Fig. 7a. GGE ANALYSIS 0Z JAN. 21, 1979

GEOP HT VS TEMPERATURE AT 300 MB

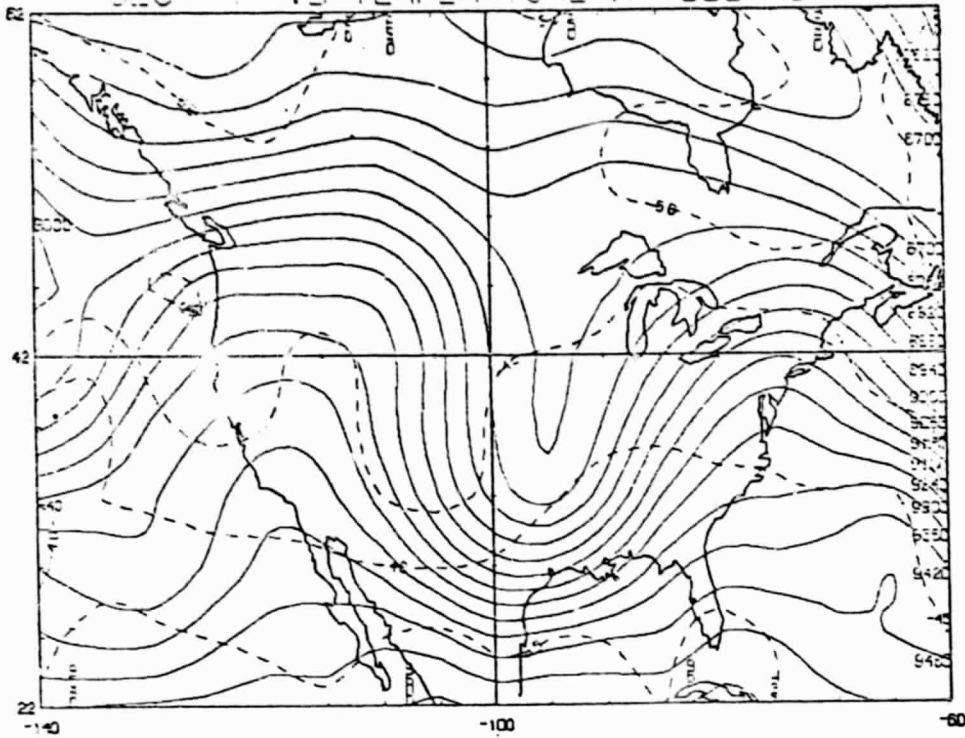


Fig. 7b. NORA0B ANALYSIS 0Z JAN. 21, 1979

GEOP HT VS TEMPERATURE AT 300 MB

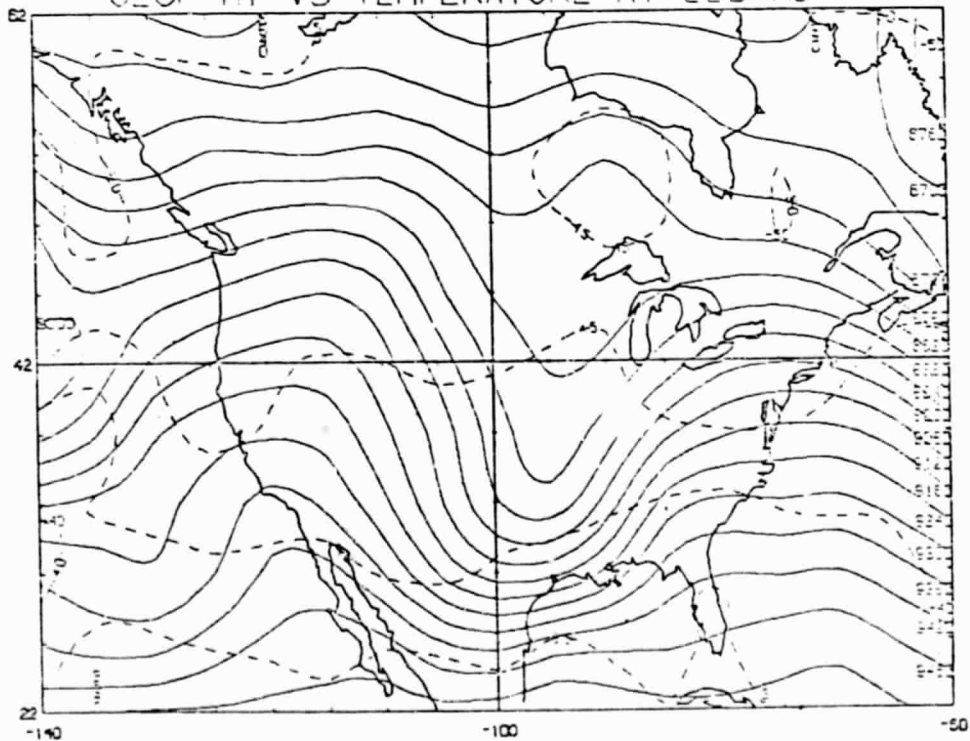


Fig. 8a. FGGE ANALYSIS 0Z JAN. 21, 1979

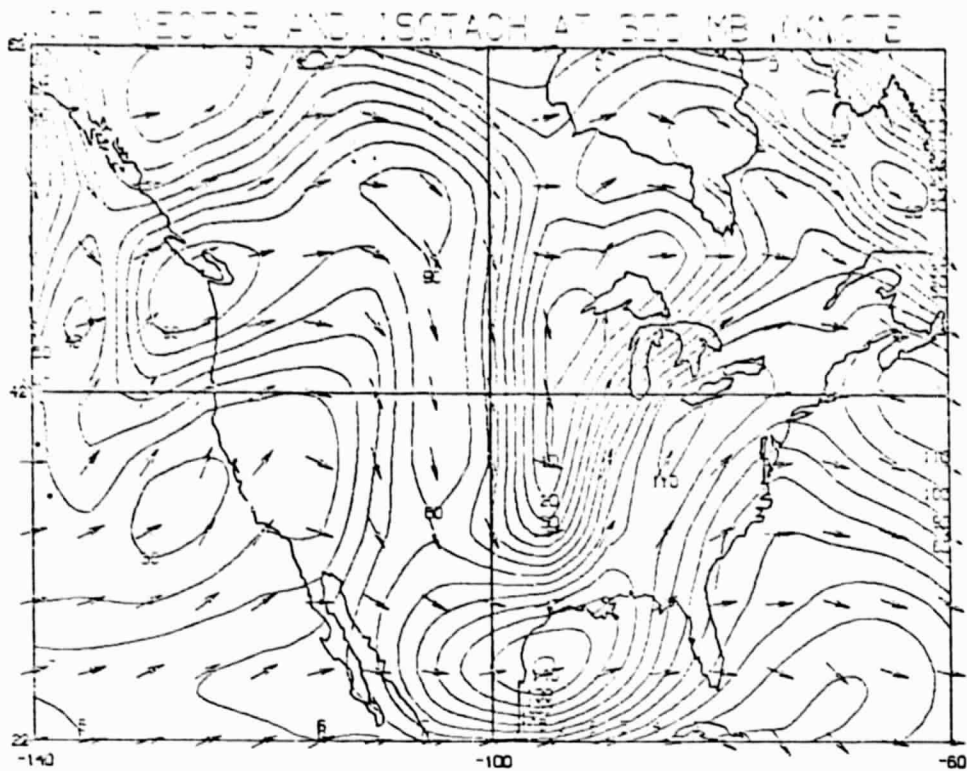


Fig. 8b. NORA0B ANALYSIS 0Z JAN. 21, 1979

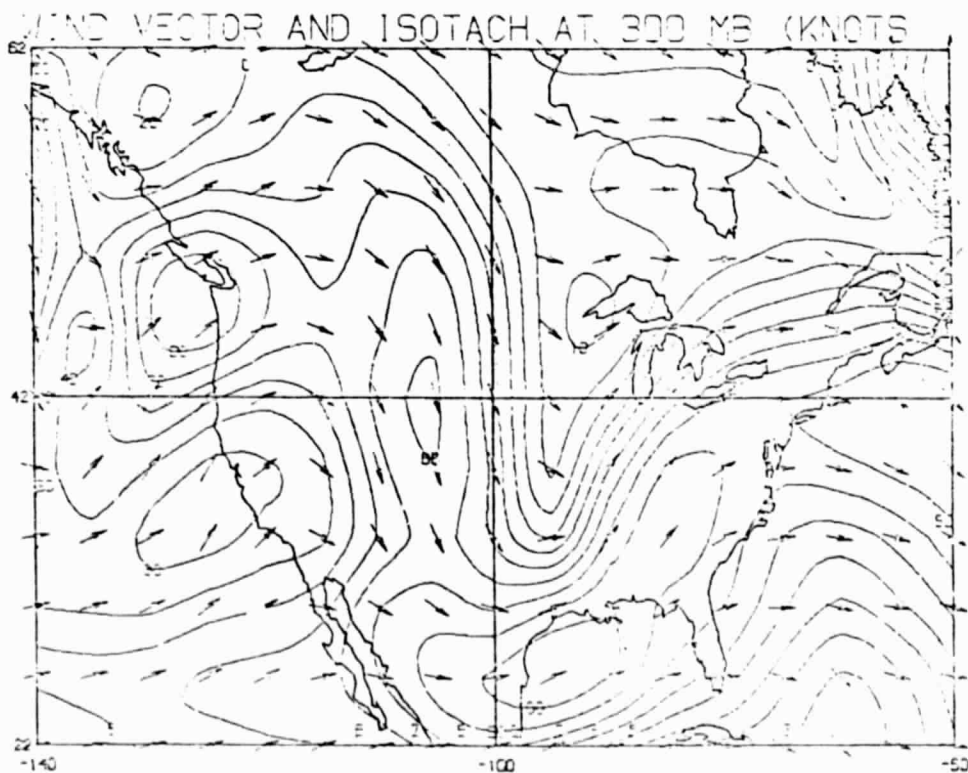


Fig. 9b. 3-DAY 500 mb S1 SKILL SCORE

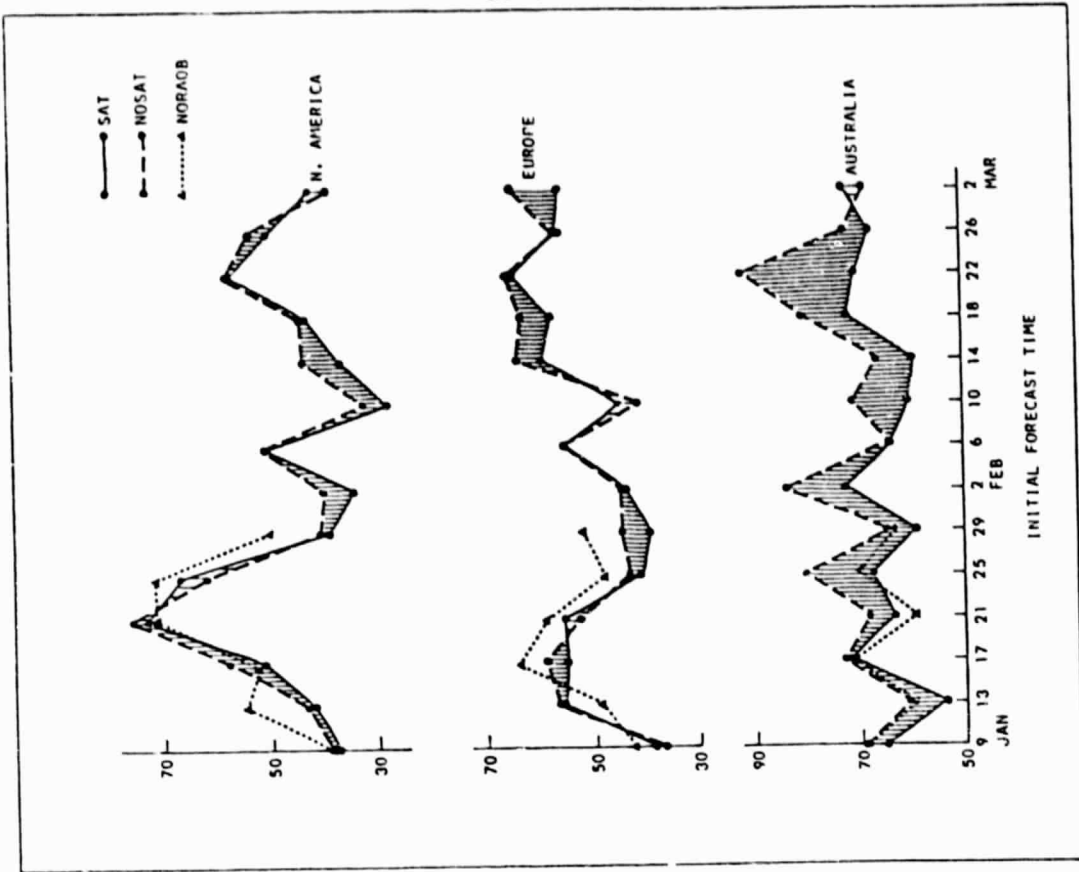
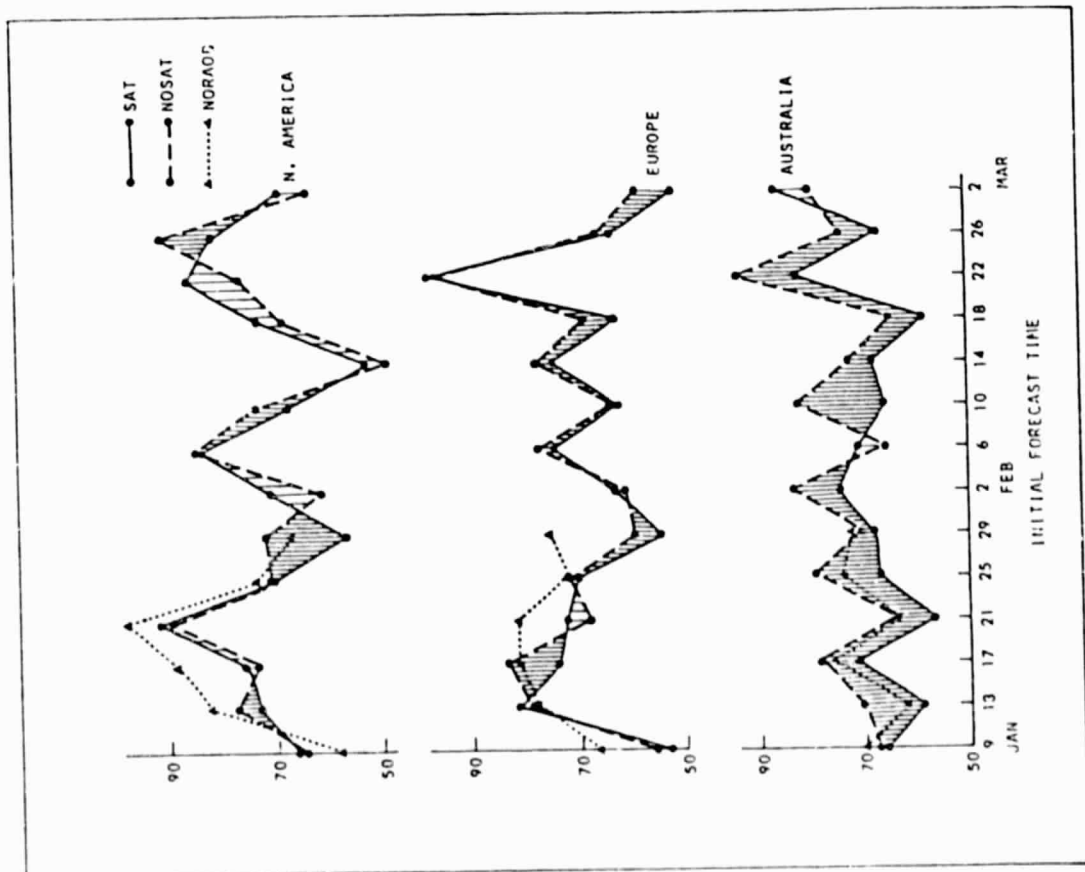


Fig. 9a. 3-DAY SLP S1 SKILL SCORE



## NUMERICAL PREDICTION OF THE LARGE SCALE TROPICAL FLOW

E. Kalnay, W. E. Baker and J. Shukla

## 1. INTRODUCTION

The problem of numerical forecasting is more difficult in the tropics than in mid- and high-latitudes for the following reasons: 1) There has always been a lack of reliable large scale observations in the tropics. This is partly due to the low land coverage in the tropics, and more importantly, to the need to measure the wind field rather than the mass field, which results in a challenging problem of instrumental accuracy. 2) The fact that the dominant instability in the tropics is convective rather than baroclinic as in the extratropics. This implies very fast growth rates, and requires an accurate representation of sub-grid scale forcing, especially convective heating, which is one of the most difficult problems of atmospheric modeling. 3) The "no skill competition" persistence, against which numerical forecasts are compared, is more accurate in the tropics than in the extratropics, and therefore more difficult to be improved upon (Shukla, 1981).

During the Global Weather Experiment (GWE or FGGE) year of 1979, a special effort was made to gather data in the tropics including unconventional observing systems such as satellite temperatures and cloud-track winds, dropwindsondes, research aircraft, etc.

In this study we examine the mean error characteristics of two series of forecasts of the tropical flow. By using as initial conditions analyses made with and without the FGGE special observing system, we estimate the impact that initial data has on the accuracy of the forecasts.

## 2. DESCRIPTION OF THE EXPERIMENTS

The results reported here are obtained from the global assimilation and forecast experiments performed by Halem *et al.* (1982) for the purpose of assessing the impact of satellite data upon extratropical analysis and forecasting.

The GLAS analysis/forecast system for producing a global gridded analysis consists of an objective analysis scheme which makes use of the continuity provided by a first guess which is a 6 hour forecast from the previous analysis. The first guess is then corrected by all the data collected within a + 3 hour window about each analysis time. The analysis scheme (Baker *et al.*, 1981) is a modified successive correction method (Cressman, 1959) which takes into account the density and the quality of the observations. The model used in both the analysis cycle and the forecast is the GLAS fourth-order global atmospheric model described in Kalnay-Rivas *et al.* (1977) and Kalnay-Rivas and Hoitsma (1979). It is based on an energy conserving scheme with all horizontal differences computed with fourth-order accuracy. A 16th order Shapiro filter is applied periodically to remove unresolved scales. The parameterization of subgrid physical processes is identical to that of the GLAS climate model (Shukla *et al.*, 1981). It includes long and short wave radiation with a diurnal cycle, which allows a convective cloud parameterization, conditional instability supersaturation clouds, a bulk formula parameterization of surface fluxes and

a realistic orography. The resolution used in these experiments,  $4^\circ$  latitude x  $5^\circ$  longitude and 9 vertical levels, is somewhat coarse, but this is partly compensated by the improved accuracy of the finite differences used in the model.

Two analysis cycles were performed for the first FGGE Special Observing Period (SOP-1), from January 5 to March 5, 1979. In one of them, denoted FGGE, all available FGGE II-b data were assimilated. In the second experiment, denoted NOSAT, only conventional data (rawinsonde, pilot balloon, aircraft and surface land and ship reports) were utilized (Table 1, from Halem *et al.*, 1982).

Fourteen 5-day numerical forecasts were then generated every four days from the initial conditions of both the FGGE and the NOSAT assimilation experiments.

### 3. RESULTS

We present here preliminary comparisons of the mean and standard deviations of the forecast error. The mean errors represent the systematic forecast errors which may be due either to the parameterization of forcing, or to systematic observational errors or lack of data. The standard deviation of the forecast error is a measure of the skill in predicting the evolution in time of the atmospheric systems.

The error has been computed by subtracting the GLAS FGGE analysis from the forecast. Even though the choice of analysis clearly influences the "error," over most of the globe, the forecast error after one day is larger than the uncertainty in the analysis. A comparison made with the NMC operational analysis, based on a very different analysis/forecast scheme, and which used only NESS operational winds and no satellite temperatures in the Northern Hemisphere, agrees well with the results presented here in most regions.

#### 3.1 FGGE forecasts

Figs. 1 to 3 correspond to the forecast error in the meridional velocity  $v$  as computed from FGGE initial conditions. Fig. 1 presents the average error in  $v$  at 850 mb after 1, 3, and 5 days. It may be seen that at low levels the systematic errors are dominated by large scales, both in the tropics and in the extratropics. This, combined by the fact that their phase is rather constant, indicates that they are associated with forcing, both thermal and orographic. For example, the fact that the forecasts overpredict the equatorward flow over the Andes even after one day, indicates that the mountains are generating more drag in the model than in the real atmosphere. At 300 mb, the average error in the tropics is still of planetary scale, but in the extratropics the error is of cyclonic scale. This, and the change in phase in the error after 1, 3 and 5 days, indicates that the error in the extratropics is dominated by the systematic component in the forecast of moving cyclones.

The systematic error grows in amplitude from day 1 to day 3. There is further growth from day 3 to day 5 in the extratropics, indicating further forecast skill. In the tropics the systematic errors seem to have attained their maximum amplitude by day 3.

Fig. 3 presents the ratio between the average of systematic errors and the standard deviation of the error at 850 mb and 300 mb. Values smaller than one indicate that the error is dominated by transient features, and values larger than one indicate that the systematic error is more important. It may be observed that the extratropical error is dominated by the transients, whereas in the tropics, the systematic error is very important, especially at low levels. Fig. 4 presents the heating rate at 500 mb as computed by the model during the January 1979 assimilation cycle. A comparison of Figs. 3 and 4 confirms that the large systematic errors are associated with regions of strong heating, as well as with orographic forcing.

### 3.2 Comparisons of FGGE, NOSAT and PERSIS Forecasts

Here we compare the systematic and transient errors of the forecasts obtained from the FGGE and NOSAT analysis cycles. Persistence forecasts, in which the forecasts coincide with FGGE initial conditions, are also presented and denoted PERSIS. Figs. 5 and 6 present the 3-day mean and standard deviation of the error in the zonal velocity  $u$  at 300 mb.

It may be seen that the systematic errors from NOSAT initial conditions (Fig. 5b) are only slightly larger than those of FGGE initial conditions. This indicates that systematic errors are due more to model parameterization deficiencies than to initial data. It is interesting that both forecasts show characteristics similar to those of a "warm episode" of the Walker circulation, with enhanced easterlies and stronger subtropical jets in the Pacific (Horel and Wallace, 1981; Julian and Chervin, 1978). At low levels, not presented here, the error is reversed, completing an eastwest circulation. The systematic error in the PERSIS forecast (Fig. 5c) is much smaller than either NOSAT or FGGE in the tropics. This is not surprising because, for a large enough sample, there should be no systematic errors in persistence forecasts. In the extratropics, the average PERSIS errors are dominated once again by the cyclonic scales that have the largest changes after 3 days. It should be remembered that the 14 forecasts are spaced by intervals of 4 days.

Fig. 6 presents the standard deviation of the 3-day forecast errors of  $u$ . The regions with errors smaller than  $6 \text{ m sec}^{-1}$  have been hatched, and those with errors larger than  $12 \text{ m sec}^{-1}$  are indicated by bold contours. A comparison of Figs. 6a and 6b indicates that the use of the FGGE special observing system has improved both the tropical and extratropical forecast of the transient features. We see in Fig. 6c that the PERSIS forecast of transient features is, not surprisingly, much worse than either FGGE or NOSAT in the extratropics.

The FGGE forecast errors are better than those of PERSIS in the subtropics and slightly better in the tropics, indicating some skill in predicting transient features.

The improvement in the forecast of the transient features using the FGGE analysis compared to either the NOSAT or PERSIS forecast is also clear after 5 days, both in the tropics and in the extratropics.

#### 4. CONCLUSIONS

From this preliminary study several conclusions may be drawn. We have found that the systematic error dominates the tropical forecast error. This error seems to be more dependent on model deficiencies than on the initial data and becomes large amplitude in a few days. The model forecast error then becomes comparable to the persistence forecast error in 3 to 5 days. On the other hand, the model retains some skill in the prediction of transient features in the tropics after 3 days and there is a significant impact of the FGGE data in the prediction of these transients.

This study suggests that a major obstacle in accurate low latitude forecasting is the prediction of the large scale quasi-stationary tropical circulation.

#### ACKNOWLEDGEMENTS

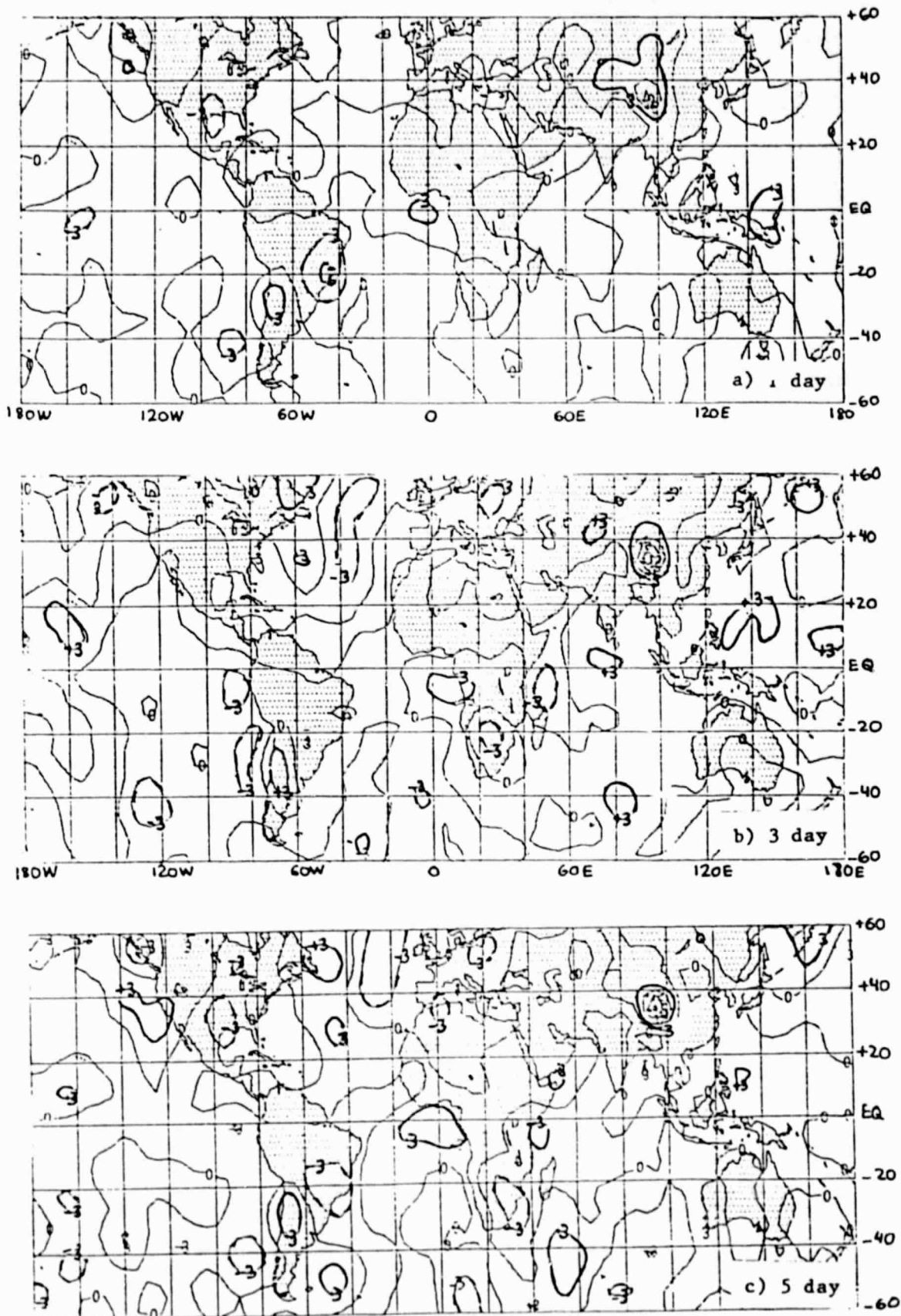
We gratefully acknowledge the encouragement and support of Dr. M. Halem. Excellent technical assistance was provided by Mr. D. Edelmann, Ms. M. Eaton, and Mr. S. Breining. The manuscript was prepared by Ms. J. Wentz.

#### REFERENCES

- Baker, W. E., D. Edelmann, M. Iredell, D. Han, and S. Jakkempudi, 1981: Objective analysis of observational data from the FGGE observing systems. NASA Tech. Memo. 82062.
- Cressman, G. P., 1959: An operational objective analysis system. Mon. Wea. Rev., 85, 367-374.
- Halem, M., E. Kalnay, W. Baker, and R. Atlas, 1982: An assessment of the state of the atmosphere as inferred from the FGGE satellite observing systems during SOP-1. Bull. Amer. Soc. Meteor., 63, in press.
- Horel, J. D., and J. M. Wallace, 1981: Planetary scale atmospheric phenomena associated with the Southern Oscillation. Mon. Wea. Rev., 109, 813-829.
- Julian, P. R., and R. M. Chervin, 1978: A study of the Southern Oscillation and Walker circulation phenomena. Mon. Wea. Rev., 106, 1433-1451.
- Kalnay-Rivas, E., and D. Hoitsma, 1979: Documentation of the fourth order band model. NASA Tech. Memo. 80608.
- Kalnay-Rivas, E., A. Bayliss, and J. Storch, 1977: The 4th Order GISS Model of the global atmosphere. Beitrag zur Physik der Atmosphere, 50, 299-311.
- Shukla, J., 1981: Predictability of tropical atmosphere. Proceedings of Tropical Met. Workshop., ECMWF, March 11-13, 1981.
- Shukla, J., D. Straus, D. Randall, Y. Sud, and L. Marx, 1981: Winter and summer simulations with the GLAS climate model. NASA Tech. Memo. 83866.

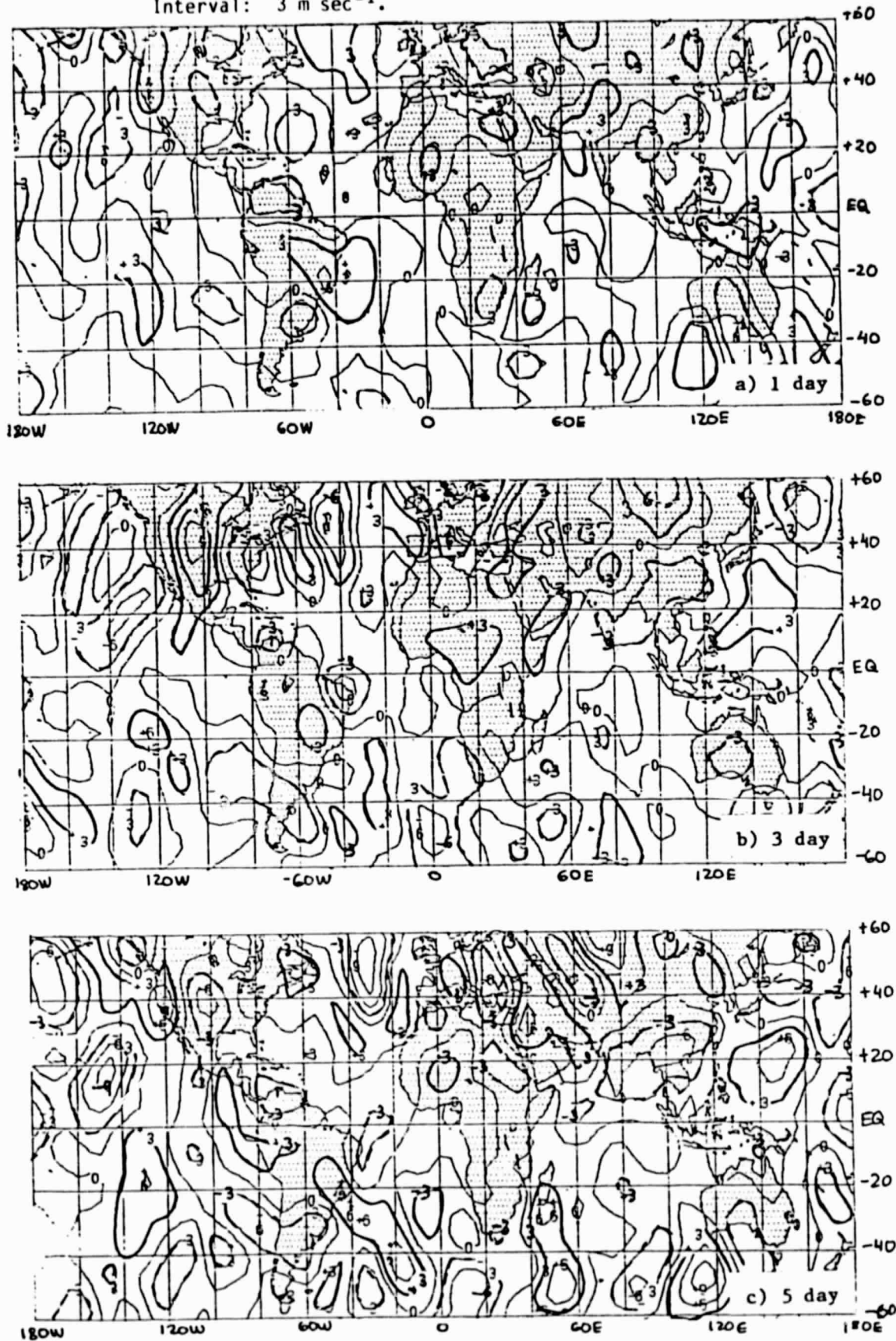
ORIGINAL PAGE IS  
OF POOR QUALITY

Figure 1. Mean forecast errors in the meridional velocity  $v$  at 850 mb.  
Interval:  $3 \text{ m sec}^{-1}$ .



ORIGINAL PAGE IS  
OF POOR QUALITY

Figure 2. Mean forecast errors in the meridional velocity  $v$  at 300 mb.  
Interval:  $3 \text{ m sec}^{-1}$ .



ORIGINAL PAGE IS  
OF POOR QUALITY

Figure 3. Ratio between the mean and the standard deviation of the 3-day forecast errors in the meridional velocity  $v$ . Interval: 0.50.

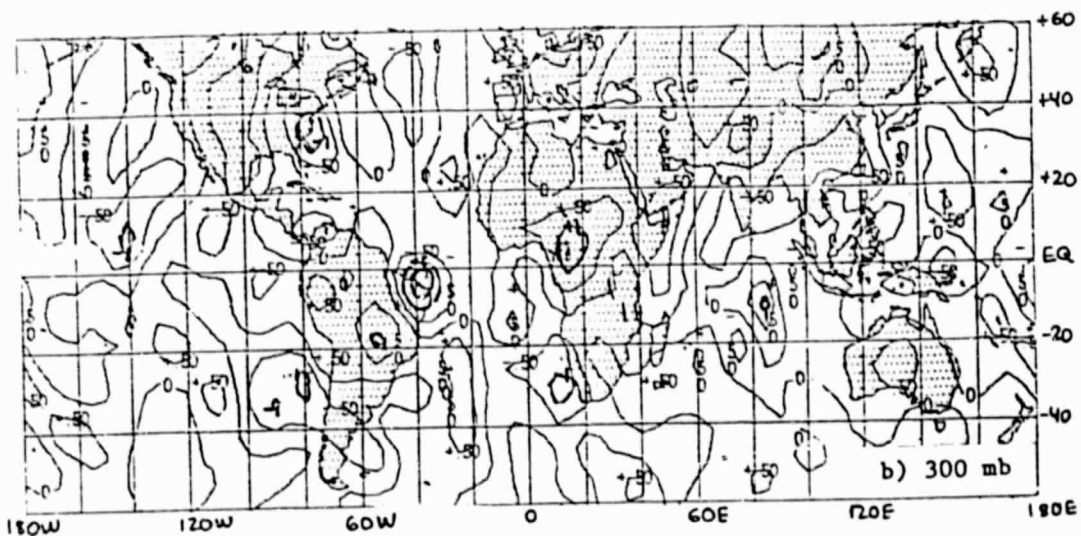
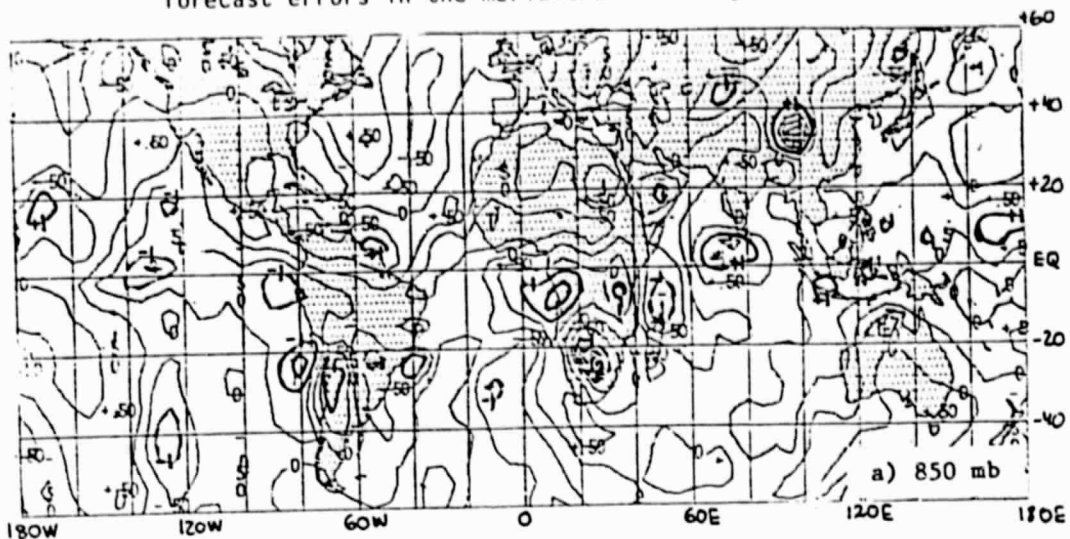


Figure 4. January assimilation heating rates at 500 mb (deg/day).

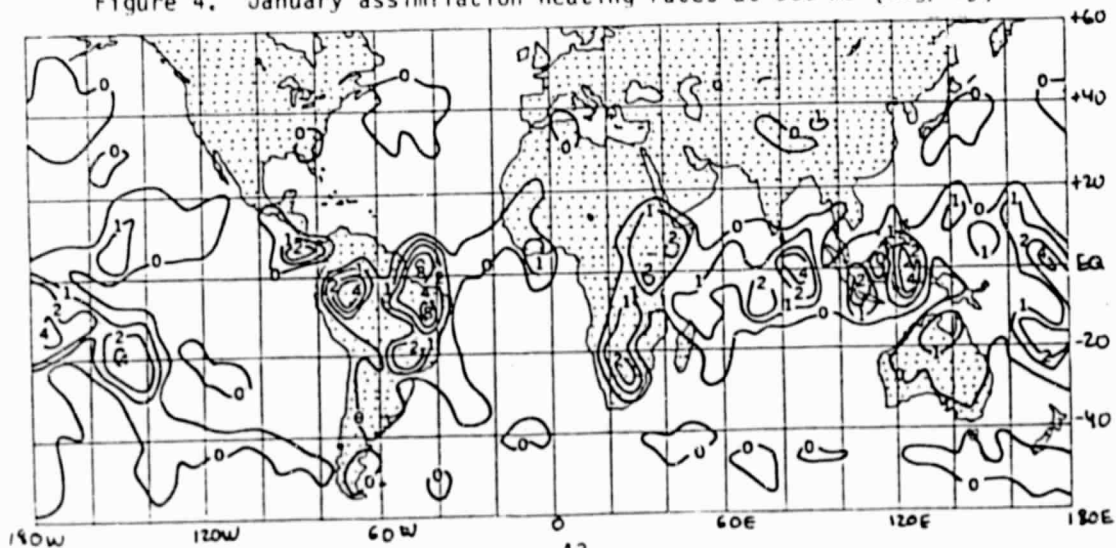
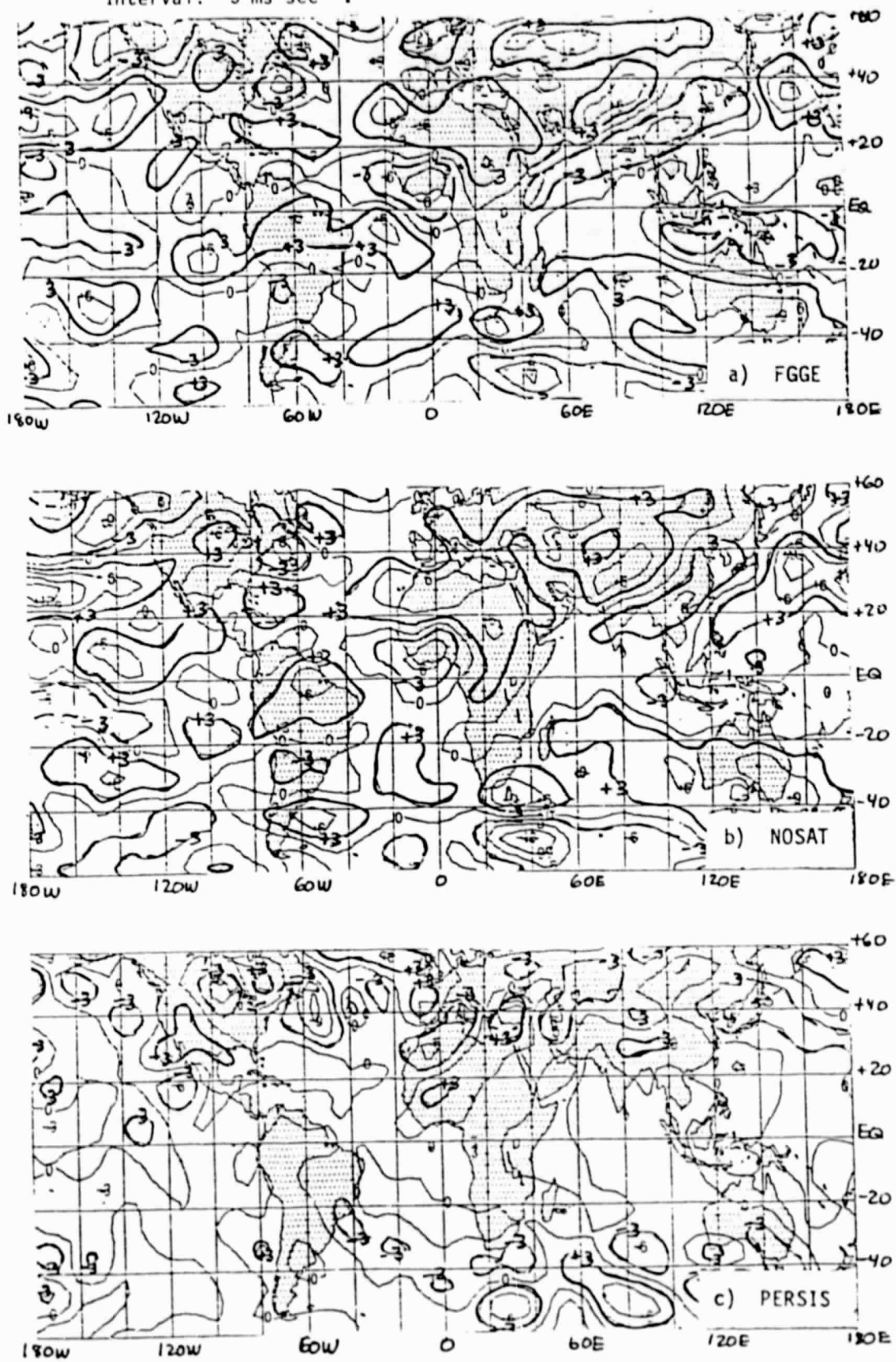
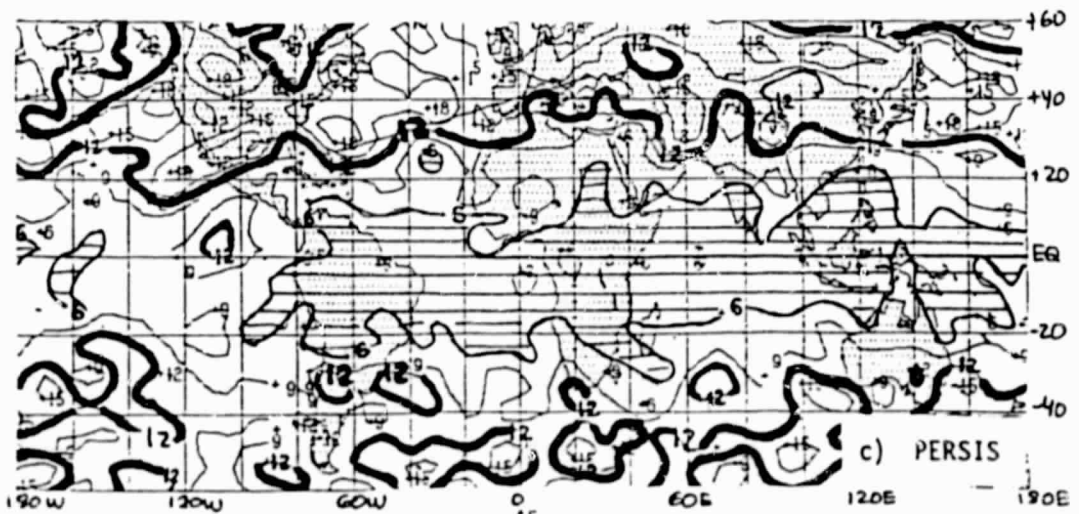
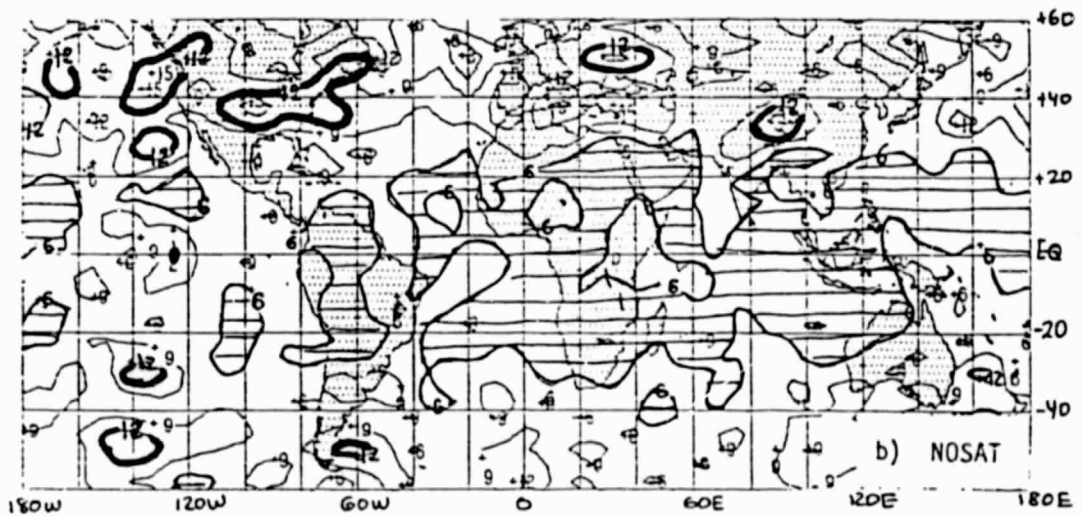
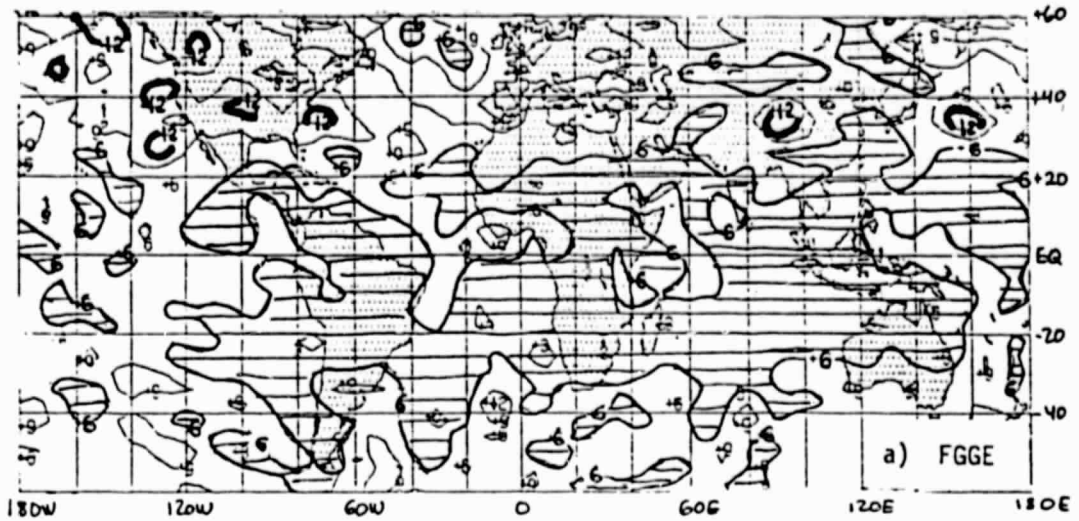


Figure 5. Mean errors in the 3-day forecast of the zonal velocity at 300 mb.  
Interval: 3 ms sec<sup>-1</sup>.



ORIGINAL PAGE IS  
OF POOR QUALITY

Figure 6. Standard deviation of the 3-day forecast errors of the zonal velocity at 300 mb. Interval:  $3 \text{ m sec}^{-1}$ .



PRECEDING PAGE BLANK NOT FILMED

**B. SATELLITE, TEMPERATURE, AND WIND  
RETRIEVALS**

## INTERACTIVE PROCESSING OF SEASAT SCATTEROMETER DATA

R. Atlas, G. Cole, A. Pursch, and C. Long

The objectives of the interactive processing of Seasat data are to (1) develop and apply techniques for the removal of alias in the SASS winds using all available data, (2) study the properties of SASS wind data in a variety of synoptic situations, and (3) provide improved analyses for meteorological diagnosis and prediction.

The Man-computer Interactive Data Access System (McIDAS), developed by the Space Science Engineering Center (SSEC) of the University of Wisconsin and adapted for the interactive processing of satellite-derived temperature soundings and cloud-track winds for the FGGE Special Effort, has now been adapted for the processing and evaluation of Seasat data. The implementation of the McIDAS Seasat processing system required (1) extensive modifications to the data base structure to store and display SASS winds, as well as all corroborative level II data, model first guess fields and level III analyses, and (2) the development of software to dealias and analyze SASS wind vectors interactively.

The procedure for the subjective dealiasing of SASS winds that has been developed for use on the McIDAS consists of the following steps:

1. Display SASS vectors.
2. Superimpose auxiliary data.
3. Remove alias where only two alias directions or ship wind data are present.
4. Use pattern recognition, kinematic consistency, and meteorological experience to streamline entire SASS wind field.
5. Remove alias of all remaining SASS vectors.
6. Insure consistency with cloud imagery.

This procedure has been applied to selected cases during the period 8-15 September 1978. For situations in which nearly uniform wind directions exist over a large area, the synoptic analyst utilizing the McIDAS may dealias the entire wind field for that area by positioning a cursor over a single SASS wind vector which indicates the correct direction. For cases in which there is large variability of the wind directions, each SASS report is dealiased separately using the same technique.

Fig. 1 presents an example of the dealiasing of SASS winds on the McIDAS. In Fig. 1a, alias SASS wind directions and wind speeds are shown for a small section of the North Atlantic on 8 September 1978. The dealiased wind field for this section is shown in Fig. 1b, where streamlines and ship report wind directions have been superimposed. Fig. 2 shows the dealiased wind field for

the entire North Atlantic from 0000-0036 GMT 8 September 1978, which incorporated the section shown in Fig. 1. The SASS winds are in good general agreement with most conventional ship reports and serve to define the synoptic and sub-synoptic scale flow with greater accuracy than is possible from the conventional data alone. Comparisons of the convergence and divergence fields associated with the SASS winds with geostationary cloud imagery shows excellent agreement.

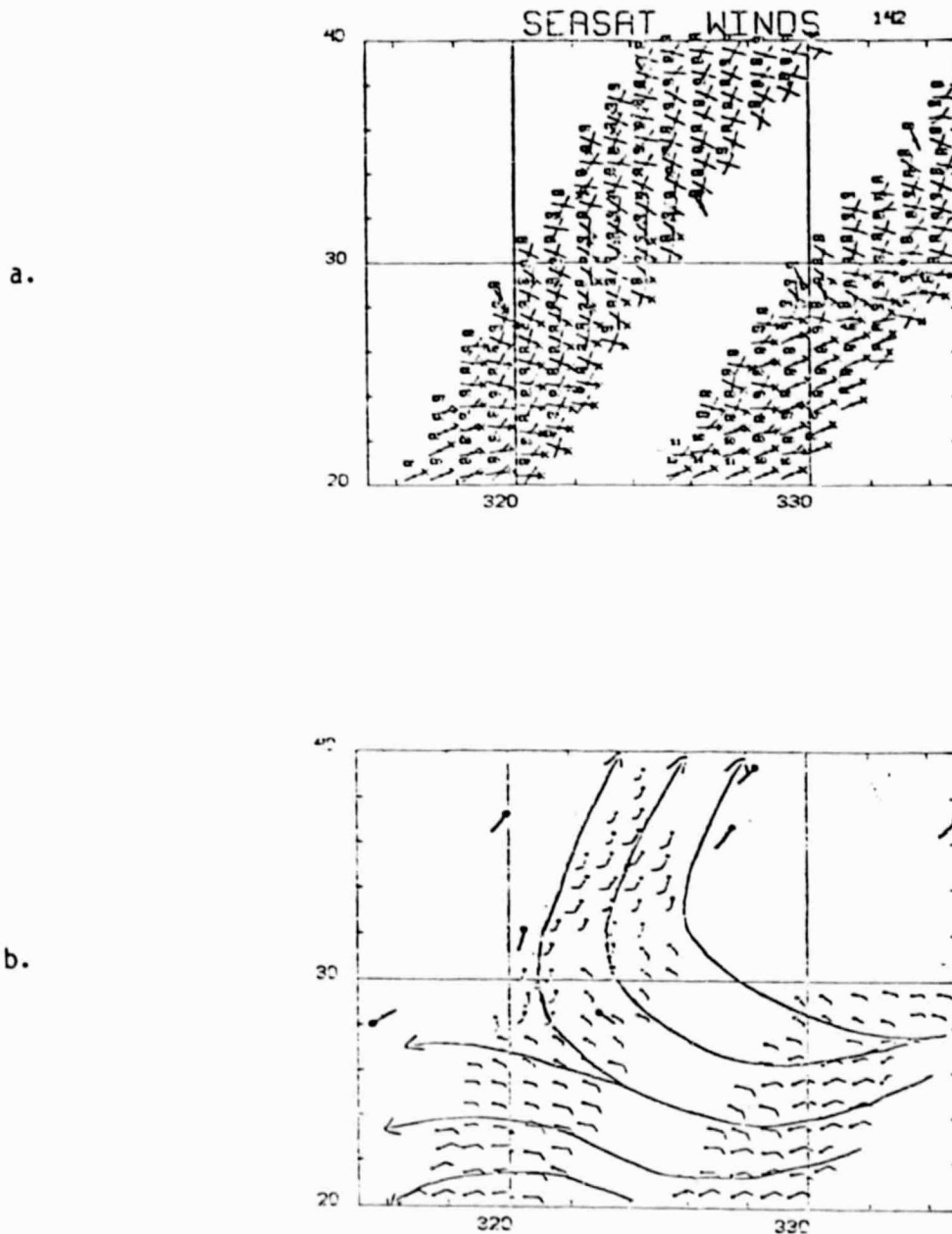


Fig. 1 Alias SASS vectors (a), and dealised vectors and ship wind directions (b) for 0024-0030 GMT 8 September 1978.

ORIGINAL PAGE IS  
OF POOR QUALITY

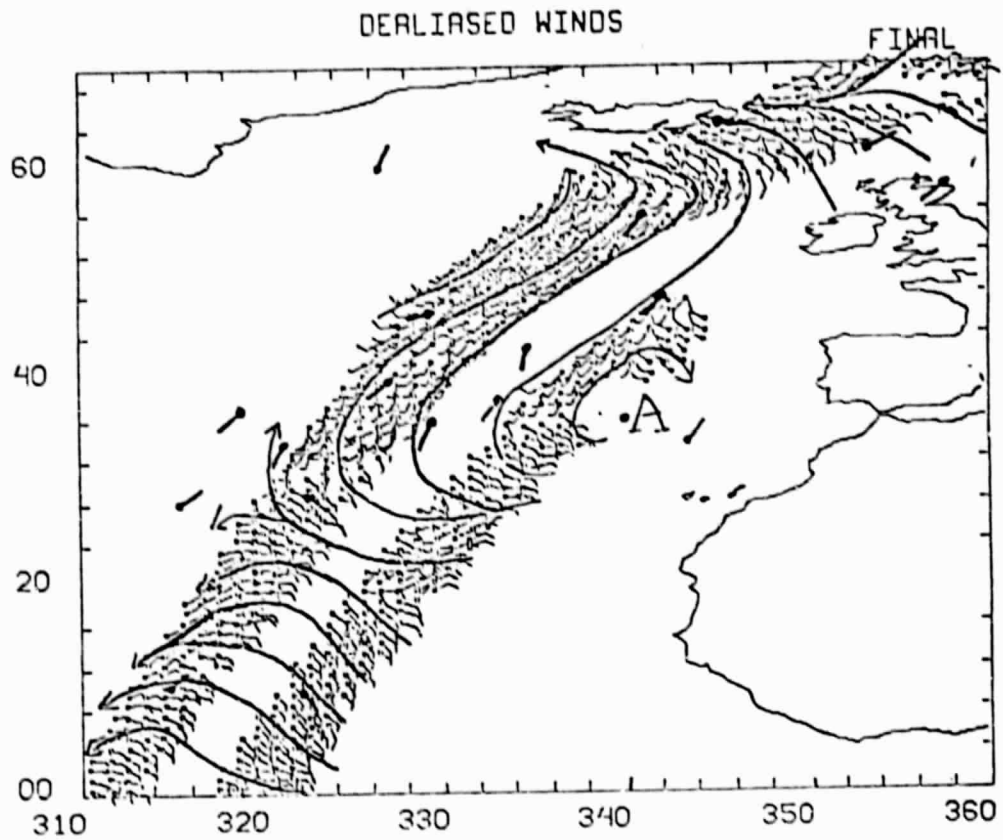


Fig. 2 Dealiased SASS winds, ship reported wind directions and surface streamlines for 0000-0036 GMT 8 September 1978.

## PRELIMINARY EVALUATION OF THE FGGE SPECIAL EFFORT FOR DATA ENHANCEMENT

R. Atlas, A. Pursch, C. Long, G. Cole, and R. Rosenberg

The FGGE Special Effort is being conducted for the two FGGE special observing periods (January to March and May to June 1978) as a joint project between NASA, NOAA, and the University of Wisconsin. Man-computer Interactive Data Access System (McIDAS) terminals developed by the Space Science Engineering Center (SSEC) of the University of Wisconsin are being utilized by experienced meteorologists at the National Meteorological Center (NMC) for data evaluation and quality assessment and at the Goddard Laboratory for Atmospheric Sciences (GLAS) for satellite data enhancement. The interactive procedures used for sounding and cloud-motion wind enhancement were originally developed by the National Environmental Satellite Service and SSEC. (Smith et al., 1978, and Menzel et al., 1978). (See Greaves et al., 1979 for a detailed description of the development and implementation of the FGGE Special Effort.)

For each synoptic period there is an initial editing of FGGE data by NMC. At this stage, quality indicators are assigned to temperature soundings from TIROS-N and to cloud-tracked wind vectors from geostationary satellites. The determination of data quality is made on the basis of synoptic considerations including horizontal, vertical and temporal consistency. Regions where data deficiencies exist or where higher resolution data is needed to adequately represent the atmospheric thermal structure are then selected for enhancement. The eastern North Pacific is routinely enhanced. In addition, cases have been preselected on the basis of meteorological interest, by an ad-hoc international committee of participating scientists. These cases include situations of blocking, cut-off low development, cyclogenesis, and tropical circulation.

The sounding data enhancement is aimed at supplementing the operational satellite sounding data set with higher resolution soundings in meteorological active regions and with new soundings where data voids or soundings of questionable quality exist. The algorithms for retrieving temperature profiles from the TIROS-N observations of radiance displayed on McIDAS are essentially the same as those used by NESS for the objective generation of operational temperature profiles. Three types of temperature retrievals are possible: (1) clear-column, and (2) partly cloudy retrievals utilizing infrared observations from the HIRS instrument aboard TIROS-N, and (3) cloudy retrievals utilizing only microwave observations from the Microwave Sounding Unit (MSU) on TIROS-N. The operational temperature profiles have a horizontal resolution of 250 km, whereas special effort temperature profiles can be retrieved at the resolution of the measurements (30 km for HIRS and 150 km for MSU).

The sounding enhancement process at GLAS is performed as follows: once an area has been selected, the McIDAS operator begins by displaying all available conventional and special FGGE data for that area and visible, infrared, and microwave images from TIROS-N. The operator notes where data deficiencies exist and, from the TIROS-N images, determines the extent of cloudiness and where the most intense atmospheric thermal gradients are located. High-resolution infrared temperature retrievals are then generated for the area. This is followed by a comprehensive manual editing of the retrievals to remove small-scale discontinuities due to cloud-induced noise while retaining significant meteorological structures. Enhanced microwave retrievals, consistent with neighboring infrared retrievals, are then generated in cloudy areas.

After the entire enhancement process is completed, a final editing and quality assessment of the enhancement data is performed at NMC. The data is then archived as supplementary Level IIb and will be utilized by NOAA's Geophysical Fluid Dynamics Laboratory (GFDL) in generating Level IIIb analyses.

Enhanced sounding data can be displayed on the McIDAS as either mandatory level temperatures or as the thickness between any two levels. Analyses of these quantities as well as thermal winds, vertical temperature profiles, and vertical cross-sections of potential temperature are routinely produced. If conventional surface data is available, then the 1000 mb geopotential height is analyzed, and the satellite-derived thickness and thermal winds are added to the 1000 mb height and 1000 mb geostrophic wind to yield geopotential height and geostrophic winds on constant pressure surfaces. In addition to the high resolution analyses performed directly on the McIDAS, enhanced soundings may be assimilated into larger scale objective analyses which then serve as initial conditions for numerical model predictions.

Subjective comparisons of enhanced soundings with all available operational soundings and radiosonde reports are performed at the end of the enhancement process. These comparisons have shown that the enhanced and operational retrievals tend to be similar in cloud-free areas. However, large differences occasionally occur. The differences are accentuated in and around cloudy areas where the interactive processing at high resolution allows for the generation of substantially more infrared retrievals and where the microwave retrievals are enhanced.

Examples illustrating some of the effects of the sounding data enhancement are presented in Figures 1 and 2. In Figure 1, 1000 mb to 300 mb thickness analyses of operational (solid lines) and Special Effort retrievals (dashed lines) and plotted radiosonde reports are shown for a section of the North Pacific at 0100 GMT 7 January 1979. Large differences in the orientation, gradient, and absolute value of the enhanced and operational thickness contours are evident. In addition, the errors relative to colocated radiosondes have been reduced by 30 to 80 geopotential meters.

In Figure 2, vertical temperature profiles of unenhanced and enhanced microwave retrievals are plotted relative to the colocated radiosonde observation at Yakutat, Alaska at 0000 GMT 11 January 1979. Differences between the retrievals are small throughout most of the troposphere in this case. However, the enhancement process has resulted in a better definition of the tropopause and a reduction of error of 4°C near the 100 mb level.

As an example of the application of Special Effort sounding to large-scale meteorological analysis and prediction, the enhancement for 0000 GMT 9 January 1979 is presented here. This was a case in which a large gap in the operational TIROS-N soundings occurred in the eastern North Pacific. Figure 3 shows the orbit of TIROS-N and the location of operational soundings from 2100 GMT 8 January to 0300 GMT 9 January. Reprocessing of observed radiances on the McIDAS allowed for the generation of enhanced soundings over a large portion of the data gap from 30° to 50°N. Additional high resolution soundings were also generated over regions adjacent to the gap to better define the atmospheric thermal structure and to insure consistency.

ORIGINAL PAGE IS  
OF POOR QUALITY

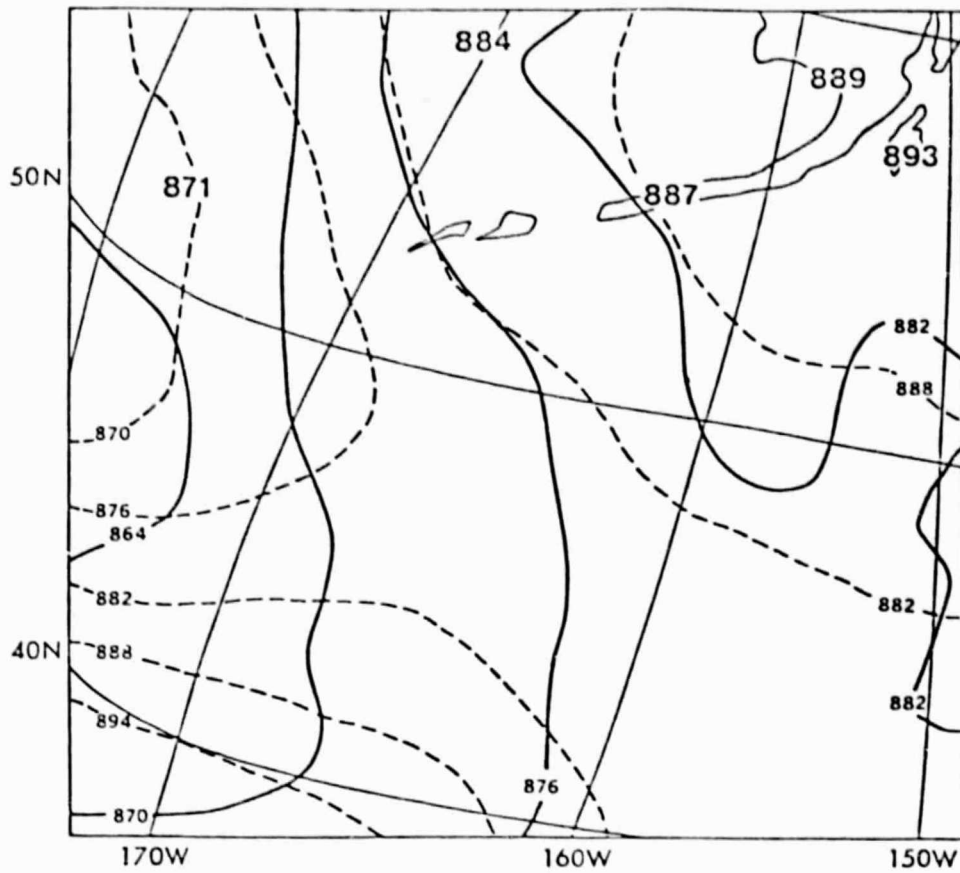


Figure 1. 1000-300 mb thickness analyses of operational soundings (solid lines) and Special Effort soundings (dashed lines) for 0100 GMT 7 Jan 79. Radiosonde observations of 1000-300 mb thickness in decameters are plotted as large numbers.

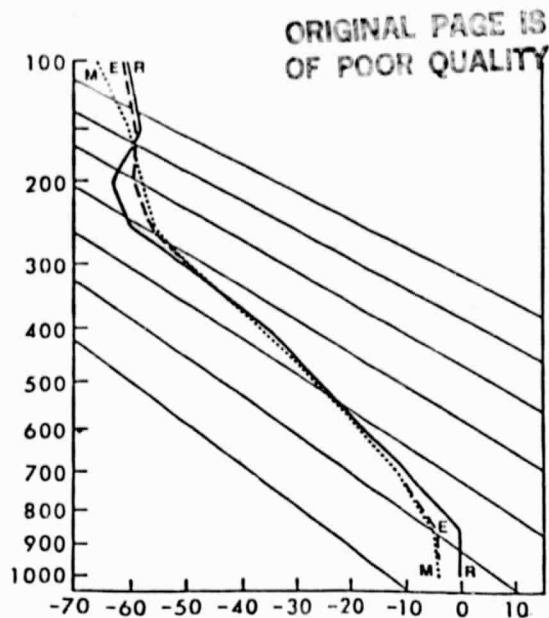


Figure 2. Vertical temperature profiles derived from unenhanced microwave (M), enhanced microwave (E), and radiosonde (R) for Yakutat, Alaska, at 0000 GMT 11 Jan 79.

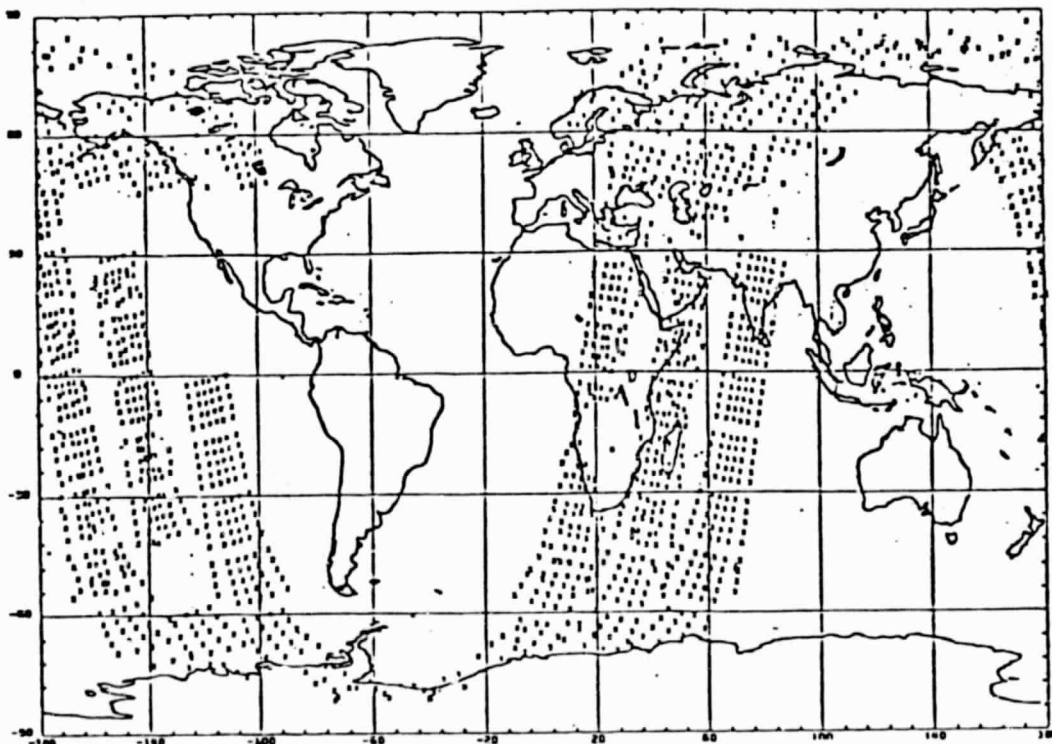


Figure 3. Location of TIROS-N retrievals from 2100 GMT 8 Jan 79 - 0300 9 Jan 79.

Figures 4 and 5 display the 1000 to 300-mb thickness analyses and thermal winds for the enhanced regions. These analyses are based completely on the high-resolution soundings, with each thermal wind barb plotted at the location of the retrieved vertical temperature profiles.

Figures 6 and 7 illustrate the effect of the enhanced soundings on the GLAS objective analysis for 0000 GMT 9 January. In Figure 6, the 300 mb height and wind analysis for all conventional and operational satellite data is presented. The corresponding analysis, which includes enhanced soundings, is presented in Figure 7. Comparison of the figures reveals that a major modification to 300 mb heights and winds has occurred just off the west coast of the United States. The enhanced soundings have increased the amplitude of the ridge at 135°W and shortened the half-wavelength between this ridge and the trough along the west coast. Elsewhere the effects are smaller due to the consistency of the operational and enhanced soundings over most of the eastern North Pacific and the averaging of the effects of enhanced soundings by the objective analysis. However, changes to the intensity of the geopotential gradient and orientation of the winds and contours are evident throughout this region.

Figures 8 and 9 show the 24-hour GLAS model forecasts of 300 mb geopotential heights and winds, which were generated from initial conditions corresponding to Figures 6 and 7, respectively. The verifying analysis is presented in Figure 10. Comparison of these figures reveals that the inclusion of enhanced soundings resulted in a large improvement in the predicted amplitude of the trough over the southwestern United States. Additional improvements are evident over the North Pacific. However, the verifying analysis is less certain in this area.

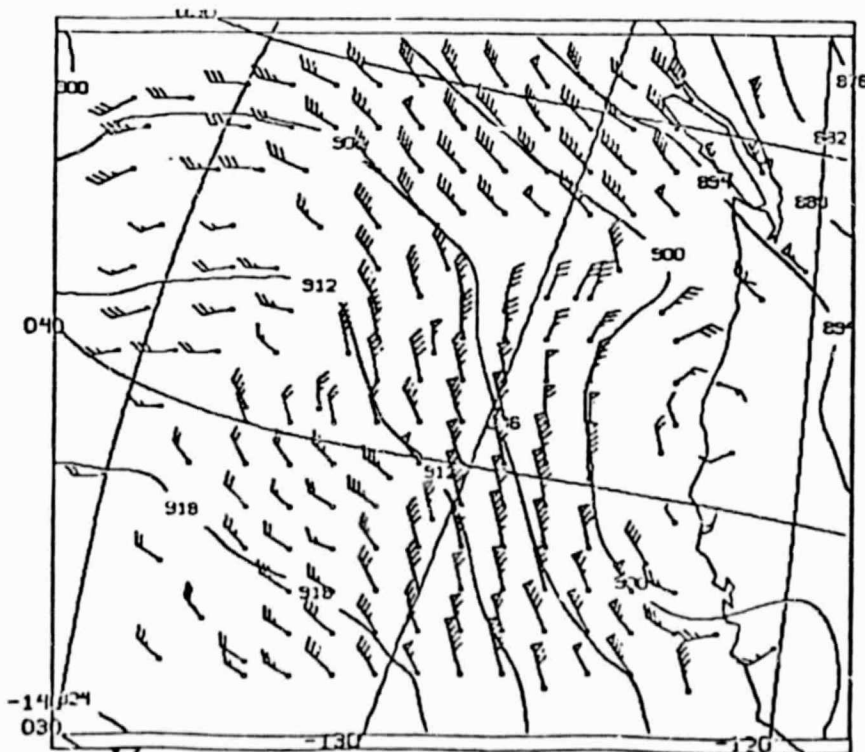
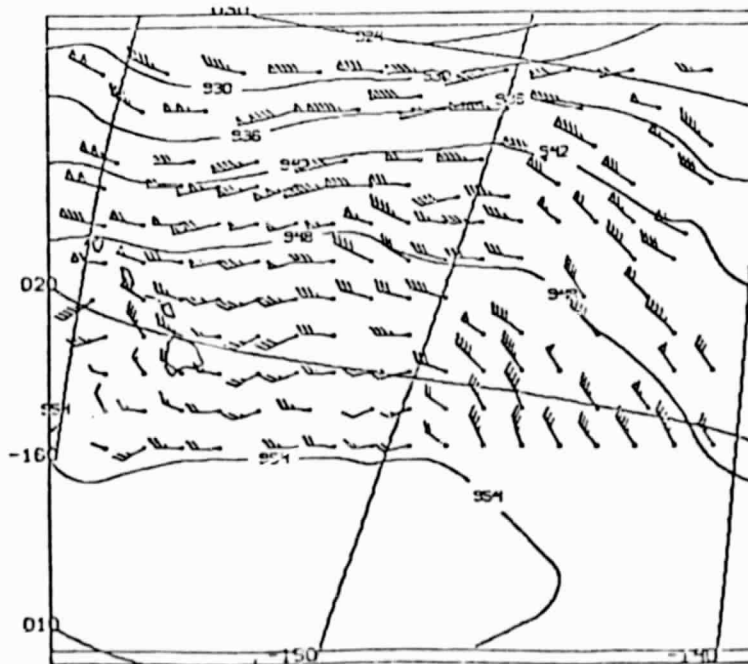
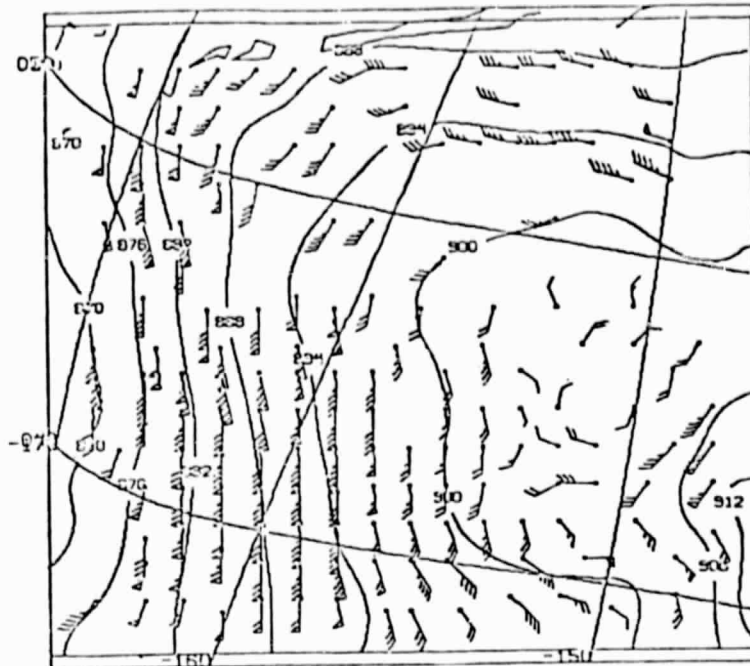


Figure 4. 1000-300 mb thickness and thermal wind at 2300 GMT 8 Jan 79 derived from high resolution TIROS-N soundings for the region 30-55°N and 120-145°W.

ORIGINAL PAGE IS  
OF POOR QUALITY



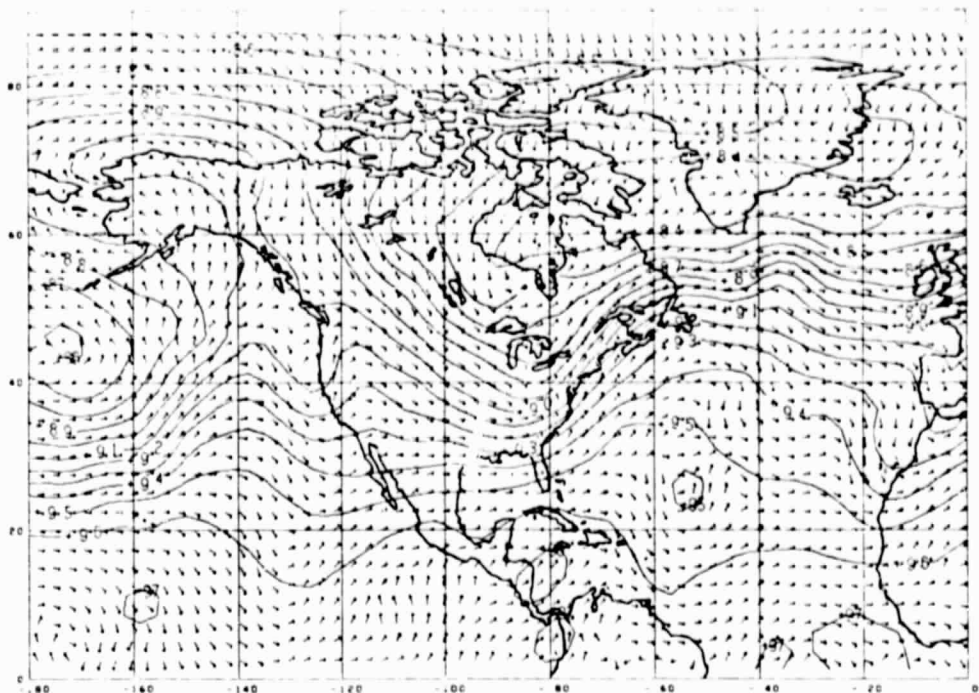


Figure 6. 300 mb geopotential height and wind analysis without enhanced retrievals for 0000 GMT 9 Jan 79.

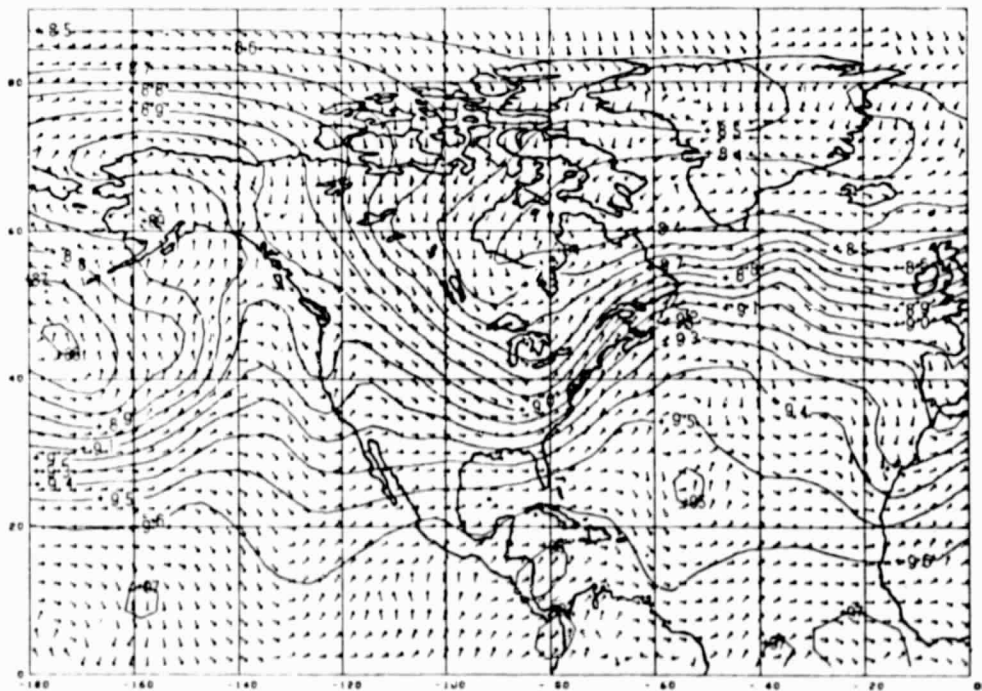


Figure 7. 300 mb geopotential height and wind analysis with enhanced retrievals for 0000 GMT 9 Jan 79.

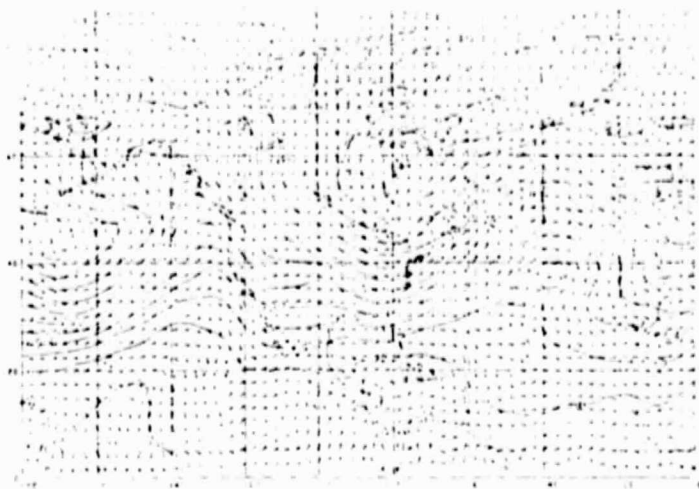


Figure 8. 24h 300 mb forecast generated without enhanced retrievals.

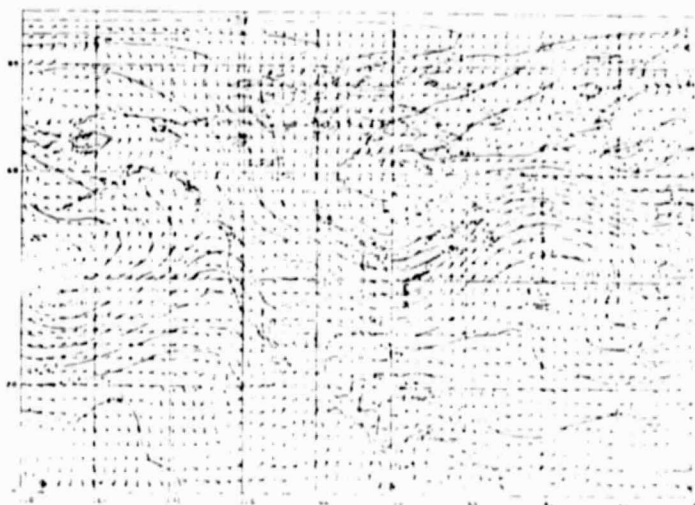


Figure 9. 24h 300 mb forecast generated with enhanced retrievals.

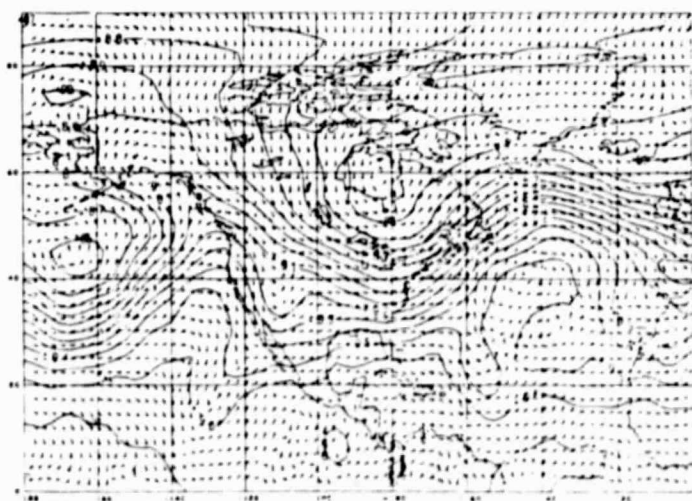


Figure 10. Verifying 300 mb geopotential height and wind analysis for 0000 GMT 10 Jan 79.

Subjective evaluation of the effects of sounding data enhancement indicate that:

1. Enhanced and operational IR retrievals are similar in most situations.
2. Large improvements in 1000 to 300 mb thickness and mandatory level temperature and intensification of atmospheric thermal gradients occasionally occur.
3. Interactive processing can fill in major gaps in the TIROS-N coverage.
4. Assimilation of Special Effort soundings can result in major modifications to large-scale analyses and prognoses.

#### REFERENCES

- Greaves, J. R., G. DiMego, W. L. Smith, and V. E. Suomi, 1979: A special effort to provide improved sounding and cloud motion wind data for FGGE. Bull. Amer. Meteor. Soc., 60, 124-127.
- Menzel, W. P., W. L. Smith, and H. M. Woolf, 1978: A man interactive technique for specifying cloud height from sounding radiance data. Proc. of the Third AMS Conf. on Atmos. Rad., Davis, California, 28-30 June.
- Smith, W. L., C. M. Hayden, H. M. Woolf, H. B. Howell, and F. W. Nagle, 1978: Interactive processing of TIROS-N sounding data. Proc. of the AMS Conf. on Wea. Forecasting and Analysis and Aviation Meteor., Silver Spring, Maryland, 16-19 October.

COMPARISON OF OBSERVED AND COMPUTED BRIGHTNESS TEMPERATURES  
FOR THE HIRS2 AND MSU SOUNDERS ON TIROS-N

J. Susskind, J. Rosenfield, and D. Reuter

Global temperature soundings from HIRS and MSU data on the TIROS-N satellite are produced at the Goddard Space Flight Center Laboratory for Atmospheric Sciences Modeling and Simulation Facility using a direct physical retrieval method. Intrinsic in the success of such a method is accurate computation of expected radiance observations, given a set of atmospheric and surface conditions. McClatchey (1976) indicated very poor agreement between radiances observed by the DMSP sounder under clear conditions and those calculated from colocated temperature humidity profiles, raising questions about the accuracy in which radiative transfer calculations can be performed in the infrared. Here, we briefly summarize our findings, showing excellent agreement between observed and computed brightness temperatures for HIRS2 and MSU under both clear and partly cloudy conditions. More details are given in Susskind *et al.*, (1982). Table 1 shows the channels, centers, and peaks of the weighting functions, or other relevant information, for the channels on MSU and HIRS2. The HIRS2 and MSU channels used in the GLAS physical inversion method are designated by \*.

Table 1

HIRS2 and MSU Channels

Channel	$\nu(\text{cm}^{-1})$	Peak of $d\tau/d\ln p$ (mb)	Peak of $Bd\tau/d\ln p$ (mb)
H1	668.40	30	20
*H2	679.20	60	50
H3	691.10	100	100
*H4	703.60	280	360
H5	716.10	475	575
H6	732.40	725	875
H7	748.30	Surface	Surface
H8	897.70	Window, sensitive to water vapor	
H9	1027.90	Window, sensitive to $O_3$	
H10	1217.10	Lower tropospheric water vapor	
H11	1363.70	Middle tropospheric water vapor	
H12	1484.40	Upper tropospheric water vapor	
*H13	2190.40	Surface	Surface
*H14	2212.60	650	Surface
*H15	2240.10	340	675
H16	2276.30	170	425
H17	2310.70	15	2
*H18	2512.00	Window, sensitive to solar radiation	
*H19	2671.80	Window, sensitive to solar radiation	
*M1	50.30a	Window, sensitive to surface emissivity	
*M2	53.74a	500	
*M3	54.96a	300	
*M4	57.95a	70	

a values in GHz

All HIRS2 observations utilized in global analysis of the data are composed of two averages of spots within a 125 x 125 km area. The two fields of view represent relatively clear and relatively cloudy areas. Both sets of radiances are used to determine a reconstructed clear-column radiance, that is, the radiance which would be observed if the areas were cloud-free (Suskind and Rosenfield, 1980). For verification purposes, HIRS2 observations during the period Jan 5 1979-Feb 25 1979 were chosen which were colocated with a select set of oceanic radiosondes (see Phillips et al., 1979) in space by 110 km, and, in time, by three hours. Only those radiosondes reporting temperatures at all mandatory levels from 1000 mb - 30 mb and humidities from 1000 mb - 500 mb were used in the comparison.

Given the radiosonde temperature and humidity profile, brightness temperatures for the temperature sounding IR channels on HIRS2 were calculated according to Suskind et al., (1982). The temperature profile was interpolated to 53 levels between 1000 and 30 mb assuming temperature to be linear in the logarithm of the pressure between the mandatory levels. The 11 levels above 30 mb were extrapolated according to climatology. The surface temperature was taken to be the climatological sea surface temperature. The specific humidity was interpolated between mandatory levels assuming a  $P^n$  dependence. A specific humidity corresponding to a climatological water vapor mixing ratio of 2 ppmv was assumed at and above 100 mb. Zonally averaged climatological ozone profiles were used to compute the ozone component of the transmittance.

Infrared radiances are potentially cloud contaminated. An estimate of the clear-column radiance,  $R_i$ , for channel  $i$  can be reconstructed from the observations in adjacent fields of view according to

$$R_i = R_{i,1} + \eta (R_{i,1} - R_{i,2}) \quad (1)$$

where  $R_{i,j}$  is the observation for channel  $i$  in the field of view  $j$  and  $\eta$  is a parameter given by  $\alpha_1/(\alpha_2 - \alpha_1)$ , where  $\alpha_1$  and  $\alpha_2$  are the cloud fractions in the two fields of view (Suskind and Rosenfield, 1980). For the purposes of this study, the parameter  $\eta$ , which is independent of channel, is best determined according to

$$\eta = \frac{R_{13}^{CC} - R_{13,1}}{R_{13,1} - R_{13,2}} \quad (2)$$

where  $R_{13}^{CC}$  is the computed clear-column radiance for channel 13, using the radiosonde temperature profile.

A value of  $\eta = 0$  corresponds to field of view 1 (always taken as the field of view containing the larger radiance in the 11um window channel) being clear. If  $\eta$  was less than 0,  $\eta$  was set equal to -0.5. In this case, the clear-column radiance is the average of the observations in both fields of view.

Two sets of statistics were calculated comparing observed and computed radiances. The first sample represents comparisons made only in those cases where at least one field of view was found to be clear, that is  $\eta < 0$ . The second sample contains only partially cloudy cases,  $\eta > 0$ , in which case comparisons were

made between radiances reconstructed from equations 1 and 2 and computed clear-column radiances. The first set of statistics refers primarily to the accuracy of the forward problem calculation. The second set includes the accuracy of the ability to account for cloud effects.

Table II shows the comparison of observed and computed brightness temperatures for the air and surface temperature sounding channels of HIRS2 and MSU in the 72 cases where the cloud filtering algorithm showed at least one field of view to be cloud-free. Those channels used in the retrieval of temperature profiles are marked by \*. Columns 2 and 3 show the mean and standard deviation of the differences between computed and observed brightness temperatures. The standard deviation between observed and computed brightness temperatures is generally better than 1°K for the HIRS2 channels used in the calculation and somewhat worse than 1°K for the MSU channels. Significant bias errors are found in some channels, however. To a large extent, these biases are due to errors in the line parameters used in the line-by-line calculations. The largest standard deviations found in the infrared channels are in channels 1-3 and 16, whose radiances are quite sensitive to the temperature profile above 30 mb, and channels 8, 18, and 19, the surface temperature sounding channels, where agreement is limited by the accuracy of the climatological sea surface temperature. Channel 16 is also affected by non-local thermodynamic equilibrium, which was not accounted for in the calculation. Channel 17, which is affected even more greatly by non-local thermodynamic equilibrium, was not included in the calculation. Observations in channels 18 and 19 are affected by contributions of reflected solar radiation to the radiances. In addition, agreement in all channels is degraded somewhat by sampling differences between radiosonde and satellite observations.

The systematic errors can be removed by empirically tuning the transmittance functions in the form

$$\tau_i(p) = \tau_i(p)^{1+\epsilon_i} \quad (3)$$

which is equivalent to multiplying the effective channel optical depths by  $1+\epsilon_i$ .

Tuning coefficients were found for channels, 4-7, 13-15, and M2-M4 which minimized the bias and standard deviations in the brightness temperature errors computed in the sample of clear cases. The tuning coefficients obtained for these channels are shown in column 6 of the table and the resulting mean and standard deviation of the errors of the brightness temperature using the tuned transmittances are shown in columns 4 and 5. No attempt was made to tune the remaining channels because of the considerations discussed above. The empirical tuning coefficients found in Table II are similar to those found by Weinreb (1979).

After tuning, the mean errors for all channels except 1, 3, and 16, which are not used in analysis of the HIRS data, are insignificant. With the exception of the stratospheric sounding channel 2, the standard deviation of the 15 $\mu$ m and 4.3 $\mu$ m brightness temperatures in channels used for retrievals of temperature profiles are of the order of 0.7°. These errors are sufficiently small so as not to seriously effect the accuracy of retrievals. Agreement in channel 7, used only for cloud height determination, is somewhat worse, possibly because of the effects of incorrect surface temperature. Likewise, agreement in the microwave channels is about 50% worse than the infrared channels, possibly

because of higher noise in the microwave measurements. The sixth column of Table II shows the standard deviations of the measurements for each channel. The ratio of the standard deviation of the observations to the standard deviation of the errors may be thought of as a signal to noise for each channel.

Agreement in channels 18 and 19 appears to be very poor, with a large negative bias in the observations. This is due to the effects of solar radiation, which were not included in the calculations of brightness temperatures for these channels. In the physical inversion of sounding data, the two observations for channels 18 and 19 are analyzed simultaneously to compute a surface temperature and a correction for solar radiation (Suskind and Rosenfield, 1980; Chahine, 1980). That procedure was not done here because it would force agreement between observed and computed brightness temperatures. To assess the accuracy of the forward calculation for these channels, statistics were gathered for observations at night (21 cases). These are shown in the last two columns of Table I for the window channels 18, 19, and 8. The general agreement is good and again limited by the accuracies of the climatological sea surface temperature. The two shortwave windows are shown to be somewhat more accurate than the 11  $\mu\text{m}$  window channel. This is most likely due to the lesser effect of absorption due to water vapor continuum on the radiances in the 3.7  $\mu\text{m}$  region. Absorption due to water vapor continuum is not thoroughly understood and less well parameterized than the other sources of atmospheric absorption.

Agreement of reconstructed and computed brightness temperatures in an independent sample of 149 partially cloudy cases is shown in Table III. The tuning coefficients shown in Table II, which were determined from the sample of clear cases, are used in the calculations. The third column shows the root mean square difference of the reconstructed clear column brightness temperatures and the observations in the warmer field of view. In channels 1-3, sounding the stratosphere, the reconstructed clear column radiances are taken as the average of the radiances in the two fields of view, both of which are assumed to be unaffected by clouds. In these channels, the difference of observed and reconstructed brightness temperature is a measure of the instrumental noise. In the other channels, it represents the correction made to the brightness temperature in accounting for cloud effects.

The mean and standard deviations of the errors of computed compared to reconstructed clear-column brightness temperatures are shown in columns 2 and 3. The bias errors are small, indicating the applicability of tuning coefficients determined from a set of clear observations for use on a set containing different, partially cloudy, observations. The general agreement in those channels used in the analysis is comparable to, though slightly worse, than that in the clear cases. The lower tropospheric 15  $\mu\text{m}$  channels 5-7 are degraded somewhat under partially cloudy conditions, but are not used in the analysis. Agreement in the window channels is shown at right in the last two columns and show comparable accuracy to that in clear cases. The "errors" in channel 13 are zero because this channel is used for the cloud correction.

The results of this study indicate that infrared radiative transfer calculations can be done with the same, if not better, accuracy than microwave radiative transfer calculations in cloud-free and partially cloudy conditions. The agreement of observed brightness temperature with those computed using colocated radiosonde information is sufficient to allow for accurate physical retrievals from the satellite data in both clear and partially cloudy conditions.

TABLE II

COMPARISON OF OBSERVED AND COMPUTED BRIGHTNESS TEMPERATURES (°K), CLEAR CONDITIONS

		DAY AND NIGHT (72)				NIGHT (21)		
CH	UNTUNED	STD DEV	MEAN (COMP-OBS)	TUNED	$\epsilon$	VAR. OF OBS.	MEAN COMP-OBS	STD DEV
	MEAN COMP-OBS			STD DEV				
1	2.39	3.27				2.84		
* 2	.04	1.47				3.80		
3	1.71	1.25				3.50		
* 4	1.92	.79	.04	.70	.12	2.34		
5	.70	.58	-.04	.61	.03	4.26		
6	.25	.69	-.04	.69	.01	5.08		
7	.31	1.05	-.03	1.04	.02	4.95		
8	-.36	1.65				6.32	-.48	1.85
*13	-.20	.71	-.20	.71	0	6.83		
*14	.87	.67	-.03	.64	.04	6.96		
*15	.92	.62	-.02	.61	.035	6.01		
16	.61	1.75				2.86		
18	-1.71	2.63				8.37	.14	1.29
19	-4.61	4.52				8.22	-.84	1.33
M1	0	0	USED FOR EMISSIVITY 10.72					
*M2	.33	1.01	-.06	1.00	.02	6.86		
*M3	1.25	1.26	.09	1.13	.07	3.90		
*M4	.02	1.32	.02	1.32	0	7.27		

TABLE III

## COMPARISON OF RECONSTRUCTED AND COMPUTED BRIGHTNESS TEMPERATURES, CLOUDY CONDITIONS

DAY AND NIGHT (140)

NIGHT (64)

TUNED		STD DEV	RMS (RECON. -OBS.)	VAR. OF RECON.	NIGHT (64)	
MEAN (COMP-RECON)					MEAN (COMP-RECON)	STD DEV
1	2.72	3.98	1.34	3.97		
* 2	-.06	1.65	.38	5.14		
3	1.25	1.47	.29	5.02		
* 4	.04	1.13	1.10	3.19		
5	.08	1.34	2.52	4.83		
6	-.00	1.61	3.82	5.91		
7	.27	1.82	5.06	5.84		
8	.39	1.44	7.31	7.21	.35	1.17
*13	-.00	.00	3.87	8.11	USED FOR CLOUD CORRECTION	
*14	-.09	.56	3.14	8.23		
*15	.03	.96	2.26	6.86		
16	.64	2.19	.64	3.32		
*18	-1.05	2.74	4.14	9.64	.37	1.17
*19	-4.38	5.19	3.71	9.54	-.54	1.25
M1	0	0		10.69		
M2	.03	.98		7.61		
M3	-.15	1.06		4.52		
M4	-.52	1.51		8.55		

## REFERENCES

- Chahine, M. T., 1980: Infrared remote sounding of sea surface temperature. Remote Sensing of Atmospheres and Oceans, pp. 411-435. A. Deepak, Editor, Academic Press, New York, NY.
- McClatchey, R., 1976: Satellite temperature sounding of the atmosphere: Ground truth analysis. AFGL-TR-76-0279. Air Force Geophysical Laboratory, Hanscom AFB, Bedford, Massachusetts, 01731.
- Phillips, N., L. McMillin, A. Gruber, and D. Wark, 1979: An evaluation of early operational temperature soundings from TIROS-N. Bull. Amer. Meteor. Soc., 60, 1188-1197.
- Susskind, J., J. Rosenfield, and D. Reuter, 1982: Comparison of observed and computed brightness temperatures for the HIRS2 and MSU channels on TIROS-N. Submitted to J. Geophys. Res.
- Susskind, J., and J. Rosenfield, 1980: The GLAS physical inversion method for analysis of TIROS-N data. VAS Demonstration Sounding Workshop, NASA Conference Publication 2157, pp 41-55. NASA/Goddard Space Flight Center, July 15, 1980.
- Weinreb, M., 1979: Atmospheric transmission for remote temperature sounding. SPIE, 195, Atmospheric Effects on Radiative Transfer, 22-30.

PRECEDING PAGE BLANK NOT FILMED

C. ANALYSIS AND MODEL DEVELOPMENT

SOLUTION OF LINEAR SYSTEM OF EQUATIONS  
WHEN THE MATRIX IS CIRCULANT

R. C. Balgovind

The objective of this note is to make "could be users" aware of the existence of such a methodology. This type of tool has been in use since the introduction of the Fast Fourier transform (see all references except the following). Here we introduce the general circulant matrix and show how to "invert" it. Evans (1980) has shown that the Quin-diagonal system can also be solved by L-U factorization.

1. PROBLEM AND THE METHOD OF SOLUTION

Our interest is to solve the system

$$Ax = b$$

Where A is the non-singular matrix of the form:

$$A = \begin{bmatrix} C_0 & C_{n-1} & C_{n-2} & C_{n-3} & C_{n-4} \dots C_3 & C_2 & C_1 \\ C_1 & C_0 & C_{n-1} & C_{n-2} & C_{n-3} \dots C_4 & C_3 & C_2 \\ C_2 & C_1 & C_0 & C_{n-1} & C_{n-2} \dots C_5 & C_4 & C_3 \\ \dots & \dots & \dots & \dots & \dots & \dots & \dots \\ C_{n-3} & C_{n-4} & C_{n-5} & C_{n-6} & C_{n-7} \dots C_0 & C_{n-1} & C_{n-2} \\ C_{n-2} & C_{n-3} & C_{n-4} & C_{n-5} & C_{n-6} \dots C_1 & C_0 & C_{n-1} \\ C_{n-1} & C_{n-2} & C_{n-3} & C_{n-4} & C_{n-5} \dots C_2 & C_1 & C_0 \end{bmatrix}$$

One can express the above matrix in the form:

$$A = f(P) = C_0 I + C_1 P + C_2 P^2 + \dots + C_{n-1} P^{n-1}$$

where

$$P = \begin{bmatrix} 0 & 0 & 0 & 0 & \dots & 0 & 1 \\ 1 & 0 & 0 & 0 & \dots & 0 & 0 \\ 0 & 1 & 0 & 0 & \dots & 0 & 0 \\ 0 & 0 & 1 & 0 & \dots & 0 & 0 \\ 0 & 0 & 0 & 1 & \dots & 0 & 0 \\ & & & & \dots & & \\ 0 & 0 & 0 & 0 & \dots & 1 & 0 \end{bmatrix}$$

P is the permutation matrix

I would like to recall here that

$$Pe_i = e_{i+1}, \quad i=1,2,3,\dots,n-1,$$

and  $Pe_n = e_1$  where  $e_i$  are the usual unit vectors.

Let  $w = \exp(2\pi i/n)$  and  $V_r = 1/\sqrt{n} (1, w^r, w^{2r}, w^{3r}, \dots, w^{(n-1)r})^T$ . Then  $A$  has eigenvalues  $\lambda_r = f(w^{-r})$  for  $r = 0, 1, 2, \dots, n-1$  corresponding to eigenvectors  $v_r$ , since  $Pv_r = w^r v_r$ .

Our algorithm relies on the fact that the eigenvalues  $\lambda_r$  and eigenvectors  $V_r$  of  $P$  are known. Let  $Q$  be the matrix whose columns are  $V_0, V_1, V_2, \dots, V_{n-1}$  and let  $\Lambda = \text{diag}(\lambda_0, \lambda_1, \lambda_2, \dots, \lambda_{n-1})$ . Then  $Q^*Q = I$ ,  $Q^*AQ = \Lambda$  and it follows from equation (1) that

$$x = Q(\Lambda^{-1}(Q^*b)).$$

Since these correspond to a direct and an inverse Fourier transform, they can be performed efficiently by Fast Fourier transform algorithm.

## 2. EXAMPLE

Let us look at an example that arises when

$$\left( c + \frac{\partial^2}{\partial x^2} \right) u = \text{RHS}$$

(for  $u$  periodic and  $c$  constant) is approximated with a 9-point fourth order scheme. This gives us a matrix of the form:

$$A = \begin{bmatrix} c_0 & c_1 & c_2 & c_3 & c_4 & 0 & \dots & 0 & 0 & c_4 & c_3 & c_2 & c_1 \\ c_1 & c_0 & c_1 & c_2 & c_3 & c_4 & \dots & 0 & 0 & 0 & c_4 & c_3 & c_2 \\ c_2 & c_1 & c_0 & c_1 & c_2 & c_3 & \dots & 0 & 0 & 0 & 0 & c_4 & c_3 \\ c_1 & c_2 & c_1 & c_0 & c_1 & c_2 & \dots & 0 & 0 & 0 & 0 & 0 & c_4 \\ c_4 & c_3 & c_2 & c_1 & c_0 & c_1 & \dots & 0 & 0 & 0 & 0 & 0 & 0 \\ 0 & c_4 & c_3 & c_2 & c_1 & c_0 & \dots & 0 & 0 & 0 & 0 & 0 & 0 \\ \dots & \dots \\ 0 & 0 & 0 & 0 & 0 & 0 & \dots & c_0 & c_1 & c_2 & c_3 & c_4 & 0 \\ 0 & 0 & 0 & 0 & 0 & 0 & \dots & c_1 & c_0 & c_1 & c_2 & c_3 & c_4 \\ c_4 & 0 & 0 & 0 & 0 & 0 & \dots & c_2 & c_1 & c_0 & c_1 & c_2 & c_3 \\ c_3 & c_4 & 0 & 0 & 0 & 0 & \dots & c_3 & c_2 & c_1 & c_0 & c_1 & c_2 \\ c_2 & c_3 & c_4 & 0 & 0 & 0 & \dots & c_4 & c_3 & c_2 & c_1 & c_0 & c_1 \\ c_1 & c_2 & c_3 & c_4 & 0 & 0 & \dots & 0 & c_4 & c_3 & c_2 & c_1 & c_0 \end{bmatrix}$$

ORIGINAL PAGE IS  
OF POOR QUALITY

In this special case (where matrix A is symmetric) we have that

$$f(x) = C_0 + C_1 x + C_1 x^2 + C_3 x^3 + C_4 x^4 \\ + C_1 x^{n-1} + C_2 x^{n-2} + C_1 x^{n-3} + C_4 x^{n-4} .$$

So the characteristics corresponding to the eigenvectors  $V_r$  are

$$\lambda_r = f(w^{-r}) \\ = C_0 + 2C_1 \cos(r(2\pi/n)) + 2C_2 \cos(2r(2\pi/n)) \\ + 2C_3 \cos(3r(2\pi/n)) + 2C_4 \cos(4r(2\pi/n)) \\ \text{for } r = 0, 1, 2, \dots, n-1 .$$

This scheme, combined with block reduction method, may be used to solve 2-d problems.

#### REFERENCES

- Buzbee, B. L., G. H. Golub, and C. W. Nielson, 1970: On direct methods for solving Poisson's equations. SIAM J. Numer. Anal., 8, 627-656.
- Evans, D. J., 1980: On the Solution of Certain Symmetric Quindagonal Linear Systems. Intern. J. Computer Maths., 271-284.
- Fischer, D., G. Golub, O. Hald, C. Leiva, and O. Widlund, 1974: On Fourier Toeplitz methods for separable elliptic problems. Mathematics of Computations, 28, 349-368.
- Ghil, M., and R. Balgqvind, 1979: A Fast Cauchy-Riemann Solver. Mathematics of Computations, 33, 585-635.
- Hockney, R. W., 1975a: A fast direct solution of Poisson's equation using Fourier analysis. J. Assoc. Comput. Mach., 12, 95-113.

AN ANALYSIS OF INTERMITTENT UPDATING  
FOR THE SHALLOW WATER EQUATIONS

K. P. Bube

1. INTRODUCTION

Numerical weather prediction (NWP) is the attempt to solve an initial-value problem for a system of nonlinear partial differential equations. One of the major difficulties in NWP is the specification of initial conditions; that is, the initial data are known only incompletely and inaccurately. Fortunately, observations of the system distributed over a time interval preceding initial time are also available. The problem of four-dimensional data assimilation is to construct a complete, accurate set of initial data for a NWP model from all of the measured data.

The most common practical procedure that used data available at times preceding the initial time is intermittent updating. The model is provided with the best available data at some preceding time, and is integrated forward in time. Additional data replace the model values as they become available. When the integration reaches the initial time, an initial state has been constructed. Many variations of this procedure have been proposed and studied (Bengtsson (1975); Ghil, Halem, and Atlas (1979)). Recently, the application of the estimation theory to improve the procedure has been studied (Ghil, *et al.* (1981)).

The purpose of this work is to analyze the method of intermittent updating for a model system. We want to understand analytically how the updating of one variable of the system affects the other variables, what the factors are which influence the rate of convergence of this procedure, and how measurement error affects the procedure. Preliminary results appear in Bube and Olinger (1977), Bube (1978), and Bube and Ghil (1981). Talagrand (1977, 1981) has also studied this procedure analytically.

2. UPDATING WITHOUT ERRORS

We present here results for the model system

$$\begin{aligned} \phi_t &= a \phi_x + b u_x, \\ u_t &= b \phi_x + a u_x, \end{aligned} \tag{1}$$

with periodic boundary conditions in  $x$ . The linearized shallow water equations for purely zonal, one-dimensional flow around a circle of latitude can be written in this form, where  $\phi$  is the geopotential,  $u$  is the zonal velocity, and  $-a = U$  and  $-b = \phi$  are the zonal velocity and geopotential of the basic state. We assume that we have measurements of  $\phi(x, t)$  for all  $x$  and for  $t = j\tau$ ,  $j = 0, 1, 2, \dots, m$ , where  $\tau > 0$  is the time interval between observations of  $\phi$ .

We start with the initial measurement of  $\phi$  and an initial approximation to  $u$  at  $t = 0$ . As we integrate forward in time, we replace the computed values of

$\phi$  by the measured values at times  $t = j\tau$ . The error in the computed  $u$ , which we call  $\epsilon(x,t)$ , will decrease because of the linkage between  $u$  and  $\phi$  in the system.

For the analysis, we expand  $\phi$ ,  $u$ , and  $\epsilon$  in Fourier series in  $x$ :

$$\phi(\xi, t) = \int_0^1 e^{-2\pi i \xi x} \phi(x, t) dx, \quad (2)$$

$$\phi(x, t) = \sum \phi(\xi, t) e^{2\pi i \xi x}, \quad (3)$$

where  $\xi$  is the wave number (an integer). We can show that

$$|\epsilon(\xi, (j+1)\tau)| = \rho(\xi, \tau) |\epsilon(\xi, j\tau)|, \quad (4)$$

where

$$\rho(\xi, \tau) = |\cos(2\pi b \xi \tau)|. \quad (5)$$

The effect of each update interval is to multiply each Fourier coefficient of the error in  $u$  by a decrease factor  $\rho(\xi, \tau) \leq 1$ . If  $\rho(\xi, \tau) \ll 1$ , then  $\epsilon(\xi, j\tau)$  approaches zero slowly as  $j$  increases.

For  $t = j\tau$ ,

$$|\epsilon(\xi, \tau)| = \sigma(\xi, \tau)^j |\epsilon(\xi, 0)|, \quad (6)$$

where

$$\sigma(\xi, \tau) = \rho(\xi, \tau)^{1/\tau}. \quad (7)$$

For  $\xi \neq 0$ ,  $\sigma(\xi, \tau)$  increases as  $\tau \rightarrow 0$ , and

$$\lim_{\tau \rightarrow 0} \sigma(\xi, \tau) = 1 \quad (8)$$

Updating  $\phi$  more frequently (i.e. decreasing  $\tau$ ) does not necessarily make  $\epsilon(x,t) \rightarrow 0$  faster as  $t$  increases. We must allow enough time for the energy of the error to pass from  $u$  to  $\phi$ , and then out of the system as  $\phi$  is updated.

Note that  $\rho$  and  $\sigma$  depend on both the wave number  $\xi$  and the updating interval  $\tau$ . For  $\xi = 0$ ,  $\rho = \sigma = 1$ ; no improvement is made in the mean velocity  $u(0,t)$ . For other values of  $\xi$ , the best updating interval is

$$\tau = \frac{1}{4|b\xi|}. \quad (9)$$

If the entire error in  $u$  is in only one wave number  $\xi$ , then  $\tau$  can be chosen by (9) to decrease the error quickly. In practice,  $\epsilon(\xi, 0) \neq 0$  for many

values of  $\xi$ . If  $\tau \gg 1/(4|h\xi|)$ , then  $\rho(\xi, \tau)$  is just as likely to be close to 1 as it is to be close to 0. The best  $\tau$  for a small wave number may give a  $\rho \approx 1$  for some large wave numbers. If  $\tau$  is too large, waves with high wave numbers may converge slowly; if  $\tau$  is too small, waves with low wave numbers will converge slowly.

One possible solution is to use several different updating intervals  $\tau_1, \dots, \tau_p$ , and to repeat them in a cycle. If there is a  $\tau_j$  satisfying (9) for each wave number  $\xi$  of interest, then convergence should be reasonably rapid for all corresponding wave numbers. Numerical experiments with system (1) confirm these theoretical results.

A similar analysis can be performed on a 3 x 3 version of the linearized shallow water equations, with Coriolis parameter  $f$ , and northerly wind component  $v$ :

$$\begin{aligned}\phi_t + U \phi_x + \phi(u_x + v_y) &= 0, \\ u_t + U u_x + \phi_x - fv &= 0, \\ v_t + U v_x + fu &= 0.\end{aligned}$$

In this case, the decrease factor (depending on  $\xi$  and  $\tau$ ), when  $\phi$  alone is measured, is a 2 x 2 matrix. When a single updating interval  $\tau$  is used, the magnitude of the largest eigenvalue of this matrix determines the rate of convergence for this  $\xi$  and  $\tau$  (see Talagrand (1981)). If different  $\tau$ 's are used in succession, the situation becomes more complicated and deserves further investigation.

### 3. UPDATING WITH ERRORS

Consider the situation discussed in the previous section using system (1), but now suppose that the measurements of  $\phi(x, j\tau)$  for  $j = 0, 1, \dots, m$  have errors. Suppose that the expected value of the square of the error in  $\phi(x, j\tau)$  is  $r(\xi)$ , for  $j = 0, 1, \dots, m$ . Let  $q(\xi, t)$  be the expected value of  $|\epsilon(\xi, t)|^2$ . Then we can show

$$q(\xi, n\tau) = r(\xi) + \rho(\xi) + \rho(\xi, \tau)^{2n} (q(\xi, 0) - r(\xi)).$$

Thus, the expected value of the error in the computed  $u$  decreases down to the expected value of the error in the measurements of  $\phi$ , in a manner which is analogous to that of the error-free case. A corresponding result holds when a cycle of different updating intervals is used.

Further analysis incorporating systematic error into these procedures is planned; the first model to be considered is the discrepancy between the solutions of a differential equation and solutions of corresponding difference schemes.

## REFERENCES

- Benqtsson, L., 1975: 4-dimensional assimilation of meteorological observations. GARP Publications Series, No. 15, World Meteorological Organization, Geneva.
- Bube, K. P., 1978: The Construction of Initial Data for Hyperbolic Systems from Nonstandard Data. Ph.D. Dissertation, Dept. of Mathematics, Stanford University, Stanford, California.
- Bube, K. P., and M. Ghil, 1981: Assimilation of asymptotic data and the initialization problem. Dynamic Meteorology: Data Assimilation Methods, Applied Mathematical Sciences, Springer-Verlag, New York. To be published.
- Bube, K. P., and J. Olliger, 1977: Hyperbolic partial differential equations with nonstandard data. Advances in Computer Methods for Partial Differential Equations II, IMACS, Rutgers University, New Brunswick, N.J., pp. 256-263.
- Ghil, M., M. Halem, and R. Atlas, 1979: Time-continuous assimilation of remote-sounding data and its effect on weather forecasting. Mon. Wea. Rev., 107, 140-171.
- Ghil, M., S. Cohn, J. Tavantzis, K. Bube, and E. Isaacson, 1981: Applications of estimation theory to numerical weather prediction. Dynamic Meteorology: Data Assimilation Methods. Applied Mathematical Sciences, Springer-Verlag, New York, to be published.
- Talagrand, O., 1977: Contribution a l'assimilation quadridimensionnelle d'observations meteorologiques. These de doctorat d'etat es sciences. Universite Pierre-et-Marie Curie, Paris.
- Talagrand, O., 1981: A study of the dynamics of four-dimensional data assimilation. Tellus, 33, 43-60.

# ASSIMILATION OF ASYNOPTIC DATA AND THE INITIALIZATION PROBLEM<sup>1</sup>

K. P. Bube and M. Ghil<sup>2</sup>

We discuss a mathematical framework for the use of asynoptic data in determining initial states for numerical weather prediction (NWP) models (Bengtsson et al., 1981). A set of measured data, synoptic and asynoptic, is termed complete if it determines the solution of an NWP model uniquely. We derive theoretical criteria for the completeness of data sets. The practical construction of the solution from a complete data set by intermittent updating is analyzed, and the rate of convergence of some updating procedures is given (Bube and Ghil, 1981).

It is shown that the time history of the mass field constitutes a complete data set for the shallow-water equations. Given that the time derivatives of the mass field are small at initial time, we prove that the velocity field obtained by the diagnostic equations we derive will also have small time derivatives. Hence our diagnostic equations also solve the initialization problem for this system; namely, they provide an initial state which leads to a slowly evolving solution to the system (Bube and Ghil, 1981).

Finally, we review the bounded derivative principle of Kreiss. It states that in systems with a fast and a slow time scale, initial data can be chosen so that the solution starts out slowly. For such initial data, the solution will actually stay slow for a length of time comparable to the slow time scale. The application of the principle to the initialization problem of NWP is discussed.

## REFERENCES

- Bengtsson, L., M. Ghil, and E. Kallen (eds), 1981: Dynamic Meteorology: Data Assimilation Methods. Springer-Verlag, New York, in press.
- Bube, K. P., and M. Ghil, 1981: Assimilation of asynoptic data and the initialization problem. In Bengtsson et al. (1981).

---

<sup>1</sup> This work was presented at The Seminar on Data Assimilation Methods, 15-19 September 1980, The European Centre for Medium Range Weather Forecasts, Reading RG2 9AX, England. It will appear in "Dynamic Meteorology."

<sup>2</sup> Courant Institute of Mathematical Sciences, New York University, New York, New York 10012.

APPLICATIONS OF ESTIMATION THEORY TO NUMERICAL WEATHER PREDICTION

S. Cohn, M. Ghil<sup>1</sup> and E. Isaacson

Numerical weather prediction (NWP) is an initial value problem for a system of nonlinear partial differential equations in which the initial values are known only incompletely and inaccurately. Data at initial time can be supplemented, however, by observations of the system distributed over a time interval preceding it. Estimation theory has ~~been~~ successful in approaching such problems for models governed by systems of ordinary differential equations and of linear PDEs. ~~We develop~~ estimation-theoretic methods for NWP *are developed.*

A model exhibiting many features of large scale atmospheric flow important in NWP is the one governed by the shallow fluid equations. ~~We study~~ the estimation problem for a linearized formulation of these equations. ~~A finite~~ *is studied* difference version of the equations is used as a forecast model to simulate the numerical models used in NWP.

At each observation time, observed-minus-forecast residuals are multiplied by a matrix of weighting coefficients, then added to the forecast itself to produce the "analyzed" field from which the forecast then proceeds. The standard estimation-theoretic approach is to use the so-called Kalman-Bucy (K-B) filter as the matrix of weighting coefficients.

The specific character of the equations' dynamics gives rise to the necessity of modifying the usual K-B filter. The goal of the modification is to eliminate the high-frequency inertia-gravity waves which are otherwise generated by the insertion of observational data (Bengtsson et al., 1981). Our numerical experiments show that the modified filter accomplishes this, at the expense of errors which are only slightly larger than those produced by the optimal, K-B filter (Ghil et al., 1981). The modified filter, therefore, combines in an optimal way dynamic initialization (i.e., elimination of fast waves) and four-dimensional (space-time) assimilation of observational data, two procedures which traditionally have been carried out separately in NWP.

The modified filter converges rapidly to an asymptotic, constant matrix, which can then be used as a time-invariant filter. This filter is much more efficiently computable than its time-varying counterpart, and our numerical results show that these two filters perform equally well.

Finally, we compare our methods with the existing method in widest operational use, namely, optimal interpolation (OI) (Cohn et al., 1981). Our results indicate that the asymptotic filter yields a substantial improvement over OI. We expect that a suitable nonlinear version of our asymptotic filter, or a compromise between it and the one used in OI, can be implemented in an operational NWP model.

---

<sup>1</sup> Also Laboratory for Atmospheric Sciences, NASA Goddard Space Flight Center, Greenbelt, Maryland 20771.

## REFERENCES

- Bengtsson, L., M. Ghil, and E. Kallen, 1981: Dynamic Meteorology: Data Assimilation Methods. Springer-Verlag, New York/Heidelberg/Berlin, to be published.
- Cohn, S., M. Ghil, and E. Isaacson, 1981: Optimal interpolation and the Kalman filter. Preprint, 5th Conf. Numer. Weather Prediction, Monterey, California.
- Ghil, M., S. Cohn, J. Tavantis, K. Bube, and E. Isaacson, 1981: Applications of estimation theory to numerical weather prediction. In Bengtsson et al. (1981).

A STOCHASTIC-DYNAMIC MODEL FOR GLOBAL ATMOSPHERIC  
MASS-FIELD STATISTICS

M. Ghil<sup>1</sup>, R. Balgovind<sup>2</sup> and E. Kalnay<sup>3</sup>

Global atmospheric mass-field error correlations based on satellite observations and on numerical forecasts show strong and systematic latitude dependence. A model for the latitude-dependent spatial correlation structure of mass-field forecast errors is derived from dynamical considerations. The model is governed by the potential vorticity equation forced by random noise:

$$(\nabla^2 - c_0 \sin^2 \theta) \phi(\lambda, \phi; \omega) = F(\lambda, \phi; \omega) \quad (1)$$

where  $\nabla^2$  is the Laplacian operator on the unit sphere,  $\lambda$  and  $\theta$  are longitude and latitude,  $\phi$  is the geopotential error field at 500 mb and  $F$  is white noise corresponding to a random realization  $\omega$ .

The spatial covariance function  $\Gamma$  is defined by

$$\Gamma(\lambda_1, \theta_1; \lambda_2, \theta_2) = E [\phi(\lambda_1, \theta_1; \omega) \phi(\lambda_2, \theta_2; \omega)], \quad (2)$$

where  $E$  is the expected value.

Three methods of solution have been tested. In the first method, Eq. (1) was solved by expansion in spherical harmonics, and the correlation function was computed analytically using the expansion coefficients. In the second method, the finite-difference equivalent of Eq. (1) was solved using a Fast Poisson Solver. The correlation function was computed using stratified sampling of the individual realizations of  $F(\omega)$  and hence of  $\phi(\omega)$ . In the third method, a higher-order equation for  $\Gamma$  was derived from Eq. (1) and solved directly in finite differences by two successive applications of the Fast Poisson Solver. The three methods were compared for accuracy and efficiency, and the third method was chosen as clearly superior.

The results agree well with the global latitude dependence and local anisotropy of observed atmospheric correlation data. The value of the parameter  $c_0$ , which gives the best fit to the data, is close to the value expected from dynamical considerations for a baroclinic atmosphere. Differences between model and data are typically smaller than those between data for the Northern Hemisphere and those for the Southern Hemisphere. These results provide the basis for an optimal choice of coefficients for statistical analysis of atmospheric data.

---

<sup>1</sup> Courant Institute of Mathematical Sciences, N.Y.U., New York, New York 10012 and Laboratory for Atmospheric Sciences, NASA/GSFC.

<sup>2</sup> Sigma Data Services Corporation, Greenbelt, Maryland 20771

<sup>3</sup> Laboratory for Atmospheric Sciences, NASA Goddard Space Flight Center, Greenbelt, Maryland 20771

A VARIABLE VERTICAL RESOLUTION WEATHER MODEL WITH AN  
EXPLICITLY RESOLVED PLANETARY BOUNDARY LAYER

H. M. Helfand

Seasat A scatterometer surface wind stress observations over the world's oceans and seas can be very useful in the production of global weather analysis, especially since many of the regions that they cover are very sparse in conventional weather data. The surface wind stresses relate directly to atmospheric winds in the lowest few meters of the atmosphere and they are also a key to the determination of surface fluxes of heat and moisture into the atmosphere.

There was a problem, however, in assimilating surface wind stress data into the standard GLAS Weather Model. The model, with its lowest level at about 55 mb above the ocean's surface, did not offer sufficient vertical resolution to incorporate surface data. The structure of the wind profile in the lowest 55 mb of the atmosphere cannot be adequately predicted in order to relate the winds at the lowest level to surface wind stresses.

However, there is enough known about the structure of the surface layer (which is roughly 10 mb deep) to relate winds at its top to surface wind stress. One can appeal to the Monin-Obukhov similarity theory to establish such a relationship.

A new Variable Vertical Resolution version of the Fourth Order Weather Model has been developed so that the Monin-Obukhov formulation can be used. The 9  $\sigma$ -levels of this model can be arbitrarily specified, but we are currently using the following sine-squared distribution. The boundary  $\sigma_e^{n+1}$  between the nth and the (n+1)th layers of the model is specified as

$$\sigma_e^{n+1} = \sin^2 \left( \frac{n\pi}{18} \right)$$

The center  $\sigma^n$  of the nth layer is

$$\sigma^n = \frac{1}{2} (\sigma_e^n + \sigma_e^{n+1})$$

This distribution is analytically smooth in n and it has its highest resolution at the upper and lower boundaries of the atmosphere ( $\sigma_e^{n+1}$  is quadratic in  $n\pi/18$  and in  $(9-n)\pi/18$  as n approaches 0 and 9 respectively) where such resolution is most needed.

The packing of  $\sigma$ -levels in the stratosphere will, in part, make up for the inherent lack of resolution in the upper parts of the atmosphere when pressure of  $\sigma$ -pressure is used as a vertical coordinate. The packing of  $\sigma$ -levels near the ground should allow an explicit resolution of the PBL, for the lowest  $\sigma$ -level is about 15 mb or 150 m above the ground, and the layer above is located at about 75 mb or 750 m above the ground. Even the layer above that, centered at about 185 mb or 1850 m above the ground, is sometimes included within the PBL.

ORIGINAL PAGE IS  
OF POOR QUALITY

The location of the lowest model layer is close enough to the ground to expect the Monin-Obukhov surface layer similarity theory to give a reasonable approximation to surface fluxes of heat, moisture and momentum (see Panofsky, 1973). A scheme has been devised to use this theory together with the KEYPS equation (Panofsky, 1973) for the wind profile structure, and a similar interpolative formulation for potential temperature and moisture profiles in the unstable case and with a formula for the stable case which interpolates between the Businger et al. (1971) functions for a nearly neutral PBL and Clarke's (1970) observations for a moderately stable atmosphere.

An additional mechanism for turbulence is needed in this model to describe the mean fluxes of heat, moisture and momentum between those model layers that are contained within PBL. The model currently uses Richardson number adjustment scheme that is based on the ideas of Chang (1979) to calculate these fluxes only when they are appropriate. Thus the eighth or next-to-lowest layer of the model is considered as part of the PBL only when turbulent fluxes of heat, moisture and momentum enter it from below. The seventh layer is considered as part of the PBL only when there are fluxes entering both the eighth layer and the seventh layer from below.

The Richardson number adjustment scheme can predict turbulent fluxes between any two adjacent layers of the model, and so it replaces the dry convective adjustment scheme previously used.

Currently we are developing a Mellor-Yamada (1974) type of scheme to predict turbulent fluxes of heat, moisture and momentum between layers instead of the Richardson number adjustment scheme.

#### REFERENCES

- Businger, J. A., J. C. Wyngaard, Y. Izumi, and E. F. Bradley, 1971: Flux profile relationships in the atmospheric surface layer. J. Atmos. Sci., 28, 181-189.
- Chang, S. W., 1979: An efficient parameterization of convective and nonconvective planetary boundary layers for use in numerical models. J. Appl. Meteor., 18, 1205-1215.
- Clarke, R. H., 1970: Observational studies in the atmospheric boundary layer. Quart. J. Roy. Meteor. Soc., 96, 91-114.
- Mellor, G. L., and T. Yamada, 1974: A hierarchy of turbulence closure models for planetary boundary layers. J. Atmos. Sci., 31, 1791-1806.
- Panofsky, H. A., 1973: Tower Micrometeorology. In Workshop on Micrometeorology, D. A. Haugen, ed., Boston, Amer. Meteor. Soc., 392 pp.

## A FOUR DIMENSIONAL VARIATIONAL ANALYSIS EXPERIMENT

R. Hoffman<sup>1</sup>

Since we are unable to observe the atmosphere in a detailed and accurate enough fashion at a single instant of time, we must use past information. It is highly desirable to use a truly four-dimensional assimilation method (Bengtsson, 1975) to accomplish this reconstruction. Sasaki's variational analysis method (1970) for four dimensions with exact constraints, in the special case when the constraints are the governing equations (hereafter referred to as VAM4D), may be restated as a direct minimization (or nonlinear least squares) problem. Conceptually, all we need to do is find the solution of the governing equations which is closest to the observations. The works by Tadjbakhsh (1969) and by Lewis and Bloom (1978) are important precursors of this study.

As further motivation for using the governing equations as constraints, consider that all successful meteorological analysis procedures, subjective or objective, use some a priori knowledge of the atmosphere. At one extreme, radiosonde reports which violate the hydrostatic relationship, ship reports at continental coordinates, or reports which are grossly miscoded must be rejected. At a more sophisticated level, the smoothness criteria which allow the rejection of data causing bulls eyes in the analyzed fields is ultimately based on a priori knowledge of the spatial spectra of the meteorological variables. The best analyses are subjective because a human analyst can incorporate a vast amount of a priori knowledge. Therefore, we conclude that we should use all our knowledge of the atmosphere in analyzing data. A large part of our knowledge of the atmosphere is summarized by the equations governing the atmospheric dynamics; a convenient form of these equations is a numerical weather prediction (NWP) model. It is thoroughly consistent to require the analysis to satisfy the best formulation we have of the governing equations; that is, the analysis should be a solution of the NWP model. (All this with the following provisos: the time interval analyzed must be smaller than the time for which the model is valid, and it must be understood that only scales which can be represented by the model are included in the analysis.) The more complete and accurate the model, the better will be the analysis; therefore, VAM4D should, in my opinion, eventually prove to be the most satisfactory objective analysis method.

To test VAM4D, we have performed an idealized continuous assimilation experiment using a very simple model which has been described in detail by Hoffman (1981). The small alterations to the imposed heating function discussed by Hoffman and Kalnay (1981) are also included here. The experiment is an identical twin experiment; nature and the dynamical model are the same quasigeostrophic model. The observing system contaminates nature with errors which are independent for each spectral component and which have white noise temporal statistics. The standard deviation of the error added to each spectral component is 7.5% of the climate variance of that variable. Stream-function is not observed, only temperature is observed. The assimilation period is 4 days; observations are available every 12 h, and the entire experiment is 128 days long (i.e., there are 32 cases).

---

<sup>1</sup> National Research Council/Resident Research Associate

The VAM4D finds the model solution which gives the best fit to the observed data at  $t = 0$  h,  $-12$  h,  $-24$  h, ...  $-84$  h and to the analysis at  $-96$  h which is the result of the previous assimilation. (To avoid startup problems, the first case uses a perfect analysis at  $-96$  h.) The results of the experiment are shown in Fig. 1, which is the average over the 32 cases of the analysis error, as a function of time. We have normalized the analysis error by the observational error which would have been present if stream-function had been observed (Fig. 1a). The error is  $D$ , defined by

$$D^2 = (\overline{\delta\theta})^2 + (\overline{\delta\sigma})^2 + 2^{-1}(\overline{\delta(\theta - \bar{\theta})})^2 + \alpha 2^{-1}(\overline{\delta\psi})^2$$

where  $\theta$ ,  $\sigma$  and  $\psi$  are the 500 mb nondimensional potential temperature, static stability and stream-function, the overbar is a horizontal average,  $\delta x$  is the error in  $x$  and  $\alpha = 1$ . The analysis error is smaller than 25% of the observational error; the squared error is reduced by ~95%. Note that the analysis error is smallest in the center of the assimilation period close to the center of mass of the data. Also, the analysis error is smaller at  $t = -96$  h than at  $t = 0$  h reflecting the information content of the  $t = -96$  h analysis. Fig. 1b is identical to Fig. 1a except that the term involving  $\psi$  has been neglected (i.e.,  $\alpha = 0$ ), so that  $D$  is now the error projected on the observable manifold. Apparently, the stream-function field is reconstructed as well as is the temperature field.

In summary, we have shown for a perfect model and a simple (but nonlinear) system that the four-dimensional variational analysis method using the governing equations as exact constraints works successfully. First, the method is stable in an assimilation cycle. Second, it reconstructs the unobservable variables; in this case, no velocity data was observed. Third, the analysis errors are much smaller than the observing system errors.

#### REFERENCES

- Bengtsson, L., 1975: 4-dimensional assimilation of meteorological observation. GARP Publications Series No. 15, ICSU/WMO JOC. 76 pp.
- Hoffman, R. N., 1981: Alterations of the climate of a primitive equation model produced by filtering approximations and subsequent tuning and stochastic forcing. J. Atmos. Sci., **38**, 514-530.
- Hoffman, R. N., and E. Kalnay, 1981: Lagged averaged forecasting, an alternative to Monte Carlo forecasting. Seventh Conference on Probability and Statistics in Atmospheric Sciences, 2-6 November 1981, Monterey, California.
- Lewis, J. M., and S. C. Bloom, 1978: Incorporation of time continuity into subsynoptic analysis by using dynamical constraints. Tellus, **30**, 496-516.
- Sasaki, Y., 1970: Some basic formalisms in numerical variational analysis. Mon. Wea. Rev., **98**, 875-883.
- Tadjbakhsh, I. G., 1969: Utilization of time-dependent data in running solution of initial value problems. J. Appl. Meteorol., **8**, 389-391.

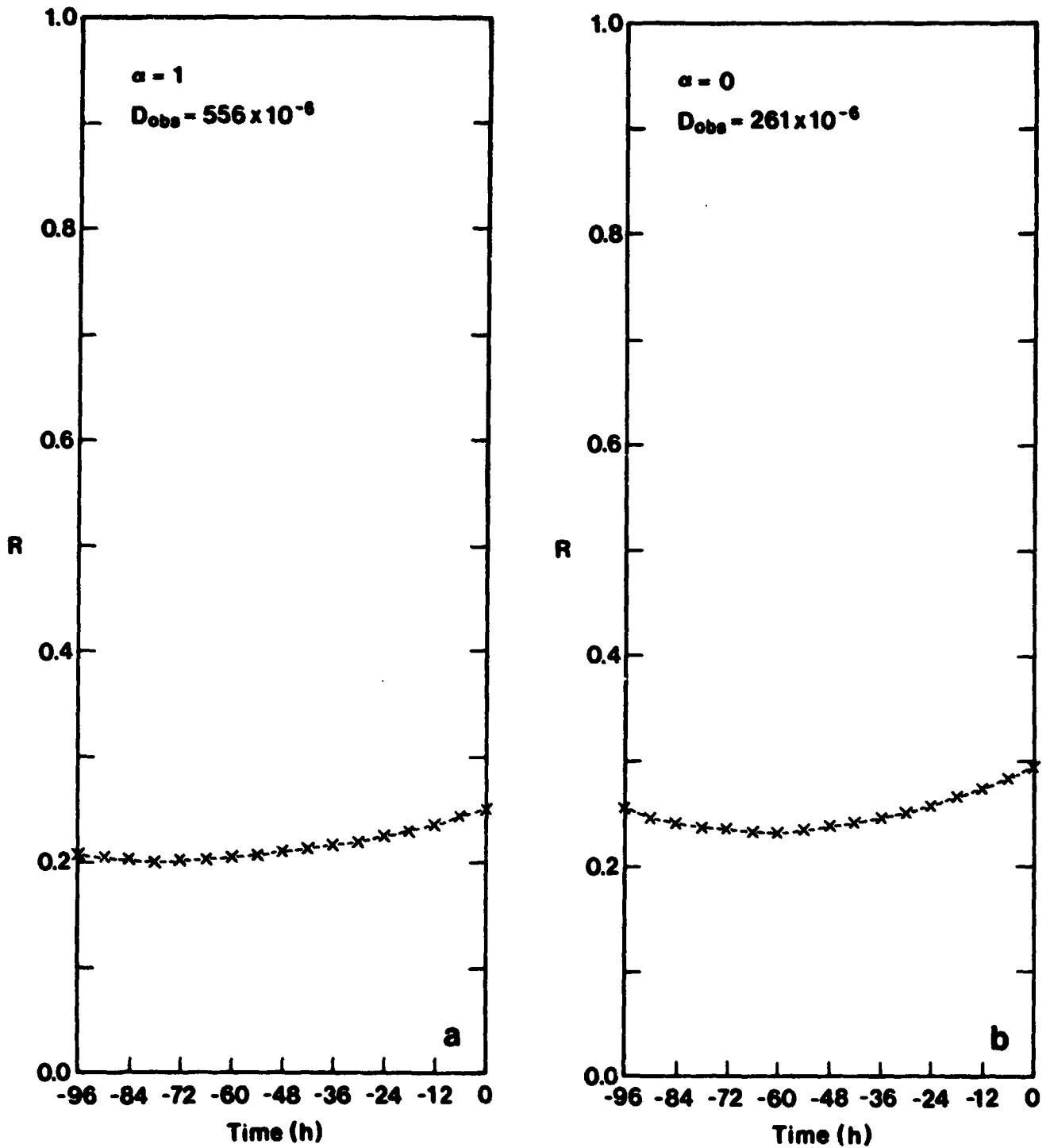


Fig. 1. The analysis error as a function of time. The quantity plotted,  $R$ , is the ratio of the analysis error  $D_{anal}$  to the observational error  $D_{obs}$  for (a) temperature and streamfunction ( $\alpha = 1$ ,  $D_{obs} = 556 \times 10^{-6}$ ) and for (b) temperature alone, ( $\alpha = 0$ ,  $D_{obs} = 261 \times 10^{-6}$ ).

# SASS WIND AMBIGUITY REMOVAL BY DIRECT MINIMIZATION<sup>1</sup>

Ross N. Hoffman<sup>2</sup>

A gridded surface wind analysis is obtained by minimizing an objective function, the magnitude of which measures the error made by the gridded analysis in fitting the SASS wind data, the conventional surface wind observations, and the forecast surface wind field. The ambiguity of the SASS winds is then removed by choosing the alias closest to the analyzed wind. Because minimizing the objective function is a problem of nonlinear least squares, the minimizing gridded analysis is not unique, and a good first guess is necessary to assure convergence to a reasonable solution. A good first guess may be generated by performing the analysis in stages.

Illustrative results are shown for a limited region in the North Atlantic containing the QE II storm and for a limited amount (~ 12 minutes) of data observed near the synoptic time 1200 GMT 10 September 1978 (Fig. 1). Within the SASS data swath the resulting gridded analysis (Fig. 2a) is a reasonable representation of the surface wind and is not sensitive to the forecast surface wind field. The analysis is sensitive to wind directions reported by ships near the center of the storm. The wind circulation center present in the forecast is moved by the analysis. The resulting dealiased SASS wind directions are noisy (Fig. 2b).

---

<sup>1</sup> Presented at the AGU 1981 Spring Meeting, Baltimore, Maryland, 25-29 May 1981. This research will be reported in full in Mon. Wea. Rev.

<sup>2</sup> National Research Council/Resident Research Associate

ORIGINAL PAGE IS  
OF POOR QUALITY

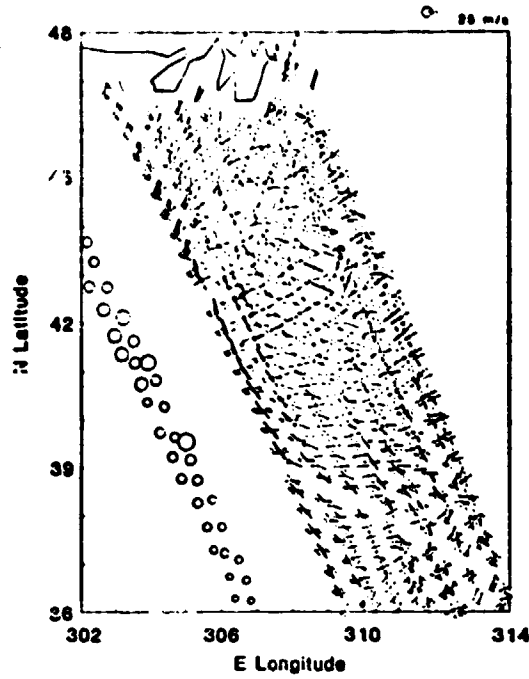


Fig. 1. The SASS data used in the analysis. All observations are near 1200 GMT 10 September 1978. Arrows originating at the data locations are proportional to wind magnitude and plotted away from the wind direction. Octagons are plotted at SASS nadir locations. (Detail shown).

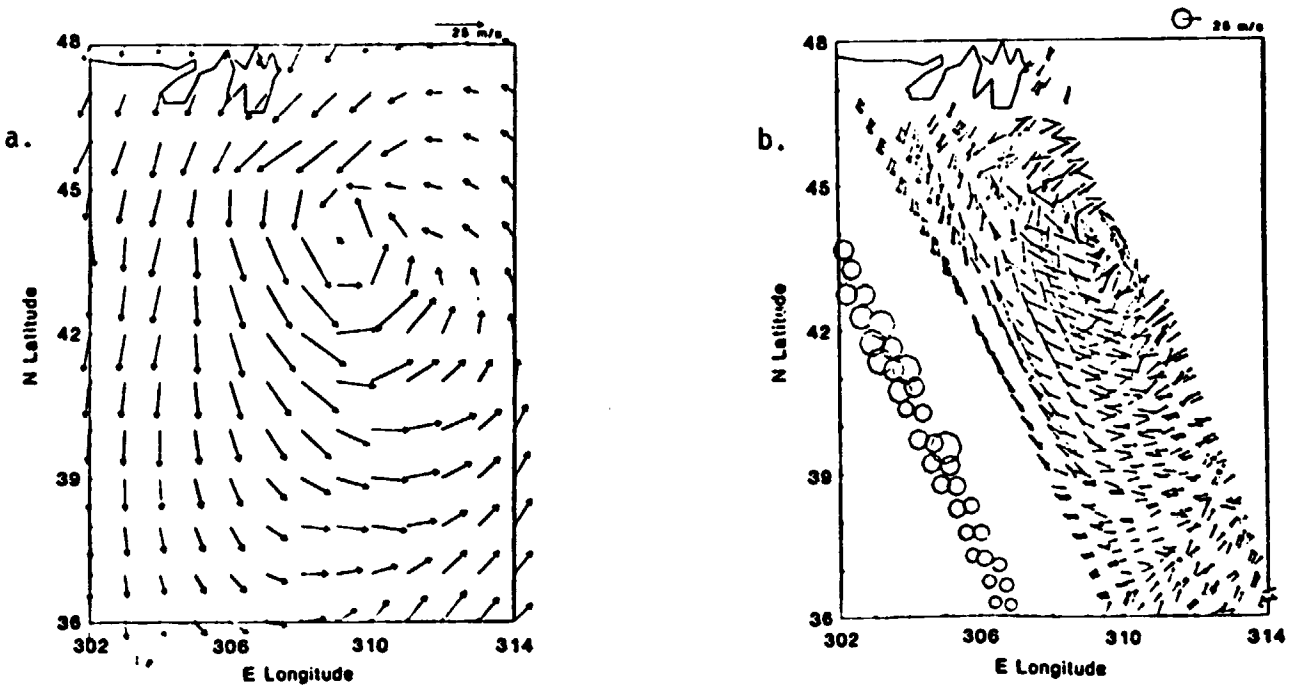


Fig. 2. Minimizing analysis (a) and corresponding dealiased SASS winds (b) obtained by the three stage analysis procedure using the NMC analysis as the forecast wind field. The NMC conventional data base was used.

A SIMPLE ATMOSPHERIC MODEL ON THE SPHERE WITH 100% PARALLELISM<sup>1</sup>

E. Kalnay and L. L. Takacs

1. INTRODUCTION

One of the most important applications of the forthcoming massively parallel computers is numerical weather prediction and climate simulations. The need for higher spatial resolution in models for weather prediction, and of very long integrations for climate studies, requires computing capabilities several orders of magnitude larger than those presently available. Only massively parallel computers will be able to fill this need. However, it will be also required to design models with a structure that can take advantage of the parallel configuration.

We present here a very simple shallow water equations model, in which spherical geometry is transformed into a formally doubly periodic configuration, which can be easily implemented on a parallel computer at 100% parallelism. Shallow water equation models have been traditionally used to test numerical weather prediction schemes because their structure is analogous to 3-dimensional models of the atmosphere.

This model has been tested on the serial Amdahl computer at the NASA/GSFC Goddard Laboratory for Atmospheric Sciences (GLAS). Its implementation on a simulator of the Massively Parallel Processor (MPP) being developed at NASA/GSFC by Dr. David H. Shaeffer is part of a joint project with Drs. David Randall and Milton Halem.

2. DESCRIPTION OF THE SCHEME

The shallow water equations on spherical coordinates are (Figure 1)

$$\frac{\partial h}{\partial t} = - \frac{1}{a \cos \phi} \left[ \frac{\partial (hu)}{\partial \lambda} + \frac{\partial (hv \cos \phi)}{\partial \phi} \right] \quad (1)$$

$$\begin{aligned} \frac{\partial (hu)}{\partial t} = & - \frac{1}{a \cos \phi} \left[ \frac{\partial (hu)u}{\partial \lambda} + \frac{\partial (hv \cos \phi)u}{\partial \phi} \right] \\ & - \frac{qh}{a \cos \phi} \frac{\partial hT}{\partial \lambda} + \left( f + \frac{u \tan \phi}{a} \right) hv \end{aligned} \quad (2)$$

$$\begin{aligned} \frac{\partial (hv)}{\partial t} = & - \frac{1}{a \cos \phi} \left[ \frac{\partial (hu)v}{\partial \lambda} + \frac{\partial (hv \cos \phi)v}{\partial \phi} \right] \\ & - \frac{qh}{a} \frac{\partial hT}{\partial \phi} - \left( f + \frac{u \tan \phi}{a} \right) hu \end{aligned} \quad (3)$$

where  $f = 2 \sin \phi$ .

<sup>1</sup> Published in Advances in Computer Methods for Partial Equations - IV. Published by IMACS, 1981.

Lets consider a spherical grid configuration, with no grid point at the pole (Fig. 2a). We take "complete" meridians as great circles formed by a meridian on the "light side" of the sphere with a longitude  $\lambda$  and its continuation on "dark side", with a longitude  $\lambda + \pi$ . We let "latitude"  $\phi$  be periodic along a complete meridian:  $-\pi/2 < \phi < \pi/2$ ,  $\cos \phi > 0$  on the "light side" and  $\pi/2 < \phi < 3\pi/2$ ,  $\cos \phi < 0$  on the "dark side." Similarly,  $\sin \phi > 0$  in the Northern Hemisphere and  $< 0$  in the Southern Hemisphere. The geometry becomes thus doubly periodic-like, with a configuration that is ideally suited for a massively parallel processor (Figure 2b). We assume that each processor is connected to its four closest neighbors, with connections "over the poles" as indicated in Fig. 2b.

We use a nonstaggered grid, with all variables defined at the grid points (circles). Let

$$\delta_{\lambda} f_{ij} = f_{i+1/2,j} - f_{i-1/2,j}; \quad \bar{f}_{ij}^{\lambda} = \frac{f_{i+1/2,j} + f_{i-1/2,j}}{2}; \text{ so,}$$

$$\text{eq, } \delta_{\lambda} \bar{f}_{ij}^{\lambda} = \frac{f_{i+1,j} - f_{i-1,j}}{2\Delta\lambda}$$

and similarly for  $\phi$ . Note that  $j=1, \dots, JMAX/2$  on the light side,  $j=JMAX/2+1, \dots, JMAX$  on the dark side,  $\Delta\lambda = 2\pi/JMAX$ ;  $\Delta\phi = 2\pi/JMAX$ , and  $\phi_j = (j-1/2)\Delta\phi - \pi/2$ .

Then a very simple parallel scheme is the following:

STEP 1: Longitudinal cycle, performed for  $j=1, \dots, JMAX/2$  with  $i$  cyclic from 1 to  $IMAX$ :

$$\frac{\partial h}{\partial t}(\lambda) = - \frac{1}{a \cos \phi} \left[ \delta_{\lambda} \bar{h} u^{\lambda} \right] \quad (4a)$$

$$\frac{\partial h u}{\partial t}(\lambda) = - \frac{1}{a \cos \phi} \left[ \delta_{\lambda} (\bar{h} u^{\lambda} u^{\lambda}) \right] - \frac{q h}{a \cos \phi} \delta_{\lambda} \bar{h}^{\lambda}$$

$$+ \left( f + \frac{u \tan \phi}{a} \right) h v \quad (5a)$$

$$\frac{\partial h v}{\partial t}(\lambda) = - \frac{1}{a \cos \phi} \left[ \delta_{\lambda} (\bar{h} u^{\lambda} v^{\lambda}) \right] \quad (6a)$$

Note that this step, as all the following ones, is performed simultaneously for all processors.

ORIGINAL PAGE IS  
OF POOR QUALITY

STEP 2: Latitudinal cycle, performed for  $I=1, \dots, I_{MAX}/2$  with  $j$  cyclic from 1 to  $J_{MAX}$ .

2a: Change sign of wind components on "dark side" (i.e., multiply  $u, v, hu, hv$  by  $d$ , where

$$d = \begin{cases} 1 & \text{on the light side} \\ -1 & \text{on the dark side} \end{cases}$$

2b:

$$\frac{\partial h}{\partial t}(\phi) = -\frac{1}{a \cos \phi} \left[ \delta \phi \overline{hv \cos \phi}^\phi \right] \quad (4b)$$

$$\frac{\partial hu}{\partial t}(\phi) = -\frac{1}{a \cos \phi} \left[ \delta \phi \left( \overline{hv \cos \phi}^\phi \overline{u}^\phi \right) \right] \quad (5b)$$

$$\begin{aligned} \frac{\partial hv}{\partial t}(\phi) = & -\frac{1}{a \cos \phi} \left[ \delta \phi \left( \overline{hv \cos \phi}^\phi \overline{v}^\phi \right) \right] - \frac{gh}{a} \delta \phi \overline{h_T}^\phi \\ & - \left( f + \frac{u \tan \phi}{a} \right) hu \end{aligned} \quad (6b)$$

Notes:

- i)  $\overline{hv \cos \phi}^\phi$  at the poles is not computed but defined as zero.
- ii)  $u, v, \cos \phi$  and  $\partial/\partial \phi$  change signs on the dark side. As a result, the equations remain unmodified.

2c: Same as 2a

STEP 3: Update the fields  $h, hu, hv$  using a suitable time step. For example, if Leap frog is used,

$$\begin{pmatrix} h \\ hu \\ hv \end{pmatrix}^{n+1} = \begin{pmatrix} h \\ hu \\ hv \end{pmatrix}^{n-1} + 2\Delta t \begin{pmatrix} \frac{\partial h}{\partial t} \\ \frac{\partial hu}{\partial t} \\ \frac{\partial hv}{\partial t} \end{pmatrix}^n (\lambda) + 2\Delta t \begin{pmatrix} \frac{\partial h}{\partial t} \\ \frac{\partial hu}{\partial t} \\ \frac{\partial hv}{\partial t} \end{pmatrix}^n (\phi)$$

### 3. IMPLEMENTATION OF THE MODEL

Since no MPP or MPP simulator is yet available, we have implemented the proposed model on the Amdahl serial machine. The parallel structure was simulated by performing STEP 1 in a FORTRAN array as in Figure 3b, changing the signs of the winds on the dark side.

The model worked very well, giving results similar to those obtained with a standard shallow water equation model with a grid point at the poles.

### 4. DISCUSSION

The simple scheme proposed here as a prototype of a 3-dimensional model has the following characteristics:

a) It is 100% parallel, so that on the MPP it should be  $IMAX \cdot JMAX$  faster than on a serial machine of the same speed. In other words, with the exception of  $(hvcos\phi)\phi$  at the poles, all operations are identical for all grid points and can be performed simultaneously. With the current values  $IMAX=72$ ,  $JMAX=46$  used in the GLAS models, this represents a factor of 3000 in speed.

b) It conserves mass and energy.

c) It is almost identical to a second order version of the Fourth-Order GLAS global atmospheric model (Kalnay-Rivas, et al., 1977), the only difference being the lack of a grid point at the poles.

d) It can be immediately generalized to Fourth-Order if four more connectors are included (Figure 4).

e) The 16th order Shapiro filter currently used in the Fourth-Order GLAS Model can be trivially implemented at 100% parallelism. The Fourier filtering at high latitudes that eliminates short unstable waves near the poles requires the development of an appropriate FFT algorithm.

f) If each processor has 1K memory, as the MPP will, the implementation of 3-dimensionality can also be done at nearly 100% parallelism. This is because all the variables in one atmospheric vertical column (a few hundred with reasonable vertical resolutions) can be contained in one processor. Since the computations within each vertical column are independent of other columns but similar; they can also be performed simultaneously.

The impact that the utilization of massively parallel computers will have on weather and climate research may be as large as that produced when the development of computers during the late 1940's and 50's made numerical weather prediction feasible for the first time (Charney et al., 1950). For example, current GLAS models require about one hour of computer time to simulate one day of atmospheric flow. At 100% parallelism, the same models would simulate eight years in one hour.

It is very remarkable that in his monumental work, Richardson (1922) developed not only many of the basic physical and numerical ideas presently used in numerical weather prediction, but also the concept of a massively

parallel processor (Figure 5). Note that in his "fantasy", there are 2000 parallel processors (columns), and 32 (human) computers for each processor. Note that he also suggested the use of simpler models for the development of improved procedures. In the preface of his book Richardson wrote: "The scheme [for weather prediction] is complicated because the atmosphere is complicated . . . Perhaps some day in the dim future it will be possible to advance the computations faster than the weather advances and at a cost less than the saving to mankind due to the information gained. But that is a dream."

The application of massively parallel processor to atmospheric modeling will truly fulfill Richardson's dream.

#### REFERENCES

- Charney, J. G., R. Fjortoft, and J. Von Neumann, 1950: Numerical integration of the barotropic vorticity equations. Tellus, 2, 237-254.
- Kalnay-Rivas, E., A. Bayliss, and J. Storch, 1977: The fourth-order GISS model of the global atmosphere. Contributions to Atm. Sci., 50, 299-311.
- Richardson, L. F., 1922: Weather prediction by numerical process. Cambridge University Press, London, 236 pp. Reprinted by Dover, 1965.

ORIGINAL PAGE IS  
OF POOR QUALITY

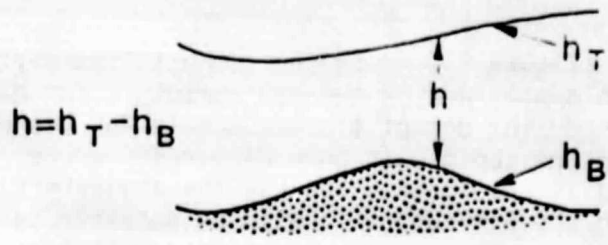


Figure 1: Schematic of shallow water model.

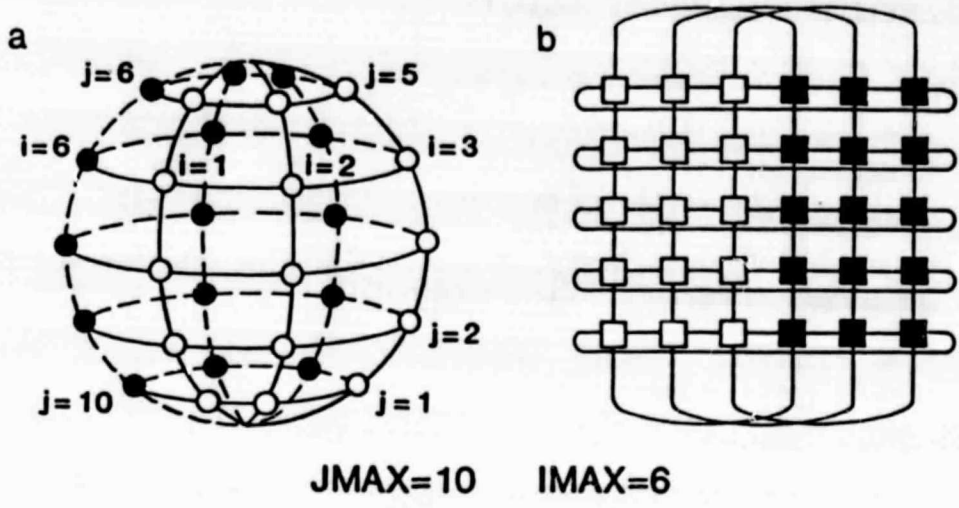
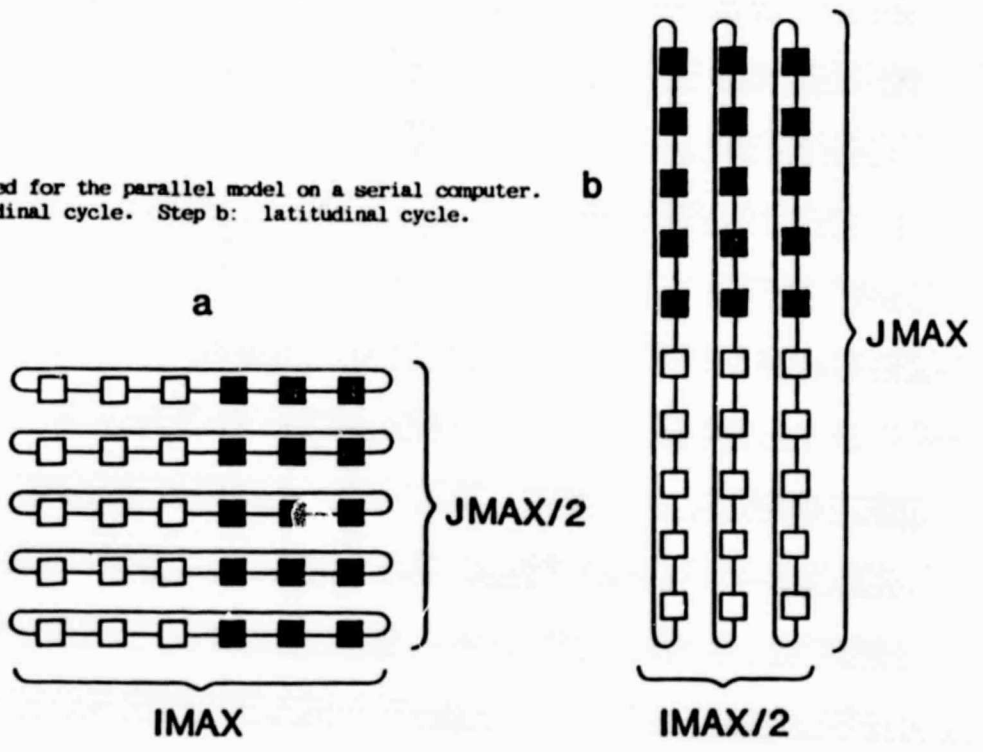


Figure 2: a) Schematic of grid points on the sphere.  
b) Schematic of the proposed corresponding MPP connectors.

Figure 3: Cyclic arrays used for the parallel model on a serial computer.  
Step a: longitudinal cycle. Step b: latitudinal cycle.



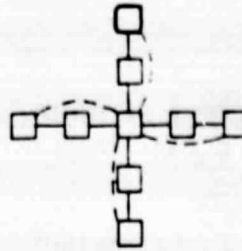


Figure 4: Connections for a fourth order scheme.

A FORECAST-FACTORY

Ch. 11/2. THE SPEED AND ORGANIZATION OF COMPUTING

It took me the best part of six weeks to draw up the computing forms and to work out the new distribution in two vertical columns for the first time. My office was a heap of hay in a cold rest billet. With practice the work of an average computer might go perhaps ten times faster. If the time-step were 3 hours, then 32 individuals could just compute two points so as to keep pace with the weather, if we allow nothing for the very great gain in speed which is invariably noticed when a complicated operation is divided up into simpler parts, upon which individuals specialize. If the co-ordinate chequer were 200 km square in plan, there would be 3200 columns on the complete map of the globe. In the tropics the weather is often foreknown, so that we may say 2000 active columns. So that  $32 \times 2000 = 64,000$  computers would be needed to race the weather for the whole globe. That is a staggering figure. Perhaps in some years' time it may be possible to report a simplification of the process. But in any case, the organization indicated is a central forecast-factory for the whole globe, or for portions extending to boundaries where the weather is steady, with individual computers specializing on the separate equations. Let us hope for their sakes that they are moved on from time to time to new operations.

After so much hard reasoning, may one play with a fantasy? Imagine a large hall like a theatre, except that the circles and galleries go right round through the space usually occupied by the stage. The walls of this chamber are painted to form a map of the globe. The ceiling represents the north polar regions, England is in the gallery, the tropics in the upper circle, Australia on the dress circle and the antarctic in the pit. A myriad computers are at work upon the weather of the part of the map where each sits, but each computer attends only to one equation or part of an equation. The work of each region is coordinated by an official of higher rank. Numerous little "night signs" display the instantaneous values so that neighbouring computers can read them. Each number is thus displayed in three adjacent zones so as to maintain communication to the North and South on the map. From the floor of the pit a tall pillar rises to half the height of the hall. It carries a large pulpit on its top. In this sits the man in charge of the whole theatre; he is surrounded by several assistants and messengers. One of his duties is to maintain a uniform speed of progress in all parts of the globe. In this respect he is like the conductor of an orchestra in which the instruments are slide-rules and calculating machines. But instead of waving a baton he turns a beam of rosy light upon any region that is running ahead of the rest, and a beam of blue light upon those who are behindhand.

Four senior clerks in the central pulpit are collecting the future weather as fast as it is being computed, and despatching it by pneumatic carrier to a quiet room. There it will be coded and telephoned to the radio transmitting station.

Messengers carry piles of used computing forms down to a storehouse in the cellar.

In a neighbouring building there is a research department, where they invent improvements. But there is much experimenting on a small scale before any change is made in the complex routine of the computing theatre. In a basement an enthusiast is observing eddies in the liquid lining of a huge spinning bowl, but so far the arithmetic proves the better way. In another building are all the usual financial, correspondence and administrative offices. Outside are playing fields, houses, mountains and lakes, for it was thought that those who compute the weather should breathe of it freely.

Figure 5: "A Forecast Factory", from Richardson (1922).

ON THE EFFECT OF HIGH LATITUDE FILTERING  
IN GLOBAL GRID POINT MODELS<sup>1</sup>

L. L. Takacs<sup>2</sup>, R. C. Balgovind<sup>2</sup>, M. Iredell<sup>2</sup> and E. Kalnay

1. INTRODUCTION

The process of filtering at high latitudes in global grid point models is fairly common in meteorological studies. This is done in order to avoid the use of a prohibitively short time step required by fast moving waves near the poles. In the Arakawa-Mintz general circulation model (Gates et al., 1971), smoothing was performed on the zonal mass flux in the divergence terms and on the zonal pressure gradient in the prediction equations, thus eliminating the fast moving gravity waves in the zonal direction. Vanderman (1972) applied a weighted average in the east-west direction to the tendencies of the dependent variables near the poles to eliminate short wave disturbances. Umscheid and Sankar-Rao (1971), Arakawa (1972), and Kalnay-Rivas et al. (1977) used Fourier filtering to eliminate the unwanted waves. We have found that when these filtering techniques are applied in a coarse resolution grid point model, the non-linear effects responsible for change in the mean zonal flow become poorly simulated, resulting in spurious energy and momentum transfers.

In this paper we will examine the effects of this phenomenon and its relationship to various filtering techniques.

2. MODEL DESCRIPTION

The model used to examine the effect of high latitude filtering is based on the shallow water equations on a sphere given by

$$\frac{\partial(hu)}{\partial t} + \frac{1}{a \cos(\theta)} \left[ \frac{\partial(hu)u}{\partial \lambda} + \frac{\partial(hu)v \cos \theta}{\partial \theta} \right] - (f + u \tan \theta) hv + \frac{gh}{a \cos \theta} \frac{\partial h}{\partial \lambda} = 0 \tag{1}$$

$$\frac{\partial(hv)}{\partial t} + \frac{1}{a \cos \theta} \left[ \frac{\partial(hv)u}{\partial \lambda} + \frac{\partial(hv)v \cos \theta}{\partial \theta} \right] + (f + u \tan \theta) hu + \frac{gh}{a} \frac{\partial h}{\partial \theta} = 0 \tag{2}$$

---

<sup>1</sup> Published in Preprint Volume: Fifth Conference on Numerical Weather Prediction, Nov. 2-6, 1981; Monterey, California. Published by the American Meteorological Society, Boston, Massachusetts.

<sup>2</sup> Sigma Data Services Corporation

$$\frac{\partial(h)}{\partial t} + \frac{1}{a \cos \theta} \left[ \frac{\partial(hu)}{\partial \lambda} + \frac{\partial(hv \cos \theta)}{\partial \theta} \right] = 0 \quad (3)$$

where  $h$  is the height of the atmosphere,  $u$  and  $v$  are the zonal and meridional wind components, and  $f$  is the Coriolis parameter. The latitudinal and longitudinal directions are given by  $\theta$  and  $\lambda$  respectively, while  $a$  is the radius of the earth. For simplicity, bottom topography has been set to zero for these experiments. The equations at the poles follow those of the GLAS 4th Order General Circulation Model (Kalnay-Rivas *et al.*, 1977).

All variables are defined on a non-staggered 'A' grid. Spatial derivatives are approximated by 4th order differences, while the time derivatives are approximated by the leap-frog scheme. A simple forward step is applied with  $\Delta t$  equal to 1/4 of its original value every 20 time steps to avoid the separation of the solution produced by the leap-frog scheme.

In these experiments the model was run under two general conditions, the first using a very small time step allowing all resolvable waves to remain computationally stable, and the second using a time step defined by the most unstable wave located at 60 degrees latitude. Poleward of 60 degrees various types of filters and smoothing operators were used to control the amplification of the shorter waves.

As the initial condition for these experiments, we followed Phillips (1959) by taking an initially non-divergent velocity field described by the stream function

$$\psi = a^2 \left[ -W \sin \theta + K \cos R \theta \sin \theta \cos(R \lambda) \right] \quad (4)$$

together with a height field derived by solving the inverse balance equation. The constants  $K$  and  $W$  in the stream function equation were both equal to  $7.848 \times 10^{-6} \text{ sec}^{-1}$ , while the wavenumber in the zonal direction,  $R$ , was equal to 4. The mean height of the atmosphere was equal to 8000m.

As discussed by Hoskins (1973) and Doron *et al.* (1974), this initial condition produces a super-rotation of the atmosphere in addition to a Rossby-Haurwitz wave which moves westward relative to the fluid. For a non-divergent barotropic atmosphere, the total solution will move from west to east without change of shape. Since we are using a free upper surface, however, some changes in the solution can be expected due to the divergent nature of our model. In these experiments we are interested in how closely the time evolution of the filtered run compares with the non-filtered run.

### 3. RESULTS

The following results were obtained by integrating the above initial conditions on a coarse grid having a resolution of 10 degrees in longitude and 8.18 degrees in latitude. Figure (1) shows, using a rectangular latitude-longitude projection, the initial height field and subsequent heights at 100, 200, and 300 hours of integration for the nonfiltered case, while Figure (2) shows the same for the filtered case. In this run, a Fourier filter with a response

similar to that used in the GLAS 4th Order Model was applied to the fields  $u$ ,  $v$  and  $h$  at every time step. This filter will be discussed in detail in section (4).

From Figure (1) we see that the initial disturbance moves eastward at a rate of about 90 degrees per 200 hrs. with relatively minor change. The  $u$  field (not shown) shows some slight tilting of the trough-ridge lines which results in  $u$ -momentum being transported meridionally. However, the overall solution appears close to that given by the non-divergent equations.

Figure (2), however, shows drastic changes occurring between 100 and 200 hours. The tilting of the trough-ridge lines becomes very pronounced in the northwest-southeast direction, and can be readily identified at 200 and 300 hours. The appearance of a closed contour low is evident at 200 hours, while the amplitude of the wave steadily decreases from 200 to 300 hours. The zonally averaged  $u$  field, which was initially positive at all latitudes, became negative at mid-latitudes in conjunction with the cut-off low.

Figures (3) and (4) show the mass weighted  $u$ -momentum transfer due to the zonally averaged eddy momentum flux at 0, 100, 200 and 300 hours. We can see from figure (3) that there is a transfer of  $u$ -momentum equatorward in the sub-tropics and a vacillating transport at mid-to high latitudes. In the filtered run, figure (4), there is no poleward transport at all but a very strong equatorward transport at mid-latitudes. As a result, the energetics of the two runs became vastly different since more energy was being fed into the zonal flow for the filtered case. Figures (5) and (6) show the zonal and eddy kinetic energy. From figure (5) we see that there is very little change in the energetics of the non-filtered solution once the initial state becomes balanced. In this run the zonal kinetic energy increased by 13% while the eddy kinetic energy decreased by 9% after 300 hours. The filtered case, however, shows significant changes at every stage. After 300 hours the kinetic energy due to the zonal flow has increased by 75% while that due to the eddy flow has decreased by 75%.

These figures show the effect of high latitude filtering in our model. Since filtering can be thought of as a latitudinal dependent dissipation function, two further experiments were performed in which a non-filtered model was run with the addition of linear damping in the  $u$ -and  $v$ -momentum equations. The time constant  $\tau$  associated with the damping was equal to 7 days. In the first run  $\tau$  was constant in latitude while in the second run  $\tau$  was multiplied by  $\sin^4(\theta)$ , thereby simulating the effect of the filter.

The results from the first run showed the Rossby-Haurwitz wave slowly moving to the east with steadily decreasing amplitude at all latitudes. No tilting of the trough-ridge lines was evident nor was there any formation of the cutoff low. The second run, however, showed results identical to those of the filtered runs. Strong tilting of the trough-ridge lines was present as well as the cut-off low in mid-to high latitudes. The results showed that the deformation of the Rossby-Haurwitz wave was a realistic response of the model to a latitudinal dependent dissipation function introduced by the filter.

These results can be understood in terms of Eliassen and Palm (1960) theory. The high latitude filtering introduces a sink of wave energy, which in turn induces a poleward flux of eddy energy. In accordance to the Eliassen-Palm theorem, this must be accompanied by an equatorward flux of westerly momentum, resulting in the strong subtropical jets observed in the filtered numerical results.

#### 4. FILTERING TECHNIQUES

In order to try to eliminate the errors produced by the filter, variations in the filtering technique and in the filter's frequency response were investigated. As pointed out earlier, some atmospheric modellers filter other quantities such as the tendencies or the pressure gradient terms rather than the field variables themselves to eliminate the fast waves near the poles. We compared the results obtained from using these filtering procedures and found that all results showed the same behavior. It appeared that the deformation caused by the filter was independent of the filter's source.

As noted earlier, the filter response used in this experiment was similar to that used by the GLAS 4th Order Band Model (hereafter referred to as the operational filter). In the filtering technique, the field variables  $u$ ,  $v$  and  $h$  were Fourier decomposed into their wave constituents which were then altered by a wave dependent damping function. The frequency response of the damping function was empirically selected after performing experiments with the GLAS 4th Order Model. The latitudes used by the filter were twice the distance from the poles than in the GLAS 4th Order Model due to the coarse resolution of the shallow water model.

Figure (7a) shows the frequency response of the damping function used in the operational filter as a function of wavenumber. Primarily, this response uses a linear damping curve over six wavelengths until complete truncation is achieved. In addition to this response, three other damping functions were tested. As shown by Arakawa and Lamb (1977), a damping function based on the linearized gravity wave equations on a sphere was derived using a staggered grid and centered 2nd-order spatial differences. This function is given by

$$F(k) = \frac{\Delta\lambda}{\Delta\theta} \frac{\cos \theta}{\sin\left(\frac{k \Delta\lambda}{2}\right)} \quad (5)$$

where  $k$  is wavenumber. The actual value used as the damping coefficient in the filtering procedure would be the minimum of 1 and equation (5). The response of this filter is shown in figure (7b).

Using a similar type of analysis as Arakawa and Lamb, a damping function using a non-staggered grid and 4th-order spatial differences was also derived and tested. The response of this function is given in figure (7c), while its functional form is given by

$$F(k) = \frac{\Delta\lambda}{\Delta\theta} \frac{\cos \theta}{\frac{4}{3} \sin(k\Delta\lambda) - \frac{1}{6} \sin(2k\Delta\lambda)} \quad (6)$$

Note that in this type of filter the shortest waves remain unchanged.

Finally, as an approximation to the implicit bi-harmonic diffusion used in the ECMWF model, a damping function derived from the longitudinal component of the bi-harmonic diffusion was also tested, given by

$$F(k) = \left[ \nu \frac{(2\cos(2k\Delta\lambda) - 8\cos(k\Delta\lambda) + 6)}{(a\cos 9 \Delta\lambda)^4} + 1 \right]^{-1} \quad (7)$$

where the constant  $\nu$  was taken as  $4.0 \times 10^{18} \text{ m}^4/\text{sec}$ . The frequency response of this function is shown in figure (7d).

By using the convolution property of the Fourier transform, the damping coefficients in wavenumber space may also be viewed as the weighting coefficients in grid space. These are shown in figure (8a-d) for the grid point nearest to the pole.

All of the above filter types have been tested using the initial conditions described earlier, and all of these experiments produced results similar to those of the operational filter. The results obtained using the damping function associated with figures (7c) and (8c) were slightly worse due to the inclusion of the poorly simulated short waves. It again appears, however, that the filtering procedure itself causes the phenomena to exist and has little dependency on minor variations in the frequency response of the filter or on the method of application.

## 5. CONCLUDING REMARKS

We have seen from the preceding sections that high latitude filtering in a coarse resolution grid point model produces spurious energy and momentum transfers which affect the solution at all latitudes. This phenomenon seems to be independent of the details of the filtering procedure and occurs even if only the time derivatives or the divergence terms are filtered. In coarse resolution global models maximum integrations seem to be limited to one week or so unless sufficiently small time steps are taken to eliminate the need for filtering.

It should be pointed out that the same experiment was also carried out with double resolution (i.e. 5 degrees in longitude X 4 degrees in latitude). Using a time step of 10 minutes and a filter identical to that of the GLAS 4th Order Model, the results were very similar to those of the nonfiltered coarse grid model and showed no evidence of spurious transfers of energy and momentum. One possible reason for this may be the fact that in the Rossby-Haurwitz wave of zonal wavenumber 4, there are strong nonlinear interactions of wavenumber 8. In the coarse resolution model, this is close to the  $4 \Delta\lambda$  wave (zonal wavenumber 9) which is strongly filtered. In the high resolution model, the  $4 \Delta\lambda$  wave has zonal wavenumber 18. Thus the coarse resolution model may have a poorer simulation of the nonlinear effects when compared to the fine resolution model.

These results point out a serious deficiency of coarse resolution grid point models used for climate simulations. We are presently studying the

effect of high latitude filtering in higher resolution models used for weather prediction as well as in models using implicit time steps.

## REFERENCES

- Arakawa, A., 1972: Design of the UCLA general circulation model. Tech. Rep. No. 7. Dept. Meteorol., Univeristy of California, Los Angeles.
- Arakawa, A., and V. R. Lamb, 1977: Computational design of the basic dynamical processes of the UCLA general circulation model. Methods In Computational Physics, Vol. 17, Academic Press, New York.
- Doron, E., A. Hollingsworth, B. J. Hoskins, and A. J. Simmons, 1974: A comparison of grid-point and spectral methods in a meteorological problem. Quart. J. Roy. Met. Soc., 100, 371-383.
- Eliassen, A., and E. Palm, 1960: On the transfer of energy in stationary mountain waves. Geophysica Norvegica, Vol. 22, No.3, pp. 2-23.
- Gates, W. L., E. S. Batten, A. B. Kahle, and A. B. Nelson, 1971: A documentation of the Mintz-Arakawa two-Level atmospheric general circulation model. Advanced Research Projects Agency Rep. R-877-ARPA, Rand Corporation, Santa Monica, California.
- Hoskins, B. J., 1973: Stability of the Rossby-Haurwitz wave. Quart. J. Roy. Met. Soc., 99, 723-745.
- Kalnay-Rivas, E., A. Bayliss, and J. Storch, 1977: The 4th order GISS model of the global atmosphere. Cont. to Atmos. Phys., Vol. 50, pp. 306-311.
- Kalnay-Rivas, E., and D. Hoitsma, 1979: Documentation of the fourth order band model. NASA Tech. Memo. 80608, Greenbelt, Maryland.
- Phillips, N. A., 1959: Numerical integration of the primitive equations on the hemisphere. Mon. Wea. Rev., 87, 333-345.
- Shapiro, R., 1970: Smoothing, filtering and boundary effects. Rev. Geophys. and Space Phys., 8, 359-387.
- Umscheid, L., Jr., and M. Sankar-Rao, 1971: Further tests of a grid system for global numerical prediction. Mon. Wea. Rev., 99, 686-690.
- Vanderman, L. W., 1972: Forecasting with a global, three layer, primitive equation model. Mon. Wea. Rev., 100, 856-868.

ORIGINAL PAGE IS  
OF POOR QUALITY

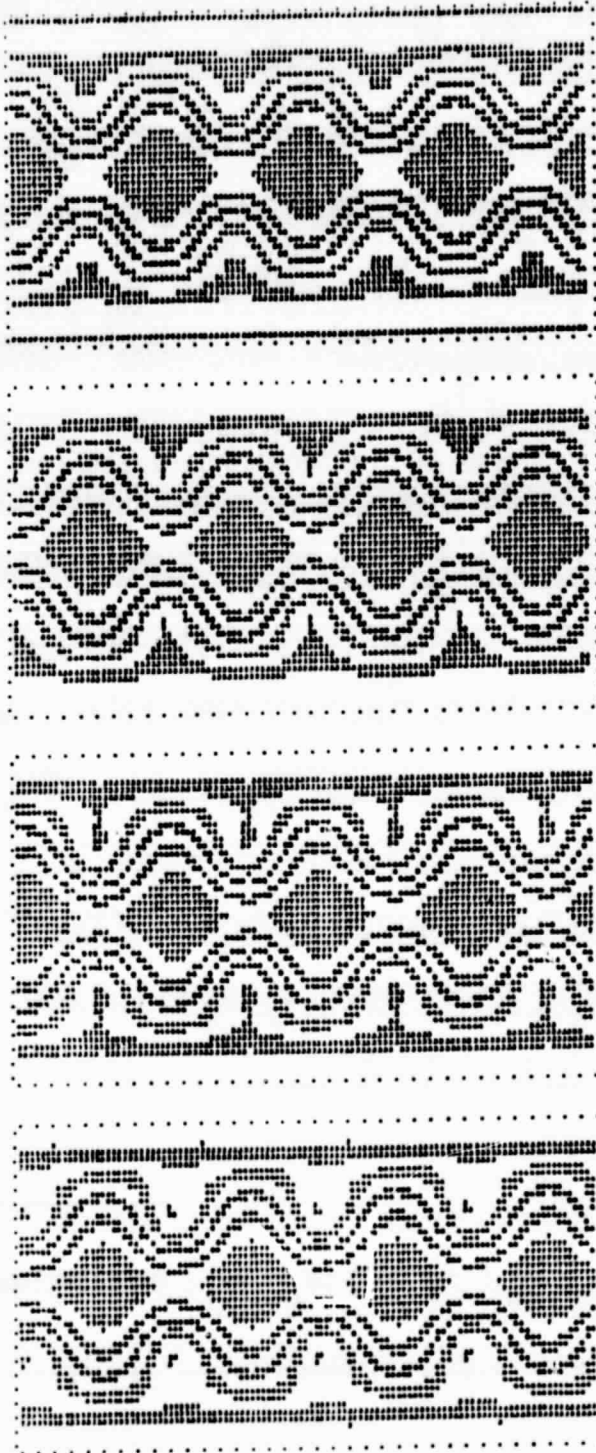


Figure 1. Initial height field (top) and subsequent height fields at 100, 200 and 300 hours for the non-filtered run.

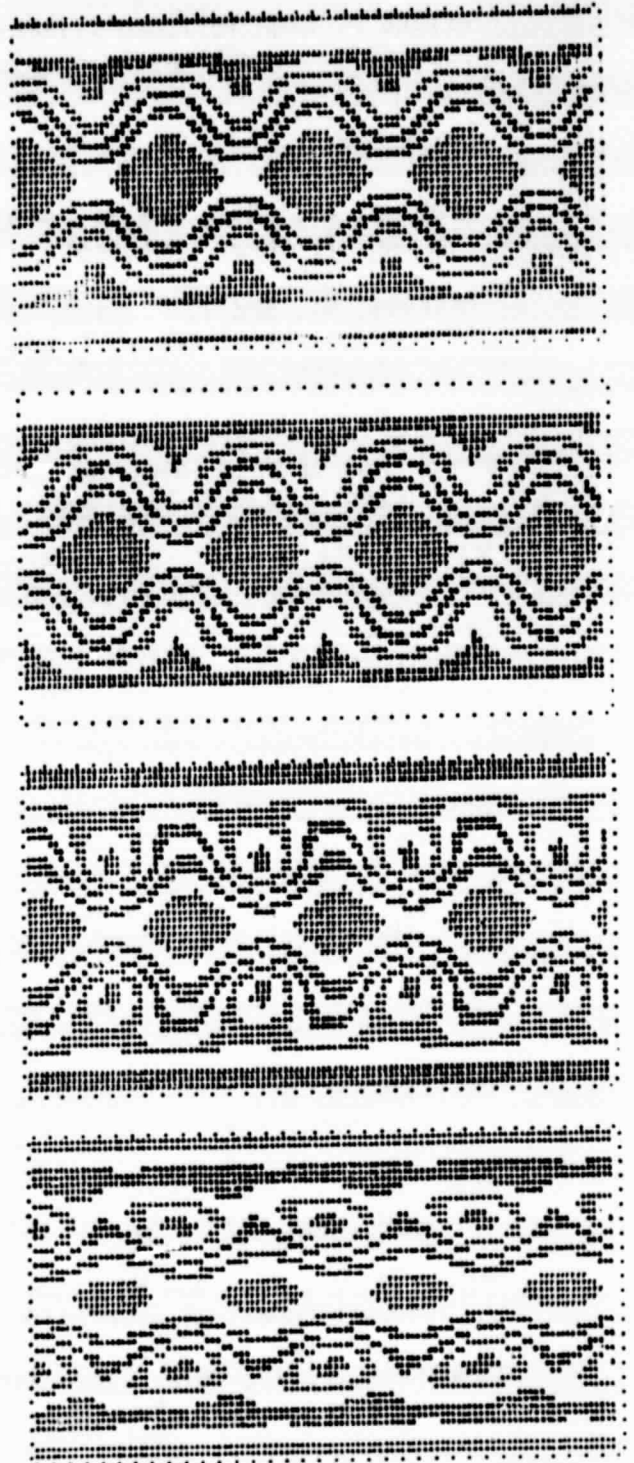


Figure 2. As in Figure 1 except for the filtered run.

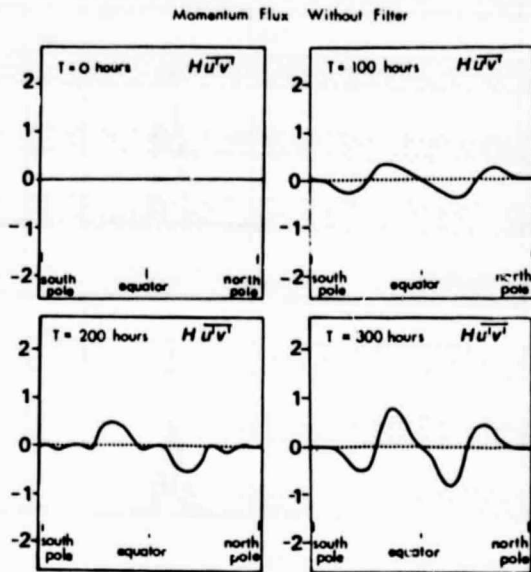


Figure 3. Mass weighted  $u$ -momentum transfer ( $\times 10^6 \text{ m}^3/\text{sec}^2$ ) due to the zonally averaged eddy momentum flux for the non-filtered run.

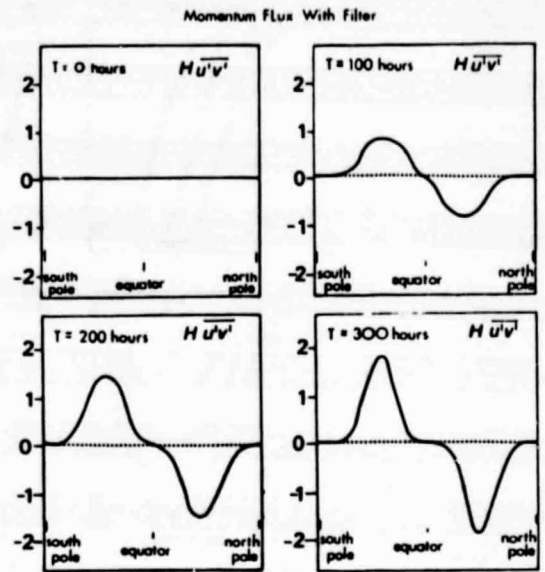


Figure 4. As in Figure 3 except for the filtered run.

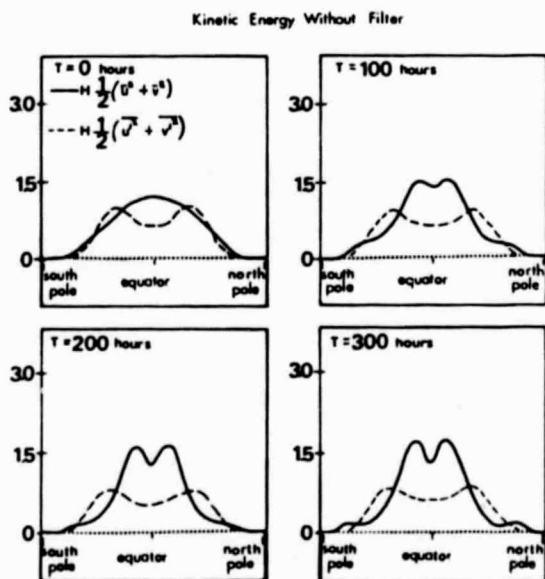


Figure 5. Mass weighted kinetic energy ( $\times 10^7 \text{ m}^3/\text{sec}^2$ ) for the non-filtered run.

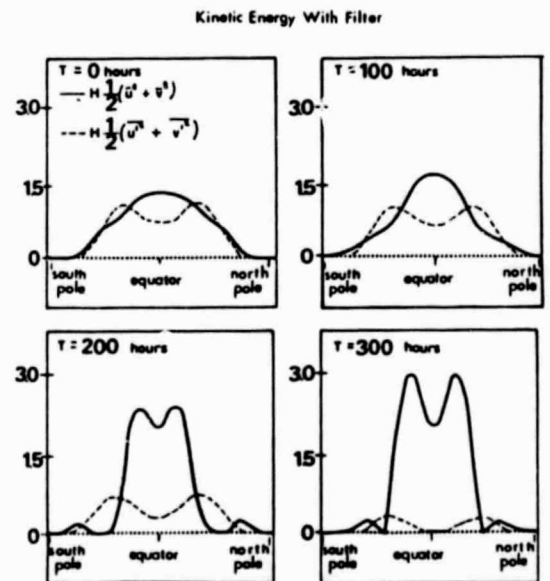


Figure 6. As in Figure 5 except for the filtered run.

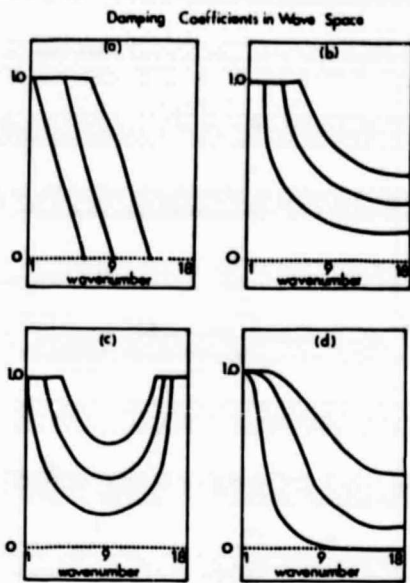


Figure 7. Damping functions used in Fourier filtering for the 3 latitudes nearest to the poles for a) operational filter, b) 2nd order filter on a staggered grid, c) 4th order filter on a non-staggered grid, d) bi-harmonic diffusion filter.

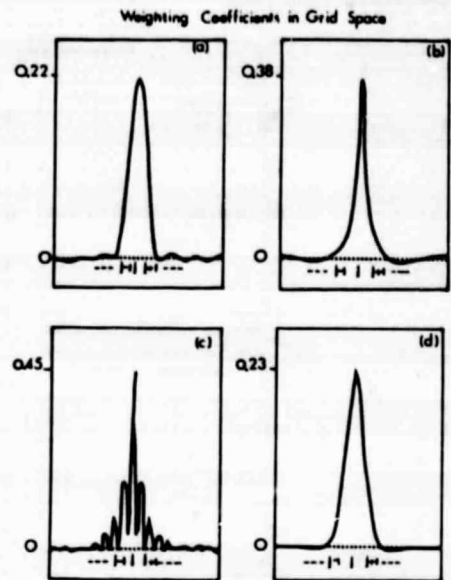


Figure 8. Weighting coefficients in real space derived from the damping function used at the latitude nearest to the poles for each filter described in Figure 7.

SHALLOW WATER EXPERIMENTS USING AN IMPROVED  
KREISS-OLIGER 2-4 SCHEME

L. L. Takacs and R. C. Balgovich

1. INTRODUCTION

Kreiss and Olinger (1973) indicated the advantages of the 2-4 scheme for meteorological purposes. This scheme consists of the second-order leapfrog scheme for time derivatives, and fourth-order space differencing for spatial derivatives. Abarbanel and Gottlieb (1980) have shown that by modifying the Kreiss-Olinger scheme in a manner similar to that done by Wilson (1978) to the multi-dimensional leapfrog scheme, a substantial improvement of the maximum time-step could be obtained. As an experiment we applied the Abarbanel-Gottlieb scheme to a global 1-level shallow water model and compared the results to those using the standard Kreiss-Olinger scheme.

2. REVIEW OF SCHEMES

For a system of equations defined by

$$\frac{\partial q}{\partial t} = \frac{\partial F}{\partial x} + \frac{\partial G}{\partial y} \quad (1)$$

where  $q$ ,  $F$ , and  $G$  are  $m$ -component vectors, the Kreiss-Olinger (hereafter referred to as KO) scheme is given by

$$q_{ij}^{n+1} = q_{ij}^{n-1} + 2\Delta t \left\{ \begin{aligned} & 4/3 \left( \frac{F_{i+1,j}^n - F_{i-1,j}^n}{2\Delta x} + \frac{G_{i,j+1}^n - G_{i,j-1}^n}{2\Delta y} \right) \\ & - 1/3 \left( \frac{F_{i+2,j}^n - F_{i-2,j}^n}{4\Delta x} + \frac{G_{i,j+2}^n - G_{i,j-2}^n}{4\Delta y} \right) \end{aligned} \right. \quad (2)$$

The Abarbanel-Gottlieb (hereafter referred to as AG) scheme expands the domain of influence of the above scheme by including off-axis grid points. This scheme is given by

$$q_{ij}^{n+1} = q_{ij}^{n-1} + 2\Delta t \left\{ \begin{aligned} & - F_{i+2,j+2}^n + F_{i+1,j+2}^n - F_{i-1,j+2}^n + F_{i-2,j+2}^n \end{aligned} \right.$$



ORIGINAL PAGE IS  
OF POOR QUALITY

height, and  $u$  and  $v$  are the two-dimensional wind components.

Assuming wave solutions of the form

$$(u_{i,j}^n, v_{i,j}^n, h_{i,j}^n) = \text{Re} \left\{ u^n, v^n, h^n e^{i(\theta x_i + \theta y_j)} \right\} \quad (7)$$

$$\text{where } \theta x = k \Delta x = 2\pi \Delta x / L_x$$

$$\theta y = l \Delta y = 2\pi \Delta y / L_y$$

and using the appropriate difference schemes, the maximum allowable time-step governing stability is given by

$$\Delta t_{\max} = 1/\sqrt{qH} \left[ \left( \frac{W_x}{\Delta x} \right)^2 + \left( \frac{W_y}{\Delta y} \right)^2 \right]_{\max}^{-1/2} \quad (8)$$

where for the K0 scheme we have:

$$W_x = \frac{4}{3} \sin \theta x - \frac{1}{6} \sin 2\theta x \quad (9)$$

$$W_y = \frac{4}{3} \sin \theta y - \frac{1}{6} \sin 2\theta y \quad (10)$$

while for the AG scheme we have:

$$W_x = \frac{1}{6} \left[ 2(\sin \theta_x - \sin 2\theta_x) \cos 2\theta_y + 2(\sin \theta_x + \sin 2\theta_x) \cos \theta_y + (\sin \theta_x - \sin 2\theta_x) \right] \quad (11)$$

$$W_y = \frac{1}{6} \left[ 2(\sin \theta_y - \sin 2\theta_y) \cos 2\theta_x + 2(\sin \theta_y + \sin 2\theta_y) \cos \theta_x + (2\sin \theta_y - \sin 2\theta_y) \right] \quad (12)$$

For simplicity, let  $dx=dy=d$ . Then equation (8) becomes

$$\Delta t_{\max} = d/\sqrt{qH} \left[ (W_x^2 + W_y^2)_{\max} \right]^{-1/2} \quad (13)$$

**ORIGINAL PAGE IS  
OF POOR QUALITY**

For the KO scheme,  $W_x$  and  $W_y$  are mutually independent and thus each can be maximized separately. This is not true, however, for the AG scheme and therefore the maximization of the sum is required. Doing so we find that

$$\begin{aligned} \text{KO:} \quad W_{x\max}^2 = W_{y\max}^2 &\equiv W_{\max}^2 = 1.882 \\ &\text{when } \theta_x = \theta_y = 1.804 \end{aligned} \quad (14)$$

while

$$\begin{aligned} \text{AG:} \quad (W_x^2 + W_y^2)_{\max} &= W_{\max}^2 = 1.882 \\ &\text{when } \theta_x = 1.804; \theta_y = 0 \\ &\text{OR } \theta_x = 0; \theta_y = 1.804 \end{aligned} \quad (15)$$

Note that for the AG scheme, the non-dimensional wavenumber which gets zeroed out will be the one associated with the largest grid length. Here, since  $dx=dy$ , the preference is unbiased. Using (14) and (15) in (13), we obtain

$$\Delta t_{AG} = \sqrt{2} \Delta t_{KO} \quad (16)$$

or, an increase in time step of  $\sqrt{2}$  can be expected when using a uniform rectangular grid with equal spacing.

We can now repeat the analysis by writing the governing equations in spherical coordinates.

$$\frac{\partial u}{\partial t} = -\frac{g}{a \cos \phi} \frac{\partial h}{\partial \lambda} \quad (17)$$

$$\frac{\partial v}{\partial t} = -\frac{g}{a} \frac{\partial h}{\partial \phi} \quad (18)$$

$$\frac{\partial h}{\partial t} = -\frac{H}{a \cos \phi} \left[ \frac{\partial u}{\partial \lambda} + \frac{\partial (v \cos \phi)}{\partial \phi} \right] \quad (19)$$

where  $a$  denotes the radius of the earth. Using the appropriate difference schemes we find

$$\Delta t_{\max} = a \cos \phi / \sqrt{gH} \left[ \left( \frac{W_\lambda}{\Delta \lambda} \right)^2 + \cos^2 \phi \frac{W_\phi W_\phi'}{(\Delta \phi)^2_{\max}} \right]^{-1/2} \quad (20)$$

where  $W_\lambda$  and  $W_\phi$  are defined analogous to equations (9)-(12). The term  $W_\phi'$  replaces  $W_\phi$  with  $W_{\phi+\Delta\phi}$ . Note again that for the KO scheme,  $W_\lambda$  and  $W_\phi$  are

**ORIGINAL PAGE IS  
OF POOR QUALITY**

mutually independent while for the AG scheme they are not. Also, the maximum time step has now become latitude dependent, reflecting the changing grid length in the zonal direction as one approaches the pole.

Tables (1) and (2) show the maximum allowable time steps in seconds for the two schemes using a course grid (10° longitude x 8.18° latitude) as a function of latitude and scale height. Tables (3) and (4) show the same using a fine grid (5° longitude X 4° latitude). For the K0 scheme a uniformly decreasing time step is observed from the equator to the pole as expected. The AG scheme, however, has a constant time step up to a critical latitude, and then begins to decrease as one continues toward the pole. This critical latitude is the latitude where  $\text{acos}(\phi)\Delta\lambda = a\Delta\phi$  (~35°). Below this latitude the grid length in the zonal direction is larger than the grid length in the meridional direction, while above the critical latitude the reverse is true. This causes a latitudinal bias as to which non-dimensional wavenumber,  $\theta_\lambda$  or  $\theta_\phi$ , gets zeroed out when the time step is maximized. The result, therefore, is a constant time step associated with  $\Delta\phi$  below the critical latitude, and a uniformly decreasing time step associated with  $\Delta\lambda$  above the critical latitude. As can be seen, the maximum gain the AG scheme can have over the K0 scheme is right at the critical latitude, given by a factor of  $\sqrt{2}$ . In practice, however, a much smaller time step than that associated with the critical latitude is needed in order to inhibit the growth of short waves near the poles. Thus, the resulting gain of the AG scheme over the K0 scheme is reduced.

TABLE 1

K0 Scheme (Course Grid)

Latitude (deg)	Scale Height (m)				
	6000	7000	8000	9000	10000
8.2	2112	1955	1829	1724	1636
16.4	2085	1930	1805	1702	1615
24.5	2037	1886	1764	1663	1578
32.7	1963	1818	1700	1603	1521
40.9	1858	1720	1609	1517	1439
49.1	1711	1584	1482	1397	1325
57.3	1509	1397	1307	1232	1169
65.5	1239	1147	1073	1011	960
73.6	891	825	771	727	690
81.8	469	434	406	383	363
90.0	0	0	0	0	0

TABLE 2

AG Scheme (Course Grid)

Latitude (deg)	Scale Height (m)				
	6000	7000	8000	9000	10000
8.2	2743	2540	2375	2240	2125
16.4	2743	2540	2375	2240	2125
24.5	2743	2540	2375	2240	2125
32.7	2743	2540	2375	2240	2125
40.9	2526	2339	2188	2062	1957
49.1	2189	2026	1896	1787	1695
57.3	1807	1673	1565	1475	1400
65.5	1388	1285	1202	1134	1075
73.6	942	872	815	769	729
81.8	476	440	412	388	368
90.0	0	0	0	0	0

TABLE 3

KO Scheme (Fine Grid)

Latitude (deg)	Scale Height (m)				
	6000	7000	8000	9000	10000
2.0	1044	967	904	853	809
6.0	1042	965	903	851	807
10.0	1038	961	899	848	804
14.0	1032	955	894	843	799
18.0	1024	948	886	836	793
22.0	1013	938	877	827	784
26.0	999	925	865	816	774
30.0	982	910	851	802	761
34.0	962	891	833	786	745
38.0	939	869	813	766	727
42.0	910	843	788	743	705
46.0	877	812	759	716	679
50.0	838	776	725	684	649
54.0	792	733	686	647	613
58.0	738	684	640	603	572
62.0	677	627	586	553	524
66.0	606	561	525	495	469
70.0	526	487	455	429	407
74.0	436	403	377	356	337
79.0	336	311	291	275	260
82.0	229	212	198	187	177
86.0	116	108	101	95	90
90.0	0	0	0	0	0

TABLE 4

AG Scheme (Fine Grid)

Latitude (deg)	Scale Height (m)				
	6000	7000	8000	9000	10000
2.0	1338	1239	1159	1092	1036
6.0	1338	1239	1159	1092	1036
10.0	1338	1239	1159	1092	1036
14.0	1338	1239	1159	1092	1036
18.0	1338	1239	1159	1092	1036
22.0	1338	1239	1159	1092	1036
26.0	1338	1239	1159	1092	1036
30.0	1338	1239	1159	1092	1036
34.0	1338	1239	1159	1092	1036
38.0	1317	1219	1140	1075	1020
42.0	1242	1150	1076	1014	962
46.0	1161	1075	1005	948	899
50.0	1074	995	930	877	832
54.0	982	909	851	802	761
58.0	886	820	767	723	686
62.0	785	726	679	641	608
66.0	680	629	589	555	527
70.0	572	529	495	467	443
74.0	461	426	399	376	357
78.0	347	322	301	284	269
82.0	233	215	201	190	180
86.0	117	108	101	95	90
90.0	0	0	0	0	0

4. THE MODEL

The model used to experimentally test the effectiveness of the AG scheme is based on the complete shallow water equations on a sphere given by

$$\frac{\partial(hu)}{\partial t} + \frac{1}{a \cos \phi} \left[ \frac{\partial(hu)}{\partial \lambda} + \frac{\partial(hu)v \cos \phi}{\partial \phi} \right] \quad (21)$$

$$- \left( f + \frac{u \tan \phi}{a} \right) h v + \frac{gh}{a \cos \phi} \frac{\partial h}{\partial \lambda} = 0$$

$$\frac{\partial(hv)}{\partial t} + \frac{1}{a \cos \phi} \left[ \frac{\partial(hv)}{\partial \lambda} + \frac{\partial(hv)v \cos \phi}{\partial \phi} \right] \quad (22)$$

$$+ \left( f + \frac{u \tan \phi}{a} \right) h v + \frac{gh}{a} \frac{\partial h}{\partial \phi} = 0$$

$$\frac{\partial h}{\partial t} + \frac{1}{a \cos \phi} \left[ \frac{\partial (hu)}{\partial \lambda} + \frac{\partial (hvcos\phi)}{\partial \phi} \right] = 0 \quad (23)$$

All variables are defined on a non-staggered grid with a 36x23 grid point domain (10° longitude X 8.18° latitude).

The model uses Fourier filtering of u,v, and h at every time step for latitudes  $|\phi| > 60$  deg. to inhibit the growth of the shorter waves near the poles. In addition, a 16th order Shapiro filter is applied to the field variables in both the zonal and meridional directions once every hour. With these filtering procedures, the total potential enstrophy remains quasi-constant for all stable runs in agreement with the results obtained by Kalnay and Hoitsma (1979). The model equations at the poles follow those of the GLAS 4th Order General Circulation Model (see Kalnay et al., 1977)

## 5. THE RESULTS

We performed three different model runs for our experiment. In each case a maximum allowable time step was determined. A scheme was considered unstable when the height field decreased by one order of magnitude. The first run (R1) consisted of updating the variables using the standard K0 scheme. The second run (R2) replaced the K0 scheme with the AG scheme in the continuity equation and in the pressure gradient terms in the momentum equation in order to increase the time step defined by the fast moving inertia gravity waves. The third run (R3) applied the AG scheme to the advective terms in the momentum equation as well. For all runs, the initial condition was a Rossby-Haurwitz wave of zonal wavenumber 1 following Phillips (1959). The mean height of the wave was 9079 m. Each run was integrated for a forecast time of 120 hours. Table (5) shows the maximum time step and the relative computing times for each run for which the scheme remained stable.

TABLE 5  
Experimental Results (Course Grid)

Model Run	Maximum Time Step	Rel. Comp. Time
R1	1000 seconds	1.000
R2	1350 seconds	0.933
R3	1400 seconds	0.936

## 6. CONCLUDING REMARKS

It can be seen that a 35% to 40% increase in the maximum allowable time step was obtained through application of the AG scheme. From the linear analysis in section (3), a gain of 20% could be expected using time steps calculated at  $\sim 60^\circ$ . Neither scheme was able to give the theoretical maximum. The overall improvement in the AG scheme found experimentally may be due to a better simulation of non-linear effects.

## REFERENCES

- Abarbanel, S., and D. Gottlieb, 1980: On improving the 2-4 two dimensional leap-frog scheme. SIAM - J. Sci. Stat. Comp., 1.
- Kalnay, E., A. Bayliss, and J. Storch, 1977: The 4th order GISS model of the global atmosphere. Cont. to Atmos. Phys., 50, 306-311.
- Kalnay, E., and D. Hoitsma, 1979: Documentation of the fourth order band model. NASA Tech. Memo. 80608.
- Kreiss, H. O., and J. Olliger, 1973: Method for the approximation of time dependent problems. GARP Publ. Ser. No. 10.
- Phillips, N. A., 1959: Numerical integration of the primitive equations on the hemisphere. Mon. Wea. Rev., 87, 333-345.
- Wilson, J. C., 1978: A note on the leap frog schemes in any number of space variables. J. Comp. Phys., 28, 433-436.

D. ATMOSPHERIC DYNAMICS AND  
DIAGNOSTIC STUDIES

**PRECEDING PAGE BLANK NOT FILMED**

## A MODEL TO DETERMINE OPEN OR CLOSED CELLULAR CONVECTION

H. M. Helfand and E. Kalnay

A simple mechanism is proposed to explain the observed presence in the atmosphere of open or closed cellular convection. If convection is produced by cooling concentrated near the top of the cloud layer, as in radiative cooling of stratus clouds, it develops strong descending currents which are compensated by weak ascent over most of the horizontal area, and closed cells result. Conversely, heating concentrated near the bottom of a layer, as when an air mass is heated by warm water, results in strong ascending currents compensated by weak descent over most of the area, or open cells. This mechanism, unlike that of Hubert (1966), does not invoke vertical variations of the eddy diffusion coefficients, and is similar to the one suggested by Stommel (1962) to explain the smallness of the oceans' sinking regions.

This mechanism is studied numerically by means of a two-dimensional, non-linear Boussinesq model. An internal heat source-sink destabilizes a layer of fluid adding no net heating. A steady state is attained. The horizontal configuration of the flow depends on the vertical distribution of the internal heating. Thus, when (a) internal cooling is concentrated near the top of the domain, (b) internal heating is concentrated near the lower surface, or (c) the internal heating profile is antisymmetric about the mid-plane of the domain (see Fig. 1), then the resulting flow pattern is respectively (a) open, (b) closed, or (c) horizontally symmetric (see Fig. 2). The mean lapse rate is unstable in the upper half of the fluid and stable in its lower half in the open case, stable in the upper half of the fluid and unstable in its lower half in the closed case, and unstable throughout in the symmetric case.

The numerical results indicate that the width of the plume produced by the cooling in the upper part of the layer or by the heating in the lower part of the layer is largely independent of the degree of vertical asymmetry of the internal heating profile (see Fig. 3). On the other hand, the compensating motion occupies a region which becomes broader as the heating profile becomes more asymmetric. In other words, if cooling is very concentrated near the top of the layer with heating spread throughout the rest of the region or if heating is very concentrated near the bottom with cooling spread throughout, the generated closed or open cells have an aspect ratio much smaller than 1. These results may help explain the small aspect ratio observed in atmospheric convection.

## REFERENCES

- Hubert, L. F., 1966: Mesoscale cellular convection. Meteor. Satellites Lab., NOAA Rept. No. 37, Washington, DC, 68 pp.
- Stommel, H., 1962: On the smallness of sinking regions in the ocean. Proc. Natl. Acad. Sci., 48, 766-772.

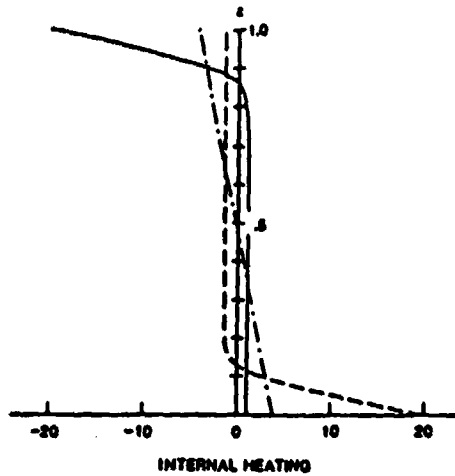
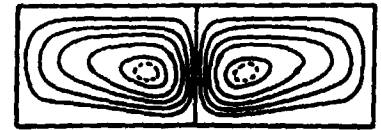
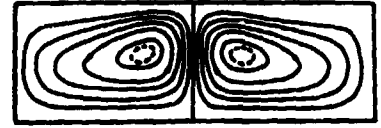


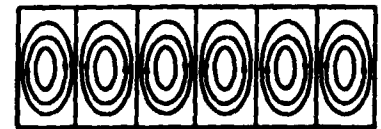
Fig. 1



(a)

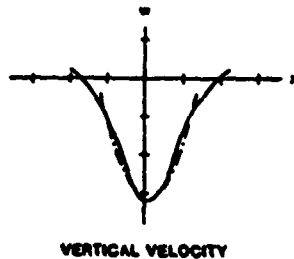


(b)



(c)

Fig. 2



VERTICAL VELOCITY

Fig. 3

- Fig. 1 Internal heating distribution (in non-dimensional units) as a function of non-dimensional height. The solid line represents the case of concentrated cooling near the top. The dashed line represents the case of concentrated heating near the lower surface. The dashed-dotted line represents the case of heating antisymmetric about the mid-plane  $z = 0.5$ . All of the profiles integrate to zero. The positive area under each curve (and the negative area, as well) is the same.
- Fig. 2 The steady-state stream functions for the cases of (a) internal cooling concentrated near the top, (b) internal heating concentrated near the lower surface, and (c) antisymmetric internal heating. The cellular convective patterns are, respectively, (a) closed, (b) open, and (c) horizontally symmetric.
- Fig. 3 The horizontal profile of vertical velocity within the downdraft for the case of internal cooling concentrated at the top (solid line) and antisymmetric internal heating (dashed-dotted line).

## LARGE AMPLITUDE STATIONARY ROSSBY WAVES IN THE SOUTHERN HEMISPHERE

E. Kalnay and M. Halem

## 1. INTRODUCTION

The First GARP Global Experiment (FGGE) has provided the most extensive atmospheric data set ever compiled. An analysis of the atmospheric structure during the first Special Observing Period (SOP-1, January 5th, 1979 to March 5th, 1979) was completed using the Goddard Laboratory for Atmospheric Sciences (GLAS) Analysis and Assimilation System. Preliminary results from this analysis were reported in Kalnay-Rivas *et al.*, 1980, where we pointed out the existence of large amplitude, short wavelength stationary waves in the lee of South America and Australia during the first 16 days of SOP-1.

The purpose of this paper is to present further observational evidence of the characteristics of these waves during the complete SOP-1, and discuss their possible origin. The observed structure and evolution of the waves are presented in Section 2. Section 3 contains a brief discussion of the possible origin of the stationary waves.

## 2. OBSERVATIONAL EVIDENCE OF STATIONARY ROSSBY WAVES

One can expect significant differences in the structure and distribution of stationary waves in the Northern and Southern Hemispheres. In the Northern Hemisphere, the geographical distribution of orographic and thermal forcing occurs on very large scales. Therefore it is not surprising that stationary waves have most of their energy in planetary wave numbers 1 to 3 (Charney and Eliassen, 1949; Smagorinsky, 1953). The Southern Hemisphere, on the other hand, is basically a homogeneous domain, with smaller isolated regions of land and sea contrast (South America, southern Africa and Australia) and one narrow major orographic chain (the Andes). No counterpart of the strong heating by the Gulf and Kuroshio western currents (Geller and Avery, 1978) exists in the Southern Hemisphere.

Van Loon and Jerne (1972) and Van Loon *et al.* (1973) studied the standing (stationary) waves in the Southern Hemisphere and compared them with those of the Northern Hemisphere. They found that at 50°S, planetary wave numbers 1 and 3 contain 99% of the variance of the annual mean, and contrary to their Northern Hemisphere counterpart, are essentially barotropic. As in the Northern Hemisphere, they did not find significant stationary waves with synoptic scales.

A very different picture emerges when one examines the FGGE data for the Special Observing Period. Figures 1a and 1b present the 300 mb meridional velocity  $v$  averaged over two consecutive 30 day periods, Jan. 5-Feb. 3 and Feb. 4-Mar. 5, 1979, respectively. In the Northern Hemisphere we observe for both months, as expected, the presence of planetary scale stationary waves. However, in the Southern Hemisphere, the January mean shows large amplitude synoptic scale waves immediately upstream and in the lee of the Andes, and weaker waves over Australia and in the South Pacific Ocean. In February, the synoptic stationary waves have disappeared and the circulation is more in

agreement with the results of van Loon et al. (1973), i.e., very weak stationary waves of planetary scale.

The amplitude of the January stationary waves in the South American region is remarkable ( $15 \text{ m sec}^{-1}$  in the mean meridional wind), especially when one considers that this is a summer, oceanic hemisphere. It is also interesting that the mean amplitude of transient waves (not shown here) is about 50% stronger in February, when the stationary waves are not present.

The January waves appear to have a virtually equivalent barotropic structure. They are barely apparent at surface levels, with an anomalous trough in the subtropical South Atlantic center of high pressure. Their amplitude increases with height, and they peak near the tropopause level. In the meridional direction, they occur in the  $20^\circ$  to  $40^\circ$  latitude band.

The wavelength of the January stationary waves over South America is about  $50^\circ$  longitude, or zonal wavenumber 7 (Fig. 2a). Their position with respect to the Andes is also anomalous. A very strong ridge appears centered at a longitude of  $70^\circ\text{W}$ . As a result, the flow over the Andes is, for the most part, from the North. On the other hand, the weak ridge upstream and trough downstream of the Andes that appears in February (Fig. 2b) is typical of the winter circulation (Palmen and Newton, 1969).

The orientation of the waves is from the NW to SE in the Southern Hemisphere. This can be better observed in the map of absolute vorticity (Figures 3a and 3b) which also indicate the regions with significant convective precipitation according to the assimilation model. It should be noted in the January map that the three major bands convective precipitation over the oceans (to the southeast of Indonesia and Brazil) coincide with regions of maximum advection of cyclonic vorticity. The orientation of the waves implies that they transport westerly momentum into the "roaring forties" latitudes.

### 3. DISCUSSION

We have shown the existence of synoptic scale stationary waves in the Southern Hemisphere for the month of January 1979. Confirming evidence comes from the examination of TIROS-N cloud pictures, indicating the permanent presence of a low level cyclonic vortex during the first two weeks of FGGE SOP-1 at about  $30^\circ\text{S}$ ,  $40^\circ\text{W}$ , in agreement with our analysis. The presence of the stationary waves over South America is also clear in the lower stratospheric temperature waves observed by Stanford and Short (1981). Other analyses, like the British Met. Office and ECMWF are also in agreement. That such waves are frequently present during periods of several weeks is very clear from the well known satellite-observed cloud and precipitation bands in the Southern Pacific and Atlantic Oceans (Rao et al., 1976).

The orientation and wavelength of these stationary Rossby waves appears similar to the numerical results obtained by Grose and Hoskins (1979) with a barotropic model forced by orography. The waves resemble in particular the solution forced by small scale topography at  $30^\circ$  latitude. In their results, higher latitude forcing generated more zonally oriented bands.

Several characteristics of the Rossby stationary waves should be explained: Why are they relatively short? Why do they occur at subtropical latitudes? Why aren't they observed in longer time averages (seasonal to interannual). To answer these questions we may be guided by several simple considerations:

a) The scale of the forcing is very important. This may be seen in Figure 4, which presents the solution of the 1-dimensional steady state barotropic vorticity equation on a  $\beta$ -plane, forced by a "chapeau"-like mountain. When the mountain is of large scale (top panel) the response is primarily of the scale of the forcing, whereas when the forcing occurs in a small isolated region (bottom panel), the response occurs in the form of a train of stationary Rossby waves, in the lee of the mountain. This agrees well with the results obtained by Kalnay-Rivas and Merkiné (1981). The first solution may be associated with the Northern Hemisphere, where forcing, both thermal and orographic, occurs on planetary scales. The second solution is closer to the Southern Hemisphere, with forcing in relatively small isolated regions.

b) Short stationary waves can occur in sub-tropical regions where the vertically-averaged zonal flow is positive but small as may be inferred from the frequency dispersion relationship of Rossby waves. The region where this condition is likely to hold is in the subtropical summer hemisphere, with weak easterlies at low levels and westerlies in upper levels. Because of their dependence on the zonal flow, the waves are not so apparent in longer term averages.

c) The strong correlation between oceanic convective bands originating in Brazil and the Indonesian convergence zones, and the monthly averaged regions of cyclonic vorticity advection associated with the stationary waves, suggest that latent heat release may be the cause of their large amplitude. It is possible that a CISK-type of instability occurs, in which the stationary Rossby waves determine the regions of low level convergence and ascending motion, and the resulting convective activity amplifies the stationary waves. Longer stationary waves occurring at higher latitudes where the vertically-averaged zonal wind is stronger, would not be as effective in producing convective precipitation. The fact that the waves appear to be equivalent barotropic also suggests that they are not a result of baroclinic instability. Sea surface temperature anomalies may also play a role if their phase is favorable for intensification of the waves through a CISK-mechanism.

d) The large amplitude stationary flow over the Andes is poleward, rather than equatorward as required in order to generate perturbation kinetic energy (Kalnay-Rivas and Merkiné, 1981, and Figure 4). This also suggests that orography may not be generating the waves, but rather anchoring them at preferred regions.

e) The extent of the tropical easterlies is smaller in January than in February 1979. In January, at 500 mb, the westerlies were present throughout most of the tropical Pacific, with speeds of up to  $10 \text{ m sec}^{-1}$  NE of Australia. In February there were easterlies throughout most of the  $20^{\circ}\text{S}$  to  $15^{\circ}\text{N}$  latitude band. The release of latent heat, in the Pacific convergence zone which according to the assimilation model is maximum at 500 mb, was stronger during January than during February. One may speculate that the reduced extent of easterlies at level of maximum release of latent heat was more favorable (Charney, 1973, p. 293) for the propagation of waves originated in the Indonesian-South Pacific

convergence zone into the South American domain. However, it is not clear whether this had an effect on the generation of waves in the South American region.

#### 4. CONCLUSION

We have pointed out the existence of large amplitude, short wavelength stationary Rossby waves in the Southern Hemisphere during the month of January 1979. They appear to be associated with observed stationary cloud bands in the South Atlantic and Pacific Oceans. Although we suggest that they attain their amplitude through a CISK mechanism, much further study is necessary to explain their origin and their role in the general circulation of the Southern Hemisphere.

#### REFERENCES

- Charney, J. G., 1973: Planetary fluid dynamics. Dynamic Meteorology, Morel, Editor. D. Reidel, Dordrecht, Holland.
- Charney, J. G., and A. Eliassen, 1949: A numerical method for predicting the perturbations on the Middle latitude westerlies. Tellus, 1, 38-54.
- Geller, M. A., and S. K. Avery, 1978: Northern Hemisphere distributions of diabatic heating in the troposphere. Mon. Wea. Rev., 106, 629-636.
- Grose, W. L. and B. J. Hoskins, 1979: On the influence of orography on large-scale atmospheric flow. J. Atmos. Sci. 36, 223-234
- Kalnay-Rivas, E., W. Baker, M. Halem, R. Atlas, and D. Edlmann, 1980: GLAS experiments with FGGE II-b data. Proceedings of the International Conference on Preliminary FGGE Results. Bergen, Norway, June 1980.
- Kalnay-Rivas, E., and L. Merkinė, 1981: A simple mechanism for blocking. J. Atmos. Sci., accepted for publication.
- Palmen, E. and C. W. Newton, 1969: Atmospheric Circulation Systems. Academic Press, New York.
- Rao, M. S. V., W. V. Abott III, and J. S. Theon, 1976: Satellite-derived global oceanic rainfall atlas (1973 and 1974). NASA SP-410, NASA, Washington, D. C.
- Smagorinsky, J., 1953: The dynamical influence of large-scale heat sources and sinks on the quasi-stationary mean motions of the atmosphere. Quart. J. Roy. Meteor. Soc., 79, 342-366.
- Stanford, J. L. and D. A. Short, 1981: Evidence for wave-like anomalies with short meridional and large zonal scales in the lower stratospheric temperature field. J. Atmos. Sci., 38, in press.
- Van Loon, H. and R. L. Jenne, 1972: The zonal harmonic standing waves in the Southern Hemisphere. J. Geoph. R., 77, 3846-3855.

Van Loon, H., R. L. Jenne and K. Labitzke, 1973. Zonal harmonic standing waves.  
J. Geoph. R., 78, 4463-4471.

#### ACKNOWLEDGEMENTS

It is a pleasure to acknowledge useful discussions with Jan and Julia Paegle, L. Merkin, Y. Mintz and D. Duffy. Particular acknowledgement is extended to Wayman Baker for providing the analysis scheme to study these waves. Joan Wentz typed the manuscript, and Laura Rumburg drafted the figures.

Fig. 1a. 300 mb MEAN MERIDIONAL WIND COMPONENT (JAN)

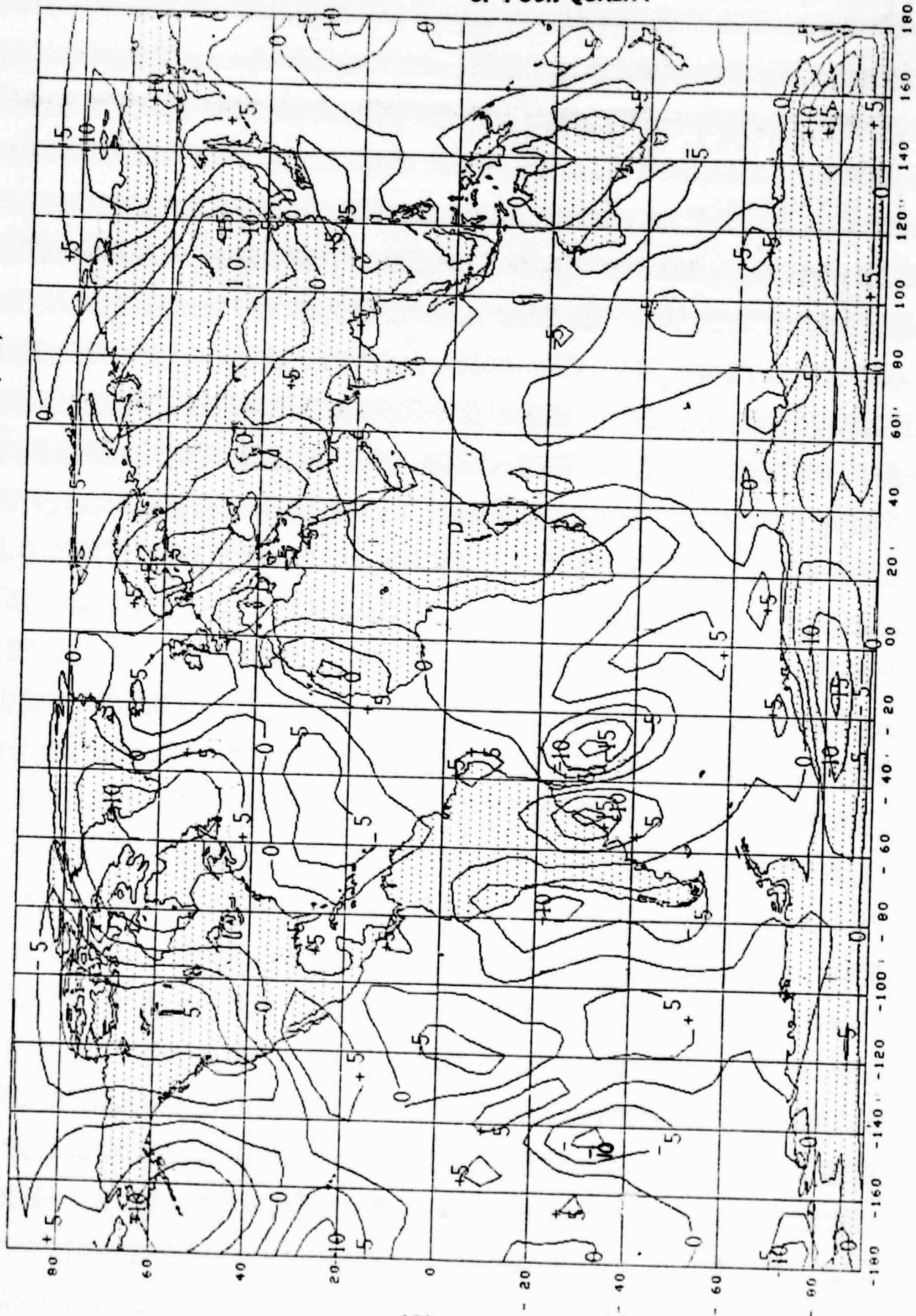
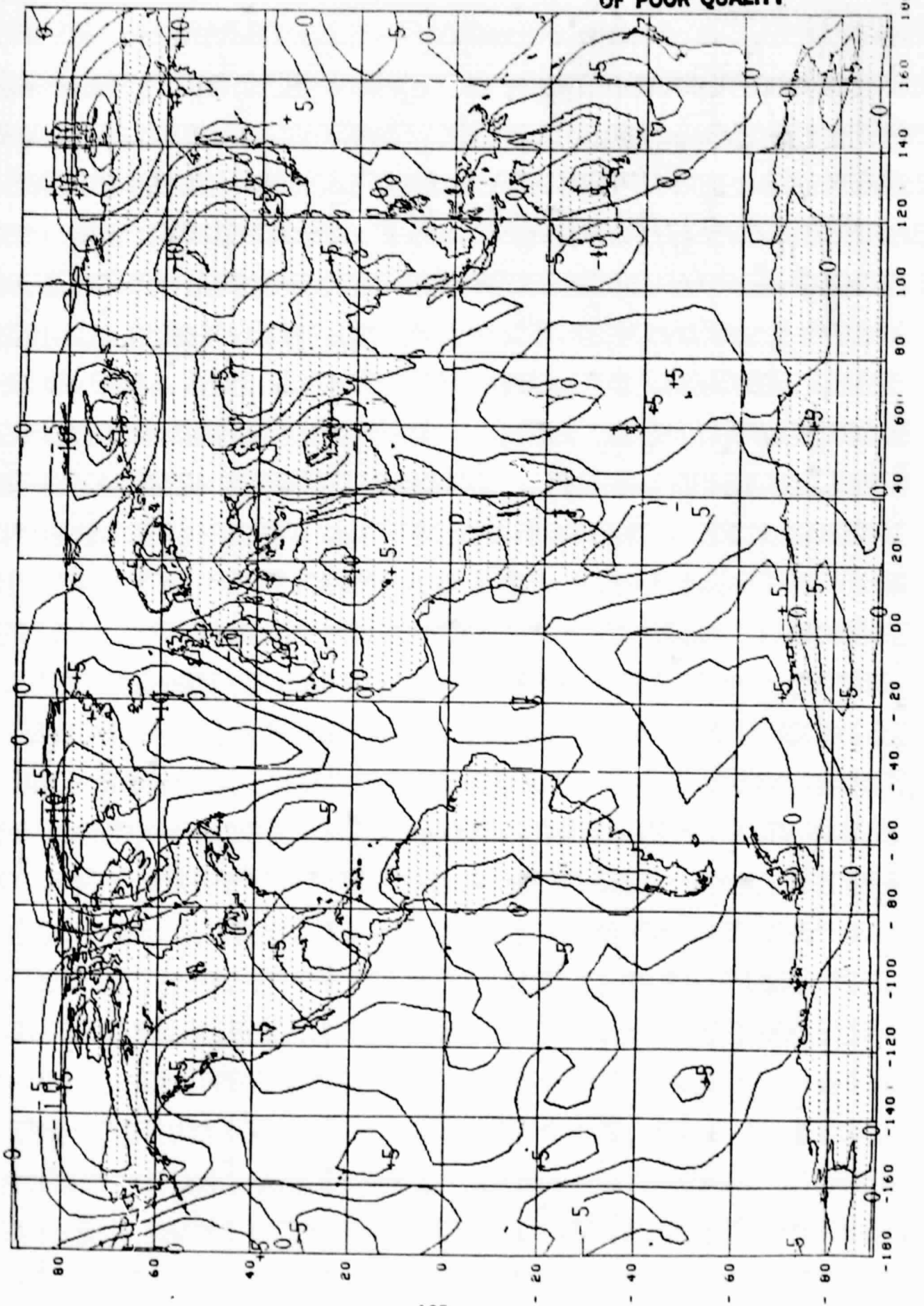


Fig. 1b. 300 mb MEAN MERIDIONAL WIND COMPONENT (FEB)



ORIGINAL PAGE IS  
OF POOR QUALITY

Fig. 2a. 300 mb MEAN GEOPOTENTIAL HEIGHT (JAN)

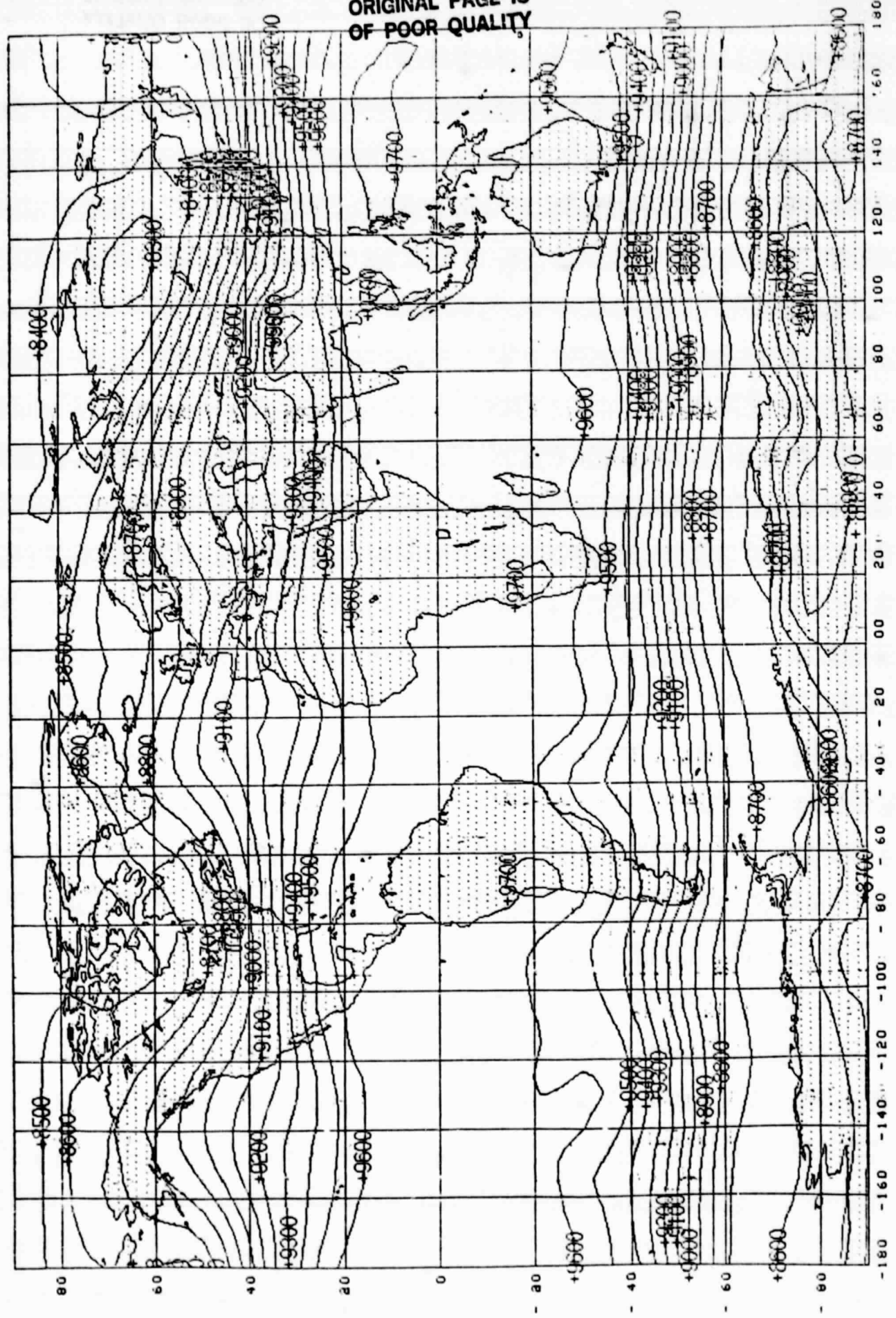
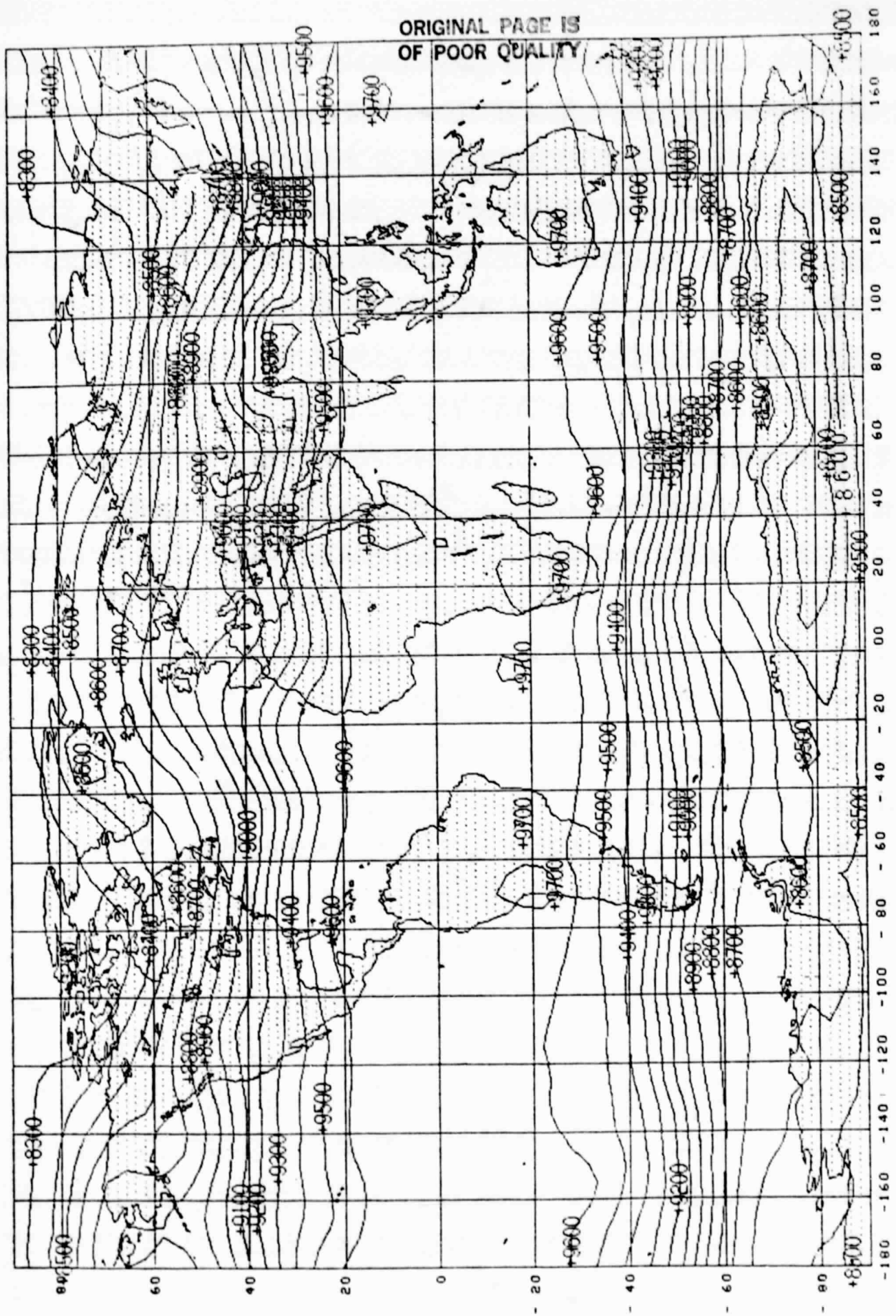
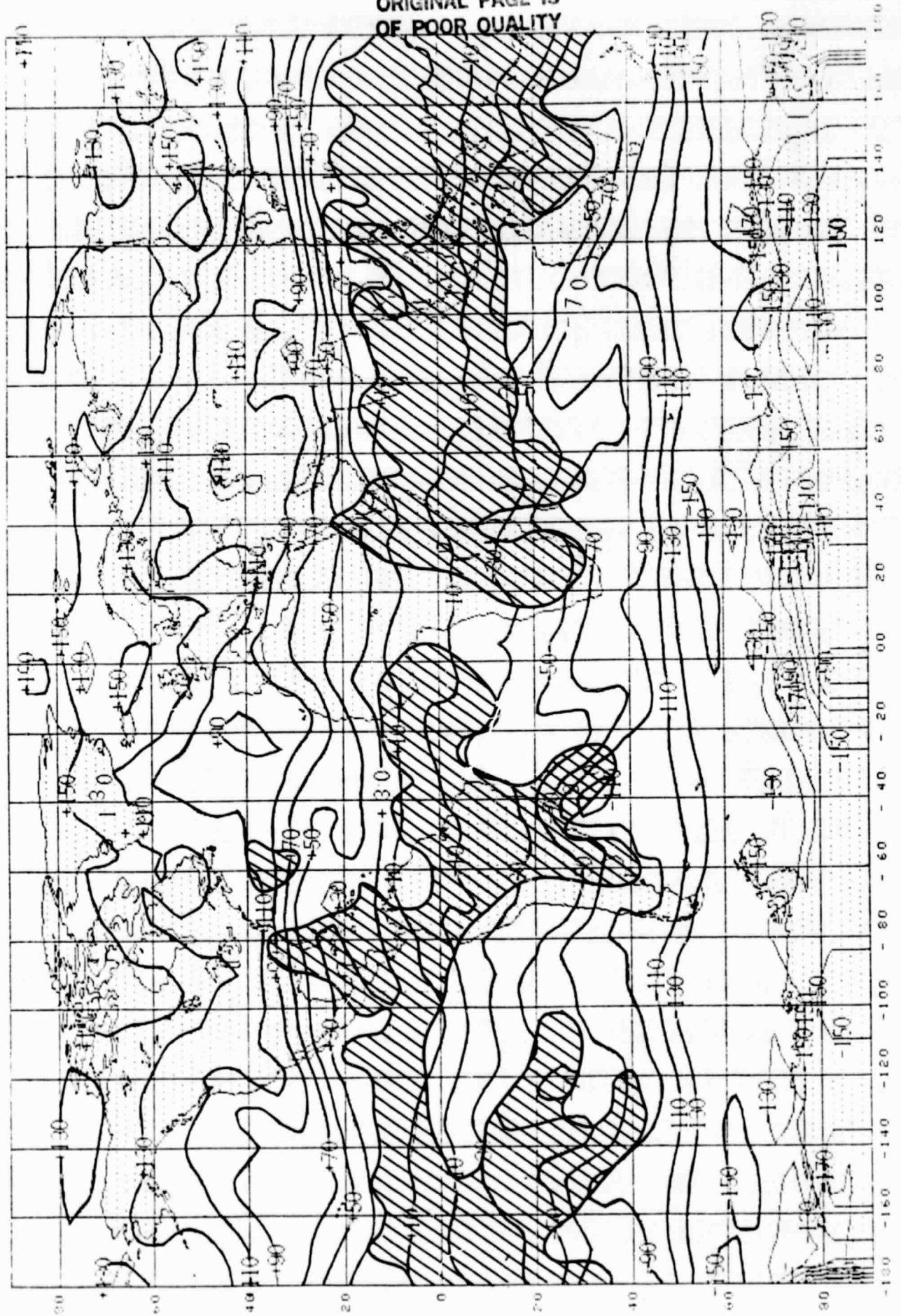


Fig. 2b. 300 mb MEAN GEOPOTENTIAL HEIGHT (FEB)



ORIGINAL PAGE IS  
OF POOR QUALITY

Fig. 3a. 300 mb MEAN ABSOLUTE VORTICITY (JAN)  
(HATCHED REGION DENOTES CONVECTIVE PRECIPITATION LARGER THAN 5mm/day)



ORIGINAL PAGE IS  
OF POOR QUALITY

Fig. 3b. 300 mb MEAN ABSOLUTE VORTICITY (FEB)  
(HATCHED REGION DENOTES CONVECTIVE PRECIPITATION LARGER THAN 5mm/day)

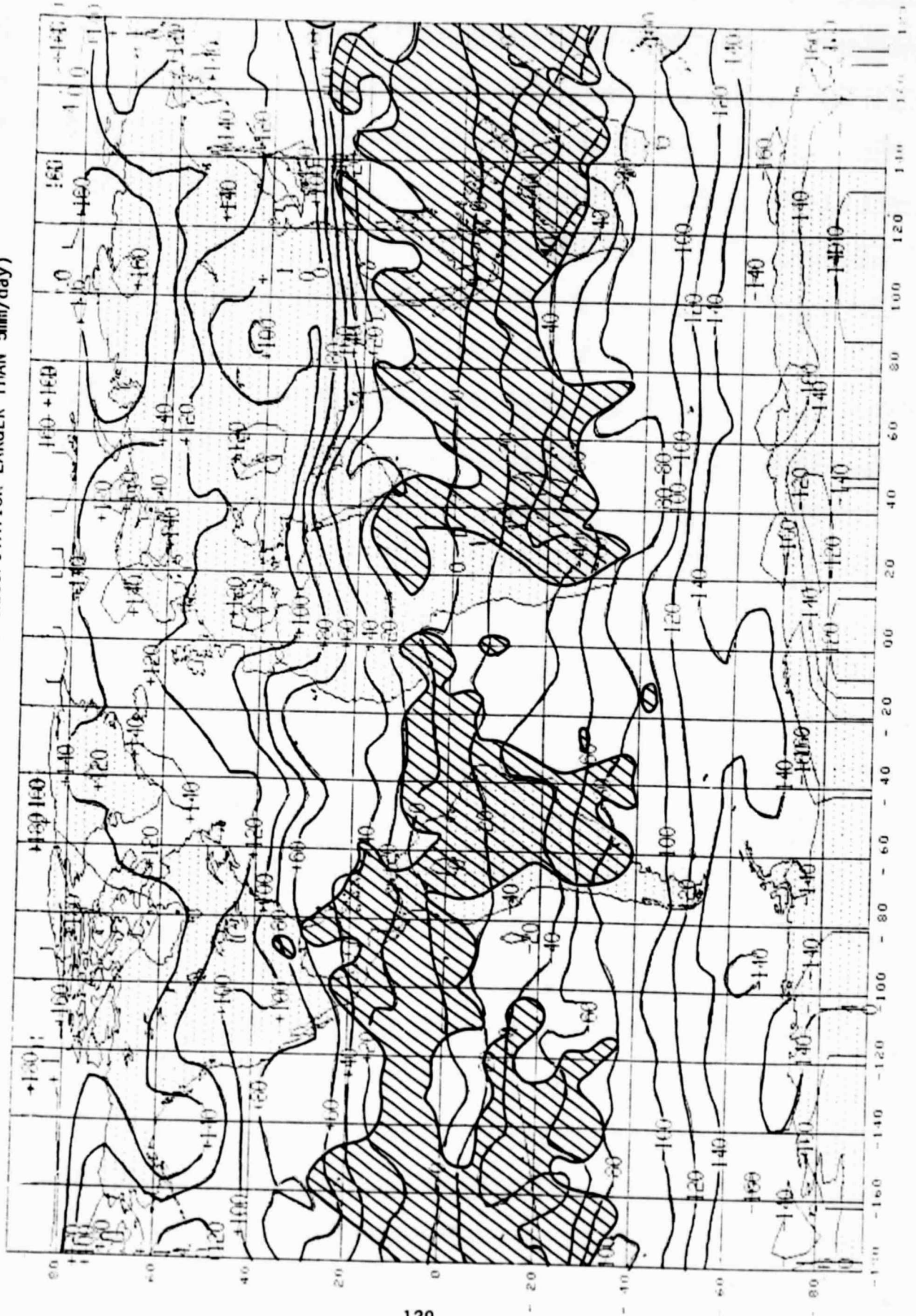
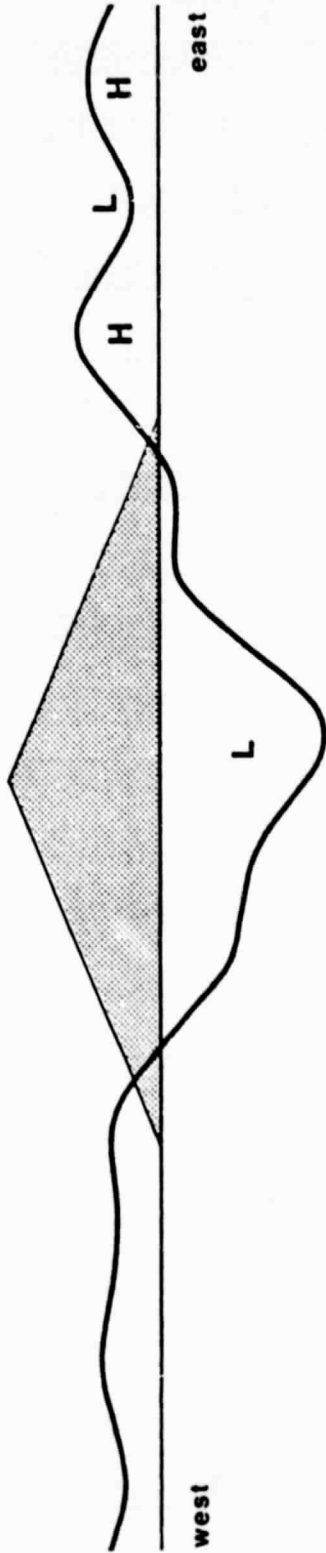
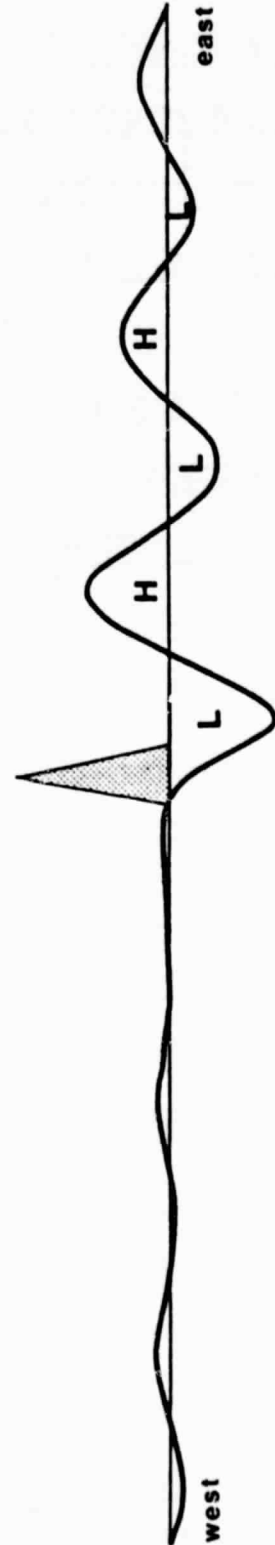


Fig. 4. SOLUTION OF THE BAROTROPIC VORTICITY EQUATION FORCED BY ISOLATED OROGRAPHY

a. Planetary scale forcing.



b. Small scale forcing.



2001

MULTIPLE EQUILIBRIA AND VACILLATION ON THE SPHERE,  
WITH APPLICATION TO BLOCKING<sup>1</sup>

B. Legras<sup>2</sup> and M. Ghil<sup>3</sup>

We study the barotropic vorticity equation on the sphere, including forcing and dissipation. A simplified orography, symmetric around the Equator, and a forcing which corresponds to a mid-latitude jet is used. The non-dimensional parameters of the problem are a Rossby number of the forcing  $R_0$  and a dissipation coefficient  $\alpha$ .

The model is discretized in spherical harmonics, with a variable triangular truncation. Most of the study retains 25 real modes, while both lower and higher truncation is used in some experiments.

Multiple equilibrium solutions obtain for the same value of  $(R_0, \alpha)$ ; among these are low-index and split-jet, blocked flows. The dependence of equilibria on  $(R_0, \alpha)$  is studied, along with their stability and bifurcation properties.

Stable periodic, as well as aperiodic, vacillatory solutions are also obtained. The change in the character of solutions and in their stability is associated with foldings of the stationary solution sheets in parameter space. In the aperiodic case, solutions exhibit persistence periods longer than two weeks, as well as irregular, strongly oscillatory behavior. We also study the frequency spectrum of solutions as a function of  $(R_0, \alpha)$ .

Both equilibria and vacillatory solutions seem to be structurally stable with respect to the number of modes used in the discretization.

---

<sup>1</sup> This work was presented at the 3rd Conference on Atmospheric and Oceanic Waves and Stability of the Amer. Meteor. Soc., 19-23 January 1981, San Diego, CA. It will also be presented at the IAMAP Symposium on the Dynamics of the Atmospheric General Circulation, 3-7 August 1981, Reading, England.

<sup>2</sup> Laboratoire de Meteorologie Dynamique, Centre National de la Recherche Scientifique, 75231 Paris, Cedex 05, France.

<sup>3</sup> Courant Institute of Mathematical Sciences, New York University, New York, NY 10012, U.S.A.

THE ROLE OF ZONALLY ASYMMETRIC HEATING IN THE VERTICAL AND TEMPORAL STRUCTURE  
OF THE GLOBAL SCALE FLOW FIELDS DURING FGGE SOP-1<sup>1</sup>

J. Paegle<sup>2</sup>, E. Kalnay, and W. E. Baker

1. INTRODUCTION

The global scale structure of atmospheric flow is best documented on time scales longer than a few days. Theoretical and observational studies of ultra-long waves have emphasized forcing due to global scale variations of topography and surface heat flux, possibly interacting with baroclinically unstable or vertically refracting basic flows (Charney and Eliassen, 1949; Smagorinsky, 1953; Bates, 1977; Grose and Hoskins, 1979; Holopainen, 1970; Lindzen and Tung, 1979, and many others). Additionally there have been studies of the long term effects of tropical heating gradients (Ramage, 1968; Webster, 1972; Dickinson, 1971; Rowntree, 1976; Julian and Chervin, 1978, Krishnamurti et al., 1973, and others).

Although these studies have produced a number of mechanistic explanations of period wave generation, it is probably fair to conclude that our understanding has remained insufficient to produce uniformly accurate deterministic predictions beyond a few days for any space scales, including global scales. One reason for this may be that until the FGGE year, observational evidence about completely global scale short term variations was rather incomplete. Consequently, it has been difficult to verify theories of short term variations of global scale waves. Indeed, virtually all of the above mentioned theories that have quantitative form either emphasize local mid-latitude structure or long time (or time mean) interactions with the tropics.

The present paper documents our analyses of SOP-1 data in terms of global scale spherical harmonics, with emphasis upon weekly transitions.

2. APPROACH

Level II-b observed data have been analyzed (Baker, 1981) to generate a set of level III-b data on a 4° x 5° lat-lon grid. The 4th order GLAS GCM (Kalnay-Rivas et al., 1977; Kalnay-Rivas et al., 1979) served as the assimilation model. From this data set we have computed the vorticity ( $\zeta$ ) and the divergence ( $\delta$ ) from

$$\zeta = \mathbf{k} \cdot \nabla \times \mathbf{V} \quad (1)$$

$$\delta = \nabla \cdot \mathbf{V} \quad (2)$$

---

<sup>1</sup> Published in Condensed Papers and Meeting Report: International Conference on Early Results of FGGE and Large-Scale Aspects of its Monsoon Experiments, Jan. 12-17, 1981; Tallahassee, Florida. Published by the World Meteorological Organization, Geneva, Switzerland.

<sup>2</sup> On leave from the Dept. of Meteorology, University of Utah.

where  $V$  is the horizontal wind,  $\nabla$  is the finite difference gradient operator and  $1K$  is the unit vertical vector. The vorticity and divergence can be re-written in terms of a streamfunction ( $\psi$ ) and the velocity potential ( $\chi$ )

$$\zeta = \nabla^2 \psi \quad (3)$$

$$\delta = \nabla^2 \chi \quad (4)$$

These equations have been solved for  $\psi$  and  $\chi$  employing a technique described by Paegle and Tomlinson (1975). The algorithm gives the exact solution of the algebraic system of equations arising from the finite difference approximation of the Poisson equation.

Fields of  $\psi$ ,  $\chi$  and geopotential height ( $Z$ ) were subsequently spectrally decomposed as:

$$\psi = \sum_{n=0}^N \sum_{|m| < n} \psi_n^m P_n^m(\phi, \lambda) \quad (5)$$

$$\chi = \sum_{n=0}^N \sum_{|m| < n} \chi_n^m P_n^m(\phi, \lambda) \quad (6)$$

$$Z = \sum_{n=0}^N \sum_{|m| < n} Z_n^m P_n^m(\phi, \lambda) \quad (7)$$

where  $\psi_n^m$ ,  $\chi_n^m$ ,  $Z_n^m$  are amplitudes of the spherical harmonics ( $P_n^m$ ), of degree  $n$ , order  $m$ .

### 3. INDIVIDUAL MODES

Fig. 1 presents  $Z_2^0$  as a function of pressure level for a 2 day period starting at 0Z, January 28.  $Z_2^0$  is the amplitude of a zonal harmonic possessing 3 nodal latitudes between the poles, but no longitudinal variation. In general, within the tropics, the low pressure belt at the surface reverses to a high pressure belt at high levels (because of the relative warmth of the tropical zone). In mid-latitudes, however, the zonally averaged pressure generally decreases poleward at all levels. The fact that  $Z_2^0$  maintains the same sign at all tropospheric levels suggests that the mid-latitude structure projects more amplitude upon this zonal harmonic than does the vertically reversing tropical structure.

A rather different conclusion holds for the  $Z_3^3$  mode (Fig. 2). This model represents a field with three waves on each latitude circle and latitudinal nodes only at the poles. The complex amplitude of this mode reverses almost completely with height. This vertical variation is more symptomatic of monsoonal patterns (possessing low pressure at low levels and high pressure at high levels) than it is of typical mid-latitude waves (which generally display only mild vertical phase tilts or nearly equivalent barotropic vertical structure, et. Paegle et al., 1979).

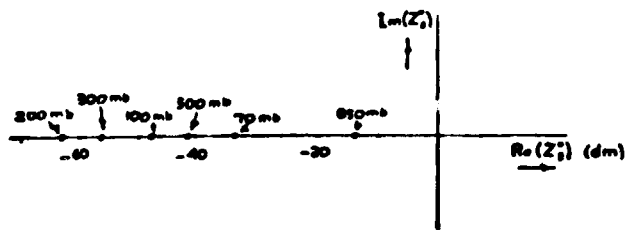


Figure 1. The amplitude of the zonal height harmonic  $Z_2^0$ . It is a real quantity because this mode has no longitudinal variation.

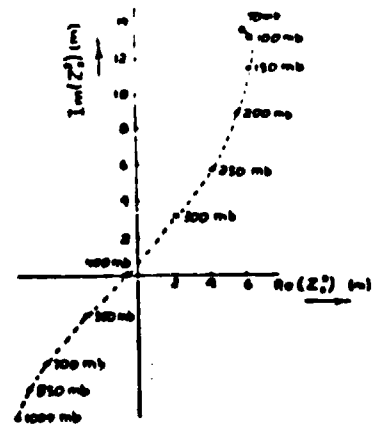


Figure 2. The complex amplitude of the height harmonic  $Z_3^0$ .

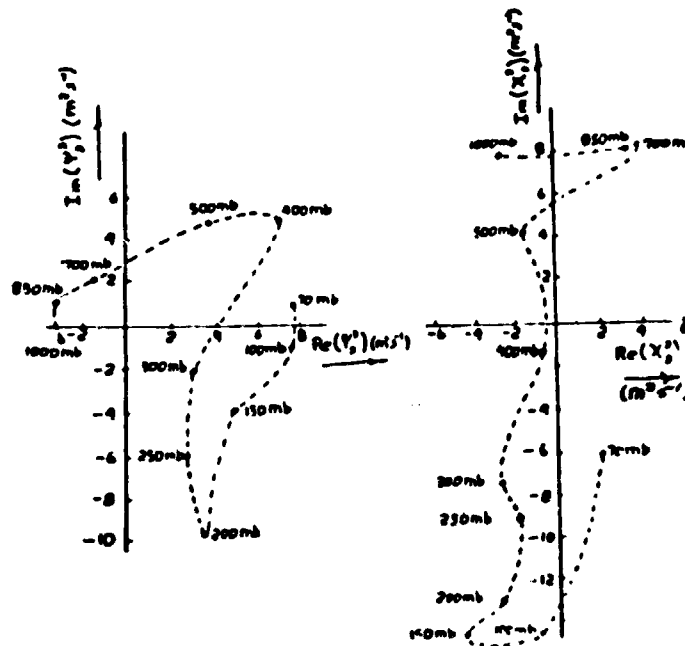


Figure 3. Complex amplitude of mode  $\psi_3^3$  of the streamfunction (left) and of mode  $X_3^3$  of the velocity potential (right). Each unit represents  $10^3 \text{ m}^2/\text{s}^2$ .

Although an individual spherical harmonic of the height field has no direct physical relation to an individual spherical harmonic of the divergence and vorticity fields, some of the characteristics of  $Z_3^3$  are also evident in  $\psi_3^3$  and  $X_3^3$ , (Fig. 3). Each of these also reverses with height within the troposphere. Furthermore, both maximize in the upper troposphere where  $X_3^3$  is about 50% larger than  $\psi_3^3$ . This means that the divergence is larger than the vorticity for this mode<sup>3</sup> at this level and time.

These diagrams are representative of much of the SOP 1 data that we have examined. The planetary modes with increasing latitudinal structure tend to tilt only slightly with height in the troposphere, or to be nearly equivalent barotropic. Low order modes retaining east-west structure and latitudinal nodes only at the poles are strongly divergent and height reversing.

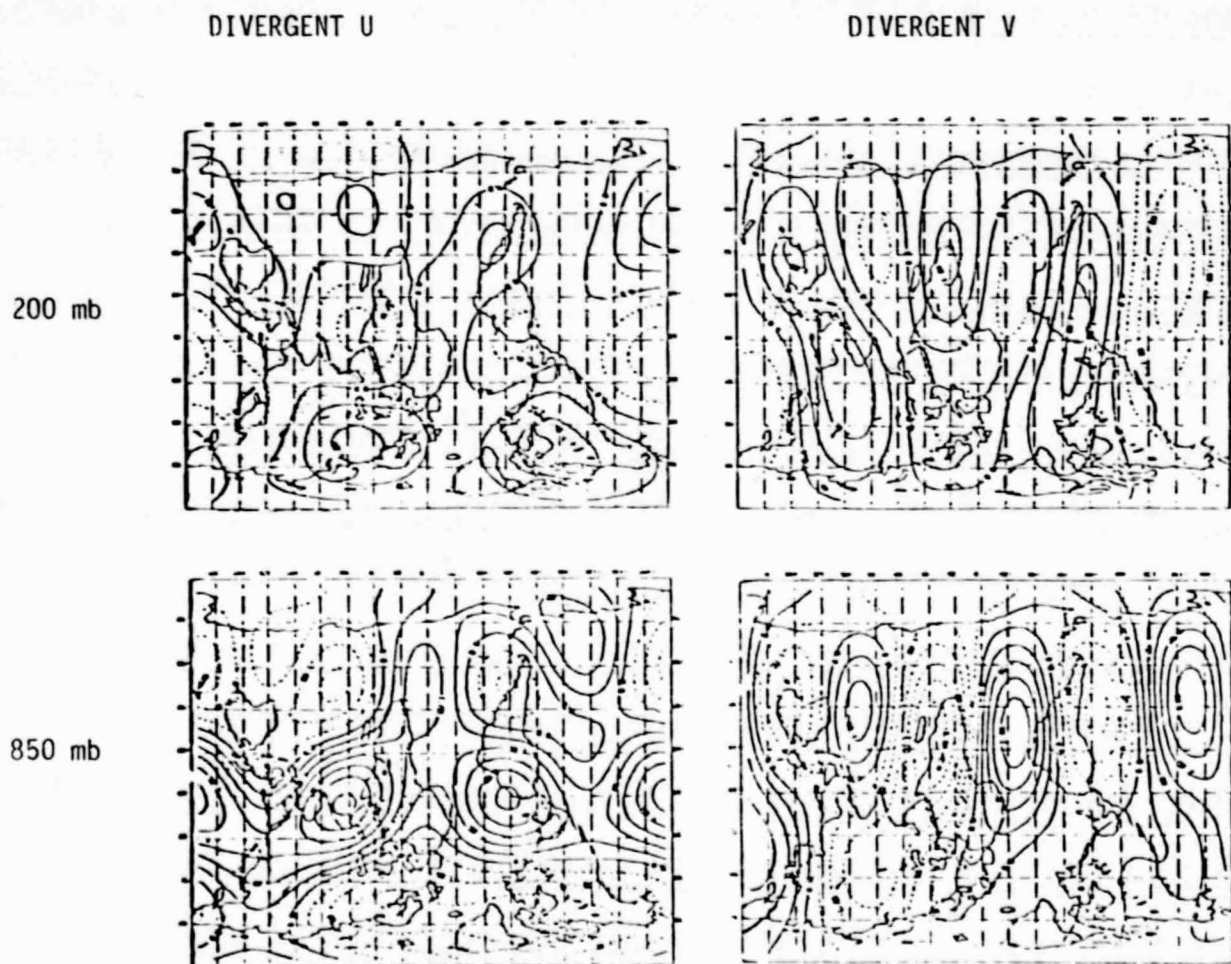


Figure 4. Divergent velocity components for the planetary scale modes, averaged over the 6 day period beginning 0Z, January 28, and ending 18Z, February 2. The isoline interval is .5 m/s, and negative values are dashed.

#### 4. HIGHLY TRUNCATED FIELDS

Highly truncated sums of the rotational and divergent winds (obtained from truncated sums of  $\psi$  and  $\chi$ ) exhibit an east-west structure that also tends to reverse with height. Figs 4 and 5 display 6 day average wind fields truncated by choosing  $N=4$ . Peak zonal winds to this truncation are about 30 m/s and are almost entirely rotational. Meridional winds, obtained by summing the rotational and divergent components, peak at about 6 m/s and the divergent component is about 50% of the rotational component.

Thus, while the zonal flows are essentially rotational to this truncation, the distribution of meridional meanders is significantly impacted by the divergent flow field, especially in the upper troposphere. Additionally, the rotational wind field itself retains a markedly monsoonal character. In particular, the southerlies in the rotational meridional flow reverse to northerlies in height, and the maxima of the 200 mb zonal rotational flow are generally far removed from the 850 mb maxima.

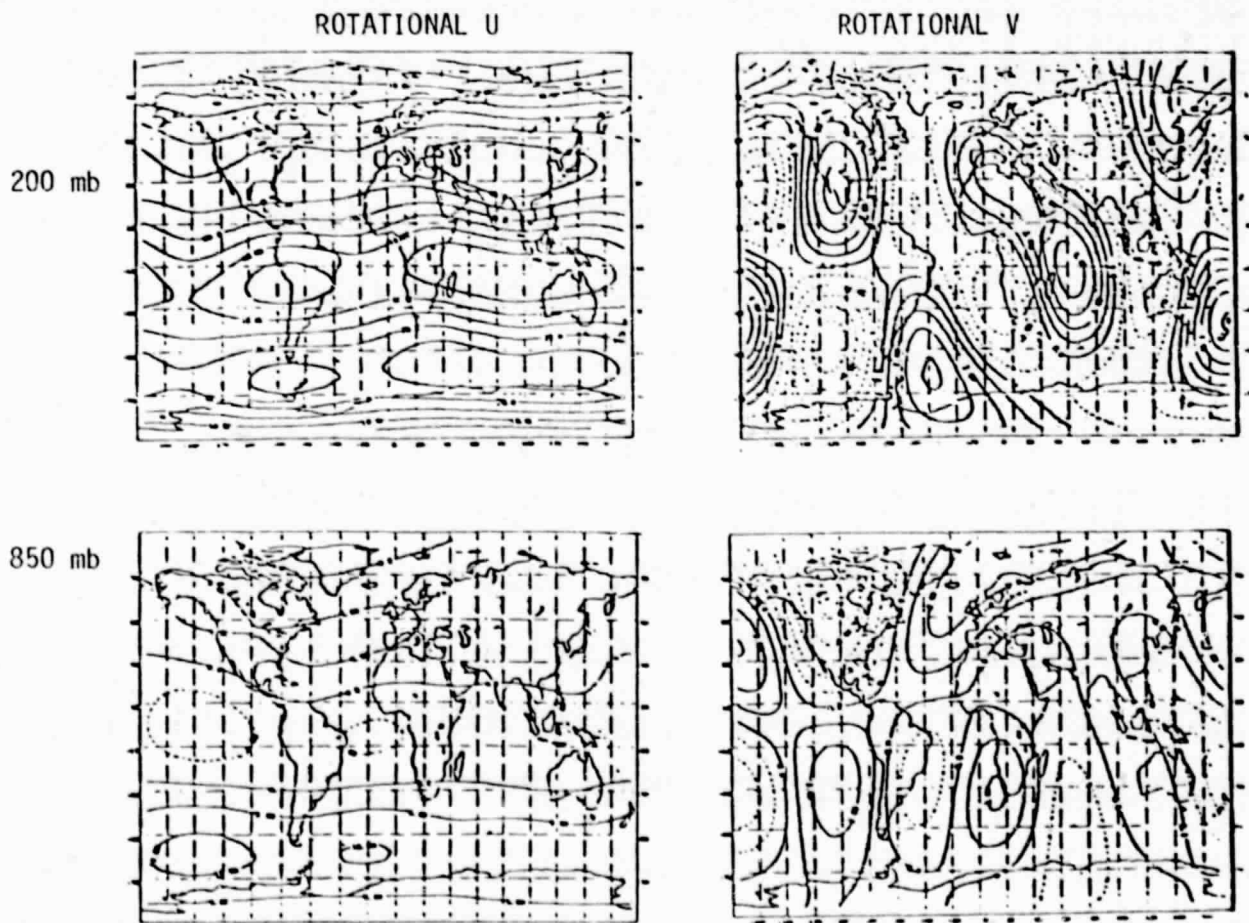


Figure 5. The same as Figure 4, for the rotational wind field. The isoline interval is 5 m/s for U and 1 m/s for V.

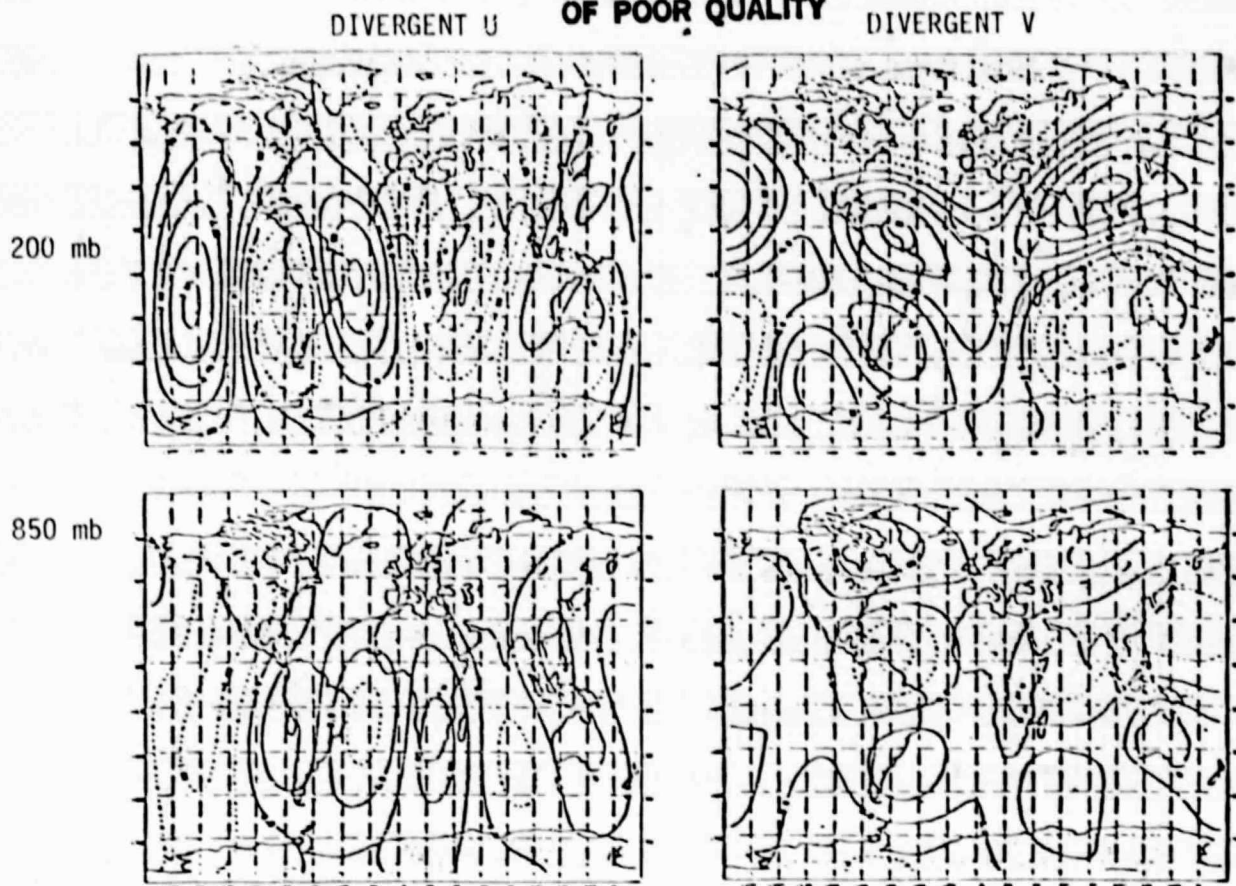


Figure 6. The same as Figure 4, for the second 6 day period, beginning 0Z, February 3, ending 18Z, February 8.

## 5. IMPLICATIONS

Since we are describing the fields in terms of an arbitrary mathematical basis of expansion, possessing no a priori physical content, we can only speculate about the physical implications of these results. One implication of the presently described distribution is that tropical monsoons may be relevant to the longitudinal distribution of troughs and ridges, as well as jet streams and storm tracks (Krishnamurti, et al., 1973).

Similar hypotheses are also drawn in earlier studies by Bjerknies (1969), Ramage (1968) and Webster (1972), who have made comparisons of local Hadley cell enhancement with subtropical jet streams on long (seasonal) time scales. The subject is currently receiving much attention in association with seasonal abnormalities.

Much of this research suggests that an enhanced meridional overturning out of the tropical South Central Pacific, during the Northern Hemisphere winter, enhances the subtropical jet stream in similar longitudes. In the present study, for the sector from Central America, westward to the dateline, there is a rather enhanced poleward divergent flow in the first 6 day period relative to the second 6 day period (compare Figs 4, 5, with 6, 7). Our interpretation of this result is complicated by the fact that, to this truncation the zonal flow does not change substantially.

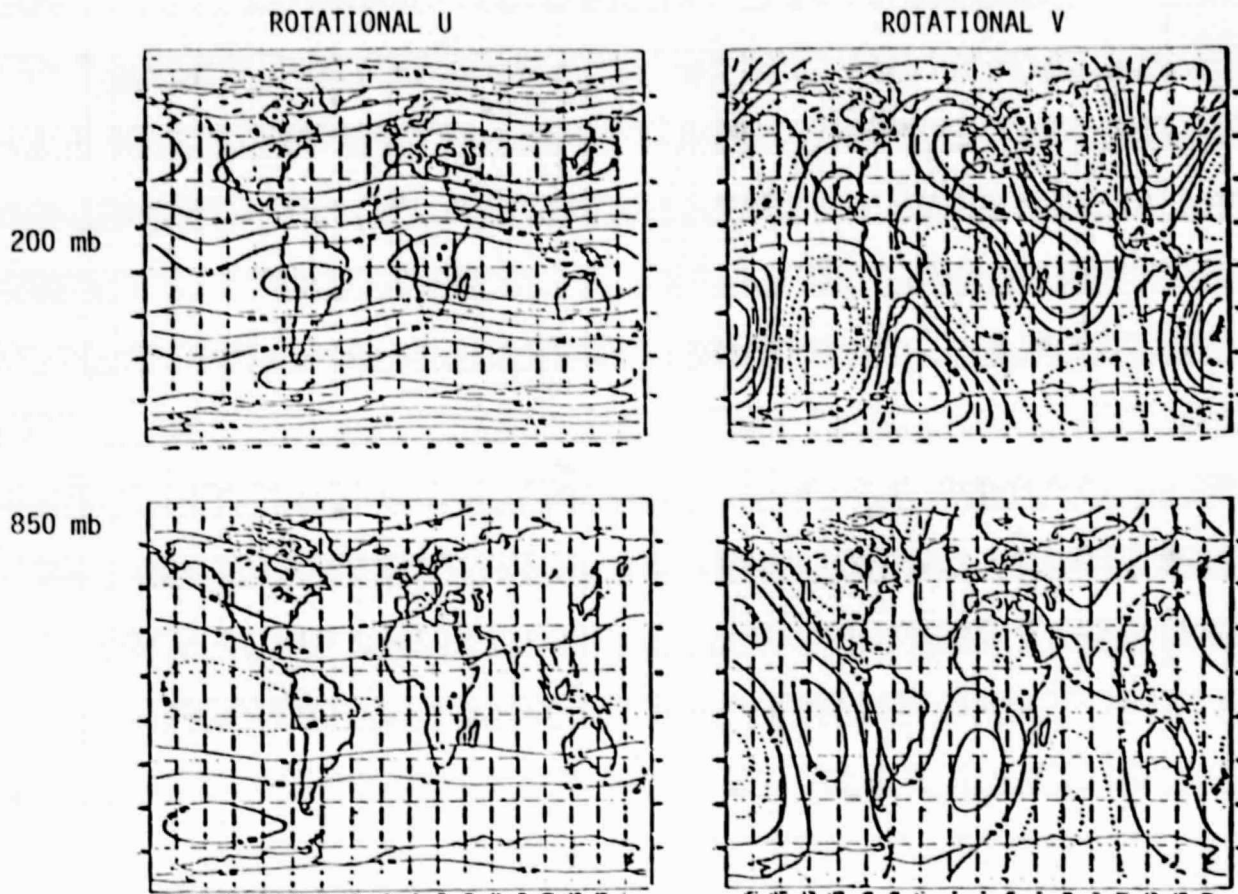


Figure 7. The same as Figure 5, for the second 6 day period, beginning 0Z February 3, ending 18Z February 8.

However, the potential relevance of tropical higher latitude interactions on weekly time scales cannot be dismissed, even here. The rotational flow couples the divergent flow to the extent that angular momentum is conserved, i.e.

$$\frac{d(\zeta + f)}{dt} = -(f + \zeta)\delta \quad (8)$$

The appearance of the Coriolis parameter as well as nonlinearity, in the relation also tends to produce finer scale structures in the rotational flow response to changes of divergence, than are present in the divergence itself. In particular, the product of the Coriolis term with the divergence produces finer scales in the latitudinal structure of the evolving vorticity than are present in the divergence.

At sufficiently high resolution, the discrepancy between the spectral truncation of the vorticity and of the divergence term of the vorticity equation should not be important. Because of this, we have also decomposed the longitudinal variation of the stream-function and velocity potential in Fourier series truncated at wavenumber 4, and then computed the latitudinal amplitude structure of each of these modes to the full resolution of the  $4^\circ$  latitudinal grid spacing.

The 200 mb divergent meridional wind field that results at 18°N latitude is plotted as a function of longitude for each 6 day period in Fig. 8a. The strongest poleward flow (over 5 m/s) during the first period is found at about 60°E over the Arabian Sea. This maximum diminishes markedly to about 3 m/s during the second 6 day period, while shifting eastward. A secondary maximum of about 3 m/s, centered at about 110°W (over the Eastern Pacific), during the first 6 days diminishes to a relative minimum of 1 m/s during the next 6 days as a new poleward maximum (emanating from the eastern Amazon Basin) strengthens over the Central Atlantic Ocean.

The 200 mb rotational zonal flow structure at 30°N during the same two periods is displayed in Fig. 8b. At 90°W the 70 m/s zonal wind of the first period reduces to 43 m/s during the second 6 days, as a new maximum of 60 m/s establishes just off the East Coast of North America. A less dramatic weakening and eastward shift occurs in the jet stream around South-East Asia. These jet stream shifts appear to be consistent with the above-mentioned theories and regional shifts of the meridional overturnings.

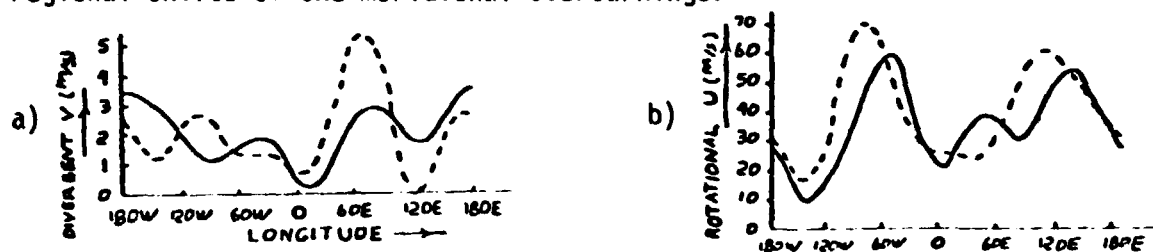


Figure 8a. Divergent meridional wind at 18°N, obtained as described in the text. The dashed curve represents the first 6 day average, the solid curve depicts the second six day average

Figure 8b: The rotational zonal wind at 30°N, obtained as described in the text. The dashed curve represents the first 6 day average, the solid curve depicts the second 6 day average.

The jet stream changes were accompanied by rather significant changes of weather over the United States. The cold wet weather over the South-Western states of the first 6 day period diminished during the second 6 days, as the storm track focused more strongly over the South-Eastern part of the country.

In the instance of seasonal time scales, it appears that enhanced regional Hadley cell circulations are sometimes associated with warmer than normal tropical sea surface temperatures and precipitation. It is possible that stronger local latent heating provides a regional energy source for the subtropical jet stream, thereby modifying subtropical jetstream meanders induced by other effects such as topography, baroclinity and wave interactions.

Analogously, in the present case, it seems reasonable to suppose that regionally enhanced divergent meridional circulations over a period of a week are associated with locally enhance ITCZ or monsoonal activity. However, it is not possible to discern, without further analysis, whether mid-latitude effects produced meanders of the jet stream that induced stronger local tropical overturnings or whether the latter may have had more independent origins. The question requires more detailed analysis, perhaps including numerical model experiments. One relevant comparison of such experiments to nature is to compare the model forecast global scale flows to their atmospheric counterparts.

## ACKNOWLEDGEMENTS

The interest and support of Dr. Milton Halem is gratefully acknowledged. Essential computational support was provided by the staff of Sigma Data Services Corp., and we are particularly appreciative of the assistance from Mr. Diego F. Edelmann, Mr. Mark Iredell, Mr. Steven Breining, Mr. Bert Katz, and Mr. Herb Carus. J. Paegle has been supported by the National Research Council.

## REFERENCES

- Baker, W. E., 1981: Objective analysis and assimilation of observation data from FGGE SOP 1. To be submitted to Mon. Wea. Rev.
- Dates, J. R., 1977: Dynamics of stationary ultra-long waves in middle latitudes. Quart. J. Roy. Meteor. Soc., 103, 397-430.
- Bjerknes, J., 1969: Atmospheric teleconnections from the equatorial Pacific. Mon. Wea. Rev., 97, 163-172.
- Charney, J. G., and A. Eliassen, 1949: A numerical method for predicting the perturbations of the middle latitude westerlies. Tellus, 1, 38-54.
- Dickinson, R. E., 1971: Cross-equatorial eddy momentum fluxes evidence of tropical planetary wave sources. Quart. J. Roy. Meteor. Soc., 97, 554-558.
- Grose, W. L., and B. J. Hoskins, 1979: On the influence of orography on large-scale atmospheric flow. J. Atmos. Sci., 36, 223-234.
- Holopainen, E. O., 1970: An observational study of the energy balance of stationary disturbances in the atmosphere. Quart. J. Roy. Meteor. Soc., 96, 626-644.
- Julian, P. R., and R. M. Chervin, 1978: A study of the Southern Oscillation and Walker Circulation Phenomenon. Mon. Wea. Rev., 106, 1433-1451.
- Kalnay-Rivas, E., A. Bayliss, and J. Storch, 1977: The 4th order GISS model of the global atmosphere. Beite. Phys. Atmos., 50, 299-311.
- Kalnay-Rivas, E., and D. Hoitsma, 1979: The effect of accuracy, conservation and filtering on numerical weather forecasting. Preprints Fourth Conf. on Numerical Weather Prediction, Silver Spring, Maryland. Amer. Meteor. Soc., 302-312.
- Krishnamurti, T. N., M. Kanamitsu, W. J. Koss and J. D. Lee, 1973: Tropical East-West circulations during the northern winter. J. Atmos. Sci., 30, 780-787.
- Paegle, J., J. N. Paegle, F. P. Lewis and A. J. McGlasson, 1979: Description and interpretation of planetary flow structure of the winter 1976 DST data. Mon. Wea. Rev., 107, 1506-1514.
- Paegle, J., and E. M. Tomlinson, 1975: Solution of the balance equation incorporating Fourier transform and Gauss elimination techniques. Mon. Wea. Rev., 103, 528-535.

- Ramage, C. S., 1968: Role of a tropical "maritime continent" in the atmospheric circulation. Mon. Wea. Rev., 96, 365-370.
- Rowntree, P. R., 1976: Tropical forcing of atmospheric motions in a numerical model. Quart. J. Roy. Meteor. Soc., 102, 583-606.
- Smagorinsky, J., 1953: The dynamical influence of large-scale heat sources and sinks on the quasi-stationary mean motions of the atmosphere. Quart. J. Roy. Meteor. Soc., 79, 342-366.
- Webster, P. J., 1972: Response of the tropical atmosphere to local steady forcing. Mon. Wea. Rev., 100, 518-541.

## INTEGRATED AND SPECTRAL ENERGY FLOWS OF THE GLAS GCM

J. Tenenbaum

Analysis of the generation, transport, and dissipation of energy represents one of the primary methods of studying geophysical fluid flows. Lorenz proposed subdividing atmospheric energy into kinetic and available potential forms and in turn subdividing these categories into zonal kinetic energy and eddy kinetic energy categories. Further subdivision into the spectral domain was suggested by Saltzman (1970) and followed by similar observational studies (Tenenbaum, 1976; Baker *et al.*, 1978). Our previous work in this area was summarized in last years annual report (Tenenbaum, 1980) and in a recent paper (Tenenbaum, 1981).

During the past year these energetics analyses have been pursued in several directions. First, the longitudinal and time dependence on the energy flow to the stratosphere has been examined as a function of geographical sector. Second, the cases of strong and weak energy flows have been correlated with the skill of medium range forecasts. Third, the one-dimensional spectral results (Fourier services around latitude circles) have been extended to spherical harmonics over a global domain. Fourth, the validity of vertical velocities derived from mass convergence have been examined in terms of their effect on the conversion of eddy-available potential energy to eddy kinetic energy.

One result in Tenenbaum (1981) is the existence of a weak vertical shear above the subtropical jet in all nominally 10-level general circulation models. When examined in more detail this phenomenon is correlated with an anomalous growth of kinetic energy in the GLAS model's stratospheric level (120 to 10 mb). This energy growth is closely related to the locations of strong initial jet streams and can be characterized geographically. For the North American and European sectors, the jet must be both quite strong and quite high for the anomalous energy rise to occur. Approximately one-third of the prominent jets in the initial states satisfy this criterion. In the East Asian sector, orography normally keeps the jets high. Thus 90% of the initial jets are anomalous.

The forecast correlation studies dealt with whether the cases of significant energy rise were related to the downstream forecast skill. Two very suggestive results were found by examining the initial states of 14 forecasts made from FGGE data. The energy rise over North America was moderately correlated with the initial state divergence averaged over North America. The European 500 mb forecast skill at day 5 was even more correlated with this initial state divergence (Fig. 1). These results were independent of the size of the averaging region but possessed a very strong signal as one varied the location of the averaging region.

For the two-dimensional spectra, preliminary analyses have been made at the end of the project year. The vertical velocity studies have been made using the geostrophic approximation to the diagnostic omega equation including both moist and dry terms. Initial results have shown unphysically smooth vertical velocity fields. We are currently examining whether the forcing terms in the omega equation (an elliptic partial differential equation) have the necessary scale of spatial variation to permit physically reasonable results.

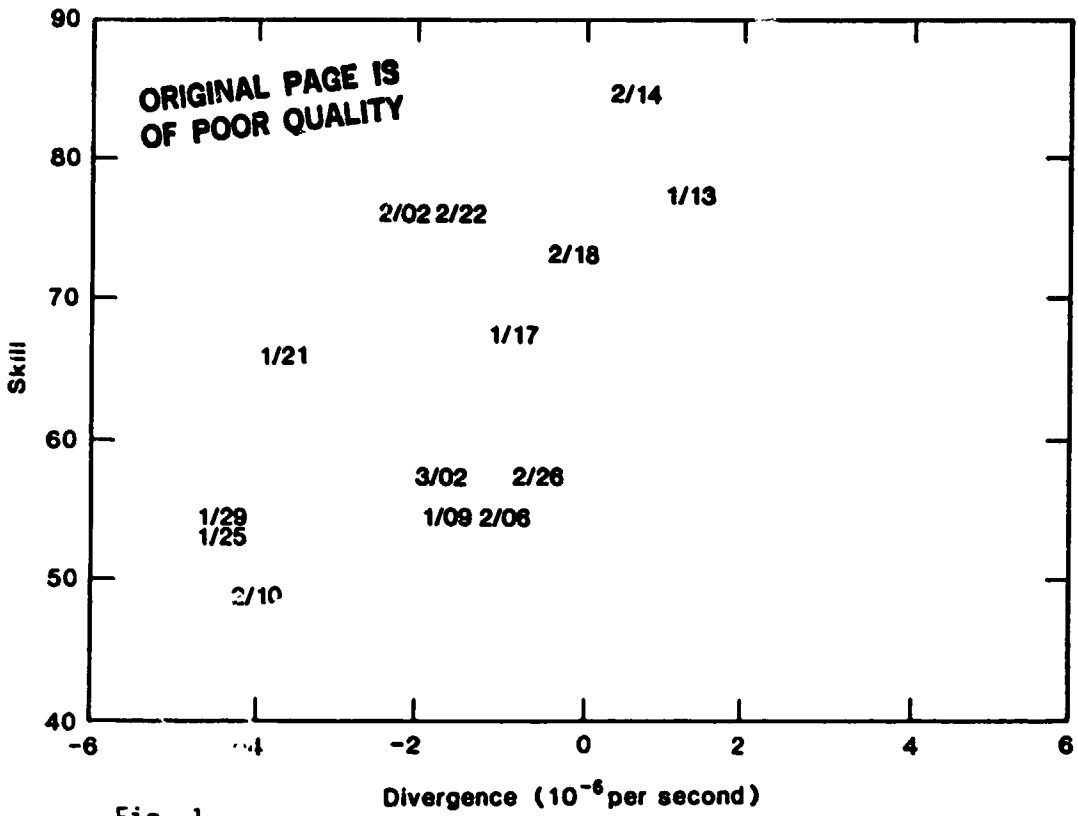


Fig. 1

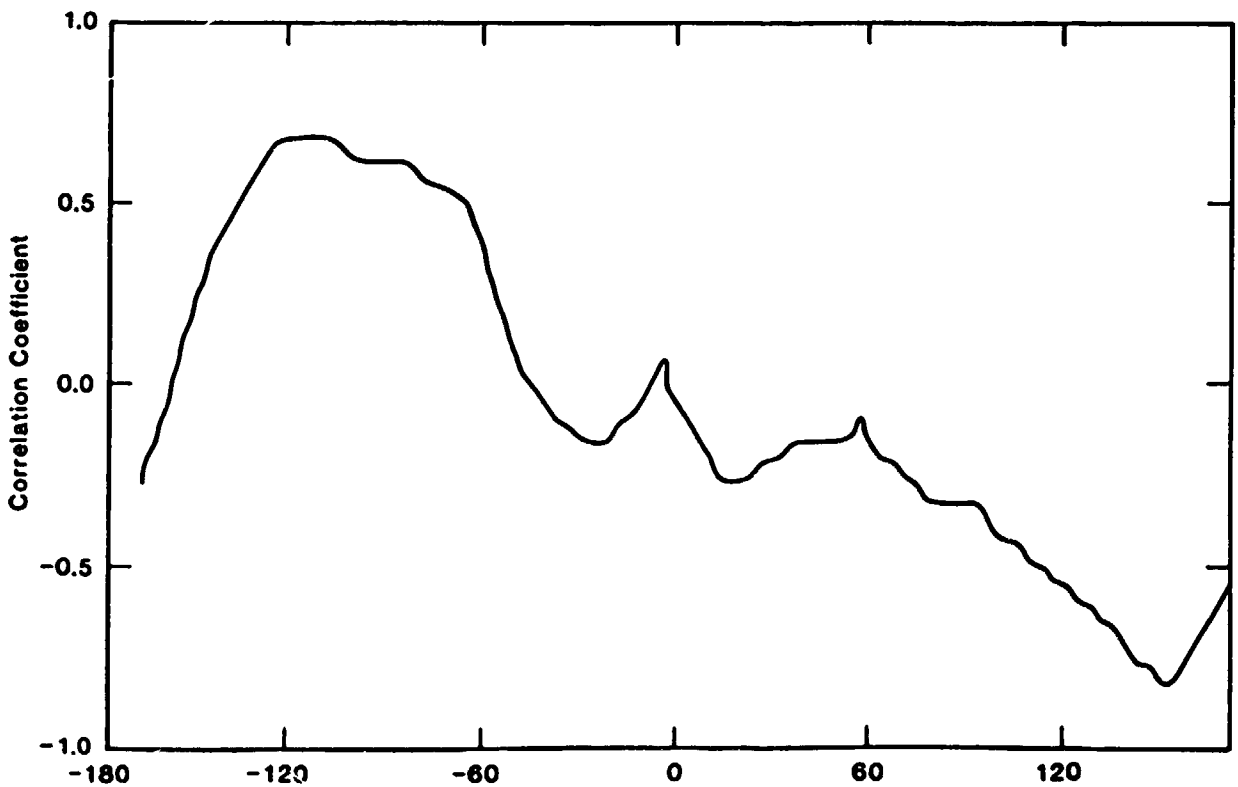


Fig. 2

## REFERENCES

- Baker, W. E., E. C. Kung, and R. C. J. Somerville, 1978: An energetics analysis of forecast experiments with the NCAR general circulation model. Mon. Wea. Rev., 106, 311-323.
- Saltzman, B., 1970: Large scale atmospheric energetics in the wavenumber domain. Rev. Geophys. Space Phys., 8, 289-302.
- Tenenbaum, J., 1976: Spectral and spatial energetics of the GISS model atmosphere. Mon. Wea. Rev., 104, 15-30.
- Tenenbaum, J., 1980: Integrated and spatial energetics of the GLAS general circulation model. Atmospheric and Oceanographic Research Review - 1979. Laboratory for Atmospheric Sciences, Modeling and Simulation Facility. NASA TM 80650.
- Tenenbaum, J., 1981: Integrated and Spectral energetics of the GLAS general circulation model. (Submitted to Mon. Wea. Rev.).

# A NUMERICAL MODEL STUDY OF LONG-TERM PLANETARY WAVE PREDICTABILITY

R. L. Wobus

A numerical model has been developed and used to study planetary wave behavior over periods up to four months under the influences of stochastic and diffusive forcing by synoptic-scale motions and of sea surface temperature anomalies. The model is suitable for Monte Carlo experiments which provide ensemble mean and variance predictions and permit the response to heating anomalies to be partly separated from random variability.

The model incorporates the linear-balanced dynamical equations for wind at two tropospheric levels and temperature at one level. These variables are represented over the northern hemisphere by spherical harmonics truncated at global wavenumber 8. The model atmosphere is forced by semi-empirical January heating linearly dependent on local air temperature. Topography and the lower boundary layer are represented by vertical motion and drag functions, respectively, of the lower level wind. The linear phase speeds of Rossby waves have been modified to reflect the effect of the stratosphere.

The truncation intentionally excludes synoptic disturbances and most baroclinically active waves. The unpredictable effects of these motions are simulated by uniform random forcing; the predictable effects are simulated by vertically varying quasi-horizontal diffusion of heat and vorticity. The levels of random forcing and horizontal diffusion are chosen by experiment to conform with the observed January mean circulation and the results of previous predictability studies.

Random forcing is shown to be far more significant than variation of initial conditions as a source of model unpredictability; in fact, under the influence of identical time-dependent random forcing, two model runs starting from unrelated initial states converge over a period of two months. Random forcing of the largest-scale mode produces episodes of strong baroclinic wave growth, somewhat analogous to zonal index variations in the atmosphere. An ensemble of 8 parallel 120-day runs from a common initial state shows the model's climate, variability, and short-range predictability.

In order to separate the relatively small responses to a North Pacific sea surface temperature anomaly (similar to that used in NCAR GCM studies) from the variability due to unpredictable synoptic-scale motions, the 120-day ensemble is rerun with the anomaly but with the same 8 sequences of random forcing. The ensemble of differences between corresponding runs with and without the anomaly provides a sensitive measure of the response. The ensemble mean response grows rapidly during the first two weeks and more slowly thereafter; the ensemble variance of the differences grows rapidly at first, then more slowly until day 60, overwhelming all but the local mean response after day 30. This secondary variance growth occurs primarily through episodes of strong baroclinic wave growth.

These experiments suggest, for the large-scale flow in winter, a time-spectral gap between the period over which detailed forecasts can be made from initial states (about 2 weeks) and that over which large-scale statistics follow seasonal and anomalous variations of thermal forcing (two months or

longer); in the range from two weeks to two months the uncertainty propagated into the planetary flow from synoptic-scale motions should significantly limit the skill of forecasts, even if the external forcing were completely known.

### III. CLIMATE/OCEAN-AIR INTERACTIONS

#### A. DATA ANALYSIS

## CLIMATE MODEL POSTPROCESSING

J. Abeles, E. Pittarelli and D. A. Randall

Enormous effort and expense is devoted at GLAS and at other centers throughout the world to design, code, test, and perform simulations with global general circulation models. The effort and expense are justified, since these models represent our best hope to improve our understanding of and ability to predict the vagaries of weather and climate. But in order to learn from and utilize the model results, it is necessary to create elaborate "postprocessing" software to allow analysis of the large volume of data produced. The model results would be practically useless without postprocessing software. This report briefly summarizes the development of new postprocessing software for the GMSF Climate Modeling Group.

To analyze the results of the potential-entropy-conserving general circulation model (PEGCM) and the seasonal cycle model (SCM), extensive new analysis codes have been developed.

The models produce sigma history tapes. The sigma history records are interpolated to pressure history records, which are written on a pressure history tape. This allows us to analyze the model results on pressure-surfaces, with snap-shots or time averages.

The nominal pressure surfaces used for the pressure history tape are: 100, 200, 300, 400, 500, 600, 700, 800, 900 and 1000 mb. For each of these pressure surfaces, a mask is created. If the pressure surface is below ground, the mask is zero, and if the pressure surface is above ground, the mask is one. The mask is utilized in the time averaging and plotting software.

The following diagnostic fields are written to the pressure history tape:

- |                          |                        |
|--------------------------|------------------------|
| 1) u-wind                | 8) vorticity           |
| 2) v-wind                | 9) omega               |
| 3) potential temperature | 10) omega * alpha      |
| 4) temperature           | 11) stream function    |
| 5) relative humidity     | 12) velocity potential |
| 6) specific humidity     | 13) divergence         |
| 7) geopotential          | 14) sea level pressure |

The interpolation of the various fields is done by utilizing tailored methods:

1) Potential temperature and relative humidity are interpolated linearly in  $(p/p_0)^k$  (Specific humidity is converted to relative humidity, and the relative humidity is interpolated. Specific humidity on the pressure surface is then calculated from the interpolated relative humidity.) The temperature on the pressure surface is calculated from the interpolated potential temperature.

2) The geopotential and u and v winds are interpolated using methods suggested by Prof. M. Suarez of UCLA.

3) Omega and omega + alpha are interpolated linearly in pressure.

4) Vorticity is computed directly on the pressure surfaces, using the interpolated u and v wind components.

5) Divergence on the pressure surface is calculated by differencing omegas in the straddling sigma layers.

6) Stream function and velocity potential are computed from the vorticity and divergence, using codes provided by Prof. J. Paegle of the University of Utah.

In addition, the sea level pressure is calculated.

In order to analyze time means of these fields, we time average the pressure history records. The following fields are put to disk:

- |                      |                         |
|----------------------|-------------------------|
| 1) total mask        | 11) $T^2$               |
| 2) $\bar{u}$         | 12) $\overline{SH^2}$   |
| 3) $\bar{v}$         | 13) $\overline{\phi^2}$ |
| 4) $\bar{\phi}$      | 14) $\overline{UV}$     |
| 5) $\bar{T}$         | 15) $\overline{VSH}$    |
| 6) $\overline{RH}$   | 16) $\overline{VT}$     |
| 7) $\overline{SH}$   | 17) $\overline{USH}$    |
| 8) $\bar{\phi}$      | 18) $\overline{UT}$     |
| 9) $\overline{U^2}$  | 19) $\overline{Vort}$   |
| 10) $\overline{v^2}$ | 20) $\overline{\Omega}$ |

In addition, the following total, transient and stationary variances and covariances are calculated:

- |           |        |
|-----------|--------|
| 1) KE     | 6) VT  |
| 2) Temp   | 7) UT  |
| 3) SH     | 8) VSH |
| 4) $\phi$ | 9) USH |
| 5) UV     |        |

The following is a list of some of the plots currently being produced by the climate postprocessing package, utilizing the NCAR Graphics software:

For each of the following, world map contour plots and zonal means for total, ocean and land are produced.

Geopotential Height\*  
Vorticity\*  
Temperature (K)\*  
Relative Humidity\*  
Sea Level Pressure  
Ground Temperature (C)

\*Plotted at 200, 500, 700 and 800 mb

Surface Temperature (C)  
 Total Precipitation (mm/day)  
 Convective Precipitation (mm/day)  
 Large Scale Precipitation (mm/day)  
 Evaporation Flux at the Surface (mm/day)  
 Latent Heat Flux at the Surface (watts/m<sup>2</sup>)  
 Sensible Heat Flux at the Surface and  
     at the Top of the Atmosphere (watts/m<sup>2</sup>)  
 Long Wave Radiation at the Surface and  
     at the Top of the Atmosphere (watts/m<sup>2</sup>)  
 Solar Radiation Absorbed by the Atmosphere (watts/m<sup>2</sup>)  
 Planetary Albedo  
 Radiation Balance at the Surface and at the Top of the  
     Atmosphere (watts/m<sup>2</sup>)  
 Heat Storage in Water or Ice at the Surface (watts/m<sup>2</sup>)  
 Energy Balance at the Surface (watts/m<sup>2</sup>)

The following are latitude-height plots:

Zonal average U-wind (m/s)  
 Zonal average V-wind (m/s)  
 Zonal average Temperature (K)  
 Zonal average Temperature (K) and U-wind (m/s)  
 Zonal average Specific Humidity (g/kg)  
 Zonal average Relative Humidity (g/kg)

All of these fields are plotted for total eddy, transient eddy and stationary eddy:

#### Latitude Height Plots

Kinetic Energy (m<sup>2</sup>/s<sup>2</sup>)  
 Temperature Variance  
 Specific Humidity Variance (g/kg)  
 Geopotential Variance  
 Meridional flux of Zonal Momentum (m<sup>2</sup>/s<sup>2</sup>)  
 Meridional Temperature flux (m/s)  
 Zonal Temperature flux (m/s)  
 Meridional Mixing Ratio flux  
 Zonal Mixing Ratio Flux

#### World Map Streamline Plots

Winds  
 Moisture flux  
 Transient Temperature flux  
 Momentum flux

Postprocessing software development is an ongoing project. Code has also been developed to calculate and analyze moisture flux convergence, total diabatic heating, total cloudiness, heating due to dry convective adjustment, and cumulus heating and drying.

SEASONAL CYCLE OF HEIGHTS, TEMPERATURES, AND SEA LEVEL PRESSURE  
OVER THE NORTHERN HEMISPHERE

B. Doty and K. Mo

## 1. INTRODUCTION

Recently Hsu and Wallace (1976) and White and Wallace (1978) documented the annual and semiannual cycles of sea level pressure and surface temperature over the Northern Hemisphere, using data based on NMC analyses for the Northern Hemisphere, and data described by Taljard et al. (1969) for the Southern Hemisphere. Hsu and Wallace (1976) also examined the annual cycles in the geopotential height fields for several levels. They found that the continental winter maxima in the sea level pressure field extended upward to near the 700 mb level. However, at 500 mb and above, they found that the annual cycle exhibited summertime maxima over both sea and land.

Van Loon and Jenne (1970) studied the annual cycle of 100 mb temperature using the same data sources. They found highs in the amplitude between 30 to 45 degrees North, the maximum occurring in the late winter or early spring. Reed and Vitek (1969) carried out harmonic analysis of monthly mean temperatures over the tropics to obtain the amplitudes and phases of the annual and semiannual cycles for 17 levels between 300 mb and 100 mb. They found that the annual temperature variation in the lower tropical stratosphere and its maximum amplitude just above the equatorial tropopause had nearly the same phase at that particular level throughout both hemispheres. They also discovered that the coldest stratospheric temperatures in the tropics occurred during the northern hemisphere winter.

Most analyses of annual and semiannual cycles have been done using harmonic analysis. However, Heddinghaus and Kung (1980) recently used eigenvector analysis to study annual and semiannual cycles of 700 mb and 500 mb temperatures, 700-500 mb thickness, etc. over the Northern Hemisphere using NCAR data for the period 1955 to 1974.

The annual and semiannual cycles over the Southern Hemisphere have been studied in great detail by Van Loon et al (1972) for temperatures, heights, and winds at all levels from 100 mb to sea level.

## 2. RESULTS

Data used in the analysis was obtained from NCAR, consisting of 15 years of data for heights at all standard levels, 14 years of temperatures at all levels, and 14 years of sea level pressure. Data was given twice daily from Jan 1, 1963 for heights (Jan. 1, 1964 for temperatures and sea level pressure) to December 31, 1977 on the NMC octagonal analysis grid. The data was interpolated to a 4x5 degree latlon grid, and missing and erroneous data was replaced by linear interpolation using neighboring dates (Doty and Mo, 1981).

Harmonic analysis was performed at each grid point for each variable at each level using the twice daily time series: 10958 ( $15 \times 365 \times 2 + 8$ ) time steps for heights and 10228 ( $14 \times 365 \times 2 + 8$ ) time steps for temperatures and sea level

pressure (leap years included). The annual cycle is defined as the 15th (or 14th) Fourier coefficient giving a period of 365.3 days; the semiannual cycle is defined as the 30th (or 28th) Fourier coefficient giving a period of 182.6 days.

Calculations of the standard deviations of the annual cycle amplitudes for the 15 (or 14) years were also made. This was done by calculating the annual cycle for each year separately at each grid point.

Results are presented in a vectorial format, with each vector representing the amplitude and phase, the phase being the date when the harmonic is at its maximum. The vector convection is for the length of the vector to indicate the amplitude (the scales are not uniform) and for the direction to indicate the phase. An arrow pointing south to north indicates a maximum on Jan. 1 for the annual cycle, and maxima on Jan. 1 and July 1 for the semiannual cycle. The dates become later as the arrow is rotated clockwise, so that an arrow pointing west to east indicates a maximum on Apr. 1 for the annual cycle and Feb. 15 and Aug. 16 for the semiannual cycle, etc.

Figure 1 shows the vector diagrams of the annual cycle for 200 mb and 700 mb temperatures. Figure 2 is the same as Figure 1 but for 300 mb height and sea level pressure. Results based on calculations at other levels are discussed below, but are not shown.

### 3. DISCUSSION

The phase of the sea level pressure annual cycle shows wintertime maxima over the continents with summertime maxima over the oceans. The continental wintertime maxima extends to the 850 mb level in the annual cycle of heights, especially over Asia. At 700 mb, except for a small area over Asia where weak amplitudes prevail, the maxima occur in summer.

The semiannual cycle in the height fields is stronger in the lower levels when expressed as a percentage of the strength of the annual cycle. At 850 mb the amplitude of the semiannual cycle is in places more than half the strength of the annual cycle. At higher levels, 500 mb and above, the semiannual cycle rarely exceeds one third the strength of the annual cycle.

The amplitudes of the annual cycle of temperatures from 850 mb have very similar patterns. Highs occur over North America and eastern Asia, with axes of low amplitude occurring over the easternmost portions of the oceans. The pattern changes markedly at 200 mb, where the amplitude is largest over the polar region. The standard deviations between years for the annual cycle are very noisy and are generally small (less than 1C).

The maxima of the annual cycle temperatures generally occurs in summer. At 200 mb the phase of the maxima is about one month earlier over the continents than over the oceans. The phase shifts sharply eastward from ocean to land over western North America; the shift is more gradual from ocean to land over Eurasia. The latest dates for the maxima occur generally over the eastern portions of the oceans. At higher levels the phase pattern is similar, with the ocean/land difference less well defined.

The patterns of semiannual cycle amplitudes of temperatures are similar from 850 mb to 300 mb, with highs over the pole, over western North America, and over the western Mediterranean. These amplitudes all have maxima in January or February and June or July. There is also a small relative high in the amplitudes near India, with the maximum occurring in April and October.

#### REFERENCES

- Crutcher, H. L., and J. M. Meserve, 1979: Selected level heights, temperatures and dew points for the Northern Hemisphere. NAVAIR 50-1c-52 Rev. Chief Naval Operation, Washington, DC.
- Doty, B. and K.C. Mo, 1981: Description of geopotential height temperature and sea level pressure data from NCAR. Tech Report, Sigma Data Service Corp., NASA Goddard Space Flight Center, Greenbelt, MD.
- Heddinghaus, T. R., and E. C. Kung, 1980: An analysis of climatological patterns of the Northern Hemisphere circulation. J. Atmos. Sci., 108, 1-17.
- Hsu, C. P., and J. M. Wallace, 1976: The global distribution of the annual and semi-annual cycles in sea level pressure. Mon. Wea. Rev., 104, 1597-1601.
- Reed, R. J., and C. L. Vicek, 1969: The annual temperature variation in the lower tropical stratosphere. J. Atmos. Sci., 26, 163-167.
- Taljaard, J. J., H. Van Loon, H. L. Crutcher, and R. L. Jenne, 1969: Climate of the upper air Southern Hemisphere, Vol. 1. NAVAIR 50-1c-55 Chief Naval Operations, Washington, DC.
- Van Loon, H., and R. L. Jenne, 1970: The annual wave in the temperature of the low stratosphere. J. Atmos. Sci., 27, 701-705.
- Van Loon, H., 1972: Chapter 4, Pressure in the southern hemisphere, Meteorology of the southern hemisphere. C. W. Newton, ed., Met. Monog., 13, 35.
- Van Loon, H., : Temperature in the Southern Hemisphere abid. Meteorology of the southern hemisphere. C. W. Newton, ed., Met. Monog., 13, 35.
- White, G. H., and J. M. Wallace, 1978: The global distribution of the annual and semi-annual cycles in surface temperature. Mon. Wea. Rev., 106, 901-905.

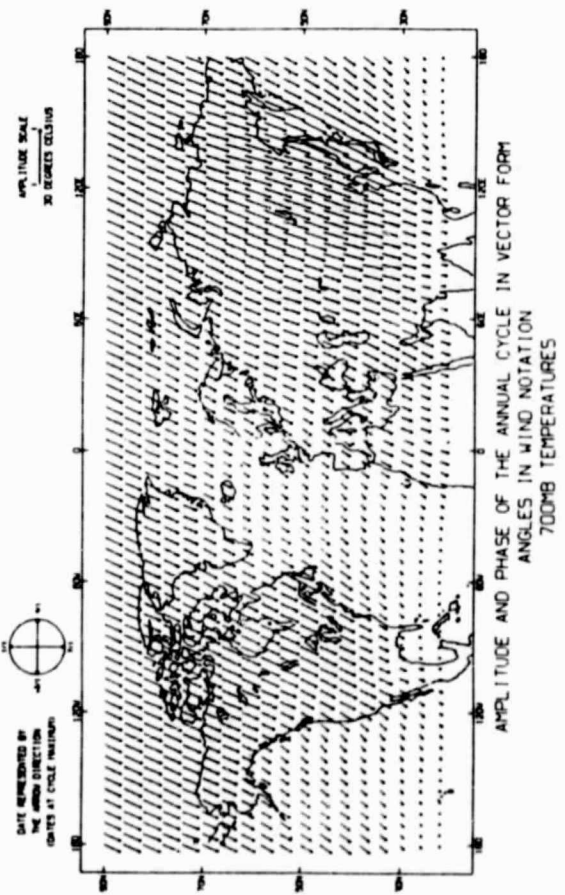
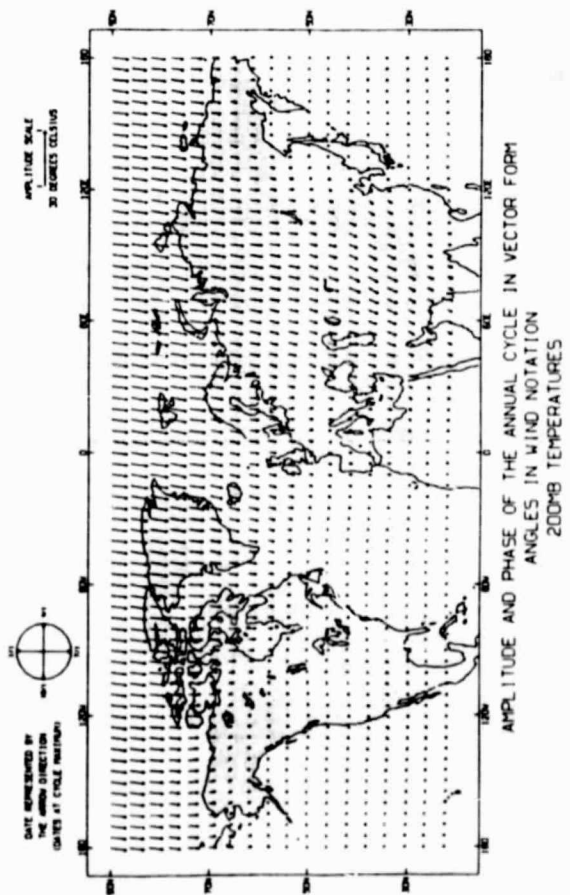
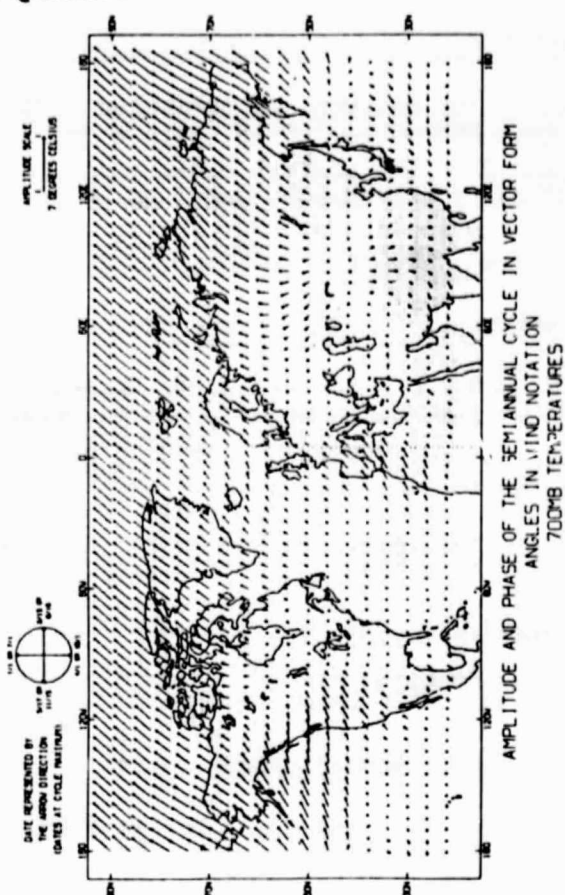
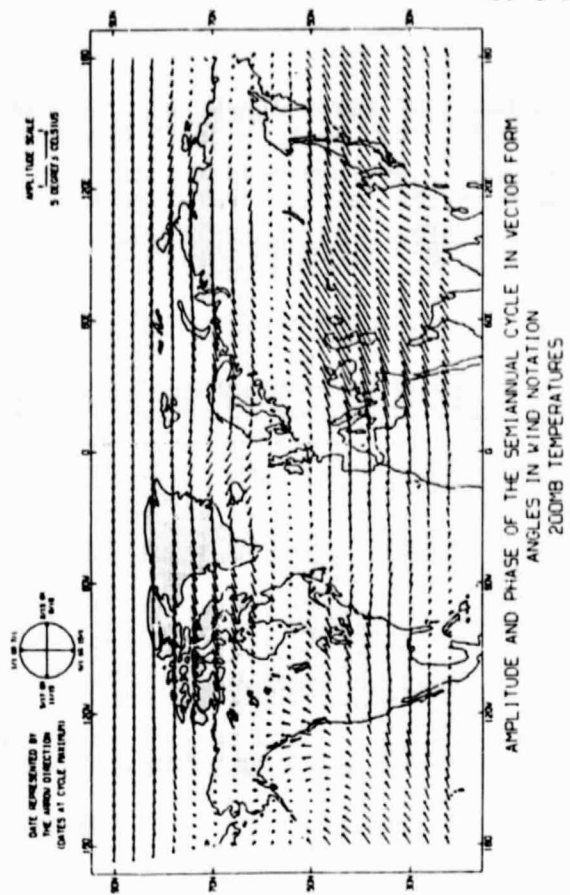


Figure 1

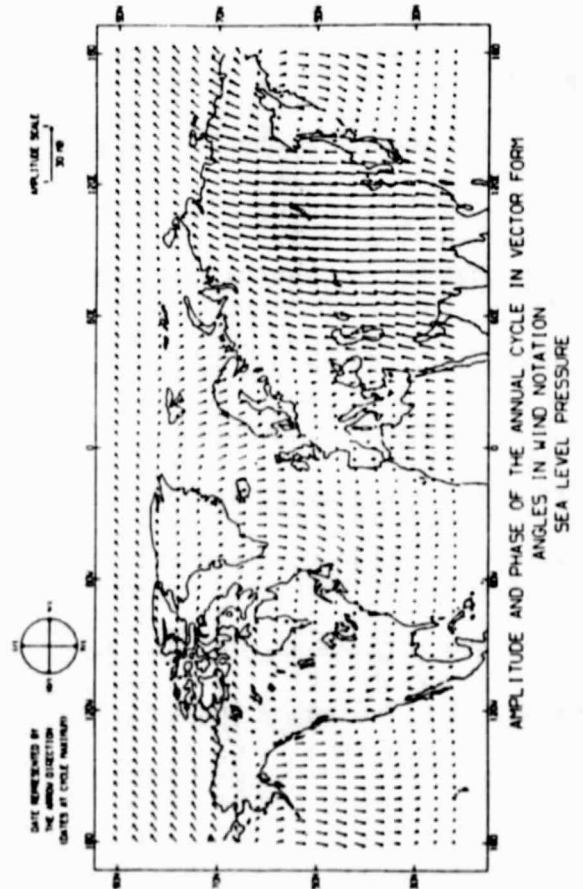
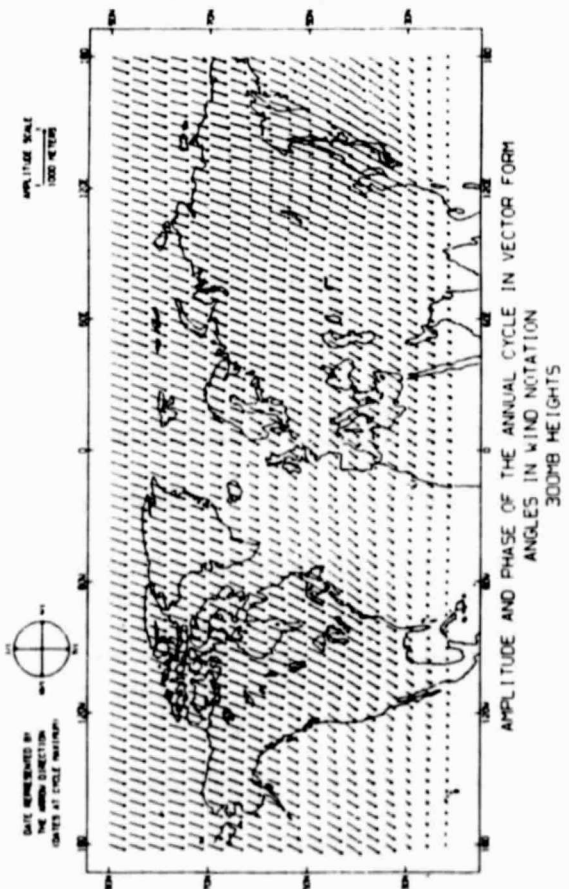
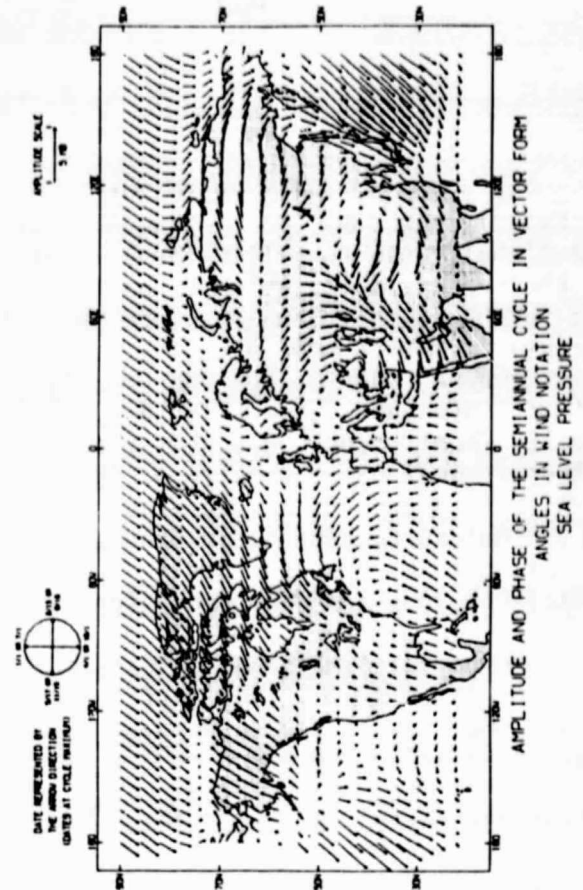
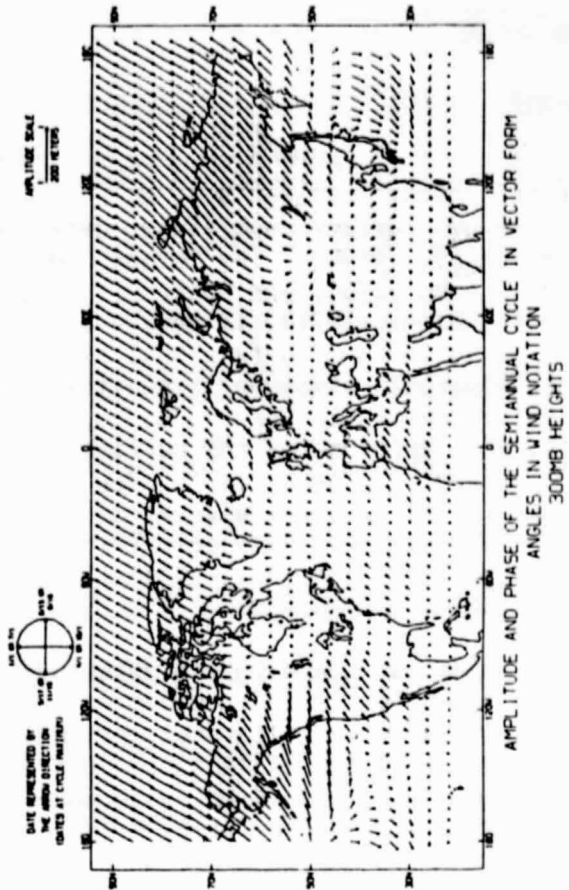


Figure 2

S. K. Esbensen

Collaboration with Professor Y.-J. Han and graduate students S.-W. Lee and Y. Kushnir has resulted in new estimates of the net surface heat fluxes over the global ocean for all calendar months (Han et al., 1980). The method used in the present calculation is patterned after Budyko (1963) and Bunker (1976). But further simplifications were made, following Haney (1971), to obtain a formula in the form  $Q_s = Q_2(T_A^* - T_s)$ , where  $Q_s$  is the net surface heat flux,  $T_s$  is the sea surface temperature,  $T_A^*$  is the "apparent" atmospheric equilibrium temperature, and  $Q_2$  is the proportionality constant. Here  $T_A^*$  and  $Q_2$ , derived from the original heat flux formulas, are functions of the surface meteorological parameters (e.g., surface wind speed, air temperature, dew point, etc.) and the surface radiation parameters. This particular formulation of the net surface heat flux together with the necessary climatological atmospheric parameters, are intended to provide a realistic and computationally efficient upper boundary condition for oceanic climate modeling.

The basic climatological data set used to compute  $T_A^*$  and  $Q_2$  was obtained from several sources. The surface atmospheric parameters were provided on a  $5^\circ \times 5^\circ$  Marsden subsquare grid by the National Climatic Center. The surface insolation under the clear sky condition was taken from the table in Kondratyev (1969), but reduced by 10 percent at all latitudes to be consistent with more recent estimates (Bunker, 1976). The total cloud cover needed for both long- and short-wave radiation calculations was obtained from Miller and Feddes (1971), who estimated the monthly mean cloud cover from the satellite measurements.

The monthly mean values of  $T_A^*$  and  $Q_2$  were computed over the global ocean for all calendar months, but only the annual mean values are shown in Fig. 1 and Fig. 2 to show the significant geographical dependence of these parameters. Although values are calculated in polar regions, the density in both the Arctic and Antarctic Oceans is not large enough to provide stable climatological means. As a result, the computed  $T_A^*$  and  $Q_2$  fields near the climatological sea-ice boundaries are noisy even in the annual mean maps.

The annual mean net surface heat fluxes (Fig. 3) were computed and compared with the earlier estimates by Budyko (1963) for the world ocean and Bunker (1976) for the North Atlantic Ocean. The flux patterns were in good agreement at middle latitudes but some significant discrepancies were found at high and low latitudes. These discrepancies are also apparent in the zonal mean values shown in Fig. 4, where more recent estimates by Ort and Vonder Haar (1976) are also plotted for comparison. A more detailed comparison of heat flux component shows that the major discrepancies are due to the estimates of the net radiation in the tropics and of the sensible heat fluxes in the high latitudes. We suspect that the solar insolation is somewhat overestimated in the present calculation mainly due to the use of the satellite-inferred cloud data which in the tropics, show systematically less cloud cover than the conventional ground observations (Fig. 5); the latter were used by both Budyko and Bunker. The relatively large heat fluxes in the high latitudes are probably due to the use of the heat transfer coefficient which are made to vary with the thermal stability and wind speed (Bunker, 1976).

In order to investigate the seasonal variability of the net flux, the monthly zonal mean values were computed and are shown in Fig. 6. The largest seasonal variabilities occur in the middle latitude oceans in both hemispheres. The relative magnitude of the variability, however, is greater in the northern oceans than in the southern oceans. This is consistent with the relatively stronger surface heat exchange processes in the northern ocean, especially in the vicinity of the major western boundary currents. For the purpose of comparison, the present result was checked with the independent calculations of Oort and Vonder Haar (1976). Their estimates of the net surface heat flux which was obtained as a residual of the vertically integrated atmospheric heat balance equation using satellite radiation measurements at the top of the atmosphere and conventional radiosonde data shows relatively less heating ( $\sim 50$  watts/m<sup>2</sup>) during the summer half year and very much less cooling at the high latitudes during the winter. The relative accuracy of these two independent estimates, however, is difficult to judge because of many uncertainties involved in the methods and data used in each estimate.

The parameterization of the net surface heat flux by  $T_s$ ,  $T_A^*$ , and  $Q_2$  emphasizes the important role of sea surface temperature in determining the net surface heating of the oceans. The comparison between the heat fluxes obtained from model-simulated and observed sea-surface temperatures for the same  $T_A^*$  and  $Q_2$  should give needed guidance for the development and verification of coupled ocean-atmosphere general circulation models.

#### REFERENCES

- Budyko, M. I., 1963: Atlas of the Heat Balance of the Earth. Akad. Nauk SSSR, Prezidium, Mezhdunarodnyy Geofiz. Komitet., 69 pp. [Also, Guide to the Atlas of the Heat Balance of the Earth, Transl. by I. A. Donehoo, U.S. Weather Bureau, WB/T-106, Washington, DC.]
- Bunker, A. F., 1976: Computations of surface energy flux and annual air-sea interaction cycles of the North Atlantic Ocean. Mon. Wea. Rev., 104, 1122-1140.
- Han, Y.-J., S.-W. Lee, S. K. Esbensen and Y. Kushnir, 1980: Computation of the seasonal cycle of the surface heat flux over the global ocean. Proceedings of the Fifth Annual Climate Diagnostics Workshop, Climatic Analysis Center, NOAA, 391 pp.
- Haney, R. L., 1971: Surface thermal boundary condition for ocean circulation models. J. Phys. Oceanogr., 1, 241-248.
- Kondratyev, K. Ya., 1969: Radiation in the Atmosphere, Academic Press, 912 pp.
- Miller, D. B., and R. G. Feddes, 1971: Global atlas of relative cloud cover 1967-1970. U.S. National Environmental Satellite Service and U.S.A.F. Environmental Technical Applications Center, AD739434, Report No. 1, Washington, DC, 237 pp.
- Oort, A. H., and T. H. Vonder Haar, 1976: On the observed annual cycle in the ocean-atmospheric heat balance over the Northern Hemisphere. J. Phys. Oceanogr., 6, 781-800.

ORIGINAL PAGE IS  
OF POOR QUALITY

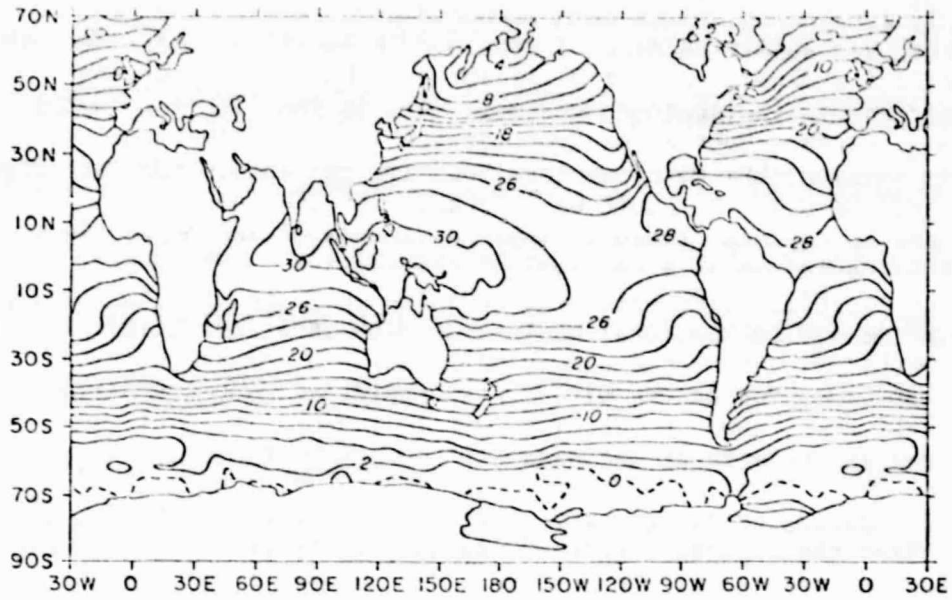


Fig. 1. Computed annual mean atmospheric equilibrium temperature ( $T_A^*$ ).  
The isolines are drawn at 2°C intervals with the 0°C isotherm dashed.

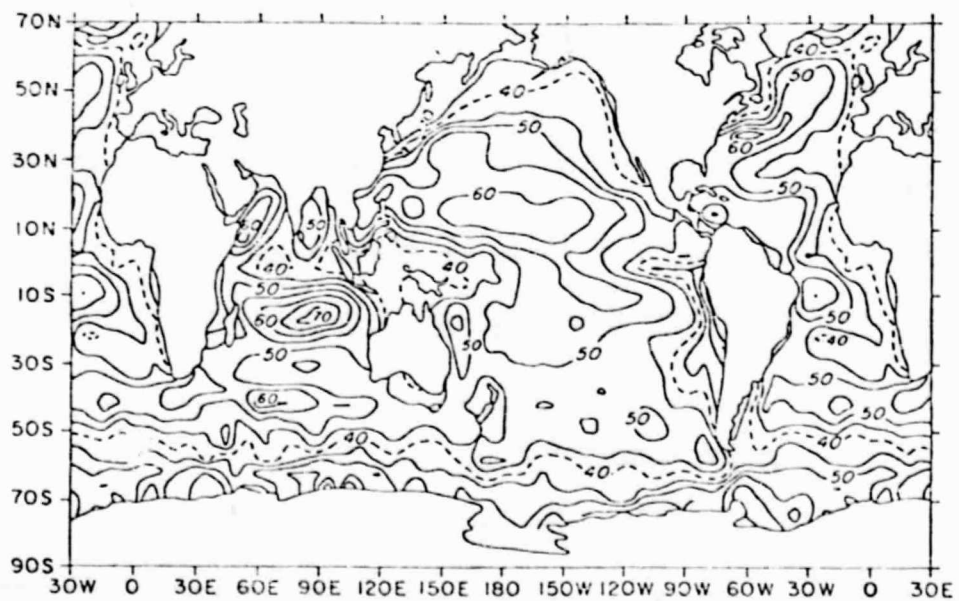


Fig. 2. Computed annual mean proportionality constant (Watts/m<sup>2</sup>/°C).  
The isolines are drawn at 5 Watts/m<sup>2</sup>/°C with the reference line (40) dashed.

ORIGINAL PAGE IS  
OF POOR QUALITY

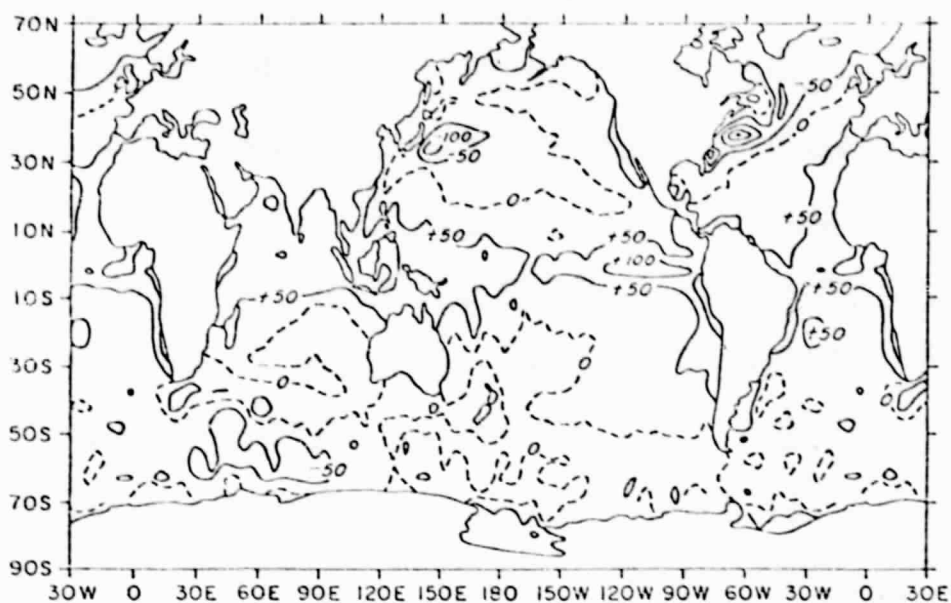


Fig. 3. Computed annual mean net surface heat flux ( $\text{Watts/m}^2$ ). The isolines are drawn at  $50 \text{ Watts/m}^2$  intervals with the reference line (0.0) dashed.

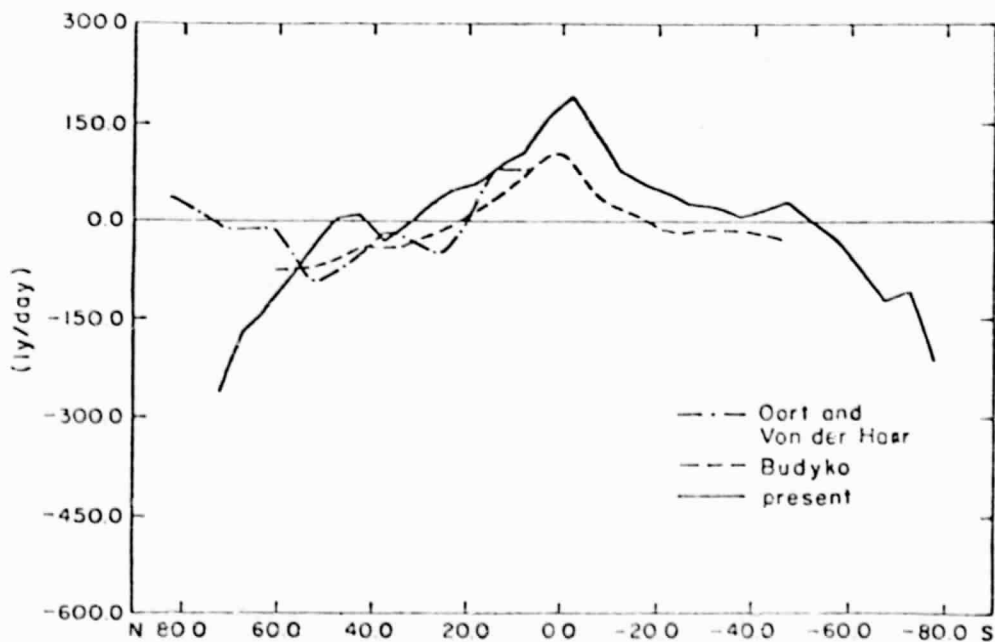


Fig. 4. Computed zonal mean of the annual mean net surface heat flux ( $\text{l}_y/\text{day}$ ).

ORIGINAL PAGE IS  
OF POOR QUALITY

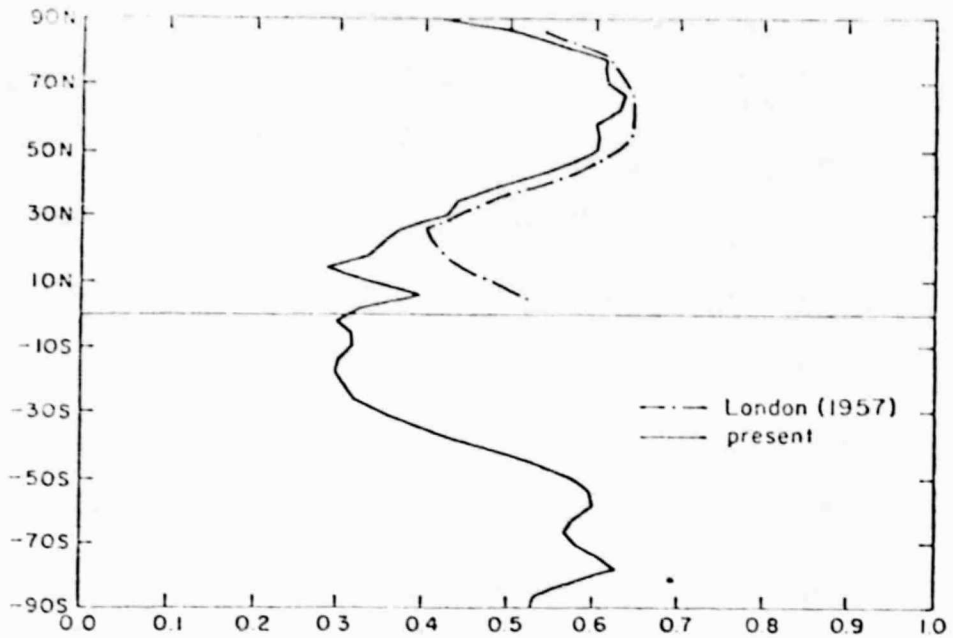


Fig. 5. Latitudinal distribution of the zonal mean of the annual mean cloud cover (fractions).

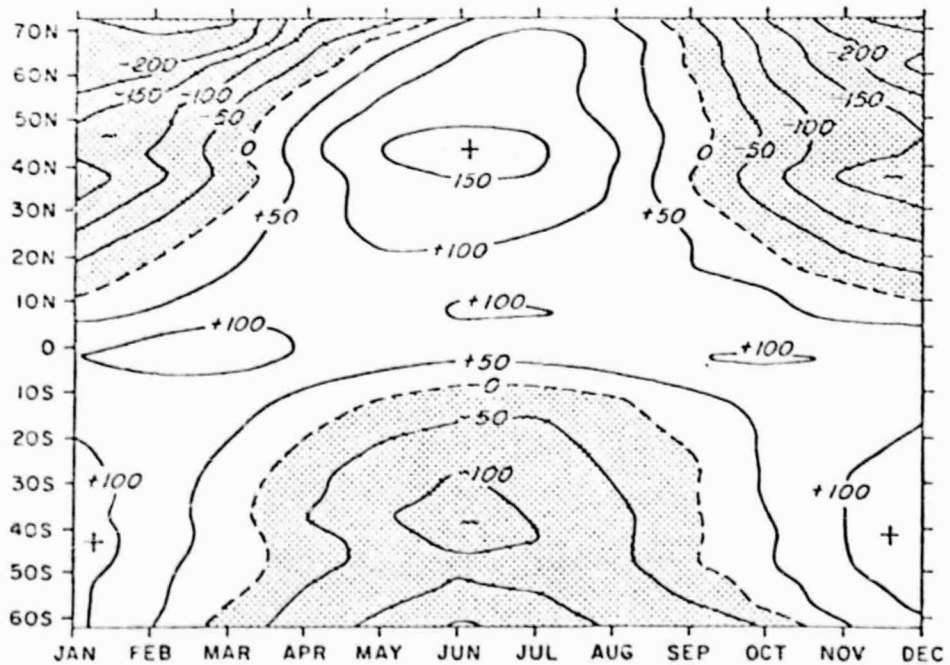


Fig. 6. Time latitude cross section of the zonal mean net surface heat flux ( $\text{Watts/m}^2$ ). The isolines are drawn at  $50 \text{ Watts/m}^2$  intervals with the zero line dashed.

## SPATIAL AND TEMPORAL SCALES OF TIME-AVERAGED 700 MB HEIGHT ANOMALIES

D. Gutzler

## 1. INTRODUCTION

The monthly and seasonal forecasting technique currently in use by the National Meteorological Center (NMC) is based to a large extent on the extrapolation of trends in the positions of the centers of time-averaged geopotential height anomalies. The complete forecasted height pattern is subsequently drawn around the forecasted anomaly centers.

To test the efficacy of this technique, we have examined time series of observed monthly mean and 5-day mean 700 mb geopotential heights. Autocorrelation statistics were generated to document the tendency for persistence of anomalies. These statistics were compared to a "red noise" hypothesis to check for evidence of possible preferred time scales of persistence. Space-time spectral analyses at middle latitudes were checked for evidence of periodicities which could be associated with predictable month-to-month trends. A local measure of the average spatial scale of anomalies was devised for guidance in the completion of the anomaly pattern around the forecasted centers.

## 2. SPATIAL SCALE

The average spatial scale of 700 mb height anomalies was determined by considering the area surrounding each gridpoint over which contemporaneous heights were highly correlated. To estimate the tendency for anomalies to cover different areas over different geographical regions, the complete set of spatial cross-correlation maps for both monthly and 5-day means was computed, following the procedure used by Wallace and Gutzler (1981). Each map shows the contemporaneous correlation coefficient between heights at a specified base gridpoint and all other gridpoints. As discussed by Wallace and Gutzler, the size of the region of high correlation surrounding each base gridpoint is an indication of the average horizontal extent of height anomalies in the vicinity of that gridpoint. To quantify this extent, the approximate area within the 0.7 contour on each cross-correlation map was computed by summing the areas associated with the  $4^\circ$  by  $5^\circ$  patch centered on each gridpoint surrounding the base gridpoint which was correlated with a coefficient greater than 0.7.

Figure 1 shows the geographical distribution of the horizontal extent statistic for wintertime monthly means plotted at each gridpoint. Southward of the thick dashed line, the calculated area of high correlation extends to the boundary of the data set, and therefore is probably an underestimate of the actual area.

Anomalies tend to be largest over the central Pacific Ocean, central Asia, northern Siberia, and Greenland. Secondary maxima in Figure 1 exist off the southeastern coast of the United States, over the northern Atlantic Ocean, and south of Japan. Regions where anomalies tend to be small include the Gulf of Alaska, the central United States, eastern China, and the North Sea.

### 3. PERSISTENCE

The autocorrelation of monthly mean data (not shown) was found to be quite low northward of 30°N.

The geographical distribution of autocorrelation for the 5-day mean time series with one lag, based on all months, is shown in Figure 2. Maxima in the autocorrelation field appear around the edge of the data set near the tropics, over the north central oceans, and over the polar region north of the Soviet Union.

Klein (1951) postulated that height variability was well simulated by a first-order autoregressive or "red noise" model, in which anomalies relax exponentially toward a climatological mean value. If there exists a preferred time scale for atmospheric persistence, as suggested by Shukla and Mo (1981), then this red noise hypothesis should not serve as a good predictor of the observed 5-day mean autocorrelation over regions of preferred persistence. The hypothesis was tested by comparing the observed 5-day mean autocorrelation with hypothetical values extrapolated from the observed daily autocorrelation at each gridpoint. Observed and hypothetical autocorrelation values generally agreed to within 30%, but distinct geographical variations could be seen. It was found that anomalies tend to relax toward climatology somewhat faster than red noise over the eastern oceans, western continents, and polar regions (particularly Siberia and northern Canada). Anomalies persist longer than a red noise model would predict over the subtropics and western oceans. The pattern of discrepancies closely resembles the band-pass variance field calculated by Blackmon (1976), which included fluctuations with periods between 2.5 and 6 days. Thus, the observed 5-day mean autocorrelation is larger than expected over regions associated with strong baroclinic wave development.

In summary, significant autocorrelation exists in the time series of 700 mb height 5-day means. This autocorrelation could be explained in terms of two components. First, long-period fluctuations account for much of the tendency for persistence over the entire hemisphere. These fluctuations comprise the variance of monthly means, and show up in the daily autocorrelation field. The large amount of this low frequency variance explains the reasonably good agreement with Klein's red noise hypothesis. Second, baroclinic disturbances create a significant component of variance at time scales too short to be reflected in daily autocorrelation statistics, but which enhance the 5-day mean autocorrelations over the storm track regions off the east coasts of the continents. Autocorrelation did not explain a significant amount of the variance of monthly means.

### 4. PERIODICITY

Periodicity in the 700 mb height time series was studied using a space-time spectral analysis. In this technique, the total space-time variance of heights along a specified latitude circle is decomposed into separate frequency and zonal wavenumber components using a Fast Fourier Transform (FFT). The routine used here is described in more detail by Straus and Shukla (1981). Height anomalies were used for the analysis, so that the stationary component of each wave was removed, and only the transient component, minus the annual cycle, was left.

The space-time spectral analysis of monthly mean 700 mb height anomalies at latitude 60°N is plotted in Figure 3. The wavenumber spectra (the columns of Figure 5) were smoothed by averaging over six discrete spectral estimates, so that each entry in Figure 3 contains twelve degrees of freedom. Isolines of variance per unit frequency interval (units  $m^2 \cdot months$ ) were drawn on the basis of the smoothed wavenumber spectra assuming that the variance was a slowly varying function of both frequency and zonal wavenumber.

The significance of maxima in the space-time analysis can be estimated from a null hypothesis that the variance is independent of both frequency and wavenumber. The total variance would then be evenly divided among the 286 spectral estimates included in Figure 3. This amounts to 340 units per estimate. Any observed spectral estimates greater than 450 units are then significant at the 99% level. It should be kept in mind that, in the absence of an a priori expectation that peaks would appear at specific frequencies and wavenumbers, 1% of the estimates are expected by random chance to exceed the 99% significance level.

The spectra for wavenumbers 1-3 are almost entirely above this level, and nearly all the variance (95%) is explained by fluctuations of the zonal mean and wavenumbers 1-4. This re-emphasizes the dominance of large-scale anomalies.

A slight tendency for redness is demonstrated by the larger variances explained by lower frequencies in all wavenumbers. This is representative of the small (but generally non-zero) magnitude of autocorrelation of monthly means shown previously. The spectral peaks observed in higher frequencies are probably not significant because of the aliasing problems inherent in a time series of monthly means, each of which is itself a finite sample of observations containing a statistical uncertainty (Trenberth, 1980).

## 5. CONCLUSION

Nap et al. (1981) verified several operational forecasting schemes (including NMC's), and found that they all possessed little skill. The slight persistence and lack of dominant periodicities in the monthly mean time series indicate that the potential for improvement in the skill of trend-based long-range forecasting techniques is not great. However, recent modeling experiments by Shukla (1981) suggest that the atmosphere is dynamically predictable for up to one month. The results here suggest that progress in long-range forecasting will come through new approaches to the problem, rather than more detailed analyses of longer time series of the same set of atmospheric variables.

## REFERENCES

- Blackmon, M. L., 1976: A climatological spectral study of the 500 mb geopotential height of the Northern Hemisphere. J. Atmos. Sci., 33, 1607-1623.
- Blackmon, M. L., R. A. Madden, J. M. Wallace, and D. S. Gutzler, 1979: Geographical variations in the vertical structure of geopotential height fluctuations. J. Atmos. Sci., 36, 2450-2466.

- Klein, W. H., 1951: A hemispheric study of daily pressure variability at sea level and aloft. J. Meteor., 8, 332-346.
- Nap, J. L., H. M. van den Dool, and J. Oerlemans, 1981: A verification of monthly weather forecasts in the seventies. Mon. Wea. Rev., 109, 306-312.
- Shukla, J., 1981: Dynamical predictability of monthly means. J. Atmos. Sci., 38, 2547-2572.
- Shukla, J., and K. Mo, 1981: Seasonal variation of blocking. Atmospheric and Oceanographic Research Review - 1980. Laboratory for Atmospheric Sciences, Modeling and Simulation Facility, NASA Goddard Space Flight Center.
- Straus, D. M., and J. Shukla, 1981: Space-time spectral structure of a GLAS general circulation model and a comparison with observations. J. Atmos. Sci., 38, 902-917.
- Trenberth, K. E., 1980: Atmospheric quasi-biennial oscillations. Mon. Wea. Rev., 108, 1370-1377.
- Wallace, J. M., and D. S. Gutzler, 1981: Teleconnections in the Northern Hemisphere geopotential height field during winter. Mon. Wea. Rev., 109, 784-812.

ORIGINAL PAGE IS  
OF POOR QUALITY

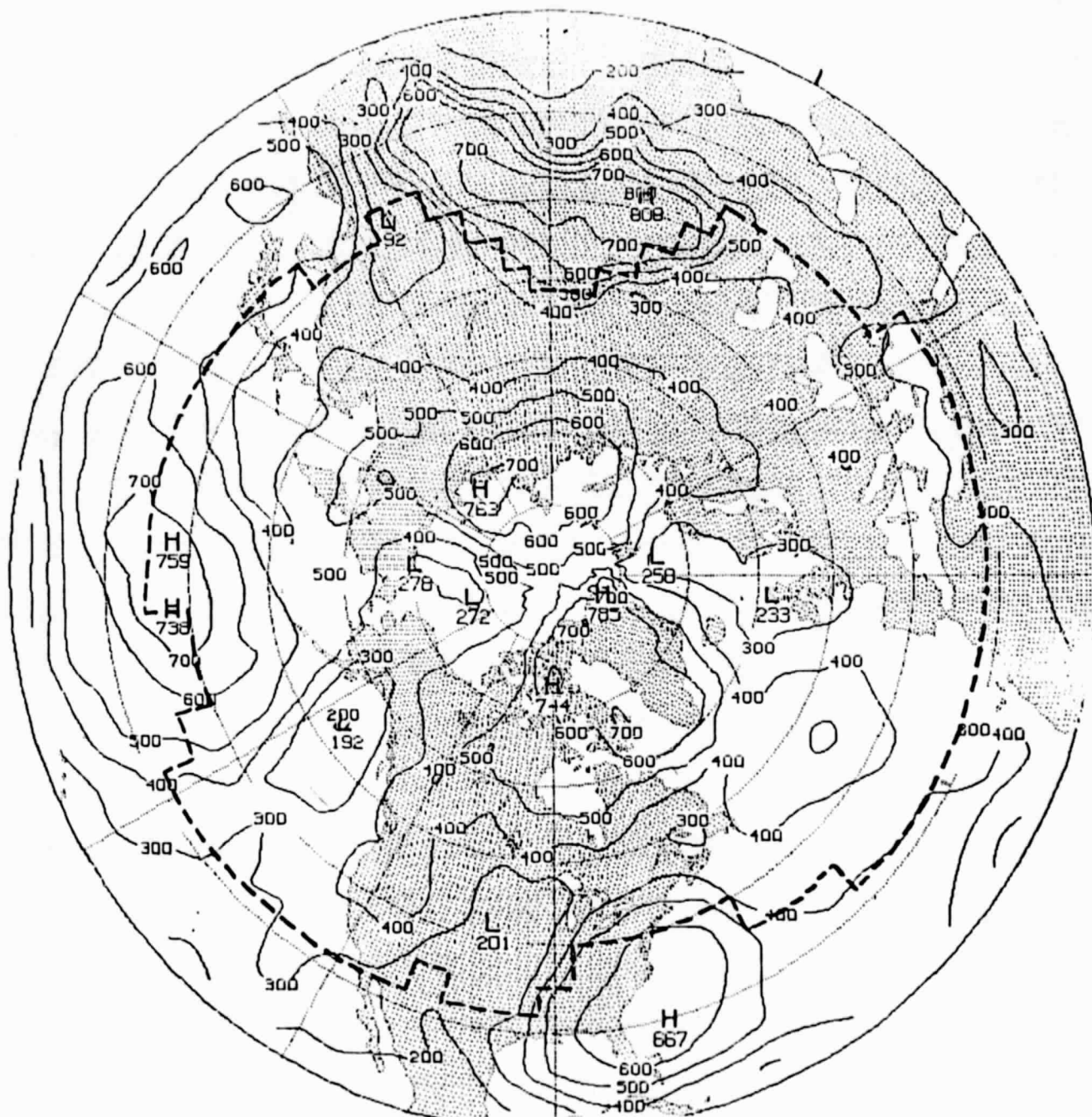


Figure 1. Geographical distribution of the area within the 0.7 contour on the spatial cross-correlation map for each gridpoint, based on a 15 winter sample of monthly mean height anomalies for the months of December, January, and February. Contour interval  $100 \times 10^4 \text{ km}^2$ . Southward of the heavy dashed line, the 0.7 correlation contour intersects the southern boundary of the data set, so that the calculated area may be underestimated.



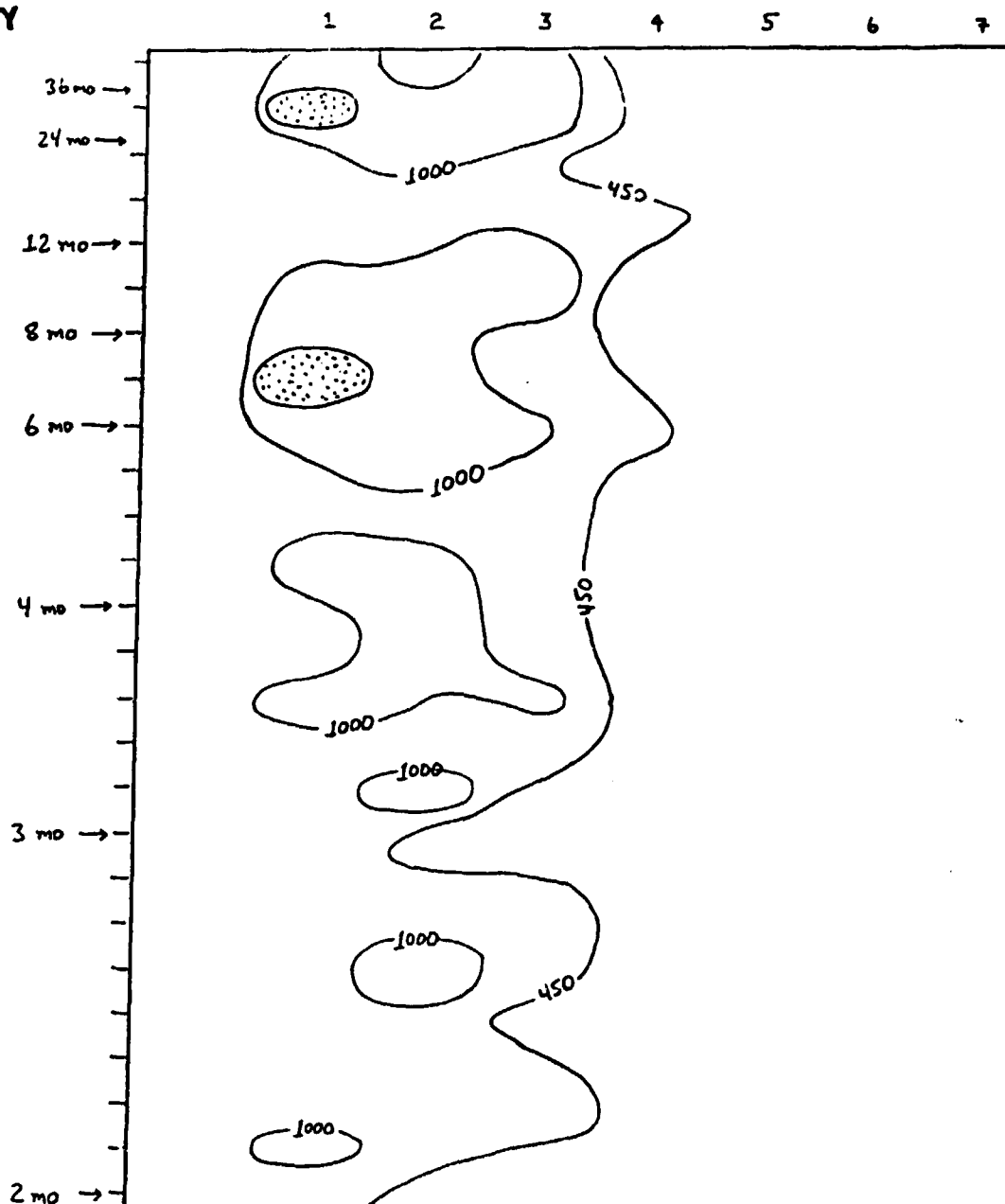


Figure 3. Variance of monthly mean 700 mb height at 60°N as a function of frequency and wavenumber for the period 1953-1978. Contours represent isolines of variance per unit frequency interval (units  $m^2 \cdot \text{months}$ ). The 450 unit contour is the 99% significant level, testing for departure from white noise. Light stippling indicates spectral peaks with magnitudes greater than 2000 units. The tick marks on the vertical axis denote the midpoint of the frequency bands, and indicate the degree of frequency resolution used.

D21

MID-LATITUDE WIND FORCED OCEAN CIRCULATION STUDIES

D.E. Harrison

A simple barotropic vorticity equation model has been developed to study some of the various modeling factors that affect the characteristics of strong western boundary currents like the Gulf Stream and Kuroshio. Successful prediction of sea surface temperature, both in the climatological mean and over periods as short as one month requires that the heating tendency, due to horizontal advection of heat by these currents, be accurately modeled. Conventional, coarse resolution ocean models do not satisfactorily reproduce the dominant features of these currents. It is important to understand why they do not and what must be done in order that they will be able to do so in the future.

The first set of calculations, making use of a simple linear bottom drag law as used by Veronis (1966), has been completed and submitted for publication (Harrison and Stalos 1981). This work establishes the vital importance of understanding the mechanisms of vorticity loss in the western boundary currents and the necessity of studying adjoining circulation systems together rather than separately. The classical wind driven ocean studies, which focus on a single subtropical gyre driven by a anticyclonic wind stress pattern, do not allow for the possibility of vorticity transport by the circulation, out of the gyre. When this process is permitted by the model boundary conditions, geometry and forcing, dramatically different-circulation patterns result (Figures 1 and 2).

Apart from these qualitative results, it is also important to understand quantitatively how the model "Gulf Streams" depend on the modeling parameters. A simple theoretical argument has been developed that predicts that the speed of the eastward flowing "separated Gulf Stream" will vary as:

$$U_j \sim \frac{L_x}{K} \frac{\text{curl}_z \tau}{D}$$

where  $L_x$  is the east-west basin dimension,  $K$  is the linear drag inverse decay time,  $\text{curl}_z \tau$  is the maximum wind stress curl and  $D$  is the mean depth of the fluid layer. The width of this current is predicted to vary like:

$$L_j \sim \frac{U_j}{(K L_x \beta)^{1/2}}$$

where  $\beta$  is the variation of Coriolis parameter with latitude, so long as

$$U_j < U_* \equiv K L_x$$

When  $U_j \gg U_x$ , the classic inertial scaling

$$L_j \sim \frac{U_j}{\beta}^{1/2}$$

should be observed. These results are confirmed by numerical experiments (Figures 3, 4). To our knowledge this is the first non-linear and viscous system whose quantitative behavior has been understood from first principles.

Further work is underway to understand how these results generalize when other frictional mechanisms are used, and baroclinic studies will be initiated after the barotropic calculations are complete.

#### REFERENCES

Harrison, D.E., and S. Stalos, 1981: On the wind-driven ocean circulation. (submitted)

Veronis, G., 1966: Wind-driven ocean circulation. Part II Deep-Sea Res. 13, 31-55.

C-3

Figure 1

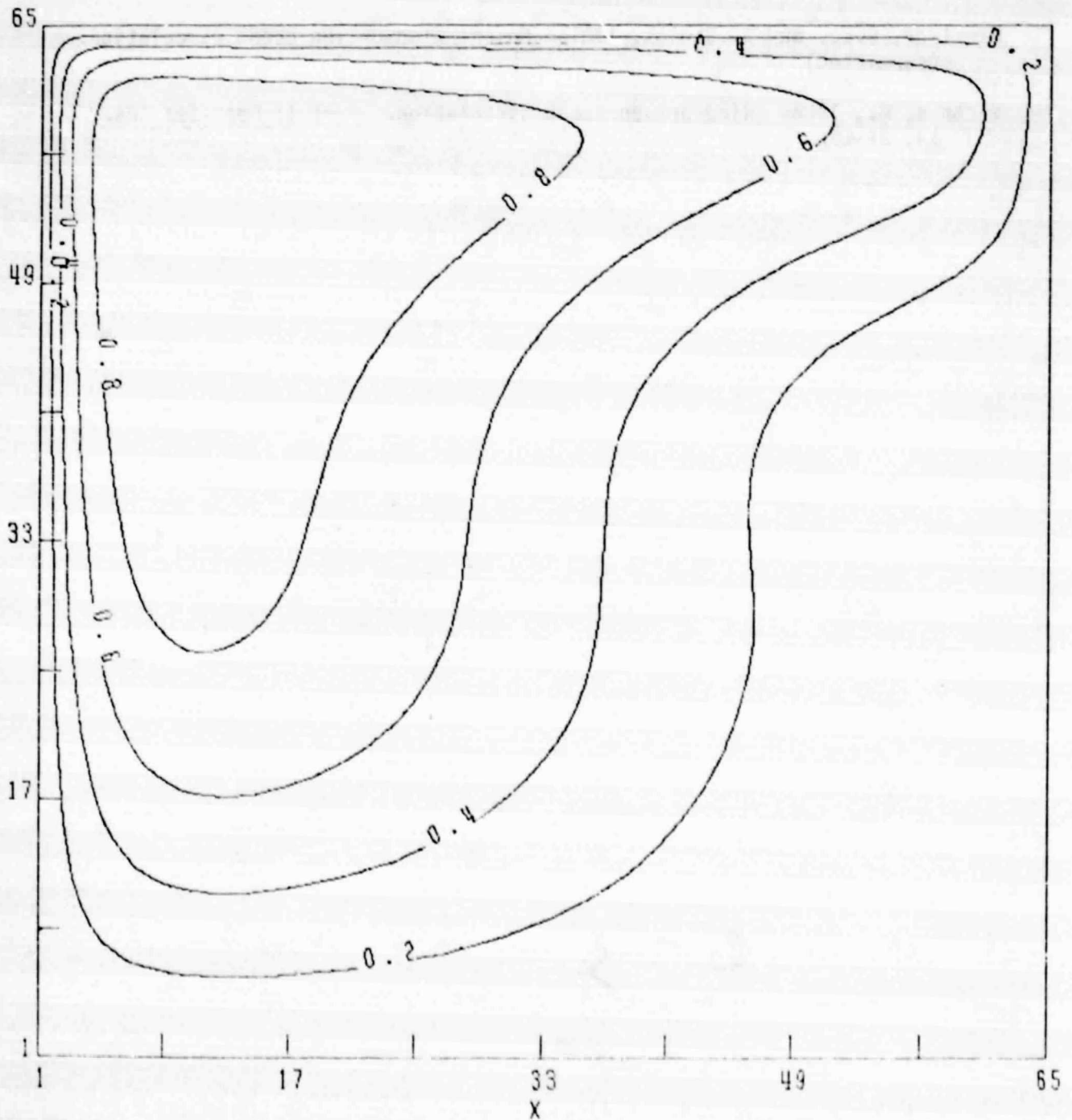
ORIGINAL PAGE IS  
OF POOR QUALITY

NORMALIZED BY  $9.853E+12$

MODEL B

$R = 2.000E-02$

$E = 5.000E-02$



Contour lines of normalized  
stream function

Figure 2

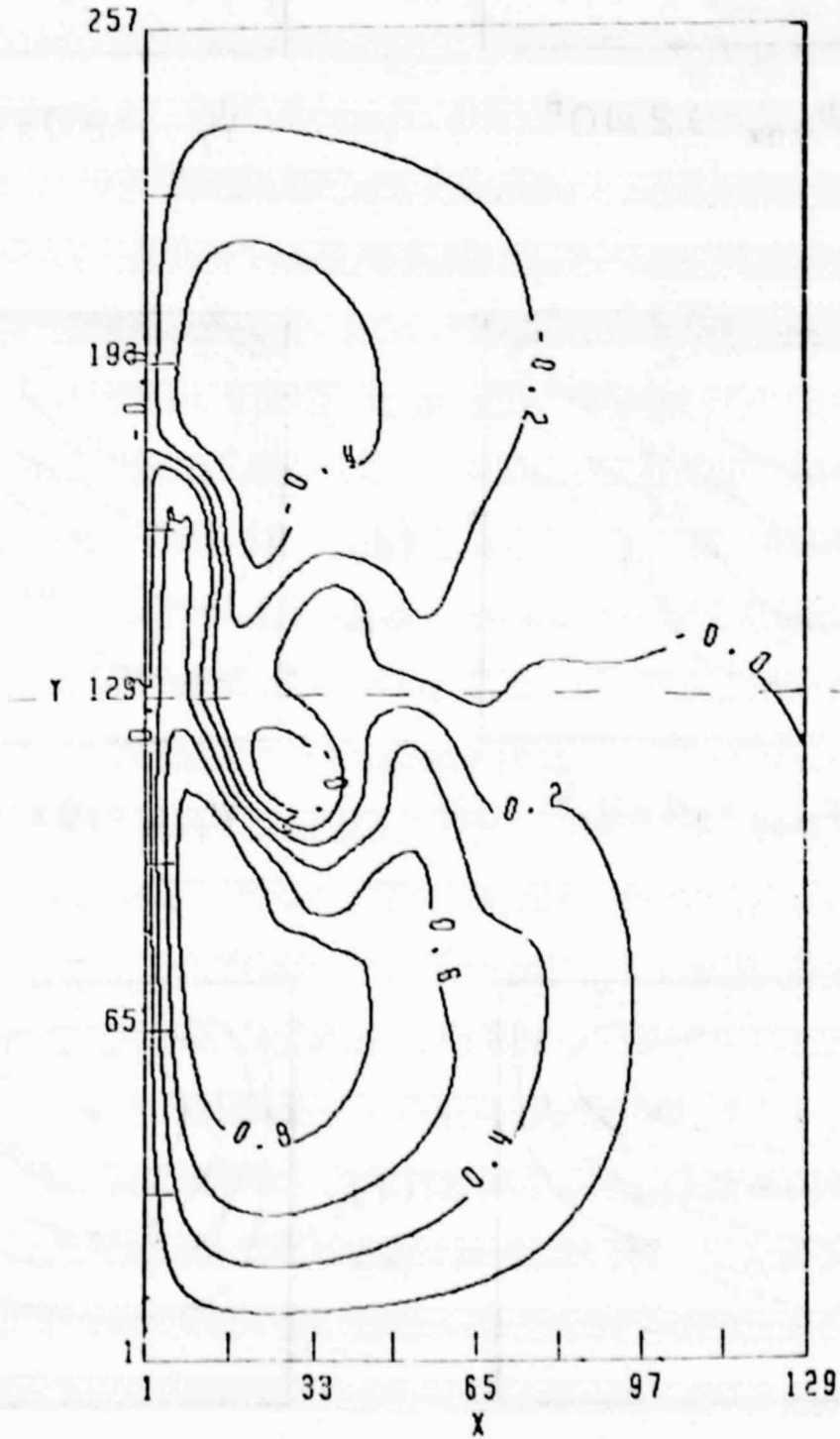
ORIGINAL PAGE IS  
OF POOR QUALITY

NORMALIZED BY  $8.941E+12$

MODEL B

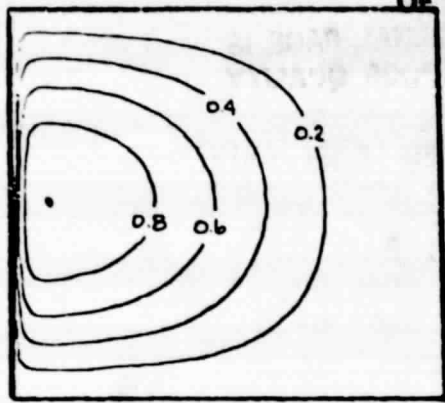
$R = 2.000E-02$

$E = 5.000E-02$



Contour lines of normalized  
stream function

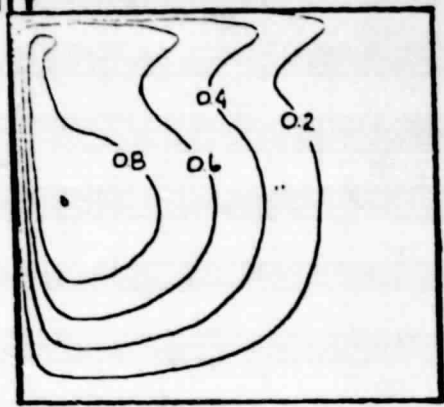
(a)



$$\psi_{\max} = 9.2 \times 10^6$$

(b)

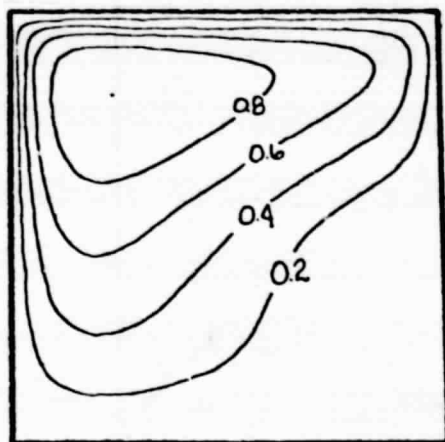
#2:



$$\psi_{\max} = 9.0 \times 10^6$$

(c)

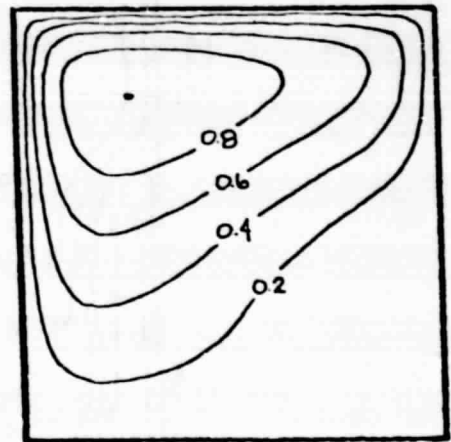
#4:



$$\psi_{\max} = 14 \times 10^6$$

(d)

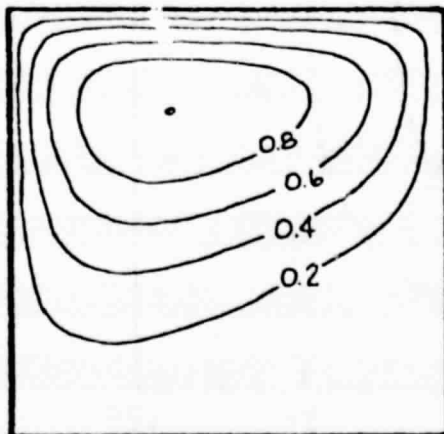
#5:



$$\psi_{\max} = 16 \times 10^6$$

(e)

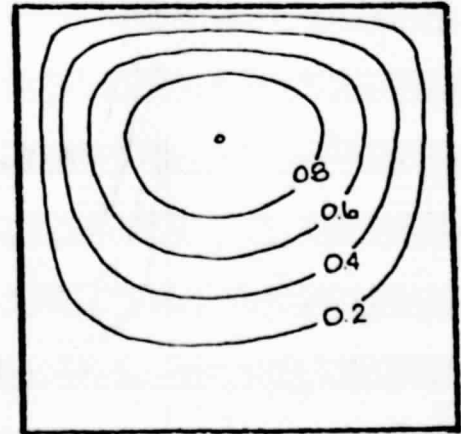
#8:



$$\psi_{\max} = 23 \times 10^6$$

(f)

#9:

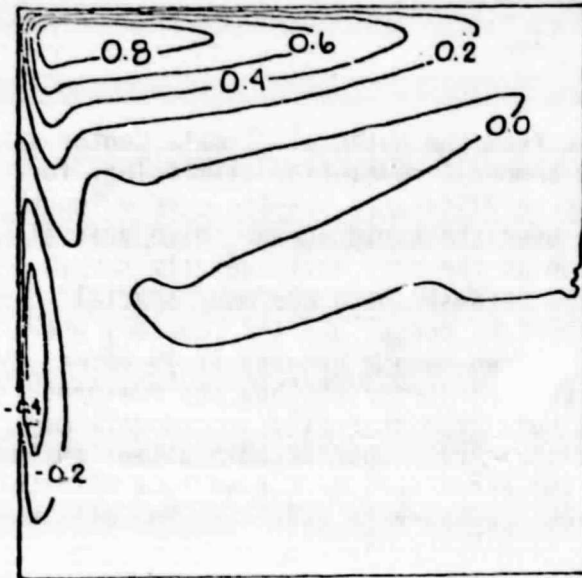


$$\psi_{\max} = 37 \times 10^6$$

Figure 3

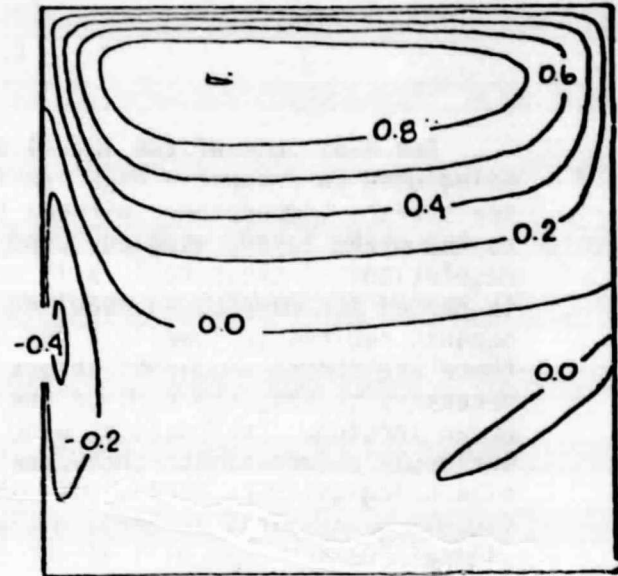
ORIGINAL PAGE IS  
OF POOR QUALITY

(a)  
 $R = 1 \times 10^{-2}$



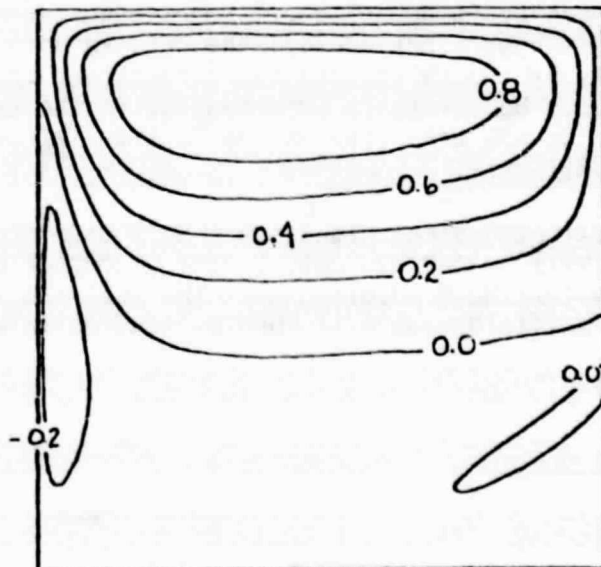
$$\psi_{\max}^D = 5.6 \times 10^6$$

(b)  
 $R = 3 \times 10^{-2}$



$$\psi_{\max}^D = 10 \times 10^6$$

(c)  
 $R = 3.5 \times 10^{-2}$



$$\psi_{\max}^D = 12 \times 10^6$$

Figure 4

## SEA SURFACE DATA STUDIES

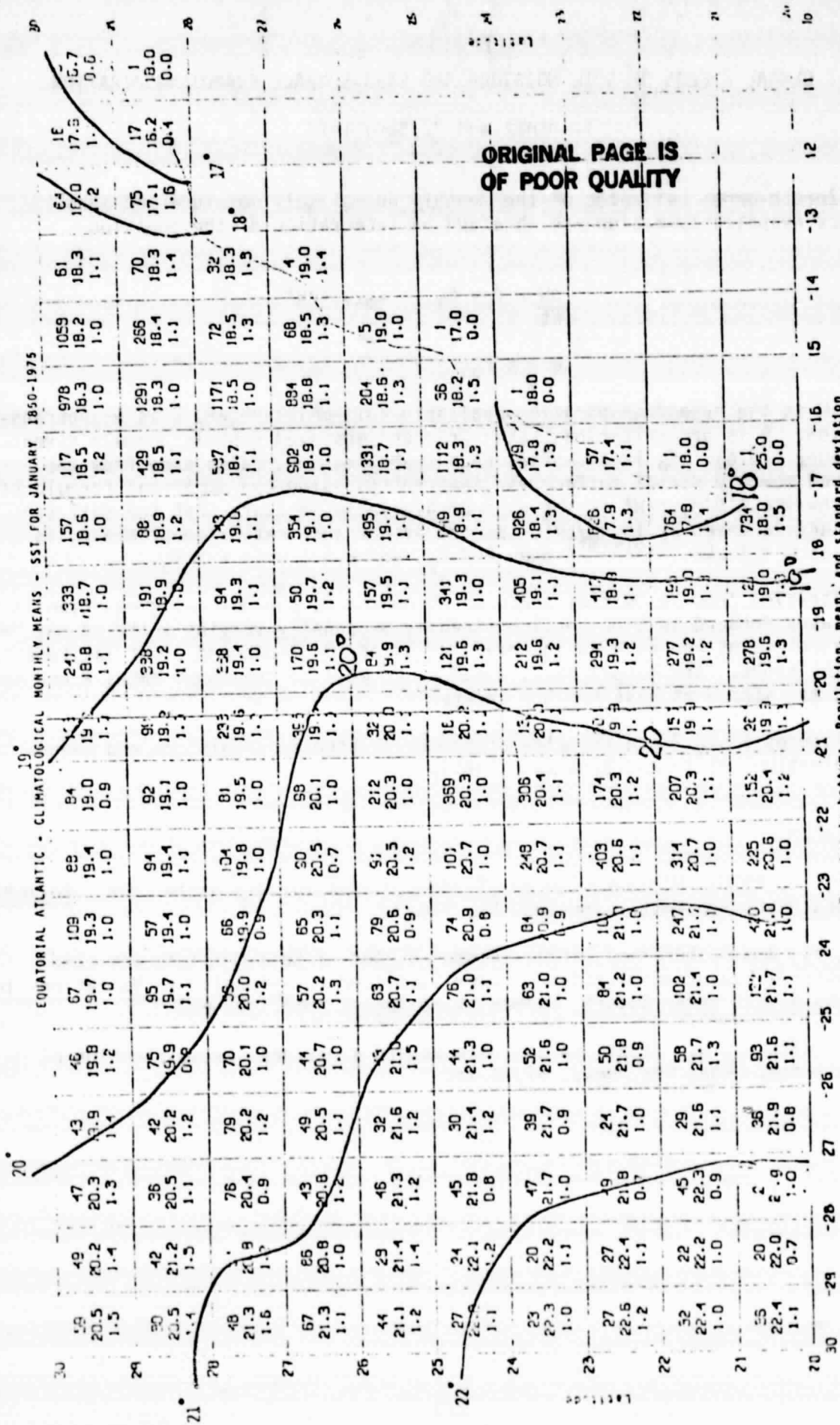
D.E. Harrison

The HSST form of the TDF-11 data set from the National Climate Center is being used to produce a high spatial and temporal resolution climatology for sea surface temperature, air-sea temperature difference kinetic energy input to the mixed layer, wind and wind stress over the world ocean. High spatial resolution, as close to  $1^\circ \times 1^\circ$  resolution as the data will usefully permit, is needed for many ocean modeling purposes because there are many special oceanic regions (primarily along or adjacent to coasts and the Equator) where there are strong gradients across a few hundred km and because it is often necessary to know the curl of the wind stress in order to know the dominant ocean forcing. Estimates of wind stress curl from spatially smooth data may seriously underestimate the magnitude of the curl. Considerable attention is also being given to making estimates of the error bars on the various climatological quantities, as error estimates are necessary to establish the climatological "noise" that will affect climate anomaly studies.

The Atlantic Ocean climatology calculations using data between 1850 and 1975 have been made, and detailed analysis of these results is now underway. Figure 1 shows SST results for January, off the African coast ( $10^\circ\text{W}$ - $30^\circ\text{W}$ ,  $20^\circ\text{N}$ - $30^\circ\text{N}$ ). Isotherms have been sketched in; the data in each  $1^\circ$  box are: number of observations, average value and standard deviation. Fig. 1 also illustrates several features characteristic of the data set: the number of observations per  $1^\circ$  square per unit time varies greatly within a  $10^\circ$  square region (from 1 observation to 1331 observations in this case), obviously spurious values can be found in the  $1^\circ$  means when the number of observations is very small (here  $< 5$  obs.) but overall the data vary quite consistently on the  $1^\circ$  scale without any smoothing, and there is strong spatial variation on the  $1^\circ$  scale that would be seriously smoothed out if the data were averaged over, say,  $5^\circ$ , squares as has been done in previous empirical orthogonal function analyses of the Atlantic.

After the climatological results are well understood and documented, anomaly studies will be carried out, to try to better document the variations from climatology that have occurred over the last 130 years in the Atlantic. The Indian and Pacific Oceans will then be studied in a similar fashion.

EQUATORIAL ATLANTIC - CLIMATOLOGICAL MONTHLY MEANS - SST FOR JANUARY 1850-1975



From top to bottom: Population, mean, and standard deviation

West Longitude

West Longitude

ORIGINAL PAGE IS OF POOR QUALITY

MIT  
GLOBAL FIELDS OF SOIL MOISTURE AND LAND-SURFACE EVAPOTRANSPIRATION

Y. Mintz and Y. Serafini

Zeroth-order estimates of the monthly normal soil moisture and land-surface evapotranspiration are obtained by integration of the equation,

$$\frac{dW}{dt} = P - E, \quad W_{\max} = W^*,$$

$$E = \beta E_p,$$

where  $W$  is the evapotranspiration-available soil moisture and  $E$  is evapotranspiration.  $P$  is precipitation, taken from the observed monthly normals given by Jaeger (1976).  $E_p$  is potential evapotranspiration, calculated from the observed monthly normal surface air temperature using the empirical formula of Thornthwaite (1948).  $W^*$  is the maximum available moisture that the soil can hold, and is taken as  $15 \text{ gm/cm}^2$ .  $\beta$ , the evapotranspiration coefficient, is taken as  $\beta = 1 \exp^{-0.8(W/W^*)}$  when  $P < E_p$ , and  $\beta = 1$  when  $P > E_p$ .

Starting from an initial state in which  $W = 0$ , the governing equation is integrated forward in time until a steadily seasonally varying state is reached. The calculations are made at intervals of  $5^\circ$  of longitude and  $4^\circ$  of latitude over the globe. The output data,  $W$  and  $E$ , as well as the input data,  $P$  and  $E_p(T)$ , are stored at half-monthly intervals.

Figures 1 and 2 are examples of the calculated soil moisture and evapotranspiration (Mintz and Serafini, 1981).

#### REFERENCES

- Jaeger, L., 1976: Monatskarten des Niederschlages für die ganze Erds. Berichte des Deutschen Wetterdienstes, Nr. 139.
- Mintz, Y., and Y. Serafini, 1981: Global Fields of Soil Moisture and Land-Surface Evapotranspiration. Paper Submitted to Symposium on Variations in the Global Water Budget, Oxford, 9-15 August 1981. xx pp.
- Thornthwaite, C. W., 1948: An approach toward a rational classification of climate. Mon. Wea. Rev., 67, 4-11.

ORIGINAL PAGE IS  
OF POOR QUALITY

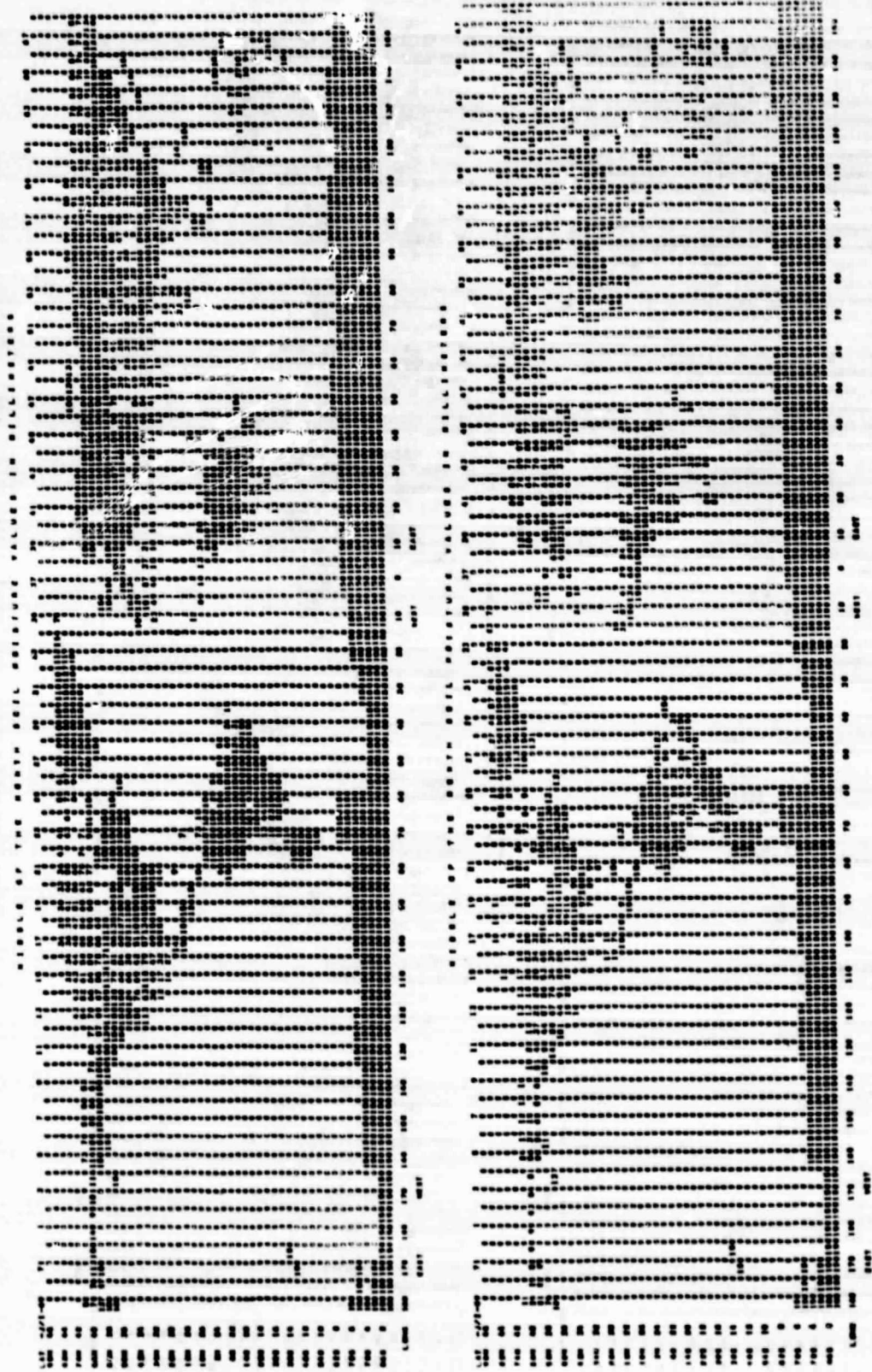


Fig. 1. Soil moisture (mm) in mid-January (top); and mid-July (bottom).

ORIGINAL PAGE IS  
OF POOR QUALITY

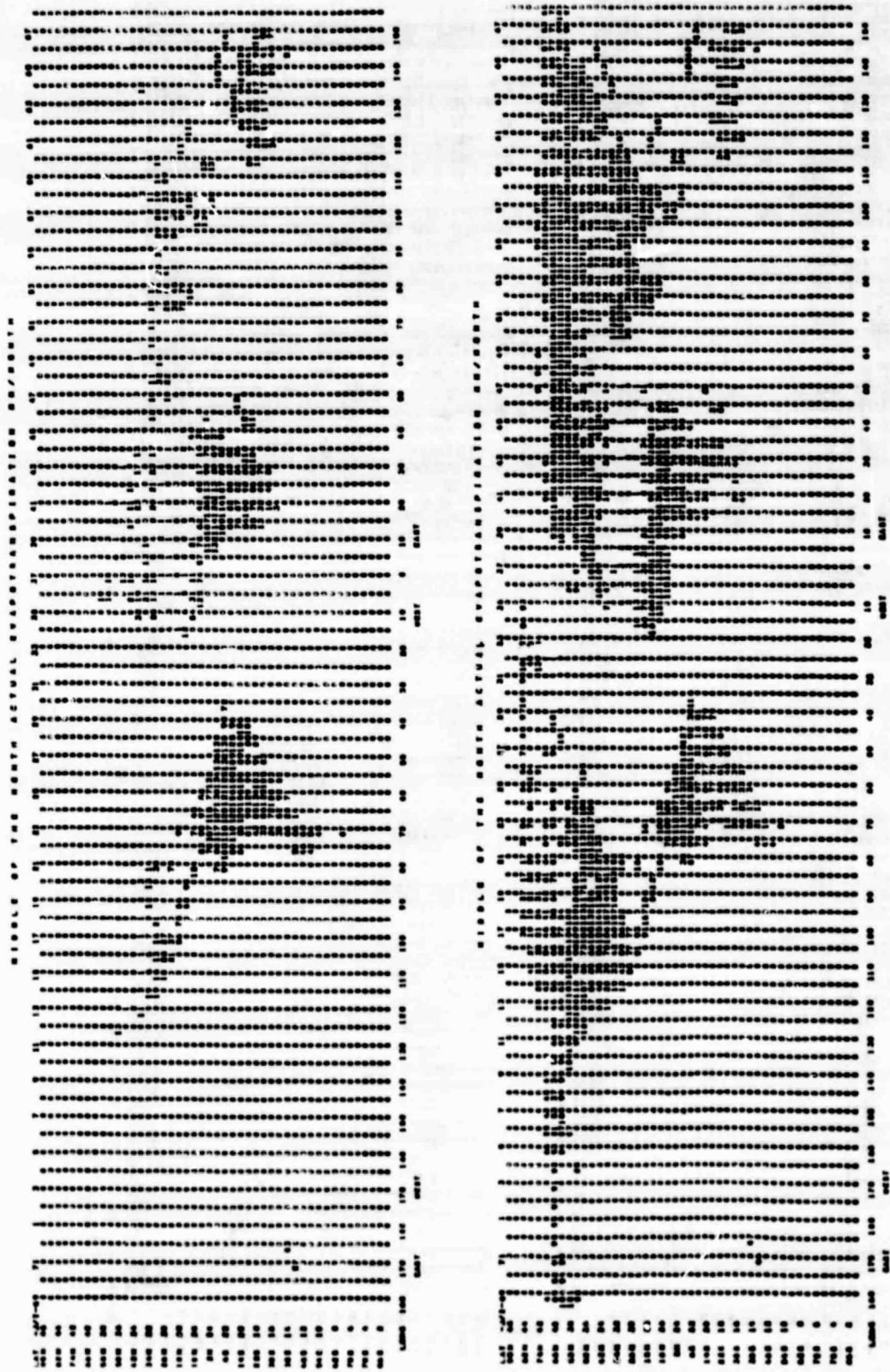


Fig. 2. Evapotranspiration (mm/day) in mid-January (top); and mid-July (bottom).

## SEASONAL VARIATION OF BLOCKING

J. Shukla and K. C. Mo

We have calculated the seasonal variation of frequency of blocking and its geographical location by examining the grid point values of daily 500 mb geopotential height over the Northern Hemisphere for 15 consecutive years (1963-1977). Blocking events are identified objectively by requiring that a large positive anomaly of a specified magnitude persist for 7 days or more. The magnitude of the threshold anomaly is assumed to be 200 gpm for winter, 100 gpm for summer, and 150 gpm for fall and spring.

It is found that the geographical locations of the maximum frequency, characterized by three distinctly different maxima, remains nearly the same in all the four seasons. These maxima coincide with the maxima of the low frequency and total variance. If the persistence criteria is changed to 1-3 days, the geographical distribution of frequency for winter is very similar to the band-pass variance, showing maximum values in the areas of storm tracks. Seasonal invariance of the locations of maximum blocking events suggests the important role of seasonally invariant forcing due to mountains.

Our principal conclusions are as follows:

1) Large scale persistent anomalies of positive sign are more frequent than those of negative sign. As also noted by Charney et al. (1981), amplified blocking ridges persist longer than either deeper troughs or weaker ridges.

2) There are three distinct centers of maximum blocking activity. They occur in the Pacific to the west of the Rockies, in the Atlantic to the west of the Alps and Scandanavian Mountain ranges, and over land to the west of Ural Mountains of USSR. These relatively preferred locations of persistent anomalies do not change with season.

3) A persistence criteria of 1-3 days represents storm tracks, and the resulting features are distinctly different from the persistence criteria of seven days or more.

4) Occurrence of anomalous seasonal mean anomalies accounts for less than 25% of the persistent anomalies identified as blocking events.

### REFERENCES

Charney, J. G., J. Shukla, and K. C. Mo, 1981: Comparison of barotropic blocking theory with observation. J. Atmos. Sci., 38, 762-779.

B. CLIMATE MODELING

PRECEDING PAGE BLANK NOT FILMED

## THE SEASONAL-CYCLE CLIMATE MODEL

L. Marx and D. Randall

The GLAS climate model has undergone several modifications in preparation for the 400 day "seasonal cycle" run. The seasonal cycle run will become the control run for the comparison with runs utilizing codes and parameterizations developed by outside investigators. The GLAS climate model currently exists in two parallel versions: one running on the Amdahl at GMSF and the other running on the CYBER 203 at Langley Research Center. These two versions are as nearly identical as machine capability and the requirement for high speed performance will allow. Developmental changes are made on the Amdahl/CMS version for ease of testing and rapidity of turnaround. The changes are subsequently incorporated into the CYBER 203 version using vectorization techniques where speed improvement can be realized.

The changes leading to the seasonal cycle version of the model can be summarized as follows:

1. Conversion of model from SSS to CMS
2. Removal of split-grid code
3. Use of Fourier filtering to maintain computational stability near the poles
4. Change to new tape format
5. Faster long wave radiation code
6. Use of potential temperature as the basic thermodynamic variable
7. Revised negative specific humidity adjustment
8. Revised dry convective adjustment
9. New planetary boundary layer parameterization
10. New moisture availability parameterization for land points

The conversion of the code from SSS to CMS was designed to ensure that the model will be running on a maintained system with minimum overhead. This conversion required some code rewriting and creation of a completely new CMS EXEC procedure for operational runs. Many features available in SSS (such as sense switch responses) have been included and in some cases expanded under CMS. The CMS version of the model allows for direct interactive debugging facilities for testing new codes and parameterizations.

The split-grid in the original climate model has been found to generate spurious noise near the boundaries of the grid mesh changes. The new model uses the standard B-Grid mesh. The impact of this change on the CYBER 203 version of the model was substantial, since that code was designed exclusively for the split-grid mesh.

The routine for maintaining computational stability near the poles was also found to be inadequate. This led to the use of a Fast Fourier Transform (FFT) scheme to remove shorter waves in a more rational manner. With the use of the FFT filter, the same time step as was used in the split-grid code can also be used in the no split-grid code, thus minimizing the speed impact of the removal of the split-grid code. For land points, moisture availability is now computed

with the aid of a new prognostic "lysimeter temperature," as suggested by Mintz and Serafini (1981). Preliminary results indicate that the simulated distribution of precipitation is greatly improved by this change.

The new tape format was introduced for the following reasons:

1. Replacement of TAU (absolute hour) by a time/date system
2. Remove need for second tape for diagnostics and accumulate all useful diagnostics for model evaluation on one tape.
3. Remove duplicate fields and remove unneeded variables from the C array.
4. Segregate C array variables by type so that they can be treated together when transferring data from one machine to another.
5. Reorder arrays and group them together at each latitude to accommodate a paging environment.
6. Save code and boundary conditions for each run on the tape so that all code and boundary condition modifications can be seen.
7. Maintain detailed records for a limited number of points to study the impact of experiments over certain key regions of the world.

Separate changes to the longwave radiation code have been made on the Amdahl and CYBER 203 versions of the model, yielding a 40% speed improvement on each machine. This yields a 20% speed improvement for the model overall. The results from both versions agree with the original longwave radiation code to within .1 degrees per day.

The basic variable of temperature was replaced by potential temperature so that the thermodynamic advection equation could be simplified.

The treatment of negative specific humidity has been changed so that the adjustment is made only after all updates have been made to the specific humidity field, thus allowing other sources to compensate for the negative humidity where possible. Negative specific humidities are removed by a routine which ensures conservation of total moisture, thus eliminating spurious sources of moisture in the model.

To ensure better control of the static stability, dry convective adjustment is performed at every hydrodynamics and physics call instead of only at every physics call.

A new planetary boundary layer parameterization has been incorporated into the model. This parameterization incorporates the surface flux parameterization of Deardorff (1972) as modified by Randall (1976). Realistic stability dependence is included, and the surface roughness has distinct values for land, ocean, and sea ice points.

The changes to the model have yielded a simple, up-to-date, and easily modified code that will serve as the reference run for investigations of new numerical schemes and physical parameterizations. The 400 day seasonal cycle run will serve as a control run for both medium and long range climate forecasts and sensitivity studies. By keeping the code simple a better understanding of model response to various influences can be achieved. This in turn will lead to a better understanding of the atmosphere.

## REFERENCES

- Deardorff, J. W., 1972: Parameterization of the planetary boundary layer for use in general circulation models. Mon. Wea. Rev., 100, 93-106.
- Mintz, Y., and Y. Serafini, 1981: Monthly normal global fields of soil moisture and land-surface evapotranspiration. International Symposium on Variations in the Global Water Budget. Oxford, England, August 10-15, 1981. (manuscript in preparation.)
- Randall, D. A., 1976: The interaction of the planetary boundary layer with large-scale circulations. PhD thesis, UCLA, 247 pp.

QUASI-LAGRANGIAN MODELS OF NASCENT THERMALS

S. Rambaldi and D. A. Randall

1. INTRODUCTION

Scorer and Ludlam (1953) suggested that atmospheric buoyant convection occurs as discrete warm bubbles or "thermals" grow near the earth's surface and break away to rise under the influence of the buoyancy force. The motions in and around an isolated thermal were studied in the laboratory by Woodward (1959), who found rising motion in the core, and sinking motion on the outside; the circulation resembled that of a vortex ring.

In an "entity cloud model," cloudy thermal is tracked, in a Lagrangian fashion, as a discrete entity; the field of motion in and around the thermal is not explicitly simulated. Such models cannot simulate the mutual interactions of neighboring clouds, since these interactions occur partly through mutual advection.

In recent years, much effort has been devoted to the development of "field-of-motion cloud models," in which the equations of motion are numerically integrated on an Eulerian grid.

There are several drawbacks to field-of-motion cloud models. They are expensive, and analysis and interpretation of the enormous volume of numerical results produced is a difficult task. Moreover, as Turner (1969, p. 35) has noted, "No way has been found so far to deal numerically with the sharp boundary between the turbulent buoyant fluid and its surroundings, which is so characteristic of the experiments." A very fine Eulerian mesh is required to resolve the sharp gradients which arise near the thermal's boundary; in other regions a much coarser mesh would suffice. The boundary must be resolved somehow, because that is where vorticity is generated, and where entrainment and detrainment occur.

These considerations show the great potential of a "hybrid" cloud model which could combine the simplicity of the entity models with the generality and flexibility of the field-of-motion models. A key problem to be overcome in the development of a hybrid model is the formulation of a mathematical framework within which the cloud dynamics can be represented. Details of the mathematical analysis are given by Rambaldi and Randall (1981).

2. THE INITIAL ACCELERATION

We have shown analytically that the initial acceleration of a cylindrical thermal of buoyancy  $B$ , which starts from rest in an unbounded neutral environment, is as depicted on the right side of Fig. 1. Buoyancy generates positive vorticity on the right side of each thermal, and negative vorticity on the left side. The generation is most vigorous where the thermal wall is vertical. The induced environmental circulation is outward from the cap, downward along the sides, and inward and upward over the base. The rising motion is strongest on the center of the base.

Outside the thermal, there is a purely upward acceleration on the vertical plane of symmetry, and a purely downward acceleration on the horizontal plane of symmetry. On the boundary, the acceleration is purely normal, and the vertical component is nowhere downward. Across the boundary, the normal acceleration is continuous, while the tangential acceleration is discontinuous. Inside the thermal, there is a uniform upward acceleration.

Similarly, we have shown that the initial acceleration of a spherical thermal in an unbounded neutral environment is as depicted on the left side of Fig. 1. There is clearly a great similarity to the slab-symmetric result, but several interesting differences are seen. One is that, for a given buoyancy  $\beta$ , the interior acceleration is more rapid for an axisymmetric thermal. The physical interpretation is that in the axisymmetric case the environmental air which must be pushed aside to allow the thermal to pass can spread out in two dimensions, while in the slab-symmetric case it can only spread out in one. As a result, an axisymmetric thermal can push through its environment more easily than a slab-symmetric thermal. For a similar reason, the environmental motion decays more rapidly with distance from an axisymmetric thermal. This is reminiscent of the numerical result, obtained by Murray (1970) and others, that compensating environmental subsidence is more vigorous around a slab-symmetric cloud than around an axisymmetric cloud. Finally, the initial acceleration on the boundary of the axisymmetric thermal is not purely normal, but has a tangential component.

### 3. DISCRETE MODELS

In general, we cannot solve our equations exactly, so we adopt an approximate method suitable for use with a computer. The method closely parallels that used by Fink and Soh (1978) to study the roll-up of the trailing vortex sheet shed by a wing.

We introduce finite-difference approximations to (2.11) and (2.12-13), taking care to avoid the singularities. These finite difference equations allow us to determine the velocity field associated with the distribution of vorticity along the boundary. The velocity field is used to predict the future positions of a finite number of equidistant points along the boundary. A "redistribution" algorithm is used to ensure that the points remain equidistant as the thermal evolves. Finally, the future values of the vorticity are predicted for each point. By repetition of this procedure we march forward in time.

### 4. NUMERICAL EXPERIMENTS

To study the organization of thermal circulations, and to demonstrate our models, we have simulated the motions of slab-symmetric and axisymmetric thermals, which are initially at rest in unbounded, neutral environments. We have used 40 segments, and a finite (nondimensional) time increment of  $2 \times 10^{-2}$ , with the second-order modified Euler time-differencing scheme (Carnahan *et al.*, 1969).

Fig. 2 shows the evolution of the thermal boundary up to a nondimensional time  $t^* = 3.2$ , for both slab-symmetric and axisymmetric thermals. The more rapid rise of the axisymmetric thermal is clearly evident. Both thermals evolve from initially circular cross-sections into flattened domes with concave bases, in qualitative agreement with the laboratory results of Richards (1963) and

Walters and Davidson (1962, 1963). Dimple formation is to be expected in view of the distribution of initial acceleration. Although both thermals have broadened, the broadening is much less pronounced for the axisymmetric thermal, apparently because it has spread out into two dimensions.

The growth of the "dimple" on the base is accompanied by a shrinking of the cap thickness, for both thermals. The cap of the axisymmetric thermal is close to breaking at the last time shown. The thermal would then become toroidal. The evolution of initially spherical bubbles into toroids has been observed in the laboratory by Walters and Davidson (1963). A cap-breaking process is also occurring (more slowly) in the slab-symmetric thermal.

Advection removes vorticity from the source regions on the sides, carrying it towards the base and into the dimple. Inside the dimple buoyancy acts to destroy vorticity as it is advected in. As a result, a local maximum of vorticity occurs near the trailing edge of each thermal. A second very strong maximum develops within the cusp. We did not anticipate the double vorticity maximum; instead, we expected to find a single maximum, so that the thermal structure would approximate a vortex ring (or pair of vortex lines). If our model were generalized to include realistic dissipation, the very strong and sharp vorticity maximum in the cusp would probably be weakened more severely than the broader, less intense maximum on the trailing edge. The two maxima might then be more comparable in magnitude.

Slightly beyond the last times shown, both thermal walls develop small-scale features near their cusps. This leads the walls to fold across themselves, so that the simulations cannot be continued.

## 5. SUMMARY AND CONCLUSIONS

We have presented new models of slab-symmetric and axisymmetric thermals, based on the idea that the sharp, moving boundary of a thermal can be considered as a self-advecting vortex sheet. The analytically-obtained initial accelerations show that both thermals tend to form dimpled bases, and that the axisymmetric thermal accelerates upward more rapidly. Numerical simulations with discrete models confirm these results, and reveal the formation of double vorticity maxima.

Our results encourage us to consider further applications. We hope that the models can eventually be used to simulate cumulus clouds.

## ACKNOWLEDGEMENTS

We are grateful to Professors Erik Mollo-Christensen, Lou Howard, Gregory Baker, and Fred Sanders for interesting discussions. Prof. Michael Ghil of the Courant Institute kindly prepared a perceptive review of the manuscript. Members of the MIT Convection Club offered useful comments.

A portion of this work was performed while D. Randall was affiliated with the Department of Meteorology at MIT. S. Rambaldi has been sponsored by The National Research Council of Italy (CNR), under contract number 7901133.98. D. Randall has been supported by NSF Grant No. 77-12534.

ORIGINAL PAGE IS  
OF POOR QUALITY

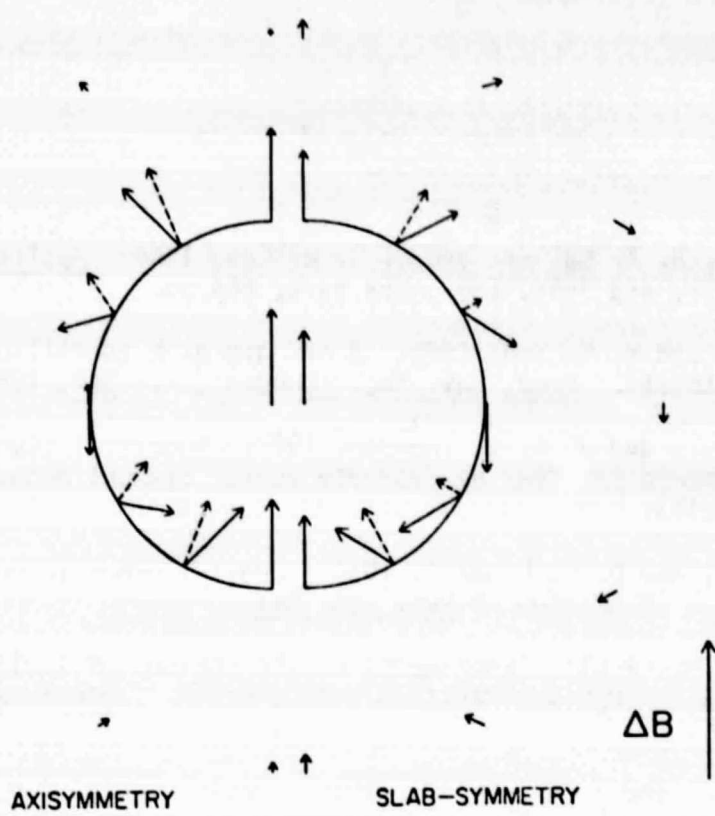


Figure 1. The analytically determined initial accelerations outside, on, and inside the thermal boundaries. The lengths of the arrows are measured relative to the buoyancy  $\Delta B$ . The solid arrows at the boundaries show the accelerations just outside the thermals, while the dashed arrows show the accelerations of the boundaries themselves.

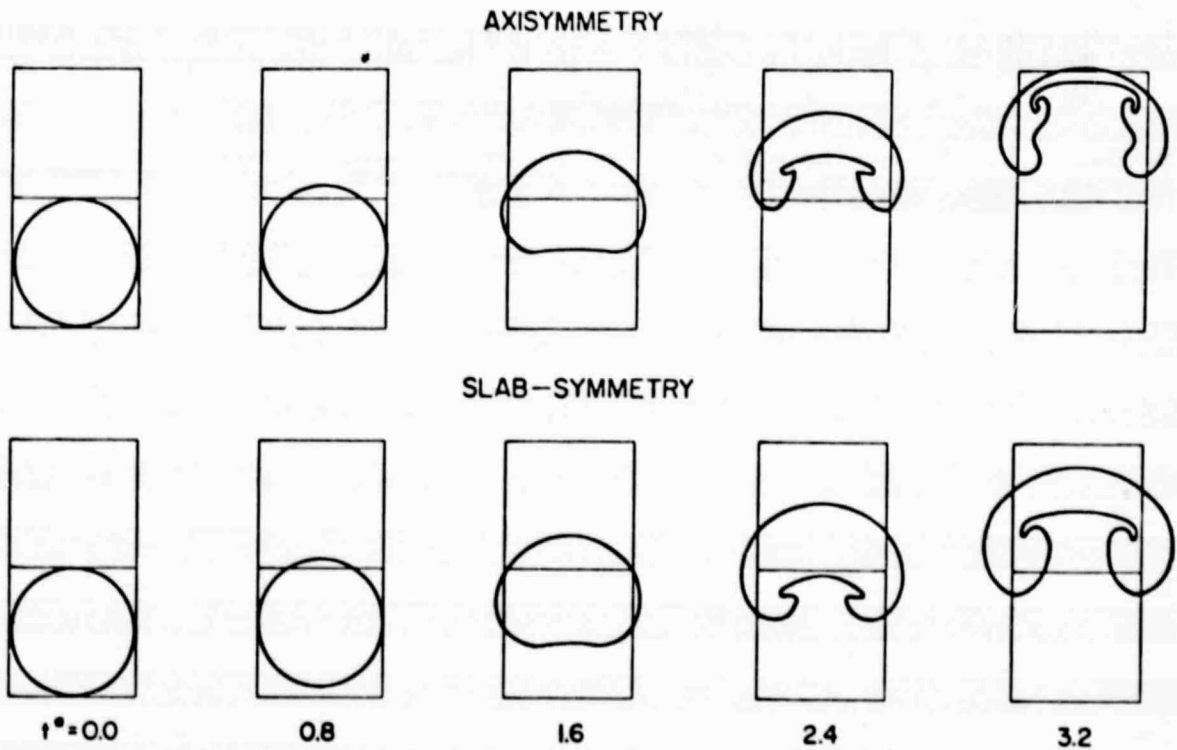


Figure 2. The time-evolution of the thermal boundary.

## REFERENCES

- Carnahan, B., H. A. Luther, and J. G. Wilkes, 1969: Applied numerical methods. John Wiley and Sons, Inc., New York, 604 pp.
- Fink, P. T., and W. K. Soh, 1978: A new approach to roll-up calculations of vortex sheets. Proc. Roy. Soc. (London), A, 362, 195-209.
- Meng, J. C. S., and J. A. L. Thomson, 1978: Numerical studies of some nonlinear hydrodynamic problems by discrete vortex element methods. J. Fluid Mech., 84, 433-453.
- Rambaldi, S., and D. A. RandaAl, 1981: Quasi-lagrangian models of nascent thermals. Submitted to Mon. Wea. Rev.
- Richards, J. M., 1963: Experiments on the motions of isolated cylindrical thermals through unstratified surroundings. Intern. J. Air Water Poll., 7, 17-34.
- Scorer, R. S., and F. H. Ludlam, 1953: Bubble theory of penetrative convection. Quar. J. Roy. Met. Soc., 79, 94-103.
- Turner, J. S., 1969: Buoyant plumes and thermals. Annual Rev. Fluid Mech., 1, 29-44.
- Walters, J. K., and J. F. Davidson, 1962: The initial motion of a gas bubble formed in an inviscid liquid, Part 1. The two-dimensional case. J. Fluid Mech., 12, 408-417.
- Walters, J. K., and J. F. Davidson, 1963: The initial motion of a gas bubble formed in an inviscid liquid, Part 2. The three-dimensional bubble and the toroidal bubble. J. Fluid Mech., 17, 321-340.
- Woodward, B., 1959: The motion in and around isolated thermals. Quar. J. Roy. Met. Soc., 85, 144-151.

0117

## SECOND-ORDER CLOSURE STUDIES OF ENTRAINMENT INTO A STRATOCUMULUS LAYER WITH DISTRIBUTED RADIATIVE COOLING

D. A. Randall and C.-H. Moeng

Recently the role of radiative cooling in determining the structure of stratocumulus-topped mixed layers has become controversial (Deardorff 1976, Kahn and Businger 1979, Lilly and Schubert 1980, Randall 1980, Shaller and Kraus 1981, and Stage and Businger 1981). Mixed-layer modelers have recognized the importance of radiative cooling and tried to clarify this aspect. However, because mixed-layer models are highly sensitive to the choice of entrainment assumption, the conclusions of these studies are questionable. To avoid explicit dependence on an entrainment assumption, a second-order closure turbulence model is used here to show the sensitivity of a cloud-topped turbulent layer to the depth of radiative cooling.

The one-dimensional second-order closure model is based on the Level 4 model of Mellor and Yamada (1974), with some modifications described in Moeng and Arakawa (1980). In order to be able to control the depth of the radiative cooling, we have omitted an explicit radiation calculation, and instead simply prescribed the distribution of the radiative cooling. A net upward radiative flux  $R = 70 \text{ watts/m}^2$  is given at the cloud top. The flux is assumed to decrease linearly to zero at the level  $\delta z_R$  below the cloud top. Three 60-hour simulations with  $\delta z_R = 20 \text{ m}$ ,  $100 \text{ m}$ , and  $200 \text{ m}$  have been performed, all with the same initial and boundary conditions. The results show that  $\delta z_R$  increases, both cloud top and cloud base descend toward the sea surface, and the depth of the layer of negative buoyancy flux increases. The surface evaporation rates at the ends of the runs are 1.33, 1.21, and 0.86 mm/day for  $\delta z_R = 20, 100, \text{ and } 200 \text{ m}$ , respectively the evaporation rate decreases as  $\delta z_R$  increases.

These results are in qualitative agreement with those obtained by Randall (1980) using a mixed-layer model. The sensitivity of cloud-topped mixed layer structure to the depth of the radiative cooling suggests that in order to simulate a realistic stratocumulus-topped boundary layer by a mixed-layer model, an accurate parameterization of the distributed radiative cooling is required.

### REFERENCES

- Deardorff, J. W., 1976: On the entrainment rate of a stratocumulus-topped mixed layer. Quart. J. Roy. Met. Soc., 102, 563-582.
- Kahn, P. H., and J. A. Businger, 1979: The effect of radiative flux divergence on entrainment of saturated convective boundary layer. Quart. J. Roy. Met. Soc., 105, 303-306.
- Lilly, D. K., and W. H. Schubert, 1980: The effects of radiative cooling in a cloud-topped mixed layer. J. Atmos. Sci., 37, 482-487.

- Mellor, G. L., and T. Yamada, 1974: A hierarchy of turbulence closure models for the planetary boundary layer. J. Atmos. Sci., 31, 1791-1806.
- Moeng, C.-H., and A. Arakawa, 1980: A numerical study of a marine subtropical stratus cloud layer and its stability. J. Atmos. Sci., 37, 2661-2676.
- Randall, D. A., 1980: Entrainment into a stratocumulus layer with distributed radiative cooling. J. Atmos. Sci., 37, 148-159.
- Stage, S., and J. Businger, 1981: A model for entrainment into a cloud-topped marine boundary layer. Part I. Model description and application to a cold air outbreak episode. Submitted to J. Atmos. Sci.
- Stage, S., and J. Businger, 1981: A model for entrainment into a cloud-topped marine boundary layer. Part II. Discussion of model behavior and comparison with other models. Submitted to J. Atmos. Sci.
- Schaller, E., and H. Kraus, 1981: The role of radiation in an inversion-capped planetary boundary layer. Part I: The need for a detailed consideration of radiative processes. Part II: The internally interactive radiative-convective model. Submitted to Boundary-Layer Meteorology.

## SOME ASPECTS OF SOUTHWEST MONSOON AS SEEN IN A GLAS GCM SIMULATION

V. Satyan

## 1. INTRODUCTION

In the past decade, several studies have been made of GCM simulations to see if they simulate the southwest summer monsoon or aspects of it. A review by Gilchrist (1977) discusses these attempts and their relative successes. In particular, the GLAS GCM simulations have also been studied with monsoon in view. This paper describes an attempt to investigate in some detail two important aspects of the summer monsoon, viz., disturbances in the monsoon flow and periodicities in the monsoon fluctuations as revealed in a GLAS GCM simulation.

Results of GLAS GCM climate simulation for 50 summer days from June 15, 1979 through August 3, 1979 (D162 C1: Run) were used in the present study. Daily mean fields were computed from these data sets for the monsoon region. The monsoon region here is defined as the region bounded by latitudes  $30^{\circ}\text{S}$ - $42^{\circ}\text{N}$  and longitudes  $45^{\circ}\text{E}$ - $120^{\circ}\text{E}$ .

## 2. MONTHLY MEAN FLOW PATTERN

First, it is necessary to examine the model climatology for July in the monsoon region. Examination of July mean horizontal wind field at 850 mb and 200 mb levels shows that the model simulates well the observed July mean southwesterly wind in the lower troposphere over the Arabian Sea and peninsular India. The 200 mb mean flow shows the anticyclonic flow over Tibet and the easterly jet over  $6^{\circ}\text{N}$ - $14^{\circ}\text{N}$ . Next, it is also seen from the July mean sea level pressure that the ridge over the Arabian Sea, the monsoon trough over northern India, the Mascarene High east of Madagascar and the low over Pakistan are simulated by the model and compare well with the observed July climatology. Thus, the overall monthly mean picture of wind flow and sea level pressure pattern are satisfactorily reproduced by the model.

## 3. DISTURBANCES IN THE MONSOON FLOW FIELD

A convenient way of studying propagating or stationary disturbances in a flow field is by constructing Hovmoller diagrams. These are diagrams showing longitude-time cross sections of the flow at fixed latitudes. Examination of the variation of sea level pressure at  $80^{\circ}\text{E}$  and  $22^{\circ}\text{N}$  during the 50 day period shows that a major low formation occurs about the 13th day (1st day is June 15, 1979). Furthermore, the plots of precipitation and the wind speed at 1000 mb level also show peaks around this time. We present the Hovmoller diagram at  $22^{\circ}\text{N}$  in Figures 1a and 1b. It is seen that a low forms around  $80^{\circ}\text{E}$  on the 13th day. Furthermore, this disturbance propagates westward with a phase speed of about 2.7 degrees longitude per day (slope of the trough-trough line). Observational statistics show that disturbances frequently originate in the Bay of Bengal region during July and they usually move in northwesterly direction along the monsoon trough axis. It is also interesting to note the formation of another disturbance around the 33rd day and this is accompanied by more rainfall than the major low described above. Hovmoller diagrams at latitudes

18°N and 26°N (not shown here) are similar to Figure 1 and reveal the latitudinal extent of the disturbance. We conclude that the model has produced a genuine physical monsoon disturbance and not a numerical illusion.

#### 4. PERIODICITIES OF A SOUTHWEST SUMMER MONSOON SYSTEM

The question of periodicity in the fluctuations of a monsoon has received some attention in the past. The studies made so far have been confined to the analysis of observed data. The subject has been reviewed by M. Murakami (1977). The conclusion that emerges from these studies is that the monsoon system exhibits two kinds of quasi-periodic variations, one around the 5-day period and the other around the 15-day period. The question arises, therefore, whether a GCM simulation also shows these periodicities in the monsoon region and whether they resemble the observed periodicities. We investigate this question in the following, using the results of a GLAS-GCM simulation.

The time series analyzed consists of 50 days of daily mean fields computed from the D162 summer simulation referred to earlier. The fields analyzed are the pressure in the monsoon trough area, pressure in the Mascarene High, tropical easterly jet and the monsoon rainfall. These are some of the major large-scale observed features which define, along with others, the monsoon system. In the present study, these fields are averaged over almost the same region as in the observational study of Krishnamurty et al. (1976) so as to afford an easy comparison with their findings. Before carrying out spectral analysis, we detrend the time series (departure from the 50-day mean) by subtracting out the linear and parabolic trends so that the red noise and the long-term variations (like the seasonal) are removed. The spectrum is studied by plotting power  $\times$  frequency against logarithm of the frequency.

Figures 2a and 2b show the day-to-day variation of the pressure in the monsoon trough and its spectral analysis, respectively. The pressure here is the daily mean sea level pressure averaged over the area bounded by latitudes 18°N-26°N and longitudes 60°E-100°E. The spectral diagram shows several peaks; the prominent ones having periods around 16.6-day, 10-day, 6-7 day and 5-day. Of these, the 16.6-day and 5-day periods may be compared with the 15-day and 5-day periods found in the analysis of observed data (M. Murakami, 1977). We also note that the time series in Figure 2a does show oscillations around the 16th day.

We present in Figures 3a and 3b the results of our analysis for the Mascarene High. This is the high pressure area to the east of Madagascar. Figure 3a shows the daily march of the pressure (averaged over the area bounded by latitudes 22°S-30°S and longitudes 45°E-70°E). The spectrum is shown in Figure 3b. We find three distinct periodicities at 16.6-day, 7.1-day and 5.1-day. This result agrees well with the observational studies (Krishnamurty et al., 1976) except for the 7.1-day oscillation.

The daily march of precipitation and its spectrum are shown in Figures 4a and 4b. Figure 4a shows the daily mean monsoon rainfall averaged over the area covered by 10°N-26°N and 70°E-90°E (central India). Considerable fluctuations seen in the precipitation vs time plot indicates that its spectrum is composed of several periodicities. In fact, we see in Figure 4b that there are six distinct periods. Besides the 16.6-day and 5-day oscillations as in the oscilla-

tions of other elements of the monsoon system one sees here prominent ones at 7.1-day, 10-day and 2.6-days. It is interesting to note that the 2.6-day period agrees very well with the 2-day period oscillation found by Krishnamurty et al. (1976) in their analysis of observed data.

We also analyzed the tropical easterly jet for periodicities. The parameter studied is the daily mean wind speed at 200 mb level averaged over area covered by latitudes 2°N-10°N and longitudes 55°E-75°E. We find that the 16.6-day period is very prominent in the spectrum. Again we see periodicities of 7.1, 5.5 days and some additional ones. The high frequency end of the spectrum shows several peaks, which may be the consequence of the local barotropic instability of the jet (Krishnamurty et al., 1976). We also find that the wind speed fluctuates considerably with time.

Thus, the GLAS GCM simulates the periodic variations of the summer monsoon system fairly well. The 5-day and 15-day periods found in the analysis of observed data are reproduced closely by the model. In addition, the model results show a 7.1-day oscillation in all the elements of the monsoon considered above. It is interesting to note that the existence of a mode around 7-day period has been discussed by Keshavamurty (1972, 1973) in his analysis of observed data.

#### ACKNOWLEDGEMENTS

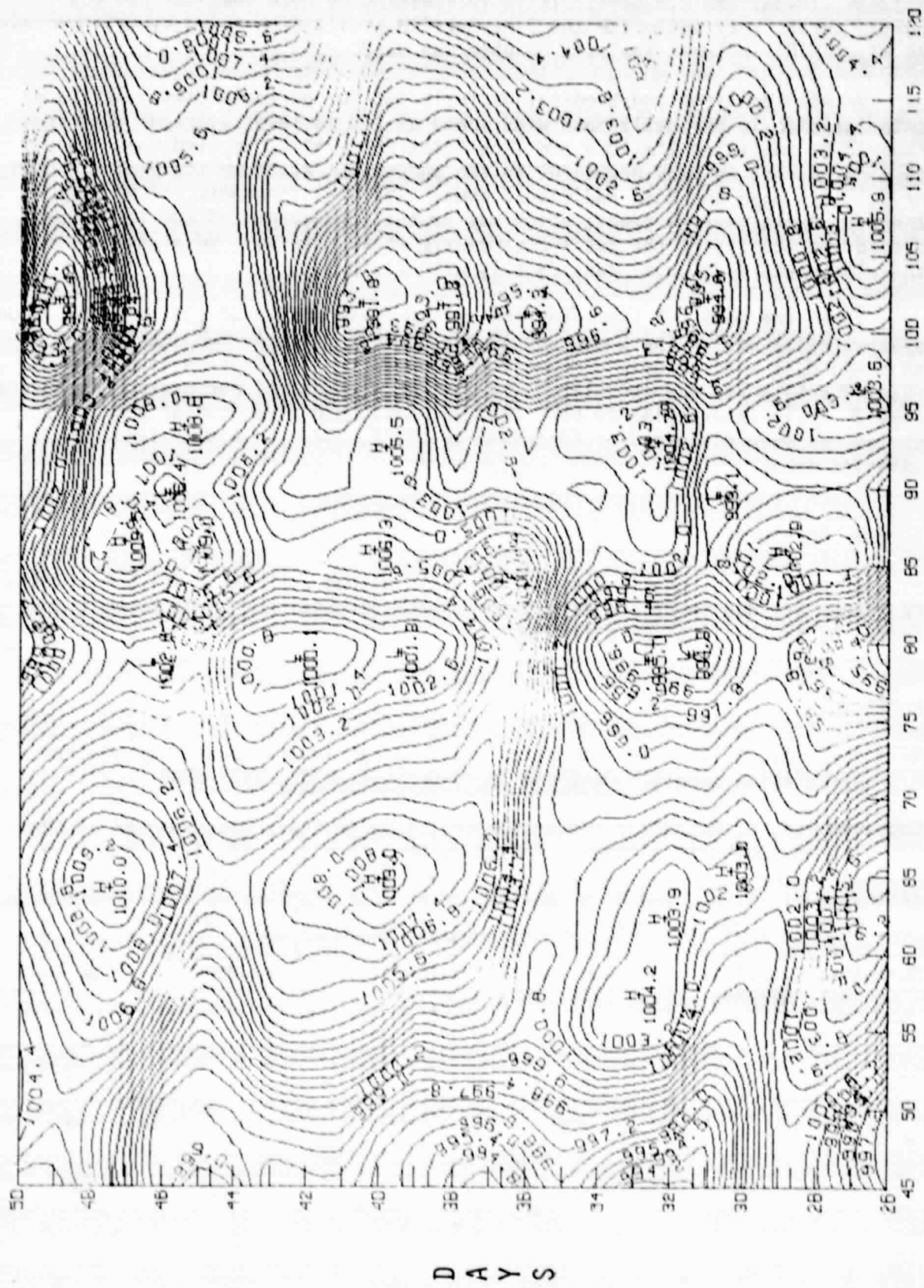
I thank Dr. J. Shukla for his interest in this work and helpful discussions. My thanks are due to Dr. D. Straus for useful discussions. This work is supported by the National Research Council.

#### REFERENCES

- Gilchrist, A., 1977: The simulation of the Asian summer monsoon by general circulation models. Pure and Appl. Geophys., 115, 1431-1448.
- Keshavamurty, R. N., 1973: Power spectra of large-scale disturbances of the Indian southwest monsoon. Indian J. Met. Geophys., 24, 117-124.
- Krishnamurti, T. N., and H. N. Bhalme, 1976: Oscillations of a monsoon system. Part I. Observational aspects. J. Atmos. Sci., 33, 1937-1954.
- Murakami, M., 1977: Spectrum analysis relevant to Indian monsoon. Pure and Appl. Geophys., 115, 1145-1166.

ORIGINAL PAGE IS  
OF POOR QUALITY

DAILY MN SLP  
OVER LATITUDES 22N



LONGITUDE EAST

Figure 1a

D A Y S

DAILY MN SLP  
OVER LATITUDES 22N



LONGITUDE EAST

Figure 1b

ORIGINAL PAGE IS  
OF POOR QUALITY

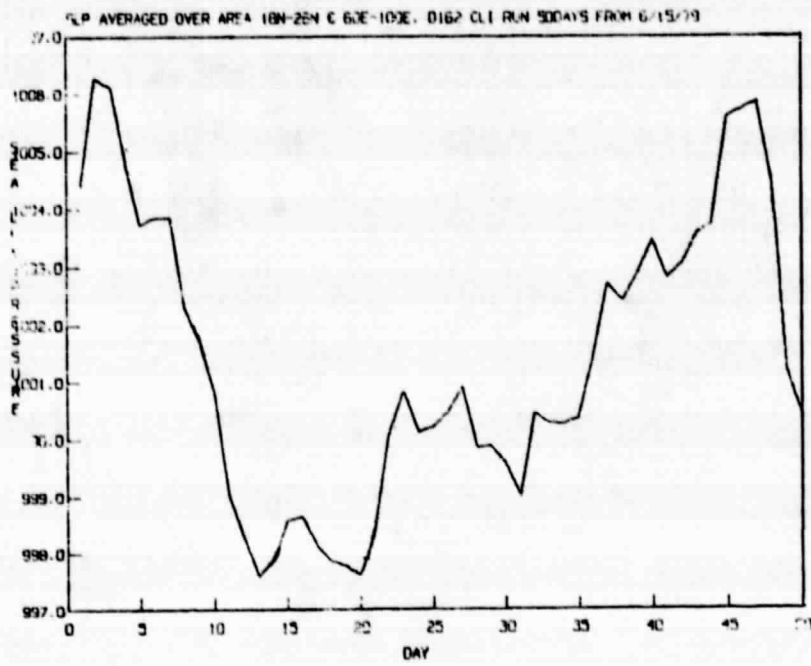


Figure 2a

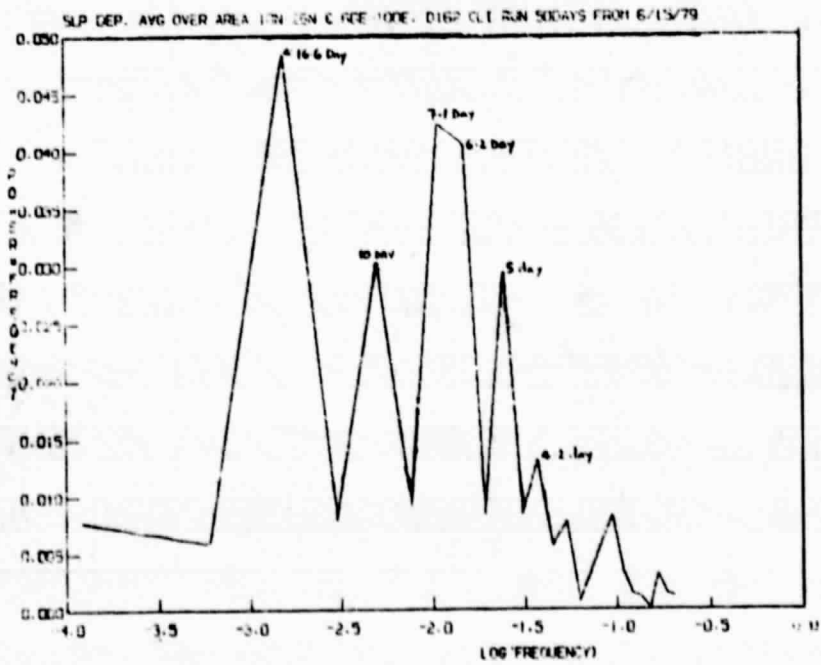


Figure 2b

ORIGINAL PAGE IS  
OF POOR QUALITY

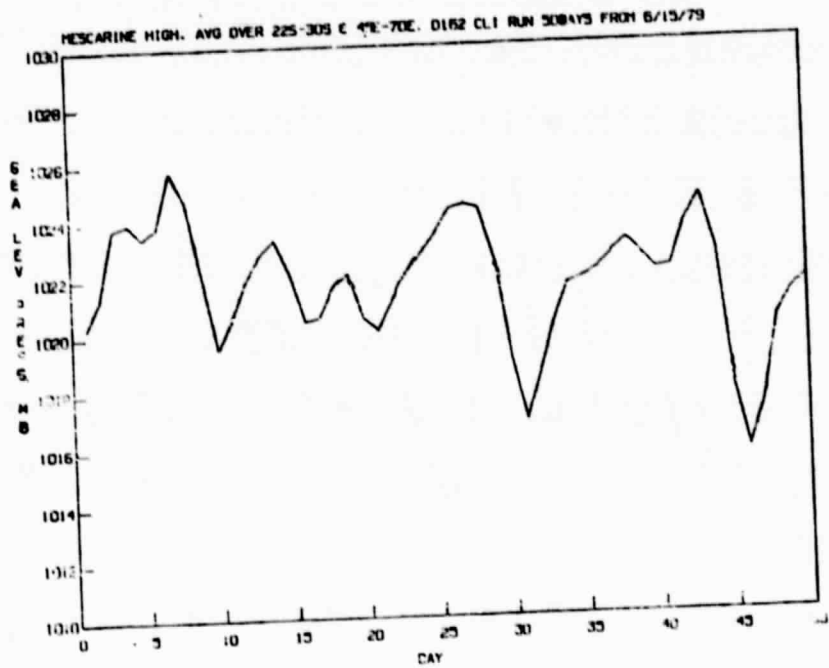


Figure 3a

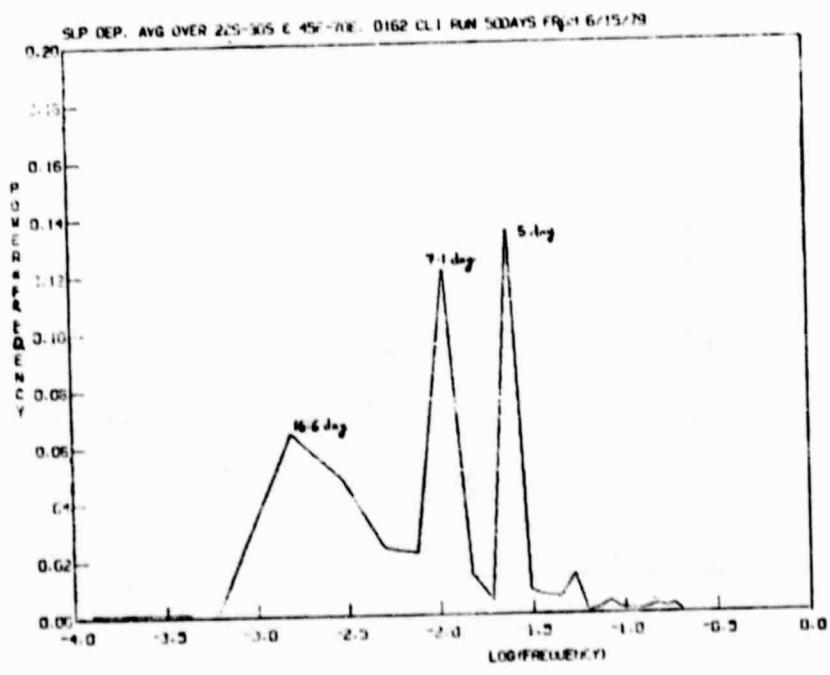


Figure 3b

ORIGINAL PAGE IS  
OF POOR QUALITY

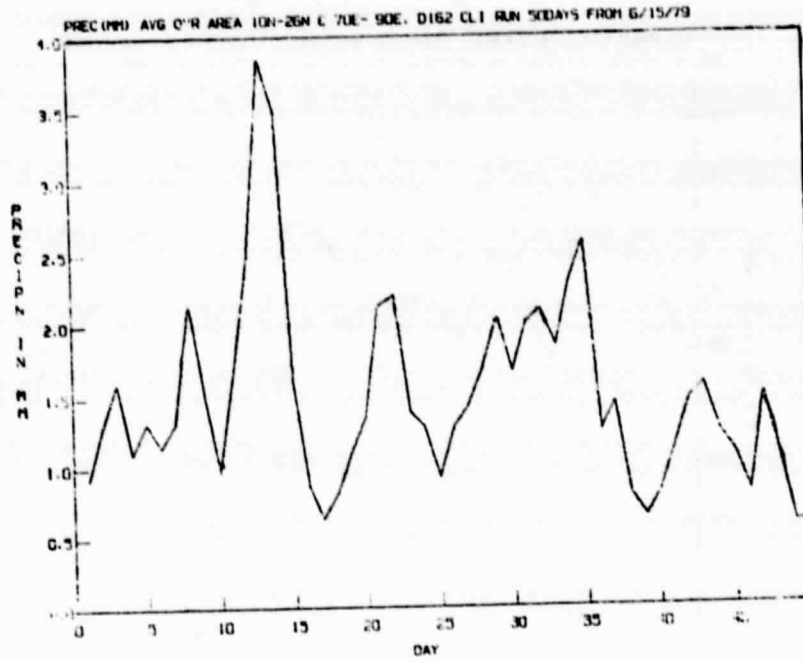


Figure 4a

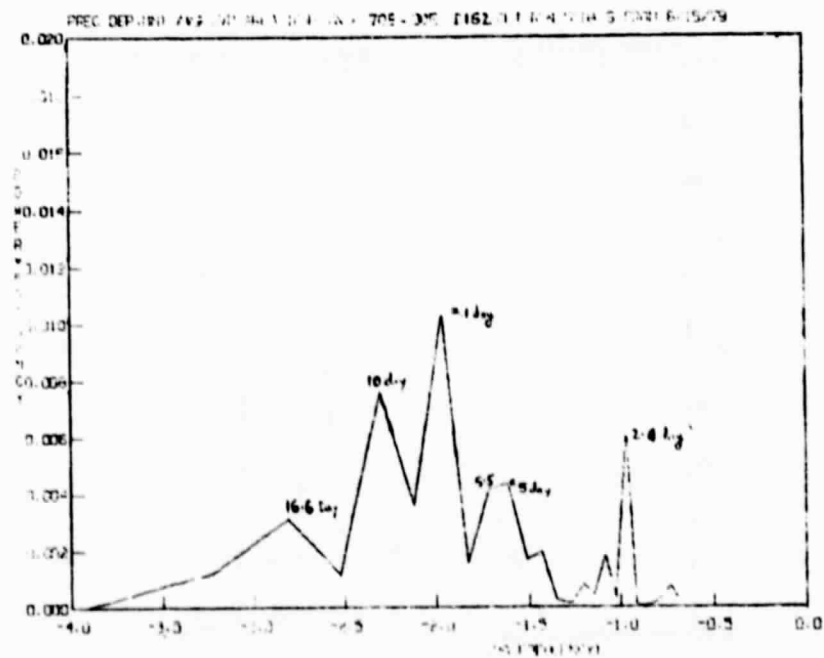


Figure 4b

## C. SENSITIVITY EXPERIMENTS

## AN ANALYSIS OF THE CLOUD FIELDS SIMULATED BY THE GLAS CLIMATE MODEL

C.-H. Moeng and D. A. Randall

In the present GLAS Climate model, it is assumed that clouds of any type fill an entire grid area, which is typically about 400 km x 400 km in horizontal and 1-2 km in vertical. This cloud cover is then used to calculate the radiative heating/cooling of the atmosphere-earth system. Subgrid-scale cumulus convection is observed to have a very small horizontal extent and, because no parameterization of subgrid-scale fractional cloudiness is currently available, it seems reasonable to ignore the existence of cumulus clouds for the radiation balance.

The purpose of this study is to analyze the cloud field produced by the model, and try to answer the following questions: (a) does the model produce reasonable cloudiness? (b) is the amount of model-generated cumulus cloudiness comparable to supersaturation cloudiness? (c) is the effect of cumulus clouds on radiation balance large?

To compare the model's cloudiness with observations, we have chosen February (D150) and July (D162) simulations. In order to make a clean comparison with satellite observations (or ground observations), we define cloudiness such that it represents the horizontal distribution of cloud-cover as one looks straight down from the top of the atmosphere (or straight up from the ground); the cloudiness is 100% if any cloud exists in the vertical grid column in any model layer, and zero if there is no cloud in any layer. These analyses have been made for cumulus clouds, supersaturation clouds, and both types clouds, individually. The method is as follows: (a) unpack cloud information at each grid point from log-9 model tapes; (b) compute the horizontal distribution of cloudiness from cumulus clouds, supersaturation clouds, and total clouds; (c) take the zonal mean for each type of cloud; (d) repeat the above steps for one-month of data, and take a monthly average.

The February and July zonal-mean cloudinesses generated by the model are shown in Fig. 1. Comparing with those of observations (Fig. 2), we find good agreement. There is about a 10% overestimation of the global cloudiness. The overall shape of the zonal mean cloudiness is very well-simulated.

The zonal mean cloudiness due to cumulus clouds between + 60° latitudes is only 1/3 of that due to supersaturation clouds. The total cloudiness of the model is mainly due to supersaturation clouds. In other words, if we completely ignore the cumulus clouds, the model-produced zonal-mean cloudiness is still comparable to that of observations.

Although the cloudiness due to cumulus clouds is small, this does not mean that the cumulus clouds occur less frequently in any particular model layer. We have analyzed the July simulation to see the distribution of the monthly cloud frequency in each model layer. The monthly cloud frequency is defined as the fraction of the time for which cloud occurs within the one month period. The cloud information is retrieved from log-9 model tapes for every 5-hour output, then the time average of the appearance of cloud at each grid point is taken. The monthly cloud frequency is obtained for cumulus clouds and supersaturation clouds, separately. For cumulus clouds in each layer, we sum over different

types of convective clouds. For example, to obtain the cloud frequency of cumulus clouds in layer 7 we sum that of low level convection and deep convection in layer 7. Examination of these results (not shown) reveals three features. First, in the mid-troposphere (layers 6 and 7) cumulus clouds occur more frequently in the low and middle latitudes and supersaturation clouds are confined to the polar regions. Second, most supersaturation clouds appear in the lowest layer. The supersaturation cloud frequency in the lowest layer is unrealistically large. The sudden decrease of supersaturation cloud frequency from layer 9 to layer 8 suggests that too much moisture is deposited inside the lowest layer; the model is unable to transport low-level moisture upward. Third, the model produces unrealistic supersaturation clouds in the stratosphere (layers 1, 2, and 3).

Many GLAS climate simulation experiments have shown that the model is sensitive to the parameterizations of radiation and to the treatment of the interactions between cloud and radiation (Wu et al., 1978; Herman et al., 1980; Shukla and Sud, 1980). This report shows that the scattered, small-scale cumulus clouds occur more frequently than the horizontally wide-spread supersaturation clouds in the low latitudes and mid-troposphere. Hence, a systematic bias exists in the model because the model treats the horizontal extent of cumulus clouds and supersaturation clouds the same. We suggest that all the subgrid-scale cumulus clouds should be ignored for the radiation budget.

#### REFERENCES

- Clapp, P. F., 1964: Global cloud cover for seasons using TIROS nephelyses. Mon. Wea. Rev., 92, 495-507.
- Herman, G. F., M. L. Wu, and W. T. Johnson, 1980: The effect of clouds on the earth's solar and infrared radiation budgets. J. Atmos. Sci., 37, 1251-1261.
- Shukla, J. and Y. Sud, 1981: Effect of cloud-radiation feedback on the climate of a general circulation model. J. Atmos. Sci., 38, 2337-2353.
- Wu, M. L., L. D. Kaplan, and R. Godbole, 1978: Influence of systematic radiation differences on the dynamics of a model atmosphere. Preprint Volume, Third Conf. on Atmospheric Radiation, Davis CA. pp. 293-302.

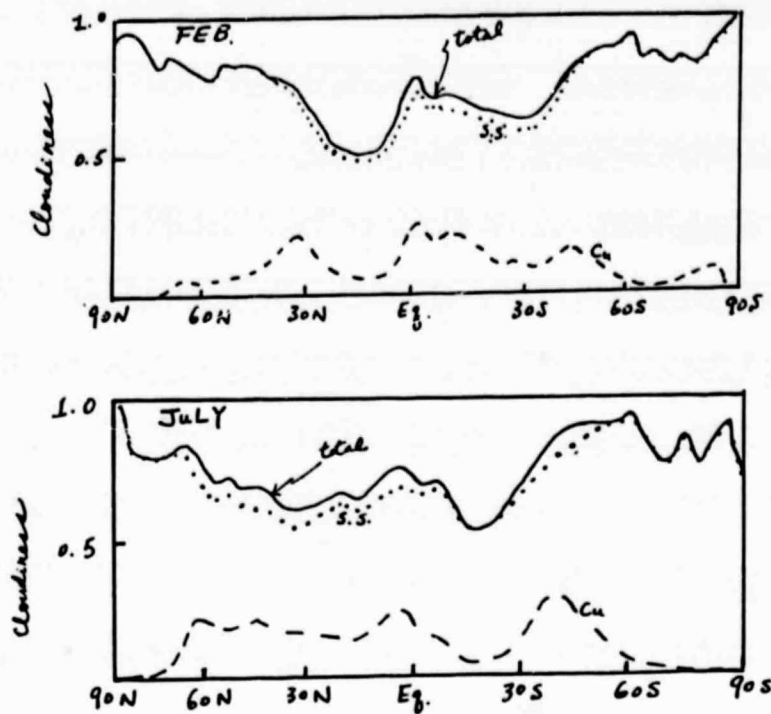


Fig. 1. Latitudinal distribution of zonally averaged cloudiness for (a) February and (b) July, from model output. (Dashed for cumulus clouds, dotted for supersaturation clouds, and solid for total clouds).

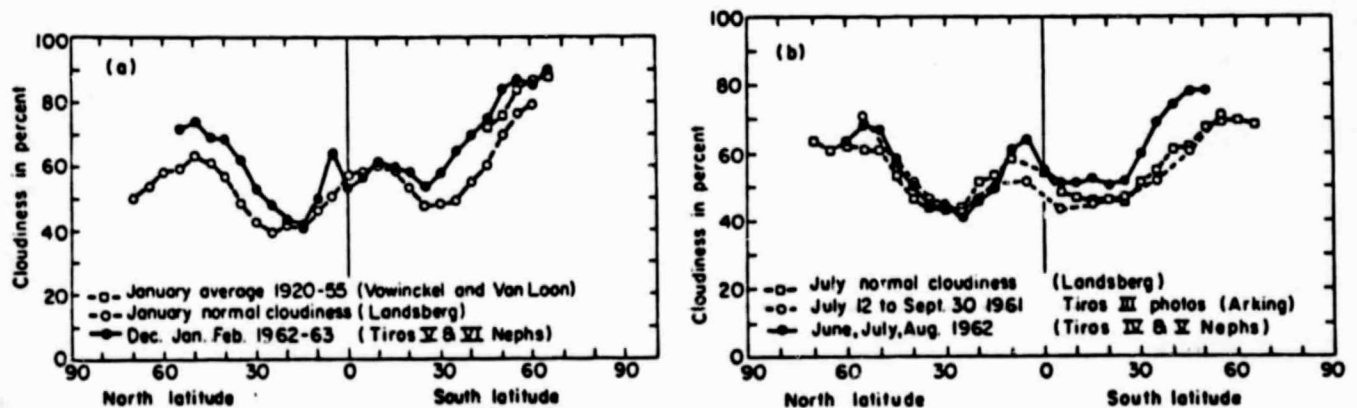


Fig. 2. Latitudinal distribution of zonally averaged cloudiness for (a) January and (b) July. The Landsberg and Vowinckel and Van Loon results are from ground observation. Other curves from satellite observations as marked. (After Clapp, 1964).

## CLIMATOLOGY OF BLOCKING IN THE GLAS CLIMATE MODEL

J. Shukla, K. C. Mo, and M. Eaton

## 1. INTRODUCTION

During the past several years, the GLAS climate model has been integrated with a variety of initial and boundary conditions. Results of winter and summer simulation by the GLAS climate model have been discussed by Halem et al., (1979) and Straus and Shukla, (1981). The model has shown remarkable success in simulating the storm tracks. The purpose of this note is to examine the model's ability to simulate the occurrence of persistent anomalies to be referred to as blocking.

## 2. DATA

We have used 17 winter and 7 summer simulations with the GLAS climate model (Halem et al., 1979; Shukla and Bangaru, 1980). The time series at each grid point for each run was fitted to a parabola to define the seasonal cycle,  $\phi_s$ ,

$$\phi_s(t) = a + bt + ct^2$$

The mean values of coefficients  $\bar{a}$ ,  $\bar{b}$ , and  $\bar{c}$  were determined by averaging the coefficients over all runs in a set and seasonal cycle was defined as:

$$\bar{\phi}_s(t) = \bar{a} + \bar{b}t + \bar{c}t^2$$

at each grid point. Anomaly  $\phi'$  at each grid point was defined as:

$$\phi'(t) = \phi(t) - \bar{\phi}_s(t)$$

If, at any grid point, an anomaly of +100 qpm or more persists for 7 days or more, we count it as a blocking event. We have calculated the frequency of blocking events at each grid point for winter and summer simulations separately and presented the results in the next section.

## 3. RESULTS

Figures 1a, 1b, 1c, and 1d show the standard deviations of daily values of geopotential height for winter and summer, respectively. Model standard deviations look more like observed band-pass variances rather than observed total variances. This suggests that the model does not simulate the low frequency components realistically (Straus and Shukla, 1981).

Figures 2a and 2b show the map of number of events for which anomaly  $\phi'$  of +100 qpm or more persisted for 7 days or more. Figure 2a shows only the Northern Hemisphere, and Figure 2b also shows the Southern Hemisphere. In the Northern Hemisphere, the centers of maxima are located near 50°N, 180°W (Pacific), 75°N, 30°W (Greenland), 60°N, 40°E (USSR), and 70°N, 135°W. An analysis of 15 years of observations (Shukla and Mo, 1981) showed only three centers of maxima; moreover, the locations of the maxima are not correctly simulated. The Pacific and

the Russian maxima are shifted southwestwards, and the Atlantic maxima is shifted northwestwards with respect to the observations. It is not appropriate to compare the magnitude of the frequency because model runs have very similar initial conditions. Shukla and Bangaru (1979) found that a large SST anomaly in the Pacific produced a persistent anomaly in the atmospheric circulation over North America. This situation is being further analysed by Chen and Shukla and it is found that SST anomaly run produced persistent low wave numbers.

Figure 2b shows that during northern winter the Southern Hemisphere has relatively lower frequency of blocking. The maxima in blocking occur between 70°-80°S. We do not have corresponding observations to compare the Southern Hemisphere results.

Figure 2c shows the frequency of blocking for summer simulations. There is almost no blocking event in the Northern Hemisphere (the maxima over Greenland is not a realistic one), and surprisingly, there is no blocking activity in the Southern Hemisphere either.

We have also examined the number of events for winter simulations for anomalies of -100 gpm or less persisting for 7 days or more. In agreement with the observations, maximum frequency maps for simulated positive and negative anomalies occur in the same region.

The model's day-to-day fluctuations are dominated by synoptic scale disturbances which give maximum variance in storm track regions, whereas, in the observations, the maxima of daily standard deviations are related with large persistent positive and negative anomalies associated with blocking.

We have calculated the characteristic time  $T_0$  for winter model runs and 15 observed winters, respectively.

$$T_0 = 2 \int_0^T \left(1 - \frac{\tau}{T}\right) R(\tau) d\tau$$

where  $R(\tau)$  is lagged autocorrelation at lag  $\tau$ , and  $T = 30$  days. We find that the model underestimates the value of  $T_0$ , indicating the model's inability to simulate persistent patterns and low frequency components.

#### 4. CONCLUSIONS

Although the GLAS climate model simulates the storm tracks (band-pass variance) quite realistically, the model is not successful in simulating the occurrence of persistent anomalies. Examination of model simulated synoptic maps shows that the blocking type of configurations appear frequently, but they do not persist.

## REFERENCES

- Halem, M., J. Shukla, Y. Mintz, M. L. Wu, R. Godbole, G. Herman, and Y. Sud, 1979: Climate comparisons of a winter and summer numerical simulation with the GLAS general circulation model. GARP Publication Series, 22, 207-253.
- Shukla, J., and K. C. Ho, 1981: Seasonal variations of blocking. Submitted to Mon. Wea. Rev.
- Shukla, J., and B. Bangaru, 1979: Effect of a Pacific SST anomaly on the circulation over North America: A numerical experiment with the GLAS model. GARP Publication Series, 22, 501-518.
- Straus, D., and J. Shukla, 1981: Space-time spectral structure of a GLAS general circulation model and a comparison with observations. J. Atmos. Sci., 38, 902-917.

ORIGINAL PAGE IS  
OF POOR QUALITY

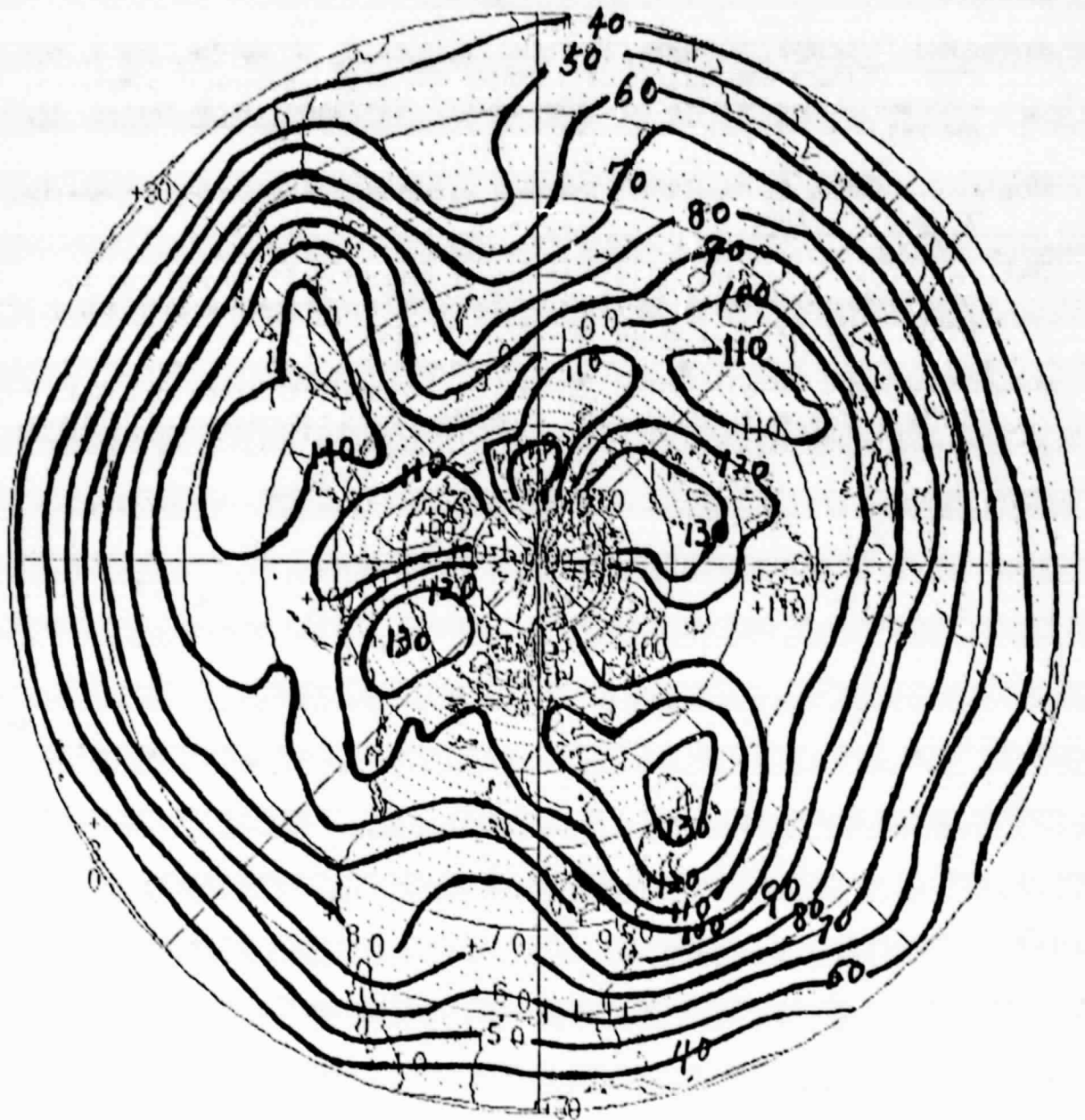


Figure 1a. The standard deviation of daily values for winter simulations.

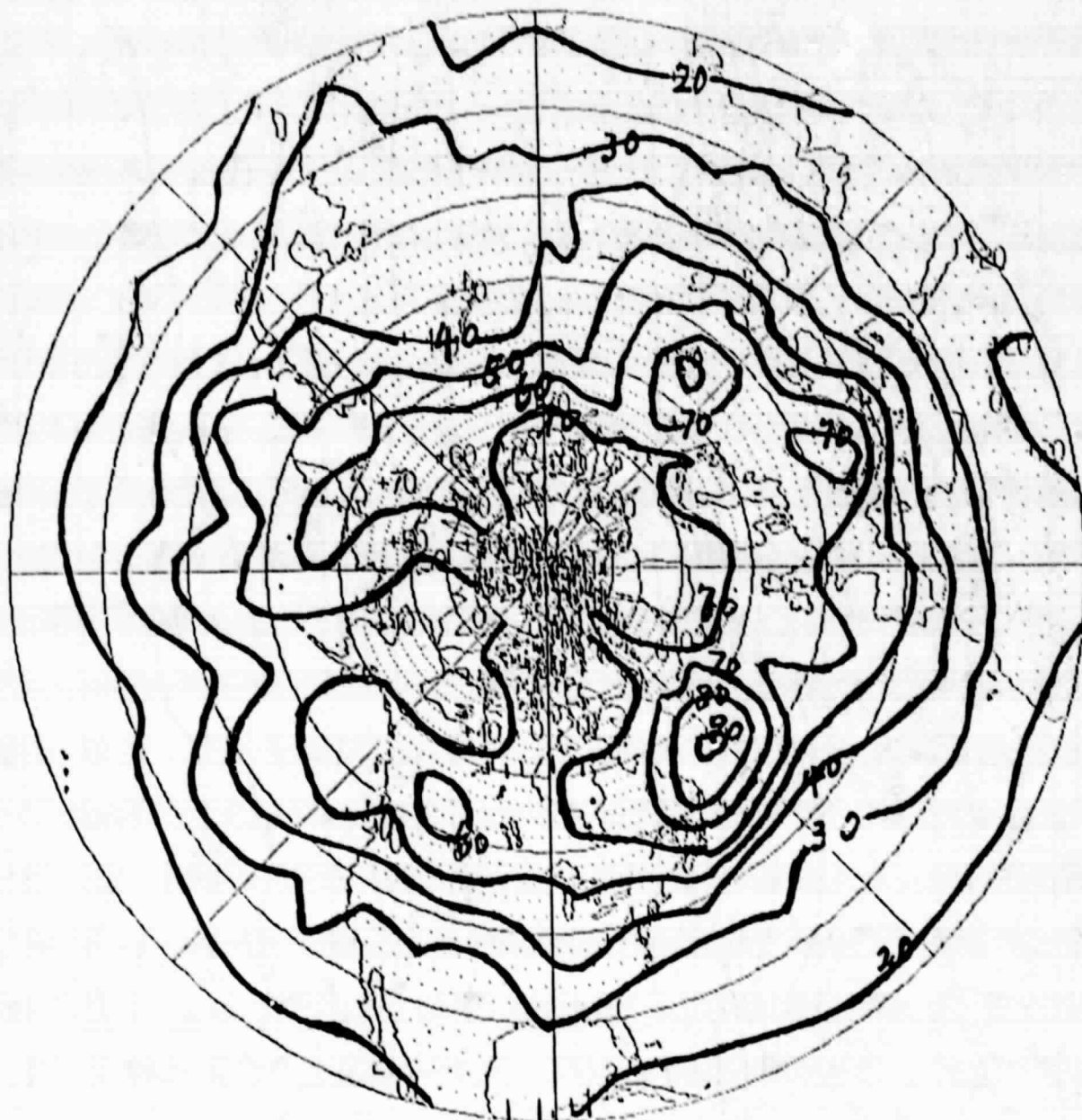


Fig. 1b. The standard deviation of daily values for summer simulations.

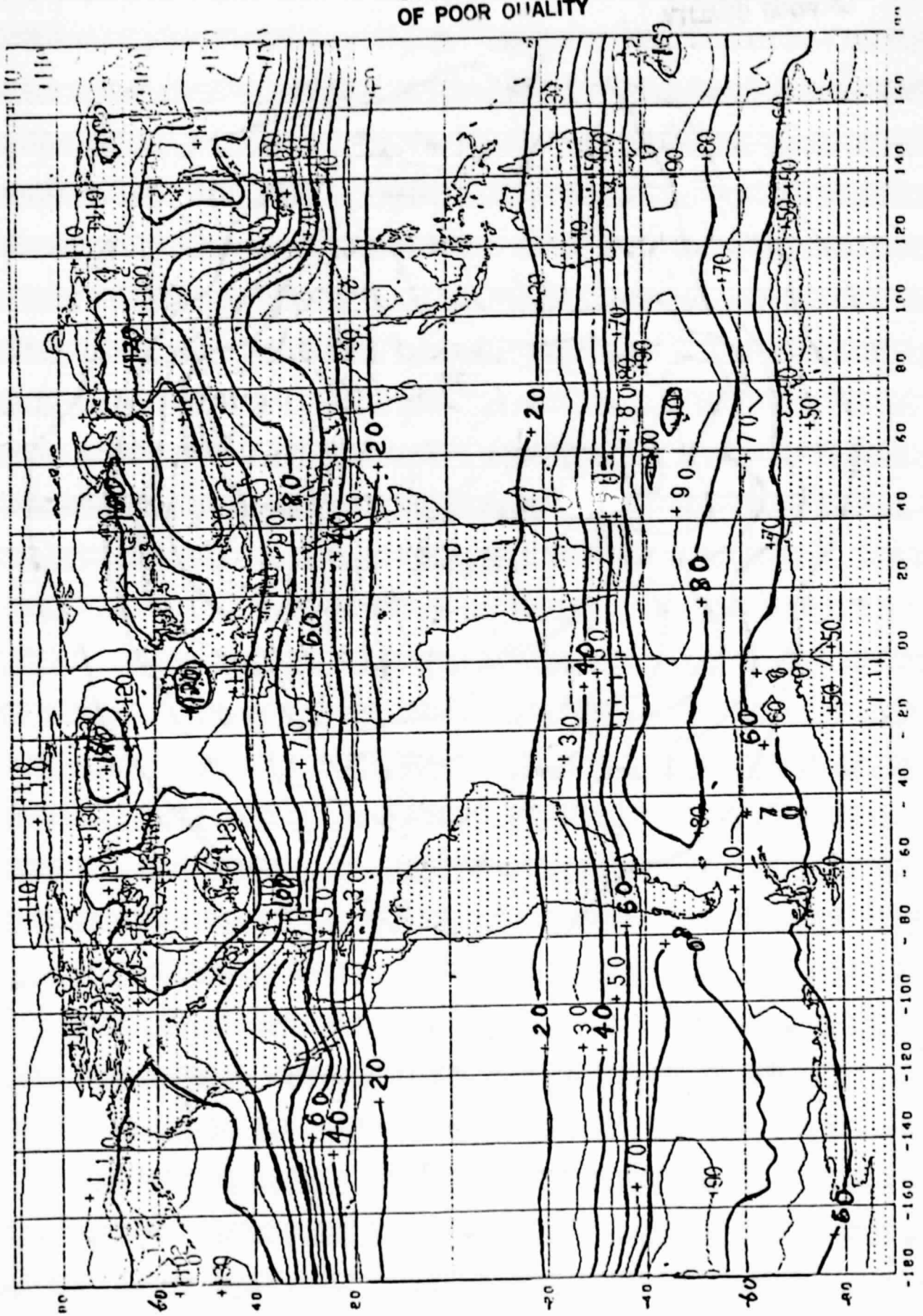


Fig. 1c. Global standard deviations for winter simulations.

ORIGINAL PAGE IS  
OF POOR QUALITY

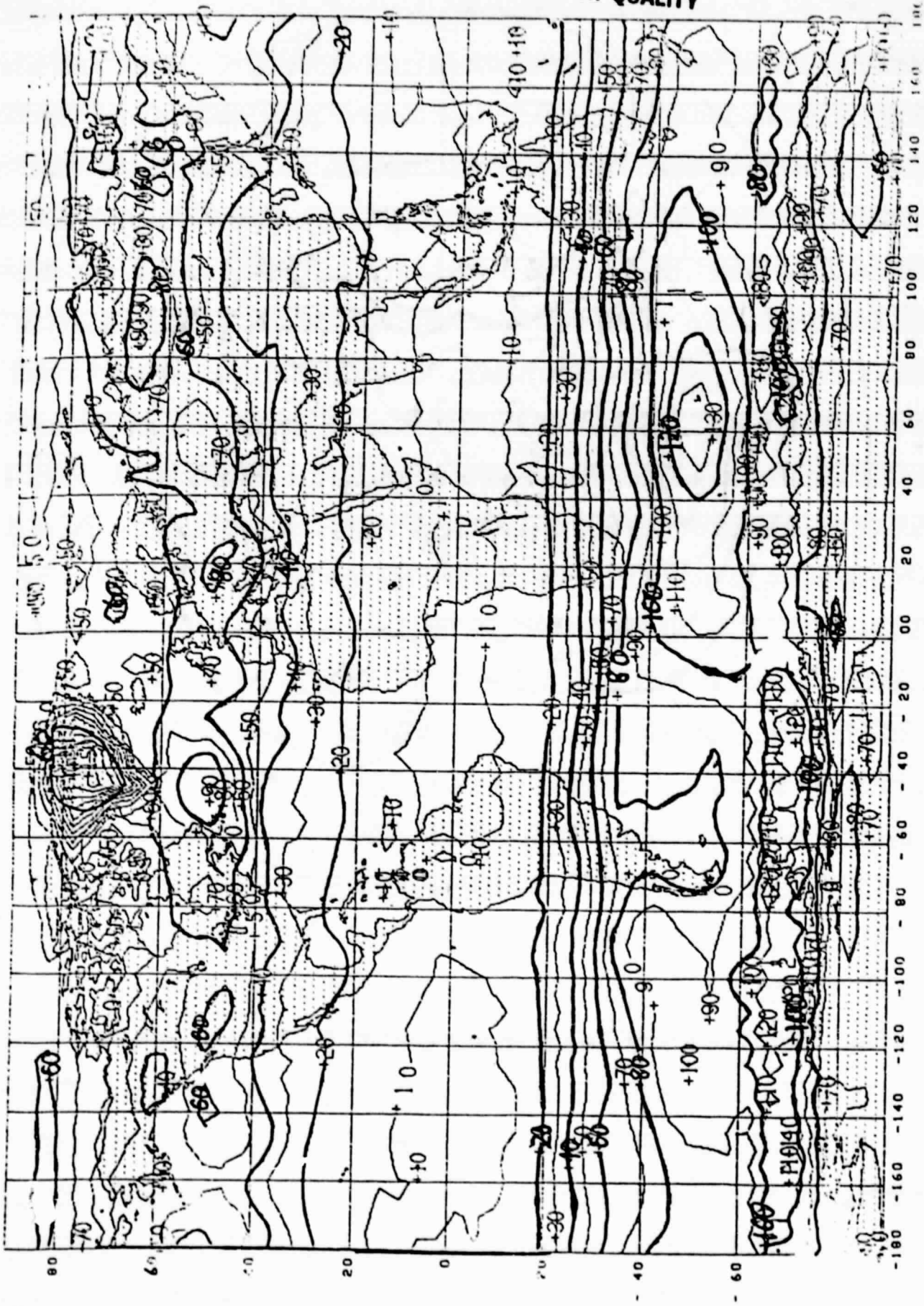


Fig. 1d. Global standard deviations for summer simulations.

ORIGINAL PAGE IS  
OF POOR QUALITY

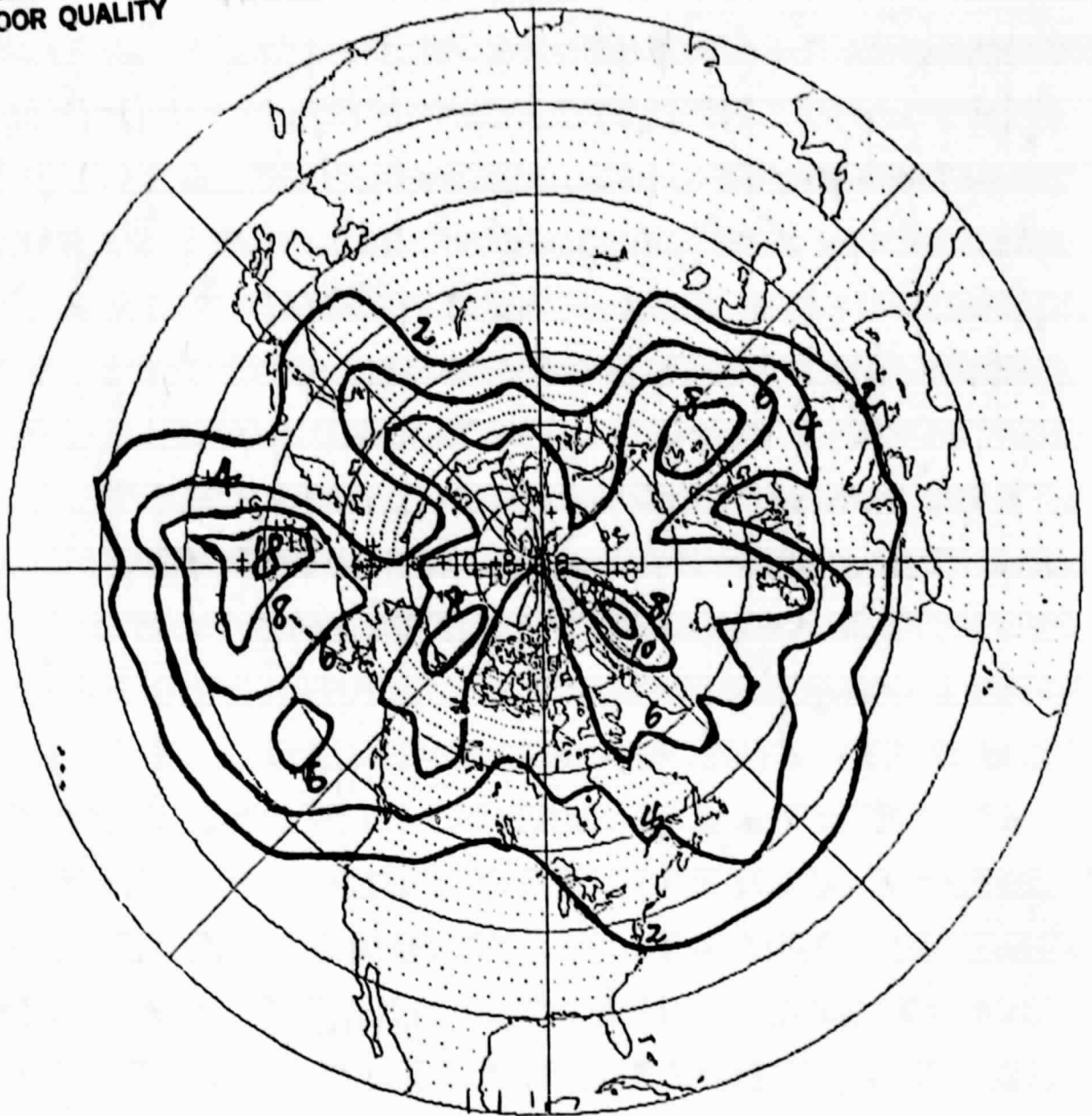


Fig. 2a. Number of events at each grid point N.H. for which positive anomaly of 100 gpm or more persists for 7 days or more for winter simulations.

ORIGINAL PAGE IS  
OF POOR QUALITY

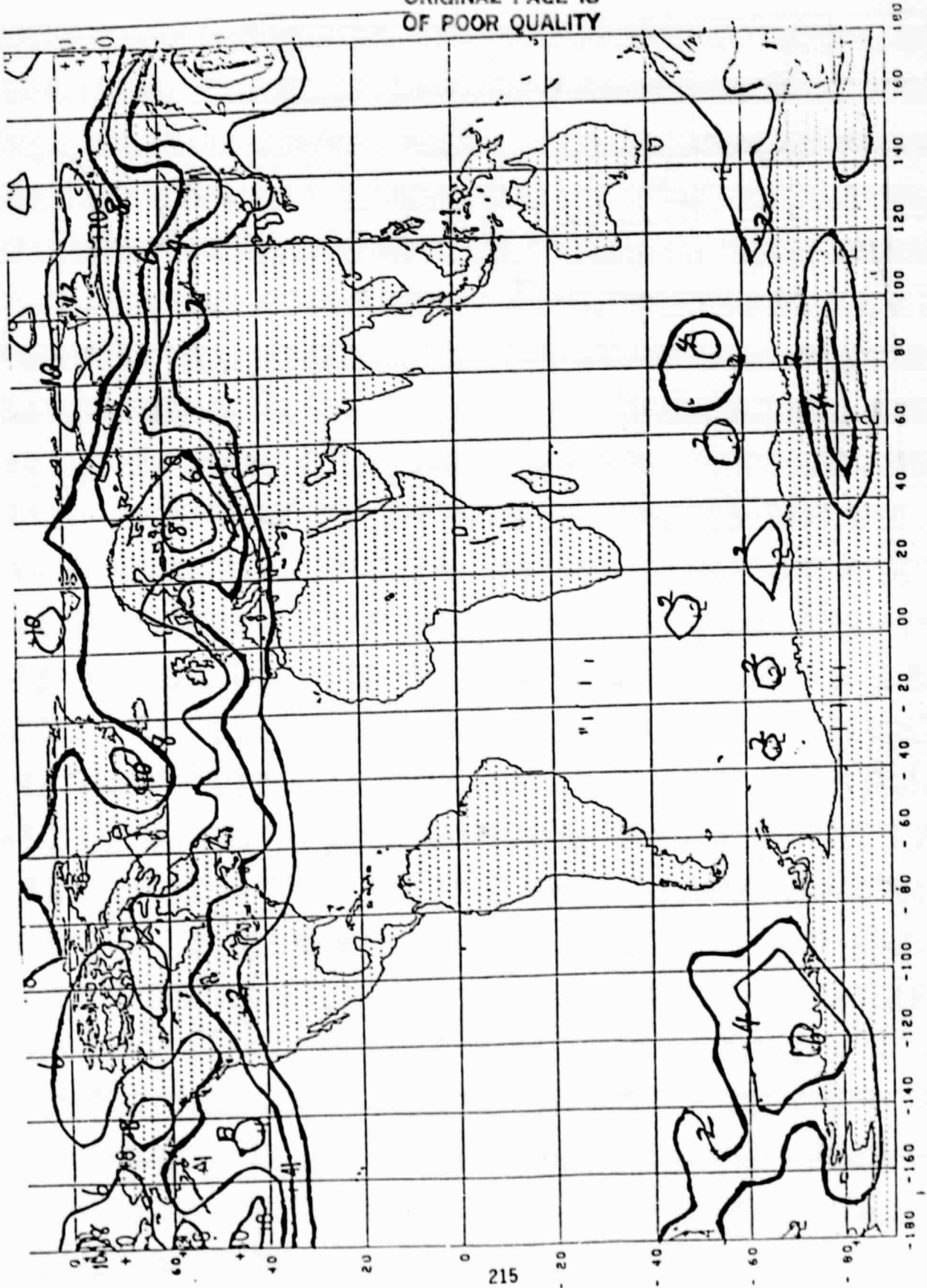


Fig. 2b. Number of events at each grid point (global) for which positive anomaly of 100 gpm or more persisted for 7 days or more for winter.

ORIGINAL PAGE IS  
OF POOR QUALITY

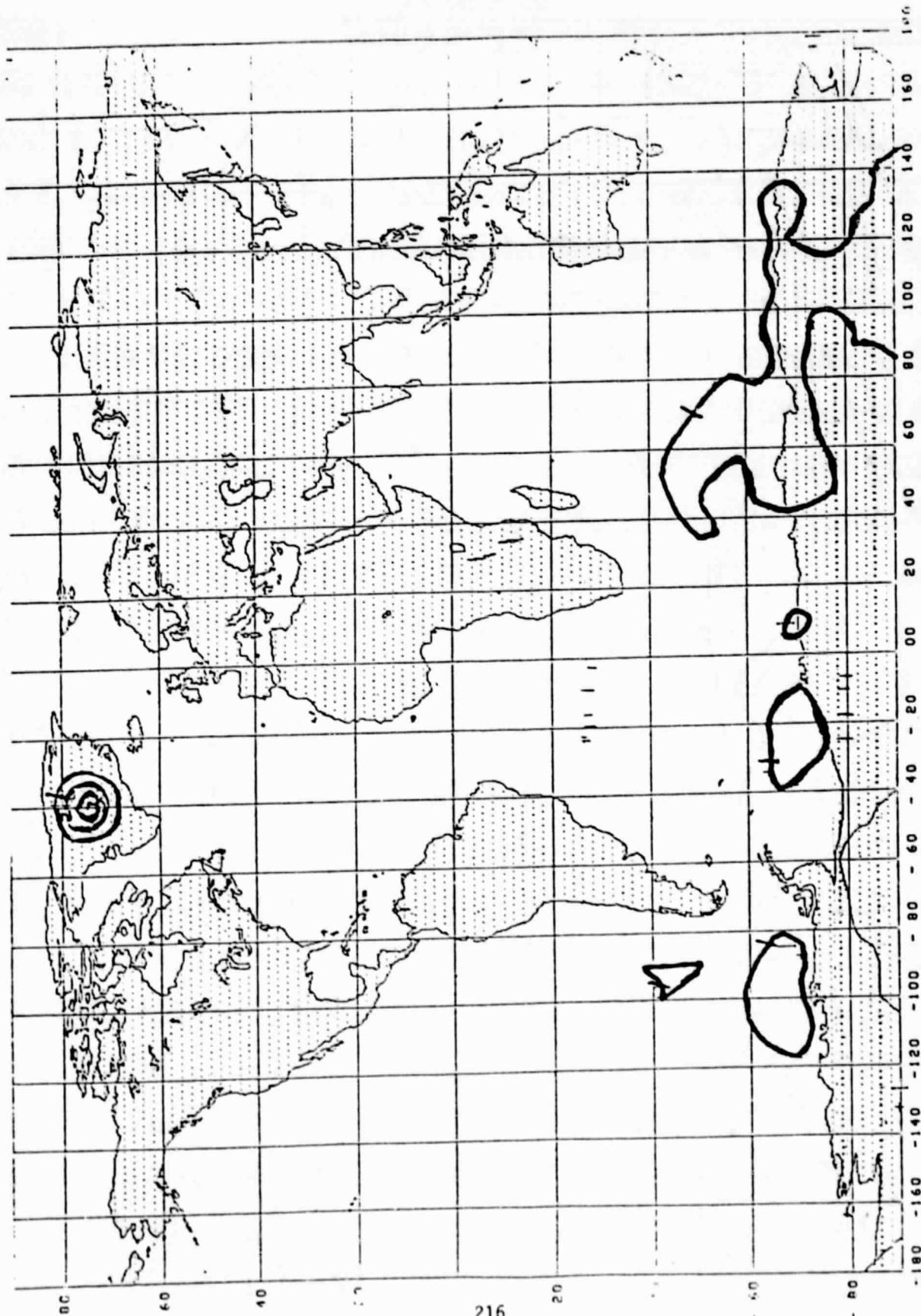


Fig. 2c. Number of events at each grid point (global) for which positive anomaly of 100 gpm or more persisted for 7 days or more for summer.

STRUCTURE AND DYNAMICS OF MONSOON DEPRESSIONS: THE MONEX  
DEPRESSION (JULY 1979)<sup>1</sup>

J. Shukla

## 1. INTRODUCTION

It is generally believed that although the initiation of the onset of the Asiatic monsoon is related to the planetary scale heat sources and sinks (due to asymmetric continentality and different thermal properties of land and ocean), the maintenance and the short term variability of the monsoon is primarily determined by the release of the latent heat of condensation, a major portion of which occurs in association with synoptic and large scale disturbances. The monsoon disturbances therefore play a very important role in the dynamics of the planetary scale monsoon circulation. Preliminary studies based on the FGGE/MONEX data tend to support the conjecture that even if the large scale thermal and dynamical circulations are conducive for onset, the onset process requires a finite amplitude perturbation for northward propagation and establishment of the monsoon over India.

There are several classes of monsoon disturbances (depending upon their space-time scales), the most important of these being the east-west oriented monsoon troughs which move north and south, and the monsoon depressions which 'appear' over the Bay of Bengal and move northwest over India. In this paper we shall confine our discussion to the mechanisms responsible for the formation of monsoon depressions.

There have been many suggestions about the mechanisms for the formation of monsoon depressions. During the first quarter of the century, there were attempts to explain the dynamics of monsoon depressions based on extra-tropical frontal dynamics models which were subsequently abandoned when upper air soundings failed to show sufficient baroclinicity. Subsequent attempts to explain the dynamics of monsoon depressions were influenced by the quasi-geostrophic development theory. In recent years, empirical evidence has been presented to show the relationship between the formation of monsoon depressions, the presence of warm pools at 200 mb (Moula, 1968), and decreased vertical shear (Raman et al., 1978).

The possibility of monsoon depression formation being forced by dynamical instabilities of the mean monsoon flow was examined by Shukla (1977, 1978). Barotropic instability analysis was carried out for each level separately and it was found that both the lower and the upper levels were barotropically unstable. However, since the upper levels, due to the presence of the westerly and the easterly jet streams, had the largest available kinetic energy, the growth rates and the amplitudes were largest for the upper level jet. The most unstable mode for the joint barotropic-baroclinic instability was also found to be dominated by the upper level instability whose phase speed was larger

---

<sup>1</sup> Published in Condensed Papers and Meeting Report: International Conference on Early Results of FGGE and Large-Scale Aspects of its Monsoon Experiments, Jan. 12-17, 1981, Tallahassee, Florida. Published by the World Meteorological Organization, Geneva, Switzerland.

than that of a typical monsoon depression. A joint CISK-barotropic-baroclinic instability analysis of the monsoon flow suggested that the latent heat of condensation is the most crucial source of energy for the growth and maintenance of the monsoon depressions. It is interesting to note that during the 1880's Elliott had suggested that the latent heat of condensation may be the primary energy source for initiation and maintenance of monsoon depressions; however, a quantitative treatment of interaction between latent heating and dynamics was not possible until recently when Charney and Eliassen (1964) and Ooyama (1964) developed the CISK theory. Based on CISK-barotropic-baroclinic instability studies it was concluded that the barotropically unstable lower layers are the primary triggers for the onset of the instability which is further amplified by the latent heat of condensation. In addition, it was conjectured that the role of the terrain is to force a large scale flow which is barotropically unstable at lower levels.

Recently, Mishra and Salvekar (1980) have shown that baroclinic instability alone can account for the growth of the monsoon depressions. This erroneous conclusion is the consequence of the choice of a highly unrealistic meridional temperature gradient at the ground and arbitrarily chosen vertical wind shear at the lower levels. In the classical baroclinic instability problem (Eady, 1949), the primary forcing comes from the meridional temperature gradient at the surface, and the choice of an unrealistic vertical shear at the lower levels is equivalent to specifying an unrealistic meridional temperature gradient at the ground. In the real atmosphere the observed vertical shear near the surface is largely determined by the frictional forces and the boundary layer dynamics. The internal jet instability (Charney and Stern, 1962) of the upper level flow calculated by Mishra and Salvekar is in agreement with the earlier calculations (Shukla, 1977; Goswami et al., (1980)); however, it does not provide the explanation for the monsoon depressions. Satyan et al. (1981) have calculated the barotropic-baroclinic instability of the monsoon flow which includes vertical shear of the meridional wind. As it was implicit in the work of Eady (1949), vertical shear of the meridional wind is always unstable because there is no stabilizing beta effect. The results of Satyan et al. therefore appear to be a mere artifact of the choice of large vertical shear in the meridional wind for which there is no observational evidence.

In most of the instability studies of the monsoon flow there has been too much emphasis on the concept of a 'preferred scale.' It is fairly clear by now that the latent heat of condensation is the most important energy source for the monsoon depressions. It is important to note that the concept of maximum growth rate as a criterion for the preferred scale, which is quite reasonable for shear instabilities, is not necessarily suitable for the condensation-driven instabilities. As was pointed out by Shukla (1978), a large growth rate does not necessarily imply that the wave will attain the maximum amplitude and dominate over the other waves. The fastest growing wave will equilibrate faster and therefore the most preferred wave will be determined by its ability to maximize the utilization of the available moisture. The potential for dominance is therefore calculated as the ratio of the imaginary and the real parts of the complex phase speed. These considerations indeed gave the most preferred scale to be about 3000 km, which is contrary to the statements by Keshavamurty et al. (1978) and Mishra and Salvekar (1980) that the earlier studies failed to get a preferred scale.

## 2. WHERE DO THE MONSOON DEPRESSIONS FORM?

It has been generally assumed that the monsoon depressions originate over the Bay of Bengal and, therefore, most of the instability studies have examined the flow over this region. A recent study by Saha et al. (1981) has shown that during the 10-year period, 1969-1978, more than 80% of the monsoon depressions appearing over the Bay of Bengal were associated with predecessor disturbances coming from the east. This suggests that the cyclogenesis over the Bay mainly involves the amplification of a pre-existing disturbance and one need not have to investigate the conditions for the growth of infinitesimal disturbances. Since the sea surface over the Bay is the warmest at that latitude and the low level flow is convergent due to the presence of the monsoon trough, the CISK mechanism appears to be the most appropriate to explain the growth of the monsoon depressions. It remains to be clarified as to why for some weak disturbances CISK mechanism leads to rapid growth and for others it does not.

It is interesting to note that the westward propagating disturbances in the tropics seem to be ubiquitous as they can be traced back to the Pacific, the Atlantic and the African land masses. The formation of the monsoon depressions, the intense easterly waves, and the cyclonic storms, etc., depends upon the existence of suitable large scale environment where these pre-existing weak disturbances can grow.

## 3. FORMATION OF THE MONEX DEPRESSION (JULY 1979)

The cyclonic circulation over the Bay of Bengal was first observed on July 5 at about 500 mb (there was no data above 500 mb) and it later descended to the lower tropospheric levels. This behavior was also noticed in the study of the past cases by Saha et al. (1981) and Raman et al. (1978). We know that the upper level easterly jet always satisfies the necessary conditions for barotropic instability and internal jet instability. Is it possible that the growth of the amplitude in the lower troposphere is caused, at least in part, by the downward radiation of wave energy? This possibility is being examined by Held and Desmukh (personal communication). However, since the upper level waves propagate westward with a large phase speed, it needs to be examined whether their stay over the Bay is long enough to build sufficient low level amplitude.

It has been shown by Saha and Shukla (1980) that there was some evidence of a westward propagating disturbance which may have amplified into a monsoon depression over the Bay of Bengal. It has also been shown by Nitta and Murakami (1980) that the lower level flow over the Bay was barotropically unstable during the growth of this depression.

It was noticed during the field phase that the extent and the organization of the clouds associated with the depression was not well defined and in spite of a well defined dynamical circulation, the cloudiness was poorly organized. It was also observed that the amplitude of the disturbance was prominent only in the lower and middle troposphere; the amplitude at 900 mb and below was rather weak. This leads to a speculation that rapid growth of the monsoon depression over the Bay of Bengal depends upon its ability to utilize the latent heat of condensation by drawing on the boundary layer moisture convergence. If the initial disturbance does not have sufficient amplitude in the lowest layers,

where the mixing ratio is the highest, moisture convergence and associated latent heating may not be adequate to intensify the disturbance. We do not understand why some of the disturbances develop large amplitudes in the lowest layers and others do not. We also do not understand what determines the downward propagation of amplitude intensity. We hope that further theoretical studies may clarify the mechanism responsible for some of these observed features. It should be pointed out, however, that the phenomena of downward build up of the disturbance amplitude is also noticed for the growth stage of the tropical cyclones and, therefore, in some respects, the growth of a monsoon depression is not very different from the growth of a tropical cyclone. The monsoon depressions, however, move over land only after a few day's stay over the Bay and therefore do not intensify into tropical cyclones.

#### 4. MOVEMENT OF MONSOON DEPRESSIONS

It is generally observed that the phase velocity of the monsoon depressions over the Bay is smaller than that over the adjoining land. Pre-depression disturbances coming from further east have different phase velocities depending upon the level at which their amplitude is most pronounced. The low level flow over the Bay is generally westerly and if the depression has large amplitude at the lower levels, the steering effect will produce eastward movement. The beta effect and the lower boundary slope effect will produce westward movement. The role of the quasi-geostrophic dynamics, by the combined effects of differential vorticity advection and thickness advection in determining the phase velocity, will depend upon the structure of the large scale and the embedded disturbance. Preliminary computations by Sanders (1981) indicated that the quasi-geostrophic dynamics was not very dominant in determining either the growth or the movement of the depression during the developing stage.

It is suggested that the rapid westward propagation is related to the vertical structure of the monsoon depressions. If the depression attains sufficient amplitude at the upper levels, the steering effect of the upper level easterlies contributes to the westward movement. The slow phase velocity of the depressions over the Bay permits a faster growth and development of a vertically coupled disturbance which can then be influenced by the upper level easterlies.

If the disturbance does not have sufficient vertical coupling, which may be either due to weak dynamical forcing and/or due to lack of organized moist convection, the vorticity maxima at different levels move with different phase velocity in different directions and the disturbance develops strong vertical tilt which is followed by the weakening and decay of the disturbance. This was the case for the MONEX depression on 7-8 July, 1979, which developed strong vertical tilt and the magnitude of the tilt was accounted for by the vorticity advection at different levels (see Sanders, 1981).

The foregoing survey of the mechanisms of formation and movement of monsoon depressions can be summarized as follows:

- (1) Monsoon depressions over the Bay of Bengal are caused either by amplification of westward propagating weak disturbances or by downward propagation of the internal jet instability of the easterly jet.

(2) The barotropic instability of the low level flow over the Bay of Bengal is conducive to the growth of weak disturbances. The presence of the surrounding terrain contributes to the establishment of such a large scale flow (monsoon trough over the head bay) which is barotropically unstable.

(3) CISK is the primary driving mechanism for the rapid growth of a pre-existing weak perturbation. However, if the amplitude of the disturbance at the lower levels is not sufficient to draw on the low level moisture convergence, the disturbance does not grow to a deep depression.

(4) Once the disturbance has attained adequate amplitude in the lower levels (either by downward propagation of wave energy or by CISK), the low level moisture convergence and latent heat of condensation is utilized more efficiently for the development of a vertically coupled deep disturbance which along with upper level easterlies contribute to the westward propagation of the disturbance. Absence of strong vertical coupling leads to vertical tilt and decay of the disturbance.

(5) Our ability to forecast the formation of monsoon depressions over the Bay of Bengal should be greatly improved with the establishment of upper air stations over the Burmese coast and further east.

#### REFERENCES

- Charney, J. G., and M. E. Stern, 1962: On the stability of internal baroclinic jets in a rotating atmosphere. J. Atmos. Sci., 19, 159-172.
- Charney, J. G., and A. Eliassen, 1964: On the growth of the hurricane depression. J. Atmos. Sci., 21, 68-75.
- Eady, E. T., 1949: Long waves and cyclone waves. Tellus, 1, 33-52.
- Goswami, B. N., R. N. Keshavamurty, and V. Satyan, 1980: Role of barotropic-baroclinic instability for the growth of monsoon depressions and mid-tropospheric cyclones. Proc. of Indian Aca. of Sci., 89, 79-97.
- Keshavamurty, R. N., V. Satyan, and B. N. Goswami, 1978: Indian summer monsoon cyclogenesis and its variability. Nature, 274, 576-578.
- Mishra, S. K., and P. S. Salvekar, 1980: Role of baroclinic instability in the development of monsoon disturbances. J. Atmos. Sci., 37, 383-394.
- Moula, K. G., 1968: Cyclogenesis in the Bay of Bengal and Arabian Sea. Tellus, 20, 151-162.
- Nitta, T., and M. Murakami, 1980: Three-dimensional structure and energy cycles of a monsoon depression developed over the Bay of Bengal. FGGE Operations Report, Volume 9, 137-144.
- Ooyama, K., 1964: A dynamical model for the study of tropical cyclone development. Geofis. Intern., 4, 187-198.

- Raman, C. R. V., Y. P. Rao, S. K. Subramanian, and Z. E. Shaikh, 1978: Wind shear in a monsoon depression. Nature, 276, 51-53.
- Saha, K. R., and J. Shukla, 1980: Further evidence of association of westward-propagating disturbances with monsoon depressions. FGGE Operations Research, Volume 9, 23-31.
- Saha, K. R., F. Sanders, and J. Shukla, 1981: Westward-propagating predecessors of monsoon depressions. Mon. Wea. Rev., 109.
- Sanders, F., 1981: Diagnostic analysis of the monsoon depression of 3-8 July, 1979. International Conference on Early Results of FGGE and Large-Scale Aspects of Its Monsoon Experiments, Jan. 12-17, 1981, Tallahassee, Florida.
- Satyan, V., R. N. Keshavamurty, and B. N. Goswami, 1981: Stability of monsoon zonal flow with a superposed stationary monsoon wave. IUTAM/IUGG Symposium on Monsoon Dynamics, December 1977, New Delhi, India.
- Shukla, J., 1977: Barotropic-baroclinic instability of mean zonal wind during summer monsoon. Pure and App. Geophys., 115, 1449-1461.
- Shukla, J., 1978: CISK-barotropic-baroclinic instability and the growth of monsoon depressions. J. Atmos. Sci., 35, 495-508.

NUMERICAL PREDICTION OF THE MONSOON DEPRESSION OF 5-7 JULY, 1979<sup>1</sup>

J. Shukla, R. Atlas, and W. E. Baker

## 1. INTRODUCTION

One of the primary objectives of the FGGE/MONEX effort is to determine the three dimensional structure of the atmosphere more accurately, thereby improving the quality of deterministic short range prediction. The detailed instantaneous structure of the monsoon circulation, which is perhaps the largest asymmetric perturbation of the general circulation of the atmosphere, had never been defined earlier because of the paucity of data over the Indian Ocean and the adjoining countries. Numerical predictions of the monsoon fluctuations, therefore, provide a good test to determine the impact of the FGGE/MONEX observing system on short range prediction. Although the large scale monsoon circulation is forced by planetary scale heat sources due to asymmetric continentality and differential heat capacity of land and ocean, the short term fluctuations are mainly caused by the synoptic scale disturbances referred to as the monsoon depressions. One such depression appeared over the Bay of Bengal during the first week of July 1979. This, fortunately, happened at a time when a large group of MONEX research scientists had gathered at Calcutta, India to observe and study the summer monsoon circulation. There were two MONEX research aircrafts (Electra from NCAR and P3 from NOAA) which could probe the formative and the growth stages of the monsoon depression. A well-defined monsoon depression was observed on July 7, 1979 which then moved over India and dissipated.

We have chosen this particular synoptic situation for two assimilation and forecast experiments. Starting from the initial conditions (provided by the NMC global analysis) of 0000 GMT 1 July 1979, one experiment utilized only the conventional surface and upper air data, and the other utilized the same conventional data plus all the available FGGE/MONEX data. We refer to these two assimilations as the control assimilation and the FGGE/MONEX assimilation. From the two initial conditions valid for 1200 GMT 7 July 1979, arrived at by assimilating the two different data sets, we have made numerical predictions with the GLAS general circulation model. In the following sections, we describe the model, the analysis and assimilation procedure, the differences in the analyses due to different data inputs, and the differences in the numerical predictions.

## 2. ANALYSIS AND ASSIMILATION OF FGGE/MONEX DATA

In this section we describe the objective analysis and assimilation procedure used with the FGGE/MONEX data.

---

<sup>1</sup> Published in Condensed Papers and Meeting Report: International Conference on Early Results of FGGE and Large-Scale Aspects of Its Monsoon Experiments, Jan. 12-17, 1981, Tallahassee, Florida. Published by the World Meteorological Organization, Geneva, Switzerland.

## 2a. The Model

The model is a global, primitive-equation model, discretized in finite-difference form. There are nine vertical layers equal in sigma with a horizontal resolution of  $2.5^\circ$  in latitude and  $3^\circ$  in longitude. The horizontal differences are second-order accurate on a staggered grid (Arakawa, 1966; 1972). The model differs from that described in Somerville *et al.* (1974) in its horizontal resolution and by the introduction of a split-grid, which at high latitudes modifies the longitudinal mesh size.

Time differencing is performed following the space-centered Euler-backward (Matsuno) scheme (Arakawa and Lamb, 1977). Due to a number of features of the difference scheme, such as the averaging required by the staggering of variables and the additional smoothing at high latitudes, the scheme is strongly dissipative. As a result, spurious high-frequency oscillations generated at the beginning of a forecast decay rapidly.

## 2b. The Data

For this study we utilized FGGE data collected from 1-7 July 1979 and the special MONEX data (dropwindsondes, aircraft, and enhanced TIROS-N retrievals). The data nominally available to the objective analysis program over the entire globe is listed by type in Table 1. Table 2 summarizes the MONEX data utilized over the Bay of Bengal.

Table 1. Typical number of "Soundings" for each 24 h period during the assimilation cycle (July 1-7, 1979).

Rawinsondes:	3000
Satellite winds:	5500
Satellite temp.:	8500
Aircraft:	3500
Constant level balloons:	250
Enhanced satellite temp. (Bay of Bengal):	175

The rms wind vector fit (final analysis vs. observations) for dropwindsondes and Wisconsin Indian Ocean clouds tracked winds was compared with that for rawinsondes. The rms fit for the dropwindsondes was quite similar to that for the rawinsondes. The Wisconsin winds exhibited a poorer fit due to less weight given in the analysis of that data and the higher data density.

An enhancement of the TIROS-N sounding data for the Bay of Bengal was performed in order to supplement the operational sounding data set with higher resolution soundings in meteorologically active areas, and with new soundings where data voids or soundings of questionable quality existed. Man-computer Interactive Data Access System (McIDAS) terminals, developed by the Space Science Engineering Center of the University of Wisconsin, were utilized for the display and enhancement of the TIROS-N soundings.

The algorithms for retrieving temperature profiles from the TIROS-N radiances were essentially the same as those used by NESS for the objective generation of operational temperature profiles. Three types of temperature retrievals are possible: (1) clear column, (2) partly cloudy retrievals utilizing infrared observations from the High Resolution Infrared Sounder (HIRS) instrument aboard TIROS-N, and (3) cloudy retrievals utilizing only microwave observations from the Microwave Scanning Unit (MSU) on TIROS-N. The operational temperature profiles have a horizontal resolution of 250 km, whereas enhanced temperature profiles can be retrieved at the resolution of the measurements. (30 km for HIRS and 150 km for MSU).

Subjective comparisons of enhanced and operational soundings and rawinsonde reports for the FGGE "Special Effort" (Atlas, 1980) have shown that the enhanced and operational retrievals tend to be similar in cloud free areas. However, large improvements in thickness and mandatory level temperature, and intensification of atmospheric thermal gradients occasionally result from the enhancement of cloudy and partially cloudy areas.

## 2c. Objective Analysis Procedure

In the GLAS objective analysis scheme (Baker et al., 1981) eastward and northward wind components, geopotential height and relative humidity are analyzed on mandatory pressure surfaces. The 6 h model forecast provides a first guess for these fields at 300 mb and sea level, where sea level pressure and sea level temperature are also analyzed. The first guess for the other levels is obtained from the model first guess modified by a vertical interpolation between the two closest completed analyses. Vertical consistency is maintained through static stability constraints. The analysis at each level is performed with a successive correction method (Cressman, 1959) modified to account for differences in the data density and the statistical estimates of the error structure of the observations. The average distance  $d$  between data points is found in a circle with a radius of 800 km centered at each grid point. Three scans are performed with a radius of influence  $R_i = c_i d$ , where the coefficients  $c_i$  (1.6, 1.4, 1.2) were chosen to minimize the analysis error (Stephens and Stitt, 1970). However, the radius of influence is not allowed to become smaller than 300 km. During this process, all data are checked for horizontal consistency. The completed analyses are smoothed and then interpolated to the model sigma levels.

The assimilation procedure provides for the intermittent analysis of batches of data grouped in a  $\pm 3$  h window about each synoptic time. In these experiments, the wind and height fields were analyzed independently with no explicit coupling or balancing.

## 2d. Differences between the control and the FGGE/MONEX assimilations

Fig. 1 shows the zonally averaged root mean square (rms) vector wind error between the control assimilation and the FGGE/MONEX assimilation for 1200 GMT 7 July 1979. It can be seen that the maximum differences occur in the southern hemisphere, especially near the poles. Since there is virtually no data in the control assimilation over that part of the globe, the control analysis on July 7 could not be very different from the model prediction except for the influences that might have propagated from the data-rich regions. These differences are

therefore, an indication of the systematic model forecast errors. The difference is the smallest over the northern hemispheric mid-latitudes which contains the highest density of the conventional upper air network. Large differences in the northern hemispheric tropics are mainly due to the large number of fairly accurate cloud-tracked winds. Given such large differences in the initial conditions, it is natural to expect differences in the forecasts.

### 3. RESULTS

Due to the limited space available here, we present the results of verification over India only. Table 3 gives the SI skill scores and rms error for sea level pressure and 500 mb geopotential height for forecasts starting from control and FGGE/MONEX assimilations on 1200 GMT 7 July 1979. Both forecasts were verified against the NMC global analysis. In general, there is a positive impact of FGGE/MONEX data; however, the differences after 24 h do not appear to be significant. The rms error for 500 mb geopotential height shows a negative impact for the first 36 h. It should also be pointed out that the location of the center of the monsoon depression in the FGGE/MONEX assimilation at 1200 GMT 7 July 1979 does not agree with a careful hand analysis.

In performing the numerical experiments, a number of problems were encountered with the tropical analyses. The horizontal resolution ( $2.5^\circ \times 3^\circ$ ) of the prediction model was too coarse to accurately define the monsoon depression. The assimilation of geopotential height data derived from satellite soundings generated gravity waves whose amplitudes were comparable to the meteorologically significant features we were attempting to predict. Gravity waves were particularly troublesome in the 6 h first guess during the assimilation cycle. The difficulty in utilizing satellite temperature soundings in the tropics was also compounded by the precipitable water contamination of the TIROS-N microwave retrievals (Phillips, 1980). The results of this study should be considered preliminary for these reasons. We plan to carry out further experiments using the official FGGE/MONEX database with improved assimilation and initialization techniques. It is only then that a more definitive statement can be made about the impact of FGGE/MONEX data on the predictability of the monsoon disturbances.

### ACKNOWLEDGEMENTS

The authors wish to acknowledge Messrs. G. Cole for his supervision of the sounding enhancement, D. Edelmann, M. Iredell and H. Carus for the preparation of the special MONEX data for analysis and E. Sabatino, R. Rosenberg and B. Doty for technical assistance and graphics support. We also wish to thank Miss D. Boyer for typing the manuscript and Ms. L. Rumburg for drafting the figure.

### REFERENCES

- Atlas, R., 1980: Evaluation of NESS soundings used in the FGGE special effort. NASA Conf. Publ. 2157, 31-40.
- Arakawa, A., 1966: Computational design for long-term numerical integration of the equations of fluid motion: Two-dimensional incompressible flow. Part I. J. Comput. Phys., 1, 119-143.

- Arakawa, A., 1972: Design of the UCLA atmospheric general circulation model. Tech. Rep. 7, Dept. of Meteorology, University of California at Los Angeles.
- Arakawa, A., and V. R. Lamb, 1977: Computational design of the basic dynamical processes of the UCLA general circulation model. Methods in Computational Physics, 17, J. Chang, Ed., Academic Press, 173-265.
- Baker, W. E., D. Edelman, M. Iredell, D. Han, and S. Jakkempudi, 1981: Objective analysis of observational data from the FGGE observing systems. NASA Tech. Memo. 82062.
- Cressman, G. P., 1959: An operational objective analysis system. Mon. Wea. Rev., 87, 367-374.
- Phillips, N. A., 1980: Two examples of satellite temperature retrievals in the north Pacific. Bull. Amer. Meteor. Soc., 61, 712-717.
- Somerville, R. C. J., P. H. Stone, M. Halem, J. E. Hansen, J. S. Hogan, L. M. Druyan, G. Russell, A. S. Lacis, W. J. Quirk, and J. Tenenbaum, 1974: The GISS model of the global atmosphere. J. Atmos. Sci., 31, 84-117.
- Stephens, J. J., and J. M. Stitt, 1970: Optimum influence radii for interpolation with the method of successive corrections. Mon. Wea. Rev., 98, 680-687.

Table 2. MONEX data over Bay of Bengal (10N-25N, 80E-100E).

		Dropwindsonde	Aircraft	Wisconsin Winds	Enhanced Soundings
July 1	00Z	-		-	
	06Z	-		18	-
	12Z	-		34	
	18Z	-	1		
July 2	00Z	-	1		
	06Z	-	0		-
	12Z	-	1	23	
	18Z	-	2		
July 3	00Z	-			
	06Z	9	6	11	110
	12Z	3	0	25	
	18Z		1		
July 4	00Z		1		
	06Z		1	9	290
	12Z			38	
	18Z		1		
July 5	00Z				
	06Z	15	2	7	188
	12Z	7	2	20	
	18Z		2		
July 6	00Z				
	06Z	6	2	15	172
	12Z	3	3	9	
	18Z				
July 7	00Z		2		
	06Z	8	7	18	135
	12Z	8	3	19	
	18Z				
July 8	00Z		1		
	06Z	17	4	27	-
	12Z	1	1	38	
	18Z		1		
July 9	00Z				
	06Z	11	3	24	-
	12Z	3	1	49	
	18Z				
July 10	00Z		1		-

Table 3. Skill score (S1) and root mean square error (RMS) over India (6N-26N, 70E-100E) for control and FGGE/MONEX initial conditions of 1200 GMT 7 July 1979 for sea level pressure (SLP) and 500 mb geopotential height (Z500).

Impact for India (6-26N I.C. 7/7/79, 12Z  
70-100E),

Hours	<u>SLP S1</u>		Impact
	Control	FGGE	
12	66.8	62.6	+4.2
24	60.6	48.8	+11.8
36	65.7	63.1	+2.6
48	52.8	52.5	+.3

Hours	<u>SLP RMS</u>		Impact
	Control	FGGE	
12	4.1	2.2	+1.9
24	4.0	2.4	+1.6
36	2.5	3.3	-.8
48	2.7	1.9	+.8

Hours	<u>Z500 S1</u>		Impact
	Control	FGGE	
12	92.1	85.1	+7.0
24	99.4	94.0	+5.4
36	100.9	94.1	+6.8
48	104.1	106.2	-2.1

Hours	<u>Z500 RMS</u>		Impact
	Control	FGGE	
12	32.4	43.9	-9.5
24	53.6	62.4	-8.8
36	49.3	51.2	-1.9
48	48.4	46.9	+1.5

ORIGINAL PAGE IS  
OF POOR QUALITY

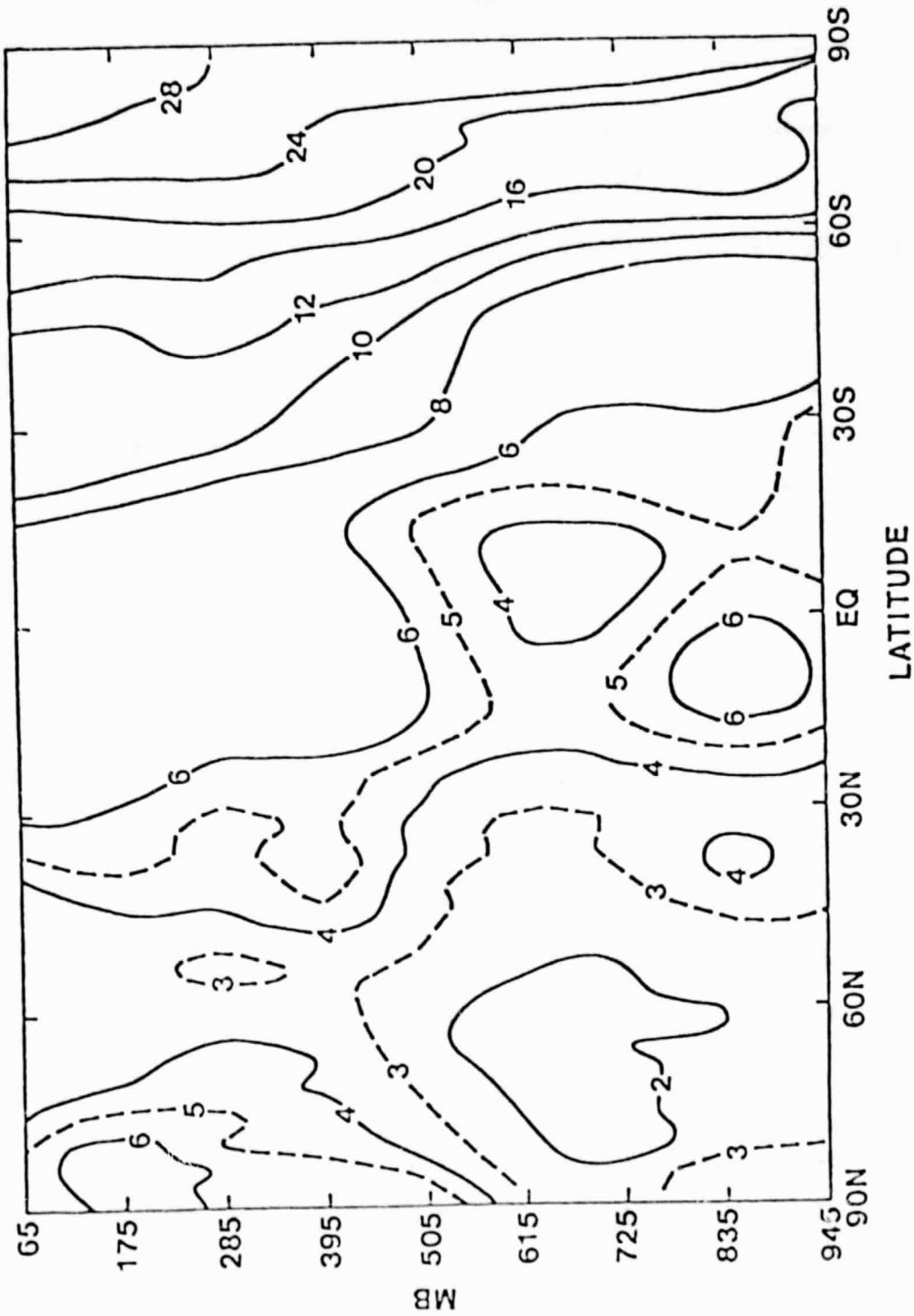


Figure 1. Rms vector wind error (m/s) between control and FGCE/MONEX assimilation.

GLOBAL AND LOCAL FLUCTUATIONS OF WINTER AND SUMMER  
SIMULATIONS WITH THE GLAS CLIMATE MODEL

D. M. Straus and J. Shukla

## 1. INTRODUCTION

Winter and summer simulations have been carried out with an improved version of the GLAS general circulation model. The model used for the simulations is basically that presented by Halem *et al.* (1979). The changes that were made to the model code involved the use an improved method of computing the boundary layer fluxes, and a more realistic specification of the albedo of snow and ice covered surfaces. (See Shukla *et al.*, 1980). The Winter integration was initialized with data valid for 0Z of 1 January, 1975, and the summer integration was initialized with data valid for 0Z of 15 June, 1979. Both integrations were carried out for 90 days, during which all the boundary conditions were prescribed to vary smoothly. The observed data consists of the NMC twice-daily analyses for the years 1963-1977. Each particular diagnostic quantity was computed from the model data and each of the 15 years of observations in precisely the same way, wherever possible. The reported observational results are averaged over the 15 winters or summers, as appropriate.

## 2. STATIONARY WAVES IN THE GEOPOTENTIAL HEIGHT FIELD

Results are presented for the stationary (time averaged) component of the geopotential height. Figure 1a shows the observed winter variance around a latitude circle of the stationary geopotential height, summed over wavenumbers 1-4. The term "stationary" refers to a 90-day average commencing on January 1. The corresponding stationary ultra-long planetary wave variance for the winter model<sup>1</sup> simulation is presented in Figure 1b.

The model results show good overall agreement with the observations, with both variances reaching a maximum in the mid-latitude upper troposphere. The model variance is slightly too weak up to the 250 mb level, above which it fails to show the decrease with height apparent in the observations. It is important to note that the stationary variance of this version of the GLAS climate model shown in Figure 1b shows remarkable improvement over the same variance calculated for the previous version of the model, as presented by Straus and Shukla (1981, their Figure 6a).

The observed summer variance of the stationary component of the geopotential height, summed over wavenumbers 1-4, is presented in Figure 1c. The corresponding model variance is shown in Figure 1d. These quantities were computed in the same manner as for the winter season, except that the averaging period was defined to be 90 days starting on June 15. The simulated ultra-long wave variance agrees well with the observations with regard to the location and strength of the three maxima: one in mid-latitudes at about 300 mb, and two in the subtropics, at 850 mb and 200 mb. Discrepancies include the fact that the

---

<sup>1</sup> The model results presented will be limited to the domain for which observations were available, namely 20°N to 90°N.

simulated mid-latitude variance does not decrease above 300 mb, the slight northward displacement in the model of the subtropical maximum at 850 mb, and the weakness of the simulated subtropical maximum at 200 mb.

### 3. LOW FREQUENCY PLANETARY WAVES

Most of the zonal and time variance of the transient geopotential height field (exclusive of the annual cycle) is contained in low frequency, planetary scale motions. More specifically, we are referring to fluctuations with periods of 7.5 to 90 days and consisting of zonal wavenumbers 1 to 4.

The vertical and meridional structure of the low frequency planetary wave variance (LFPW) observed in winter is shown in Figure 2a<sup>2</sup>. This variance reaches a maximum slightly above the 300 mb level at about 64N, and shows a decrease above this level. The model variance (Figure 2b) has a similar structure, except that the variance increases up to at least 200 mb. In addition, the model variance is somewhat too small throughout the northern hemispheric extratropical domain. As was the case for the stationary planetary waves, this result represents a great improvement over the simulation of the previous version of the model. (See Straus and Shukla (1981), Figure 2a.)

The observed summer LFPW variance is shown in Figure 2c. The structure of the summer variance is quite similar to that in winter, except that the maximum has moved northward. The magnitude of the variance is much less in the summer. The model summer LFPW variance (Figure 2d) has the same overall dependence on latitude and height as observed, but again it does not decrease above 300 mb (as do the observations), and again the model variances are, in general, too small.

### 4. LOCAL ANALYSIS OF VARIANCE

A useful description of the fluctuations of any basic field is afforded by the analysis of local variability discussed by Blackmon (1976). This method portrays the spatially local fluctuations of a particular field by the construction of maps of its RMS deviation in time. The variability due to baroclinic activity is separated by filtering the data with a 'band-pass' filter which retains fluctuations with periods of 2.5 to 6 days. In the application of this method, an estimate of the annual cycle is removed from the data before either the filtering or the computation of the RMS deviation. The band-pass RMS of the geopotential height is closely associated with regions having a high frequency of cyclonic activity, and so indicates the location of the 'storm tracks' (Blackmon, et al., 1977).

A comparison of the observed winter band-pass RMS of geopotential height (Figure 3a) with that of the model (Figure 3b) shows that there is excellent agreement in terms of both the location and strength of the major areas of cyclonic activity in the north central Pacific and western Atlantic. The observed summer band-pass RMS height field (Figure 3c) shows the two oceanic maxima that were present in the winter map. The Atlantic maximum has been

---

<sup>2</sup> For details regarding the calculation of observed and model LFPW variances, see Straus and Shukla (1981).

shifted to the east, and the magnitude of the summer RMS is generally much smaller. The corresponding map for the model (Figure 3d) indicates that the Atlantic maximum has been realistically simulated, both with respect to position and magnitude. The Pacific maximum, however, is too weak and is located too far to the west.

#### REFERENCES

- Blackmon, M. L., 1976: A climatological spectral study of the 500 mb geopotential height of the Northern Hemisphere. J. Atmos. Sci., 33, 1607-1622.
- Blackmon, M. L., J. M. Wallace, N. C. Lau, and S. L. Mullen, 1977: An observational study of the Northern Hemisphere wintertime circulation. J. Atmos. Sci., 34, 1040-1053.
- Halem, M., J. Shukla, Y. Mintz, M. L. Wu, R. Godbole, G. Herman, and Y. Sud, 1979: Comparisons of observed seasonal climate features with a winter and summer numerical simulation produced with the GLAS general circulation model. Report of the JOC Study Conference on Climate Models: Performance, Intercomparison and Sensitivity Studies, Volume I. GARP Publ. Series No. 22, 207-253. WMO, Geneva, Switzerland.
- Lau, N. C., H. Tennekes, and J. M. Wallace, 1978: Maintenance of the momentum flux by transient eddies in the upper troposphere. J. Atmos. Sci., 35, 139-147.
- Shukla, J., Y. Sud, and E. Sabatino, 1980: Preliminary results of a January simulation with an improved version of the GLAS model. Atmospheric and Oceanographic Research Review-1979, NASA Technical Memorandum 80650, pp. 121-132.
- Straus, D. M., and J. Shukla, 1981: Space-time spectral structure of a GLAS general circulation model and a comparison with observations. J. Atmos. Sci., 38, 902-917.

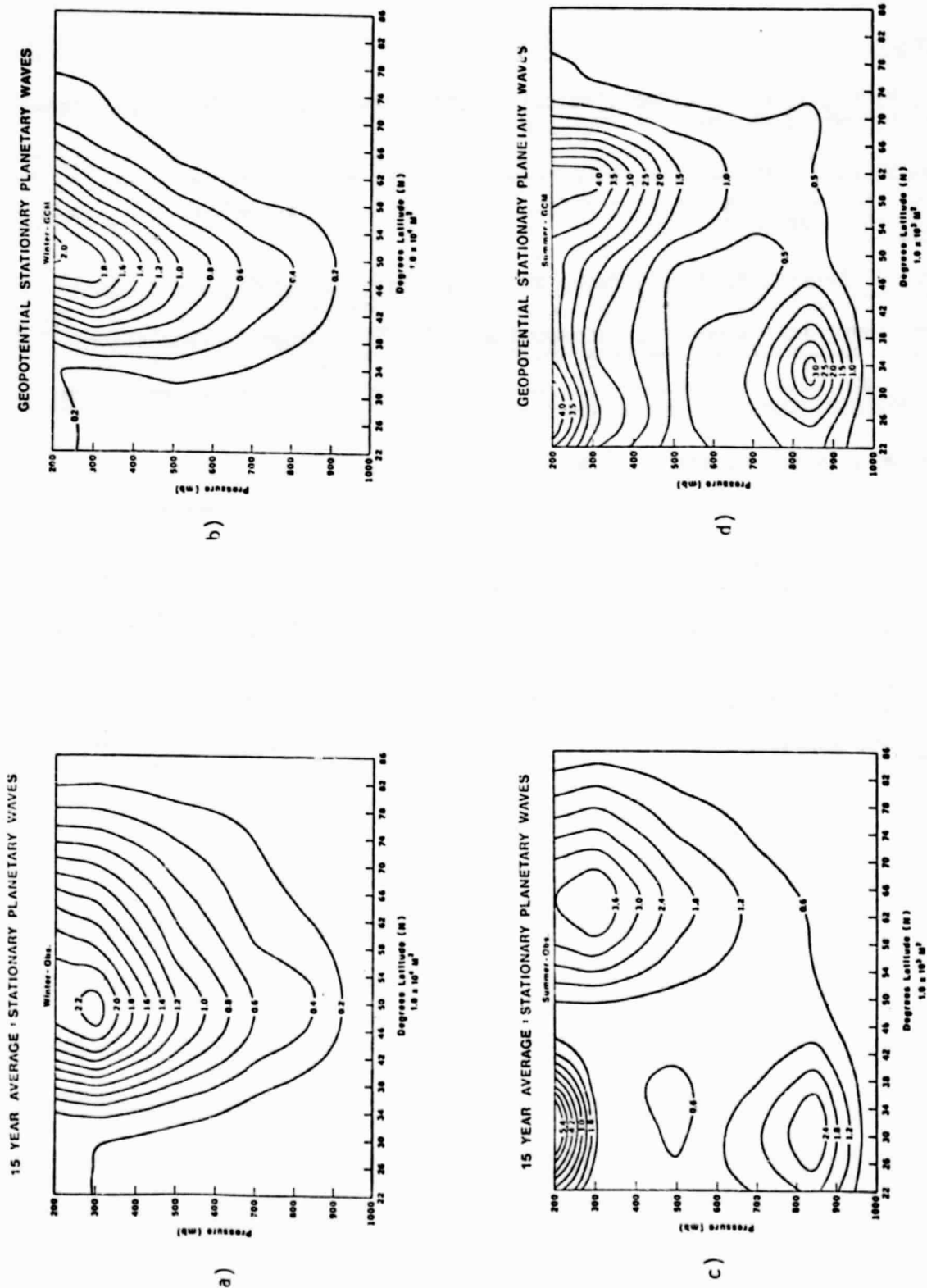


Figure 1. Stationary planetary wave variance of the geopotential height field in the Northern Hemisphere. a) Observations, winter (units of 104 m<sup>2</sup>); b) Model, winter (units of 104 m<sup>2</sup>); c) Observations, summer (units of 103 m<sup>2</sup>); d) Model, summer (units of 103 m<sup>2</sup>).

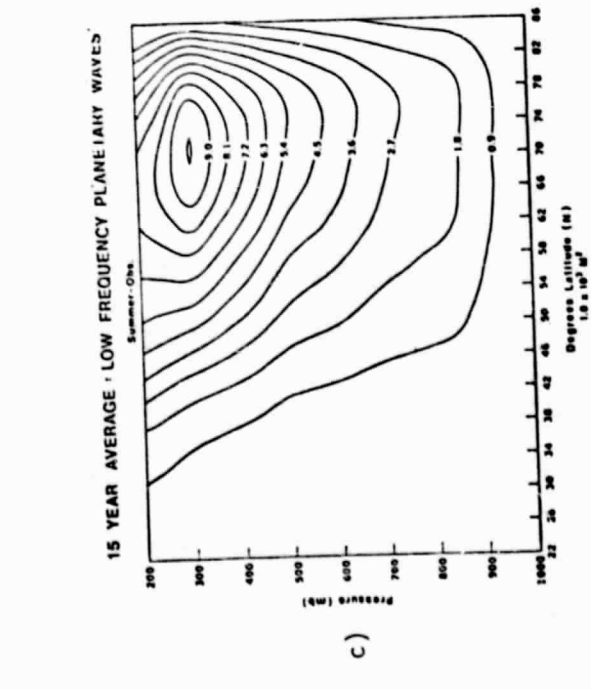
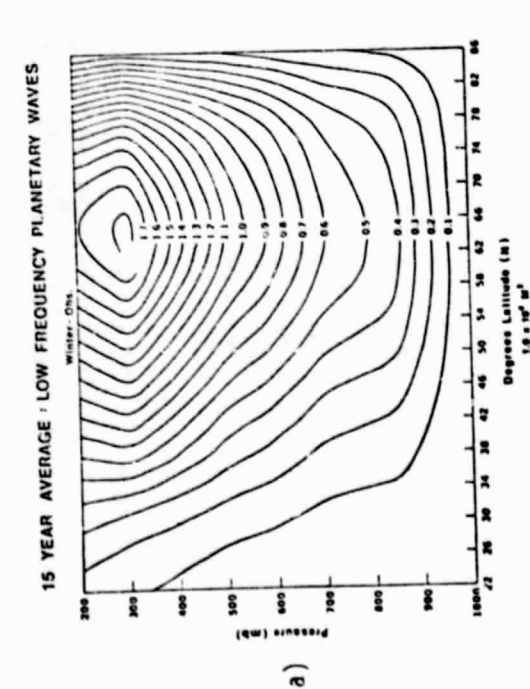
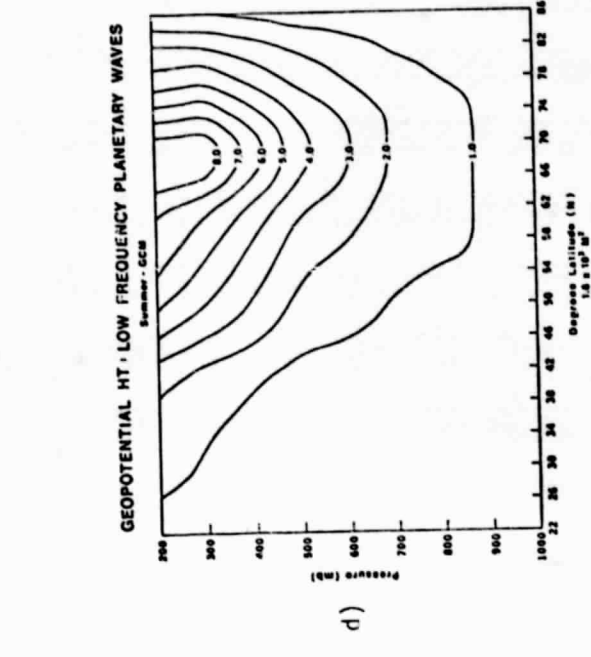
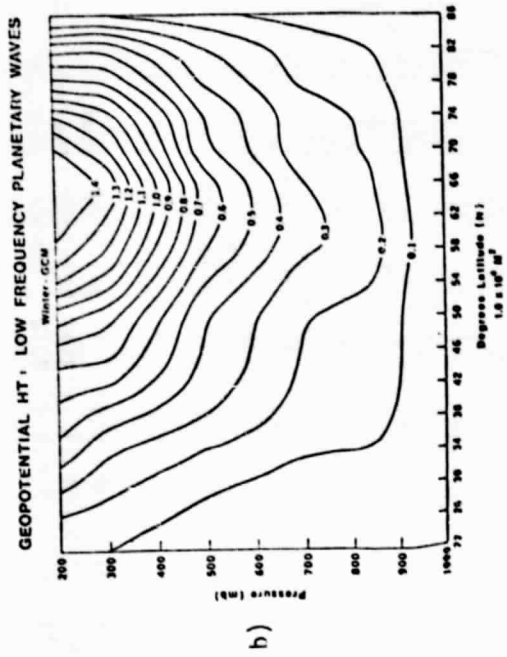


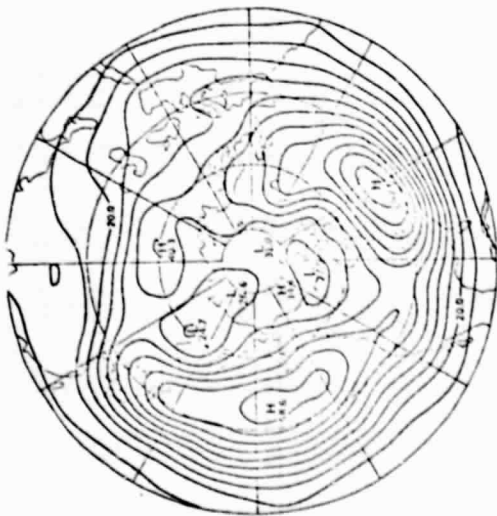
Figure 2. Geopotential height variance in low frequency planetary waves. a) Observations, winter (units of  $10^4 \text{ m}^2$ , contour interval of  $0.1 \times 10^4 \text{ m}^2$ ); b) Model, winter (units of  $10^4 \text{ m}^2$ , contour interval of  $0.1 \times 10^4 \text{ m}^2$ ); c) Observations, summer (units of  $10^3 \text{ m}^2$ , contour interval of  $0.9 \times 10^3 \text{ m}^2$ ); d) Model, summer (units of  $10^3 \text{ m}^2$ , contour interval of  $1.0 \times 10^3 \text{ m}^2$ ).



b)



d)



a)



c)

Figure 3. RMS deviation of the 500 mb band-pass geopotential height field, in units of meters. a) Observations, winter (contour interval is 5 m); b) Model, winter (contour interval is 5 m); c) Observations, summer (contour interval is 5 m); d) Model, summer (contour interval is 5 m).

INFLUENCE OF SURFACE-ALBEDO IN SUBTROPICAL REGIONS  
ON JULY CIRCULATION

Y. Sud and M. Fennessy

A simulation study to examine the influence of surface-albedo on July circulation in subtropical regions is presented. The results are based on two 47-day integrations. In the first integration, called the control run, surface albedos were normally prescribed, whereas in the second integration, called the anomaly run, the surface albedo was modified in four regions: the Sahel in Africa, the Great Plains in the United States, the Thar Desert border in the Indian subcontinent, and Brazil in South America. Each run was started from observed initial conditions for June 15, 1979 based on NMC analysis. The surface albedo in each of the regions detailed in Table 1 was arbitrarily made 30%.

The key results for examining the Charney mechanism are summarized in Table 2.

The short-wave radiation absorbed by the surface was reduced in the anomaly runs. The percentage reduction was less than the percentage change in albedo because the reduced cloudiness partially mitigated the effect of the increased surface albedo. Simultaneously, there was an increase in the outgoing long-wave radiation at the surface. Altogether the surface radiation balance was reduced. This was largely balanced by a reduction in the surface fluxes of sensible heat and evaporation. However, the precipitation reduced even more than the evaporation. It implies even larger cooling due to lack of release of latent heat. Thus, the diabatic heating in these regions reduced substantially. Consistently, subsidence was induced and adiabatic heating of the order of the diabatic cooling was obtained. The region which did not follow the above pattern precisely was the Great Plains. There, the total cloudiness and total precipitation were virtually unchanged. Although there was some reduction in the convective precipitation, it was offset by an increase in the large-scale precipitation. This region is somewhat unique due to the influence of the Rocky Mountains on large-scale flows. Thus, the lack of response of precipitation to increased surface albedo in this one realization is not surprising.

Our results differ in many ways from those of Charney *et al.* (1977). We did not find an increase in the solar radiation absorbed by the surface in the anomaly simulation. Perhaps, the excessive evaporation in their simulations was responsible for this effect. The evaporation and precipitation fields in our studies are more realistic compared to the observations. The reduction in precipitation based on 5-day averaged plots is not consistently maintained in any region except the Sahel, whereas in Charney *et al.* (1977) the differences were large and well maintained. Excessive evaporation in their simulation may have resulted in excessive moisture divergence due to subsidence, and enhanced its effect on cloudiness and precipitation. Thus, excessive evaporation is likely to amplify the albedo effect on precipitation.

However, the thermal processes induced by an increase in the surface albedo were consistent with Charney's (1975) mechanism in all the regions, including the Great Plains, where the precipitation did not reduce.

---

1 An extension of Charney's albedo experiments.

The results show that Charney's hypothesis that an arid region's large surface albedo through radiative cooling provides a feedback mechanism for the production of a drought, is well founded.

Of the several large differences in the SLP and 500 mb geopotential height fields, the one persistent difference was over Central Eurasia (see for example Fig. 1). Elsewhere there were large differences, but these were not persistent over the two 15-day averages. The occurrence of distant circulation anomalies due to albedo anomalies in the tropics is very intriguing and needs further investigation.

In any event, the changes in the surface albedo of the anomaly run used in this study were smaller than those in the Charney *et al.* (1977) study. Since the effects are non-linear, and the results were differentially affected by horizontal advection, the impact of albedo changes varies in the different regions. The purpose of this exercise was to re-examine Charney's hypothesis with a better GCM. This has been accomplished because the hypothesis is validated in the Sahel and the Rajputana region, which belong to the Sahara-Arabian-Indo-Pakistani complex of deserts, as well as in subtropical Brazil. These regions are relatively free of strong advective effects, a condition essential for the Charney mechanism to be effective in reducing the rainfall.

#### REFERENCES

- Charney, J. G., 1975: Dynamics of deserts and drought in the Sahel. Quart. J. Roy. Meteor. Soc., 101, 193-202.
- Charney, J. G., W. J. Quirk, S. H. Chow, and J. Kornfield, 1977: A comparative study of the effects of albedo change on drought in semi-arid regions. J. Atmos. Sci., 34, 1366-1385.

Table 1  
Areal Extent of Albedo Anomaly Regions

#	Region	Number of Grid Points	Latitude	Longitude
1	Sahel	22	12-16	17.5°W-47.5°E
2	Thar Desert Border	4	24°N-32°N	67.5°E-77.5°E
3	Brazil	10	4°S-8°S 4°S-20°S	32.5°W-37.5°W 37.5°W-42.5°W 42.5°W-47.5°W
4	Western Great Plains	8	32°N-48°N	97.5°W-107.5°W

ORIGINAL PAGE IS  
OF POOR QUALITY

Table 2  
Impact of Albedo Anomaly on Simulated JULY  
Regional Differences (Anomaly - Control)

REG #	Name	Albedo % age	Surface Balance W/m <sup>2</sup>		ΔE Evap. mm/day and % age	ΔP Precip. mm/day and % age	Ratio ΔP/ΔE	Δω ω = $\frac{dp}{dt}$ μb/sec	ΔQ Diab. Heat W/m <sup>2</sup>	ΔW Adiab. Heat W/m <sup>2</sup>	ΔT <sub>S</sub> /T <sub>G</sub> and T <sub>S</sub> /T <sub>G</sub> (C°)
			ΔSW Shtwve. Radtn. and % age	ΔNR Net Radtn. and % age							
I	SAHEL	13	-9.8	-16.9	-0.71	-1.46	2.1	0.044	-34.5	40.1	0.4/0.6 30.4/32.8
			-4.9%	-10.5%	-14.5%	-27.9%					
II	THAR DESERT BORDER	15	-20.0	-24.8	-0.22	-0.48	2.2	0.080	-20.3	18.1	0.7/0.3 31.8/33.9
			-8.2%	-13.3%	-8.5%	-12.8%					
III	NORTH- EAST BRAZIL	21	-32.6	-34.6	-0.28	-0.53	1.9	0.056	-38.4	27.0	-2.4/-3.1 31.8/33.9
			-16.5%	-24.3%	-12.1%	-23.8%					
IV	WESTERN GREAT PLAINS	17	-45.0	-41.3	-0.23	0.02	-0.1	0.093	-41.4	65.6	-2.4/-3.1 30.2/32.0
			-17.2%	-21.4%	-8.4%	0.7%					

† Note: Percentage changes are based on the simulated values in the control run.

IV. SUMMER LECTURE SERIES

## DOES EL NINO AFFECT OUR WINTER CLIMATE?

J. M. Wallace/University of Washington

Atmospheric phenomena associated with the interannual variability of sea surface temperature in the equatorial Pacific are examined, with emphasis on vertical structure and teleconnections to middle latitudes. This paper is specifically concerned with the interannual variability of seasonal means for the Northern Hemisphere winter during the period 1951-1978. Among the variables considered are sea surface temperature in the equatorial Pacific, 200 mb height at stations throughout the tropics, a "Southern Oscillation Index" of sea-level pressure, the mean temperature of the tropical troposphere, precipitation at selected equatorial Pacific stations, and the Northern Hemisphere 700 mb height field. Selected statistics derived from surface data are also examined for the period 1910-45. Results are presented in the form of time series and correlation statistics for the variables listed above.

Results concerning the relationships between sea surface temperature, sea level pressure and rainfall are consistent with the major conclusions of previous studies by J. Bjerknes and others. Fluctuations in mean tropospheric temperature and 200 mb height are shown to vary simultaneously with equatorial Pacific sea surface temperature fluctuations, not only in the Pacific sector, but at stations throughout the tropics. The zonally symmetric component of these 200 mb height fluctuations is considerably larger than the Southern Oscillation in 1000 mb height, and the corresponding fluctuations in the mean temperature of the tropical troposphere are on the order of nearly 1 K.

The tropical time series exhibit a well defined pattern of correlation with Northern Hemisphere 700 mb height. Warm episodes in equatorial Pacific sea surface temperature tend to be accompanied by below normal 700 mb height in the North Pacific and the southeastern United States and above normal 700 mb height over western Canada. These correlations with mid-latitude 700 mb height tend to be somewhat stronger than the corresponding correlations with mid-latitude surface temperature or pressure. The mid-latitude 700 mb heights are more strongly correlated with equatorial Pacific sea surface temperature and tropical 200 mb heights than with the Southern Oscillation Index. The pattern of mid-latitude 700 mb height correlations resembles steady-state solutions of the linearized barotropic vorticity equation on a sphere, with forcing from the tropics.

Much of the material presented in this talk is included in a manuscript by John D. Horel and John M. Wallace entitled "Planetary Scale Atmospheric Phenomena Associated with Interannual Variability of Sea Surface Temperature in the Equatorial Pacific" which has been submitted to Monthly Weather Review.

July 2, 1980

AN ATTEMPT TO SEPARATE CHANGES DUE TO STATISTICAL  
SAMPLING FROM REAL CLIMATE CHANGE

R. A. Madden/NCAR

The variance of time-averaged meteorological data is assumed to consist of two components. One is a statistical sampling variability resulting from fast-varying weather that is present even without any climate change. The other results from shifts in mean values that occur on time scales long relative to that of weather variation. The first component is presumed to be unpredictable while the second is considered potentially predictable. This paper discusses an attempt to separate these two components in time series of daily temperature for stations in the United States.

## SIMULATION OF THE JANUARY 1977 BLOCKING EVENT

K. Miyakoda/NOAA/GFDL

January 1977 was a month noted for its extraordinary weather over North America. The winter was dominated by two long-sustained, large amplitude, stationary ridges positioned over the west coast of North America and the Icelandic region of the Atlantic Ocean. A very intense trough reached deep into the eastern United States and caused one of the coldest Januaries on record, while western North America including Alaska remained warm. Several one-month integrations of various GCM's were conducted in order to test their ability to simulate the January 1977 blocking event. The GCM's used were of the finite different and spectral model types of the highest spatial resolution available at GFDL and ANMRC (Australian Numerical Meteorological Research Center). Two different initial conditions and two different external forcing conditions, were utilized by these models. In total, about 15 one-month integrations were performed. One month is the range just beyond the limit of predictability for deterministic forecasting, so the individual forecast, if successful, should be sufficiently close to reality.

In some cases, a fairly accurate forecast was obtained, and considerable skill was recognized in the simulation of the 30-day evolution in terms of the 5 day or 10 day mean flow fields, including the coldest period over the eastern United States which occurred in the last five days of January. It is concluded that a proper treatment of the subgrid-scale processes is essential for the simulation of the blocking phenomenon, in addition to the importance of a proper space resolution of the GCM.

ON THE GLOBAL DISTRIBUTION OF THE HEAT SOURCES AND SINKS OF THE ATMOSPHERE  
AND THE THERMALLY-FORCED PLANETARY SCALE RESPONSE

D. R. Johnson/University of Wisconsin

The time-averaged structure of the Asiatic summer and winter monsoon circulation and their link with planetary scale transport processes are determined from a FGGE operational data set generated by the U. S. National Meteorological Center. The rotational and irrotational components of the horizontal transport of mass and energy are determined through isentropic diagnostics.

The relations between 1) the global distribution of boundary energy flux through the earth's surface and the top of the atmosphere, 2) heat sources and sinks internal to the atmosphere and 3) planetary scale mass and energy transport processes within the isentropic stratification of the atmosphere are broadly established from transport theory and results. For the months of January, April, July and October of 1979, the global distribution of diabatic heating is determined indirectly and linked to the time-averaged mass and energy transport within large scale Hadley-type and Walker-type circulations. The results verify the global nature of monsoonal circulations that are linked to the planetary scale of differential heating in the form of large scale Hadley-type and Walker-type circulations. The primary planetary source region of energy in the region of Indonesia-Philippines-Southeast Asia is linked through quasi-horizontal mass transport with primary sink regions of energy in the two circumpolar vortices, the Sahara and subtropical anticyclonic circulations. This primary center of the source of energy in the Indonesia-Southeast Asia area moves seasonally from one hemisphere to the other. Net heating within a given region and net cooling in another region in association with differences in boundary flux through the earth's surface and the top of the atmosphere result in net energy transport from the source to the sink region, a result basic to thermally-forced circulations. The net energy transport is realized from the condition that more energy is transported by a branch of a circulation in higher-valued isentropic layers from the heat source to the heat sink than is returned by a branch of circulation within lower-valued isentropic layers. At the same time no net mass change occurs. Thus a steady time-averaged circulation that is embedded in the isentropic structure may be realized.

The winter monsoon circulation in Asia links radiative cooling over Asia to sensible and latent heat release within mid-latitude baroclinic waves and also to latent heat release in the Indonesia, Philippine and New Guinea regions through horizontal transport of mass and energy. The role of mid-latitude baroclinic waves in providing for mass and energy exchange between polar and subtropical regions within the time-averaged isentropic structure is briefly discussed.

COMPARISONS OF VISIBLE AND INFRARED DISTRIBUTIONS  
OF GLOBAL CLOUD COVERS

M. T. Chahine/JPL

Day and night mapping of the global distributions of the horizontal cloud cover and the corresponding cloud-top pressure levels can be obtained from the same set of infrared radiance data used to retrieve clear-column temperature profiles. General formulation of the problem is presented with illustrations for the simple case of a single layer of non-reflecting clouds. Experimental verifications are obtained using 15  $\mu\text{m}$  data measured by the NOAA-VTPR infrared sounder.

The upwelling radiance from a planetary atmosphere is a function of the thermal state of the atmosphere, the concentration of radiatively active gases, and the extents, heights, and radiative transfer properties of clouds and aerosols. Thus, in principle, it should be possible to recover useful information about the physical and chemical structure of an atmosphere from analysis of the upwelling radiance. However, the problem in analyzing such data lies in finding ways to uncouple the effects of these variables and retrieve the true values of each unknown parameter separately. By treating the cloud effects as short period oscillations over the clear column radiance, an analytical method was developed by Chahine to retrieve clear-column vertical temperature profiles from radiance measurements made in the presence of clouds. The uncoupling of the effects of clouds is carried out analytically without any a priori information about the amounts, heights and optical properties of the clouds in the fields of view. Once the clear-column temperature profiles are determined the same radiance data could then be used to determine the heights, amounts, and radiative transfer properties of clouds.

The determination of the clear-column temperature profiles from the VTPR data requires a a priori knowledge of the surface temperature  $T_s$ . We obtained  $T_s$  from the NOAA surface analysis. We investigated the effects of errors in the assumed surface temperature on the accuracy of the values of the effective cloud cover  $\bar{N}$  which is the product of the geometrical cover  $N$  and the cloud emissivity  $\epsilon_v$  and the mean cloud top pressure,  $P_c$ . We concluded that the effects of an error in  $T_s$  of  $\pm 2\text{K}$  on  $\bar{N}$  and  $P_c$  are small, especially for  $P_c < 700 \text{ mb}$ . Correction for the effects of water vapor on the atmospheric transmission functions were made before generating the clear-column radiances.

It should be noted here that while the determination of the clear column radiance is obtained without any assumptions about the properties of clouds, the determination of the amount and height of clouds requires the use of cloud models. In the case of the VTPR data we assumed that the difference between the reconstructed clear column radiance and the radiance measured in a given field of view is due to the presence of a single layer of non-reflecting cloud. We applied the nonreflecting cloud model to analyze radiance data from the NOAA-VTPR sounder for a period of one week from January 1-7, 1975. The VTPR global cloud distributions were calculated in 1977. The results were then averaged for a grid size of  $4^\circ$  latitude by  $5^\circ$  longitude, and only the averaged results were stored on a magnetic tape for subsequent comparison with other cloud maps to be obtained from other sources. A typical comparison of the results is shown in Figures 1, 2, and 3.

Figure 1 shows contours of cloud amounts for a region across the Pacific Ocean between 40°N-30°S and 75°W-255°W. Fig. 2 shows contours of cloud amounts derived from computations made by J. Sadler of the University of Hawaii for the same period of time and the region from photographs obtained from the Vidicon cameras of NOAA's satellite.

The results shown in Figs. 1 and 2, therefore, compare asynoptic infrared cloud maps and synoptic visual maps. Consequently only persisting cloudiness appears to be common between the two cloud maps. For this reason the zonally averaged values shown in Fig. 3 give a more realistic comparison between the amount of clouds observed in the infrared and visible. The conclusion that the effective infrared cloud amount  $\tilde{N} = N\epsilon$  is smaller than the cloud amount observed in the visible could be due to the facts that the cloud emissivity in the 15  $\mu\text{m}$  is less than one, and the VTPR sounding channels are not sensitive to detecting low level clouds below 800 mb. The average cloudiness for the region shown in Figs. 1 and 2 is 0.39 for the infrared and 0.52 for the visible, and the ratio of the infrared to the visible cloud cover is  $\sim 0.75$ .

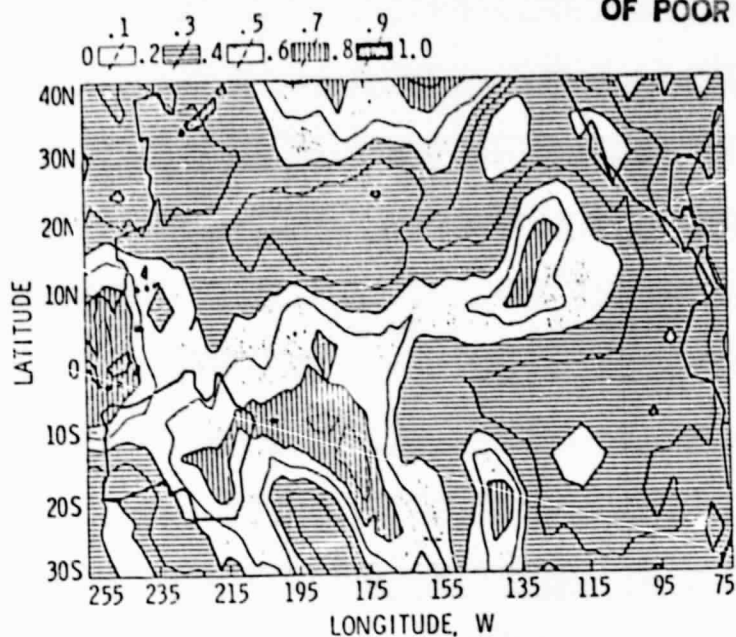


Fig. 1. Contours of cloud amounts in decimals derived from 15  $\mu$ m satellite data for the period of January 1-7, 1975.

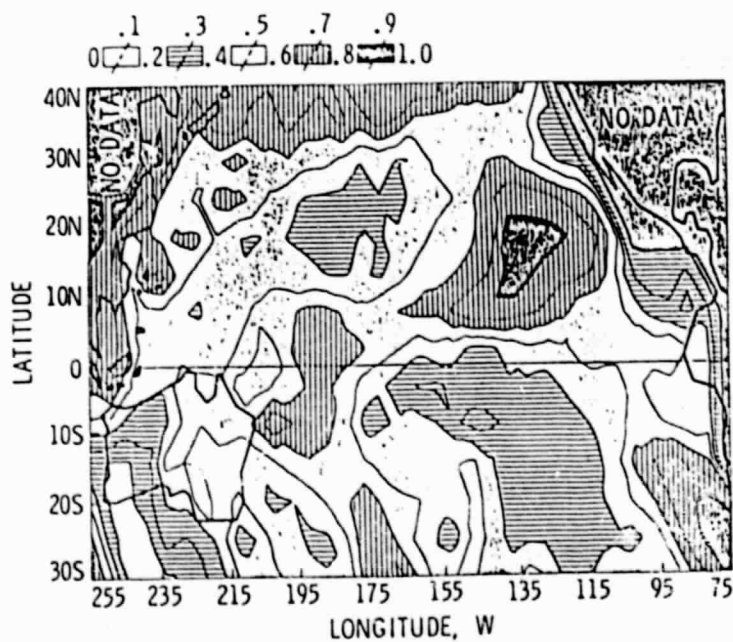


Fig. 2. Contours of cloud amounts in decimals derived from visible data by Sadler for the period of January 1-7, 1975.

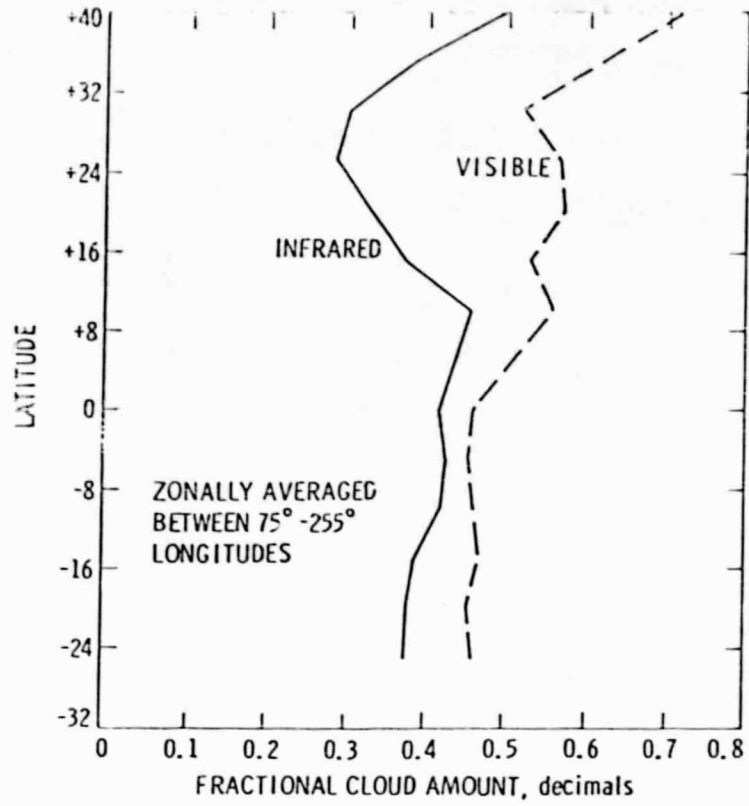


Fig. 3. Meridional profiles of zonally averaged distribution of fractional cloud cover for the data given in Figures 1 & 2.

## DYNAMICS OF SUDDEN STRATOSPHERIC WARMINGS

J. R. Holton/The University of Washington

The complex of events associated with sudden warmings in the Northern Hemisphere polar winter stratosphere provides perhaps the best natural example of planetary scale wave-mean flow interaction processes. Recent work by Andrews and McIntyre (1976) and others (cf., review by Holton, 1980) has provided new diagnostic methods for studying both observed and simulated stratospheric warmings. With the aid of these methods rapid progress is being made in understanding the origin and evolution of sudden warmings.

In this lecture I first review the observed behavior of planetary waves and the mean flows during sudden warmings. Next I review wave-mean flow interaction theory in a quasi-geostrophic framework and derive the so-called "non-acceleration" theorem. By an elementary transformation of the Eulerian mean equations I show that the net forcing of the mean flow by the waves may be expressed in terms of the divergence of the Eliassen-Palm flux, a vector in the meridional plane whose northward component is proportional to the meridional heat flux. This net forcing can alternatively be written as the poleward flux of quasi-geostrophic potential vorticity.

In the final portion of the lecture I discuss the similarities of the transformed Eulerian analysis to the more fundamental Lagrangian mean formulation, and show how the net forcing of the mean flow by the waves can be interpreted in terms of the divergence of the wave radiation stress.

## REFERENCES

- Andrews, D. G., and M. E. McIntyre, 1976: Planetary waves in horizontal and vertical shear: The generalized Eliassen-Palm relation and the zonal mean acceleration. J. Atmos. Sci., 33, 2031-2048.
- Holton, J. R., 1980: The dynamics of sudden stratospheric warmings. Ann. Rev. Earth Planet. Sci., 8, 169-190.

## THE BEHAVIOR OF EDDY HEAT FLUXES ON SHORT TIME SCALES

P. H. Stone<sup>1</sup>/Massachusetts Institute of Technology

NMC data from 30°N to 70°N for three Januaries are used to calculate time series of the tropospheric eddy flux of sensible heat and of the baroclinic stability, as measured by the difference between the zonal wind shear and the critical value of the shear in two-level models. On synoptic time scales the variance of the eddy flux is about 35% of the mean, and the variance of the stability parameter is about 2 m/s. Typically, the zonal wind shear is about 2 m/s greater than the critical value of about 10 m/s. Time-lagged correlations between the two series show a highly significant negative correlation for short time lags, indicative of "free" variations in the eddy flux on short time scales. The negative correlation peaks at about -0.45 when the stability parameter lags about one half day behind the eddy flux. The autocorrelation of the eddy flux is compared with that expected for various low-order autoregressive processes.

Application of a Bayesian information criterion indicates that the short-term behavior can be represented best by a second-order model, with a damping time of about 0.8 day and periodicity of about 5 days. Because of the relatively long periodicity, the behavior is also represented quite well by a first-order or red-noise model, with an autocorrelation time of about 0.8 day. These results support theoretical models for the finite-amplitude equilibration of unstable baroclinic waves which yield a Stuart-Watson type of equilibration equation. Such models simulate well the observed short-term fluctuations of the eddy flux of white-noise forcing is added to them, and they predict that the autocorrelation time is just one half the e-folding time of the linearly most unstable wave. The fluctuations of the stability parameter are analyzed in a similar way, and are found to be matched best by a red-noise model, with an autocorrelation time of about two days. However, the cross-correlation indicates that the forcing by the flux should be included in the model for the stability parameter. When this is done, a better fit is obtained for the autocorrelation function of the stability parameter, and an excellent fit for the cross-correlation, if the relaxation time for the stability parameter is about 1.5 days. The red-noise models are used to calculate that the variance of the January mean eddy flux is 9% of the mean, and the variance of the January mean stability is 0.5 m/s.

---

<sup>1</sup> Also authored with S. J. Ghan, D. Spiegel, and S. Rambaldi.

## NORMAL MODE INITIALIZATION AT ECMWF

## C. Temperton/European Centre for Medium Range Weather Forecasts

Normal mode initialization is an essential component of the data assimilation/analysis/forecast cycle at ECMWF; without it, unrealistic high-frequency oscillations soon degrade the quality of the analyses.

In this seminar, we review the procedure for obtaining the normal modes of a multi-level global gridpoint model (linearized about a state of rest), and show how they can be used in both linear and nonlinear initialization techniques. The linear approach does not give very good results, but the nonlinear procedure is highly successful in preventing contamination of the subsequent forecast by spurious oscillations. Moreover, it is computationally very efficient.

However, nonlinear normal mode initialization as currently applied is not entirely free of defects. It is difficult to take into account the highly nonlinear forcing by diabatic processes, and - partly as a consequence - the changes made to the original analysis (especially the surface pressure field) can be uncomfortably large. We conclude by outlining some possible approaches towards improving the procedure.

## LARGE-SCALE BOUNDARY LAYER WINDS

J. A. Young/The University of Wisconsin

Recent research conducted at Wisconsin on the behavior and dynamics of synoptic-scale wind systems in the lower atmosphere over the tropical oceans has been reviewed. Our knowledge about these winds has been substantially improved by recent observational studies such as the Monsoon Experiment and the Global Weather Experiment (1979), and by developing models of cumulus-filled planetary boundary layers. For example, one year's data for the entire low-level monsoon circulation was provided by a geostationary satellite, allowing calculation of kinematic and dynamic fields discussed below. In addition, gust-probe research aircraft data allowed quantitative estimation of scale-dependent turbulent fluxes as well as vertical profiles through the depths of the planetary boundary layer (PBL). These measurements support the need for a multi-layer approach to modeling these flows. The results presented here demonstrated

- a) the usefulness of the FGGE II-b data for diagnostic dynamics studies;
- b) the way that boundary layer processes determine wind response to pressure forces;
- c) the expectation that these understandings can be applied to the problem of data assimilation and verification influencing the surface winds;
- d) the expectation that the resulting III-b data sets, with appropriate PBL assimilations, will allow a complete air-sea interaction history for the global oceans for all of 1979.

The satellite wind fields for the summer monsoon show a dramatic intensification between May and July, with an absolute vorticity distribution which indicates (a) non-conservation along streamlines, and (b) possible inertial instability between the equator and 8N. The wind fields appear to be of sufficient quality to calculate terms in the equations of motion: the mean pressure gradient force field was calculated as a residual for the entire western Indian Ocean, showing how it changed as an accelerating air parcel trajectory was followed. The constraint that this force must be irrotational allows quantitative estimation (by relaxation of Poisson equations) of: (a) the pressure field and (b) the dominant part of the friction field at 1 km altitude.

The difficulties of PBL dynamics include the facts that the flow is highly baroclinic and accelerated in the mean and the turbulence processes depend upon scale and the role of cumulus clouds. These features were clearly seen in profiles of mean flow and fluxes taken from research aircraft data; it was noted that the stress component along the mean flow decreased from the surface, but could experience a reversal or secondary maximum when the cloud-scale eddy fluxes were included. The time scale of frictional decay of the jet flow was in the range of 0.8-3.0 days.

A predictive PBL model with wind and mass adjustments has been developed which attempts to take into account all of these observed features: it represents the PBL mean, flux and cloud activity profiles at three levels whose variation is predicted physically. The model allows the effective friction layer to be shallower than the thermal or moisture boundary layers, as observed. Results were shown for trade-wind simulations indicating dynamically determined wind structures, sensitivity to cloud flux processes, and dependence of clouds and wind profiles upon sea surface temperature. The results indicated good potential for application to III-b data assimilations at low levels.

THE ROLE OF THE OCEAN IN THE TRANSIENT CLIMATIC RESPONSE TO  
INCREASING ATMOSPHERIC CO<sub>2</sub>

K. Bryan/NOAA/Geophysical Fluid Dynamics Laboratory

Many studies have been made of the role of the oceans in absorbing excess atmospheric CO<sub>2</sub>. Less attention has been paid to the role of the ocean in any transient response of climate to rising atmospheric CO<sub>2</sub>. Due to its enormous heat capacity the ocean can delay a warming due to radiative changes in the atmosphere associated with CO<sub>2</sub>. The size of the delay depends on the rate of penetration of heat from the ocean surface to lower levels. The more effective downward pathways are, the slower will be the climatic response to rising CO<sub>2</sub>.

At GFDL a coupled ocean-atmosphere model with an idealized geometry is used to study this problem quantitatively. First, climatic equilibria were determined for normal and 4X normal CO<sub>2</sub> concentrations in the atmosphere. This was done by a relaxation procedure described in previous studies. Next, the normal CO<sub>2</sub> equilibrium climate is perturbed by a step function, 4-fold increase of CO<sub>2</sub>. The response is studied by a detailed synchronous integration of the coupled ocean atmosphere system. Let the normalized response, R, be defined as,

$$R = \frac{T - T_0}{T_\infty - T_0}$$

where T is the sea surface temperature, and T<sub>∞</sub> and T<sub>0</sub> correspond to the high and low CO<sub>2</sub> equilibrium climates. R rises much faster initially in the tropical latitudes, but after a 25 year interval it is nearly uniform at all latitudes with a value between 0.6 and 0.7. The tendency to become uniform with respect to latitude is much greater if T is defined as the surface air temperature.

Figure 1 shows the temperature anomaly after 10 years with respect to the normal CO<sub>2</sub> equilibrium climate for zonal average in the atmosphere and the ocean. Note that the penetration of heat is greatest in the subpolar region where water mass formation normally takes place. Little penetration takes place in the tropical region which is dominated by upwelling.

REFERENCES

Bryan, K., F. G. Komro, S. Manabe, and M. J. Spelman, 1981: Transient response to increasing atmospheric CO<sub>2</sub>. (submitted to Science).

ORIGINAL PAGE IS  
OF POOR QUALITY

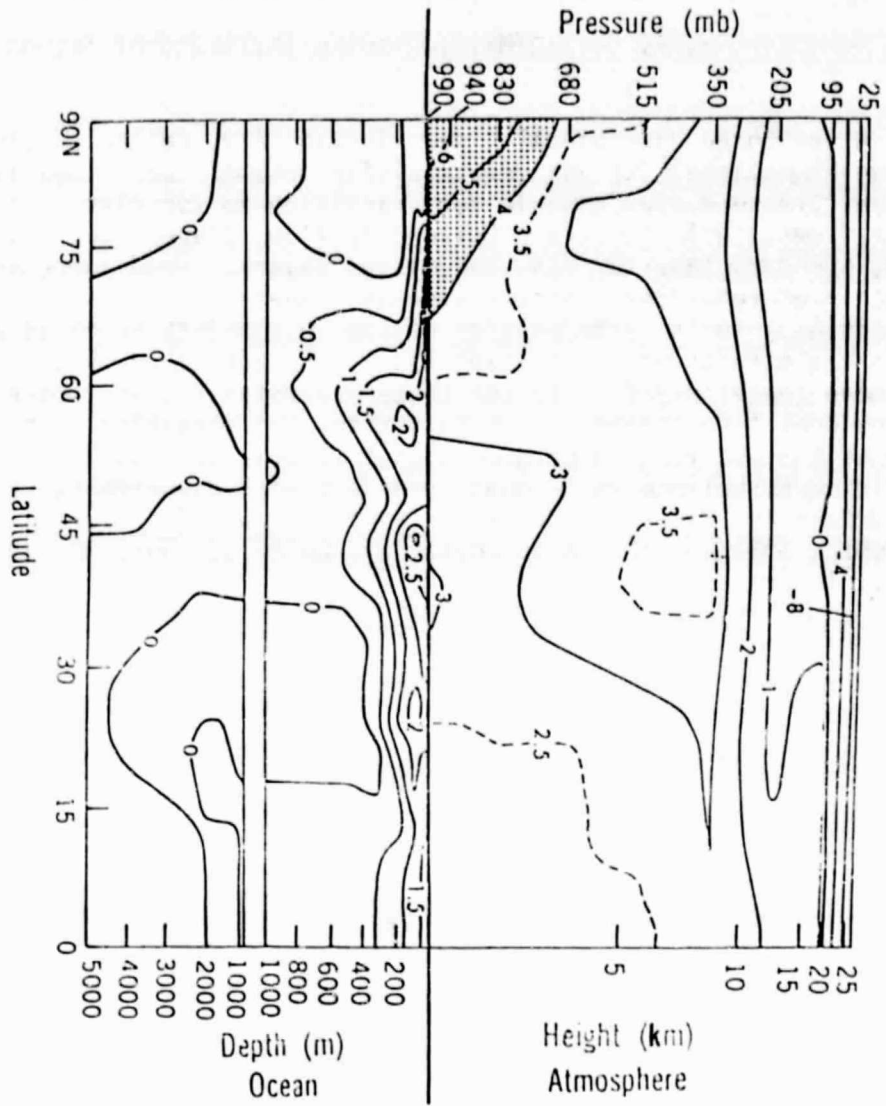


Figure 1

## TRANSITION TO TURBULENCE IN SHEAR FLOWS

S. A. Orszag/Massachusetts Institute of Technology

A new three-dimensional linear instability, called catalytic instability, of two-dimensional (or axisymmetric) finite-amplitude flows is described. This instability seems responsible for transition to turbulence in the classical shear flows, including plane Poiseuille flow, plane Couette flow, pipe Poiseuille flow, boundary layers, jets, and mixing layers. Good agreement with experiment is achieved regarding critical Reynolds numbers and the structure of early transitional spots. The physics of the instability involves a subtle interplay of vortex stretching and tilting and is characterized by energy transfer from the mean (parallel) flow to the three-dimensional disturbance with the two-dimensional flow acting as a catalyst for this transfer. The subsequent evolution of the evolving three-dimensional flow is nonlinear and chaotic. The resulting turbulence is in good agreement with experiment. For further details see Orszag and Patera, 1980; also Transition and Turbulence, ed. by R. E. Meyer, Academic, 1981, p. 127; also Phys. Rev. Letters, Sept. 21, 1981, and J. Fluid Mech., in press.

V. RECENT PUBLICATIONS

## RECENT PUBLICATIONS

- Atlas, R., 1980: Applications of the TIROS-N sounding and cloud motion wind enhancement for the FGGE "Special Effort." Proceedings of the Eighth Conference on Weather Forecasting and Analysis, June 10-13, Denver, Colorado.
- Atlas, R., R. Rosenberg, and G. Cole, 1980: A comparison between an empirical technique for the prediction of cyclogenesis and the LFM II. Proceedings of the Eighth Conference on Weather Forecasting and Analysis, June 10-13, Denver, Colorado.
- Atlas, R., 1980: Evaluation of NESS soundings used in the FGGE "Special Effort." Proceedings of the VAS Demonstration Sounding Workshop. NASA CP-2157, 31-40.
- Atlas, R., 1981: Preliminary results of an assessment of FGGE "Special Effort" data and its impact on GLAS model analyses and forecasts. Preprint volume: Fifth Conference on Numerical Weather Prediction, Nov. 2-6, 1981, Monterey, California.
- Atlas, R., M. Ghil, and M. Halem, 1981: Reply to comment by L. Druyan on time-continuous assimilation of remote-sounding data and its effect on weather forecasting. Mon. Wea. Rev., 109, 201-204.
- Atlas, R., 1981: The role of data, resolution, and physical processes in the numerical prediction of an intense winter storm. Accepted for publication in Current Problems of Weather Prediction Symposium Volume, June 23-26, Vienna, Austria.
- Atlas, R., 1980: TIROS-N sounding and cloud motion wind enhancement for the FGGE "Special Effort." Proceedings of the International Conference on Preliminary Results of the First GARP Global Experiment, June 23-27, Bergen, Norway.
- Baker, W., 1981: The effects of tropical wind data on the prediction of ultralong waves. Proceedings of the Symposium on Current Problems of Weather Prediction, June 23-26, Vienna, Austria.
- Baker, W., D. Edelmann, and H. Carus, 1981: The GLAS editing procedures for the FGGE level II-b data collected during SOP-1 and 2. NASA Tech. Memo. 83811.
- Baker, W., D. Edelmann, M. Iredell, D. Han, and S. Jakkempudi, 1981: Objective analysis of observational data from the FGGE observing systems. NASA Tech. Memo. 82062.
- Baker, W. E., H. Carus, D. Edelmann, J. Gregor, D. Sakal, and J. Wiener, 1980: Preparation of the NMC gridded data for initialization of the GLAS GCM. NASA Tech. Memo. 82007.
- Charney, J. G., J. Shukla, and K. C. Mo, 1981: Comparison of a barotropic blocking theory with observation. J. Atmos. Sci., 38, 762-779.

- Charney, J. G., and D. M. Straus, 1960: Form-drag instability, multiple equilibria and propagating planetary waves in baroclinic, orographically forced, planetary wave systems. J. Atmos. Sci., 37, 1157-1176.
- Duffy, D., 1981: A split explicit reformulation of the Regional Numerical Weather Prediction Model of the Japan Meteorological Agency. Mon. Wea. Rev., 109, 931-945.
- Germani, M. S., I. Gokmen, A. C. Sigleo, G. S. Kowalczyk, I. Olmez, A. M. Small, D. L. Anderson, M. P. Failey, M. C. Gulovall, C. E. Choquette, E. A. Lepel, G. E. Gordon, and W. H. Zoller, 1980: Concentrations of elements in the National Bureau of Standards' bituminous and subbituminous coal standard reference materials. Anal. Chem., 52, 240-245.
- Ghil, M., R. Balgovind, and E. Kalnay-Rivas, 1981: A stochastic-dynamic model for global atmospheric mass field statistics. NASA Tech. Memo. 82009.
- Halem, M., E. Kalnay-Rivas, W. Baker, and R. Atlas, 1981: The state of the atmosphere as inferred from the FGGE satellite observing systems during SOP-1. Proceedings of the International Conference on Early Results of FGGE and Large-Scale Aspects of Its Monsoon Experiments, January 12-17, Tallahassee, Florida.
- Helfand, H. M., 1981: Dependence of tropospheric temperature on the parameterization of cumulus convection in the GLAS model of the general circulation. Mon. Wea. Rev., 109, 65-76.
- Hoffman, R., 1981: Alterations of the climate of a primitive equation model produced by filtering approximations and subsequent tuning and stochastic forcing. J. Atmos. Sci., 38, 514-530.
- Hoffman, R., 1981: A computer program which calculates radiative fluxes and heating rates in model atmospheres. Scientific Rept. No. 4, Project for the Study of Climatic Fluctuations, Volcanic Aerosol, and Carbon Dioxide Changes, Department of Meteorology and Physical Oceanography, M.I.T., Cambridge, Massachusetts.
- Hoffman, R., and E. Kalnay-Rivas, 1981: Lagged averaged forecasting, an alternative to Monte Carlo Forecasting. Preprint volume: Seventh Conference on Probability and Statistics in Atmospheric Sciences, November 2-6, Monterey, California.
- Hoffman, R., and E. Kalnay, 1981: SASS wind dealiasing by direct minimization. EOS, 62, (17), 289.
- Kalnay-Rivas, E., W. Baker, M. Halem, R. Atlas and D. Edelman, 1980: GLAS experiments with FGGE II-b data. Proceedings of the International Conference on Preliminary FGGE Results, Bergen, Norway. (WMO)
- Kalnay, E., and M. Halem, 1981: Large amplitude stationary Rossby waves in the southern hemisphere. Proceedings of the International Conference on Early Results of FGGE and Large-Scale Aspects of Its Monsoon Experiments, January 12-17, Tallahassee, Florida.

- Kalnay, E., W. Baker, and J. Shukla, 1981: Numerical prediction of large scale tropical flow. Proceedings of the WMO Symposium on Meteorological Aspects of Tropical Droughts, December 1981, New Delhi, India.
- Kalnay-Rivas, E., and L. Takacs, 1981: A simple atmospheric model on the sphere with 100% parallelism. Advances in Computer Methods for Partial Differential Equations, IV, pp. 265-268.
- Kalnay, E. and Lee-Or Merkin, 1981: A simple mechanism for blocking. J. Atmos. Sci., 38, 2077-2091.
- Kaplan, L. D., and J. Susskind, 1980: Determination of CO<sub>2</sub> line shape from balloon-based solar spectra. Proceedings of the International Radiation Symposium, August 11-16, Ft. Collins, Colorado, pp. 109-111.
- Korb, C. L., L. D. Kaplan, J. L. Bufton, and C. Y. Weng, 1980: A LIDAR technique for measurement of atmospheric carbon dioxide. Proceedings of the Tenth International Laser Radar Conference. October 6-9, Silver Spring, Maryland, pp. 105-106.
- Moenq, C.-H., and A. Arakawa, 1980: A numerical study of a marine subtropical stratus cloud layer and its stability. J. Atmos. Sci., 37, 2661-2676.
- Moura, A. D., and J. Shukla, 1981: On the dynamics of droughts in northeast Brazil: Observations, theory, and numerical experiments with a general circulation model. J. Atmos. Sci., 38, 2653-2675.
- Paegle, J., E. Kalnay-Rivas, W. Baker, 1981: The role of zonally asymmetric heating in the vertical and temporal structure of the global scale flow fields during FGGE SOP-1. Proceedings of the International Conference on Early Results of FGGE and Large Scale Aspects of its Monsoon Experiments, January 12-17, Tallahassee, Florida.
- Rambaldi, S., and D. A. Randall, 1981: Quasi-Lagrangian models of nascent thermals. Mon. Wea. Rev., 109, 1939-1951.
- Randall, D. A., 1980: Conditional instability of the first kind upside-down. J. Atmos. Sci., 37, 125-130.
- Randall, D. A., 1980: Entrainment into a stratocumulus layer with distributed radiative cooling. J. Atmos. Sci., 37, 148-159.
- Randall, D. A., and G. J. Huffman, 1980: A stochastic model of cumulus clumping. J. Atmos. Sci., 37, 2068-2078.
- Russell, Irving J., C. E. Choquette, S.-L. Fang, W. P. Dundulis, A. A. Pao, and A. A. P. Pszenny, 1981: Forest vegetation as a sink for atmospheric particulates: Quantitative studies in rain and dry deposition. J. Geophys. Res., 86, 5247-5363.

C-4

- Shukla, J., and W. Baker, 1981: Analysis and prediction of the monsoon flow during the summer MONEX. International Conference on Scientific Results of the Monsoon Experiment, October 26-30, Denpasar, Bali, Indonesia.
- Shukla, J., 1981: Dynamical predictability of monthly means. J. Atmos. Sci., 38, 2547-2572.
- Shukla, J., and Y. Sud, 1981: Effect of cloud-radiation feedback on the climate of a general circulation model. J. Atmos. Sci., 38, 2337-2353.
- Shukla, J., and K. R. Saha, 1980: Further evidence of association of westward propagating disturbances with monsoon depressions. FGGE Operations Report No. 9, 23-31.
- Shukla, J., and J. G. Charney, 1981: Predictability of monsoons. Monsoon Dynamics, Cambridge University Press.
- Shukla, J., R. Atlas, and W. Baker, 1981: Numerical prediction of the monsoon depression of 5-7 July 1979. Proceedings of the International Conference on Early Results of FGGE and Large-Scale Aspects of its Monsoon Experiments, January 12-17, Tallahassee, Florida.
- Shukla, J., T. C. Chen, and H. G. Marshall, 1981: Wavenumber-frequency spectra and maintenance of large-scale moving waves by nonlinear interactions at 200 mb of GLAS general circulation model. Mon. Wea. Rev., 109, 959-974.
- Shukla, J., K. R. Saha, and F. Sanders, 1981: Westward-propagating predecessors of monsoon depressions. Mon. Wea. Rev., 109, 330-343.
- Straus, D. M., 1981: Long-wave baroclinic instability in the troposphere and stratosphere with spherical geometry. J. Atmos. Sci., 38, 409-426.
- Straus, D. M., and J. Shukla, 1981: Space-time spectral structure of a GLAS general circulation model and a comparison with observations. J. Atmos. Sci., 38, 902-917.
- Straus, D. M., and M. Halem, 1981: A stochastic-dynamical approach to the study of the natural variability of the climate. Mon. Wea. Rev., 109, 407-421.
- Susskind, J., and J. Rosenfield, 1980: The GLAS physical inversion method for analysis of TIROS-N data. VAS Demonstration Sounding Works. NASA Conference Publication 2157, pp. 41-55.
- Susskind, J., 1980: Spectroscopic requirements for weather and climate research. Spectroscopy in support of atmospheric measurements, Optical Society of America, MA2-1 - MA2-4.
- Susskind, J., and A. Rosenberg, 1980: Temperature retrievals from TIROS-N. Proceedings of Remote Sensing of Oceans and Atmospheres, May 23-25, Williamsburg, Virginia, pp. 45-66.

- Trenberth, K. E., and D. A. Paolino, 1981: Characteristic patterns of variability of sea level pressure in the northern hemisphere. Mon. Wea. Rev., 109, 1169-1189.
- Trenberth, K. E., and D. A. Paolino, 1980: The northern hemisphere sea level pressure data set: Trends, errors, and discontinuities. Mon. Wea. Rev., 108, 855-872.
- Wallace, J. M., and D. S. Gutzler, 1981: Teleconnections in the geopotential height field during the northern hemisphere winter. Mon. Wea. Rev., 109, 784-812.
- Zander, R., H. LeClerco, and L. D. Kaplan, 1981: Concentration of carbon monoxide in the upper stratosphere. Geophys. Res. Letters, 8, 365-368.

VI. G M S F S T A F F

**PRECEDING PAGE BLANK NOT FILMED**

## GMSF Staff

Civil Service

Robert Atlas  
Wayman Baker  
Debora Boyer  
Dean Duffy  
Milt Halem  
Eugenia Kalnay  
David Randall  
Jagadish Shukla  
David Straus  
Yogesh Sud  
Joel Suskind  
Joan Wentz

RRAs

Steve Bloom  
B. N. Goswami  
Ross Hoffman  
Dennis Reuter  
V. Satyan  
V. Serafini  
Richard Wobus

FRAs

Mark Cane  
Michael Ghil

University Consultants

Yale Mintz  
M.-J. Munteanu

M/A-COM Sigma Data

Jim Abeles  
Bob Alls  
Caesar Almeida  
Manina Almeida  
Ramesh Balgovind  
Steve Breining  
Yevgenia Brin  
Sol Broder  
Alex Camerlengo  
Herb Carus  
Carl Choquette  
Duane Cookson  
Amnon Dalcher  
Cheryl Derrington  
Brian Doty  
Margaret Eaton  
Diego Edelmann  
Mike Fennessy  
Lena Fornito  
Chris Frazier  
Catherine Manickam  
David Gutzler  
Eric Hackert  
Bernard Hairston  
Mark Helfand  
Becky Hendricks  
Iris Holmes  
Dan Iredell  
Mark Iredell  
Jane Jonker  
Bert Katz  
Eric Kestler  
John Limpert  
C. L. Lin  
Craig Long

Mike Lyons  
Michael Mandelberg  
Larry Marx  
Margaret McGann  
Dennis Meyers  
Richard Miara  
Kingtse Mo  
Chin-Hoh Moeng  
John Molini  
Gene Murphy  
Fred Nicholas  
Dan Paolino  
Eugene Parlata  
Ernie Pittarelli  
Andy Pursch  
Jody Reckley  
Robert Rosenberg  
Joan Rosenfield  
Dave Rosenthal  
Laura Rumburg  
Mario Salas  
Kathy Schmidt  
Stan Scott  
Rudolph Sheppard  
Rheba Silverstein  
James Sperry  
Steve Stalos  
Brian Swafford  
Lawrence Takacs  
James Tasky  
Lora Thompson  
Gerald Von Ahn  
Dave Wallace  
Ted Wessolleck  
Barbara Worley  
Mary Young